

Electronic operation and control of high-intensity gas-discharge lamps

Citation for published version (APA):

van Casteren, D. H. J. (2012). *Electronic operation and control of high-intensity gas-discharge lamps*. [Phd Thesis 1 (Research TU/e / Graduation TU/e), Electrical Engineering]. Technische Universiteit Eindhoven. <https://doi.org/10.6100/IR724482>

DOI:

[10.6100/IR724482](https://doi.org/10.6100/IR724482)

Document status and date:

Published: 01/01/2012

Document Version:

Publisher's PDF, also known as Version of Record (includes final page, issue and volume numbers)

Please check the document version of this publication:

- A submitted manuscript is the version of the article upon submission and before peer-review. There can be important differences between the submitted version and the official published version of record. People interested in the research are advised to contact the author for the final version of the publication, or visit the DOI to the publisher's website.
- The final author version and the galley proof are versions of the publication after peer review.
- The final published version features the final layout of the paper including the volume, issue and page numbers.

[Link to publication](#)

General rights

Copyright and moral rights for the publications made accessible in the public portal are retained by the authors and/or other copyright owners and it is a condition of accessing publications that users recognise and abide by the legal requirements associated with these rights.

- Users may download and print one copy of any publication from the public portal for the purpose of private study or research.
- You may not further distribute the material or use it for any profit-making activity or commercial gain
- You may freely distribute the URL identifying the publication in the public portal.

If the publication is distributed under the terms of Article 25fa of the Dutch Copyright Act, indicated by the "Taverne" license above, please follow below link for the End User Agreement:

www.tue.nl/taverne

Take down policy

If you believe that this document breaches copyright please contact us at:

openaccess@tue.nl

providing details and we will investigate your claim.

Electronic operation and control of high-intensity gas-discharge lamps

PROEFSCHRIFT

ter verkrijging van de graad van doctor aan de
Technische Universiteit Eindhoven, op gezag van de
rector magnificus, prof.dr.ir. C.J. van Duijn, voor een
commissie aangewezen door het College voor
Promoties in het openbaar te verdedigen
op maandag 27 februari 2012 om 16.00 uur

door

Dolf Henricus Jozef van Casteren

geboren te Oss

Dit proefschrift is goedgekeurd door de promotor:

prof.dr. E.A. Lomonova

Copromotoren:

dr. J.L. Duarte

en

ir. M.A.M. Hendrix

This research was supported by Philips Lighting.

A catalogue record is available from the Eindhoven University of Technology Library. ISBN: 978-90-386-3079-3

Printed by Ipskamp Drukkers B.V., Enschede, The Netherlands.

Copyright © 2012 by D.H.J. van Casteren. All rights reserved.

Summary

Electronic operation and control of high-intensity gas-discharge lamps

The ever increasing amount of global energy consumption based on the application of fossil fuels is threatening the earth's natural resources and environment. Worldwide, grid-based electric lighting consumes 19 % of total global electricity production. For this reason the transition towards energy efficient lighting plays an important environmental role. One of the key technologies in this transition is high-intensity discharge (HID) lighting. The technical revolution in gas-discharge lamps has resulted in the highly-efficient lamps that are available nowadays.

As with most energy efficient light solutions, all HID lighting systems require a ballast to operate. Traditionally, electro-magnetic (EM) ballast designs were the only choice available for HID lighting systems. Today, electronic lamp-drivers can offer additional power saving, flicker free operation, and miniaturisation. Electronic lamp operation enables additional degrees of freedom in lamp-current control over the conventional EM ballasts. The lamp-driver system performance depends on both the dynamics of the lamp and the driver.

This thesis focuses on the optimisation of electronically operated HID systems, in terms of highly-efficient lamp-driver topologies and, more specifically, lamp-driver interaction control. First, highly-efficient power topologies to operate compact HID lamps on low-frequency-square-wave (LFSW) current are explored. The proposed two-stage electronic lamp-driver consists of a power factor corrector (PFC) stage that meets the power utility standards. This converter is coupled to a stacked buck converter that controls the lamp-current. Both stages are operated in transition mode (TM) in order to reduce the switching losses. The resulting two-stage lamp-drivers feature flexible controllability, high efficiency, and high power density, and are suitable for power sandwich packaging.

Secondly, lamp-driver interaction (LDI) has been studied in the simulation domain and control algorithms have been explored that improve the stability, and enable system optimisation. Two HID lamp models were developed. The first model describes the HID lamp's small-signal electrical behaviour and its purpose is to aid the study of interaction stability. The second HID lamp model has

been developed based on physics equations for the arc column and the electrode behaviour, and is intended for lamp-driver simulations and control applications. Verification measurements have shown that the lamp terminal characteristics are present over a wide power and frequency range.

Three LDI control algorithms were explored, using the proposed lamp-models. The first control principle optimises the LDI for a broad range of HID lamps operated at normal or reduced power. This approach consists of two control loops integrated into a fuzzy-logic controller that stabilises the lamp-current and optimises the commutation process. The second control problem concerns the application of ultra high performance (UHP) HID lamps in projection applications that typically set stringent requirements on the quality of the light generated by these lamps, and therefore the lamp-current. These systems are subject to periodic disturbances synchronous with the LFSW commutation period. Iterative learning control (ILC) has been examined. It was experimentally verified that this algorithm compensates for repetitive disturbances. Third, electronic HID operation also opens the door for continuous HID lamp dimming that can provide additional savings. To enable stable dimming, an observer-based HID lamp controller has been developed. This controller sets a stable minimum dim-level and monitors the gas-discharge throughout lamp life. The HID lamp observer derives physical lamp state signals from the HID arc discharge physics and the related photometric properties. Finally, practical measurements proved the proposed HID lamp observer-based control principle works satisfactorily.

Contents

Summary	iii
1 Introduction	1
1.1 Artificial lighting	1
1.1.1 Environmental concern	3
1.1.2 Light pollution	3
1.1.3 High-intensity-discharge lighting	4
1.2 Contribution of the work	5
1.3 Thesis outline	6
1.4 Publications	6
2 High-intensity-discharge lamps	9
2.1 Gas-discharge lamps	10
2.1.1 High-pressure lamp construction	11
2.1.2 Energy conversion metal-halide lamps	13
2.1.3 Spectral power distribution	14
2.2 Stability of the arc	15
2.2.1 Transport processes	16
2.2.2 Helical instabilities	17
2.2.3 Acoustic resonances	17
2.3 Electrical lamp operation	18
2.3.1 High-intensity-discharge lamp operation phases	18
2.3.2 Time scales in lamp operation	20
2.3.3 Lamp-driver current	21
2.3.4 Lamp re-ignition	23
2.4 Discussion	23
3 Physics-based lamp model	25
3.1 Energy balance equations	26
3.2 Parameter identification	30
3.2.1 Experimental set-up	31
3.2.2 Steady-state identification	32
3.2.3 Plasma dynamics identification	34

3.2.4	Plasma dynamics identification results	37
3.2.5	Wall dynamics identification	39
3.2.6	Wall dynamics identification results	40
3.3	Electrode model	42
3.4	Experimental verification	45
3.5	Discussion	46
4	Low-frequency-square-wave drivers	49
4.1	Low-frequency-square-wave topologies	49
4.1.1	Three stage converter	50
4.1.2	Two stage converter	51
4.1.3	Other lamp-driver concepts	52
4.1.4	Power integration	53
4.2	Power-factor-correction	54
4.2.1	Voltage doubler topology	58
4.2.2	Power-factor-correction and lamp-driver interaction	62
4.3	Experimental measurements	63
4.4	Discussion	66
5	Stacked buck converter	69
5.1	Stacked buck topology	69
5.1.1	Zero voltage switching	70
5.1.2	Switching losses	71
5.1.3	Dual branch stacked buck converter	73
5.1.4	Synchronous stacked buck converter	76
5.2	Cycle-by-cycle switching control	78
5.2.1	Peak current limitation	80
5.2.2	Zero current detection	80
5.2.3	Control circuit implementation	82
5.2.4	Control signals of the dual branch converter	84
5.2.5	Control signals of the synchronous converter	85
5.3	Lamp-driver interaction	86
5.3.1	Lamp-driver interaction damping	88
5.4	Experimental set-up	89
5.4.1	Experimental measurements	89
5.5	Discussion	95
6	Lamp-driver interaction control	97
6.1	Small-signal modelling	98
6.1.1	Plasma dynamical behaviour	101
6.2	Lamp-driver interaction simulation	102
6.3	Electrode behaviour	106
6.4	Fuzzy-logic control	109
6.4.1	Fuzzy-logic controlled lamp-driver stability	112
6.5	Experimental results	113

6.6	Discussion	117
7	Light on demand in projection systems	121
7.1	Ultra high performance burner	122
7.1.1	Electrode stabilisation	124
7.2	Projection application	125
7.3	Lamp-driver control strategy	128
7.3.1	System description and varying dynamics	129
7.3.2	System modelling	130
7.4	Robust iterative learning control design	134
7.4.1	Lifted iterative learning control theory	134
7.4.2	Window selection	135
7.4.3	Lifted iterative learning control convergence	136
7.4.4	Robust learning gain design	137
7.5	Measurement results	138
7.6	Discussion	140
8	Observer-based lamp control	143
8.1	High-intensity-discharge lamp observer	144
8.1.1	Observer-based control	145
8.2	Plasma model identification	146
8.2.1	High-intensity-discharge lamp degradation	148
8.2.2	Parameter adaptation throughout lamp life	151
8.2.3	Lamp ageing factor	151
8.3	Optical measurements	153
8.4	Electrode sheath voltage	156
8.4.1	Electrode sheath voltage observation	157
8.4.2	Optical electrode observation	161
8.5	Observer and control	163
8.5.1	Accurate state observation	163
8.5.2	Lamp controller	163
8.5.3	Controller operation	164
8.6	Discussion	166
9	Conclusions	167
9.1	Concluding remarks	167
9.1.1	Highly-efficient electronic lamp-drivers	167
9.1.2	Lamp modelling	168
9.1.3	Lamp-driver interaction control	169
9.2	Thesis contributions	170
9.3	Recommendations	170
A	Simulink figures	173
	Bibliography	191

Samenvatting	193
Acknowledgements	195
Curriculum Vitae	197

Chapter 1

Introduction

1.1 Artificial lighting

The discovery of artificial lighting created a breakthrough for human civilisation, as it became independent from the light of the sun. Fire was probably the earliest source of heat and artificial light. As time passed, candles made of paraffin wax and petroleum oil lamps were developed, and in the beginning of the 19th century natural gas lamps were invented. Although gas lamps gave a better light than oil lamps and candles, the introduction of electric light marked a more significant turning point in artificial lighting. Electric light came into common use in the latter part of the last century.

The invention of the modern filament light bulb is credited to two people Joseph Wilson Swan and Thomas Alva Edison. However, historians [1] list 22 inventors of incandescent lamps prior to Swan and Edison. The contribution of Swan and Edison was that they improved upon previous designs to produce the first reliable, commercially available electric bulb. This 16 W lamp ran on dc current for up to 1500 hours, as stated in a U.S. patent in 1880 (Fig. 1.1).

Francis Hauksbee first demonstrated the principle of a gas-discharge lamp in 1705 [2]. He showed that an evacuated or partially evacuated glass globe, charged by static electricity, could produce a bright light. Because this principle creates light from electricity considerably more efficiently than incandescent lighting, discharge light sources have been researched ever since. The introduction of the metal-halide lamp, which include various metals within the discharge tube that increase the efficiency of visible spectrum emission, was a later advance that became commercially available in the 1930s [3]. Besides their high light efficiency, gas-discharge lamps offer a long life. However, they are also more complicated to manufacture, and require a ballast to provide the correct current flow through the gas.

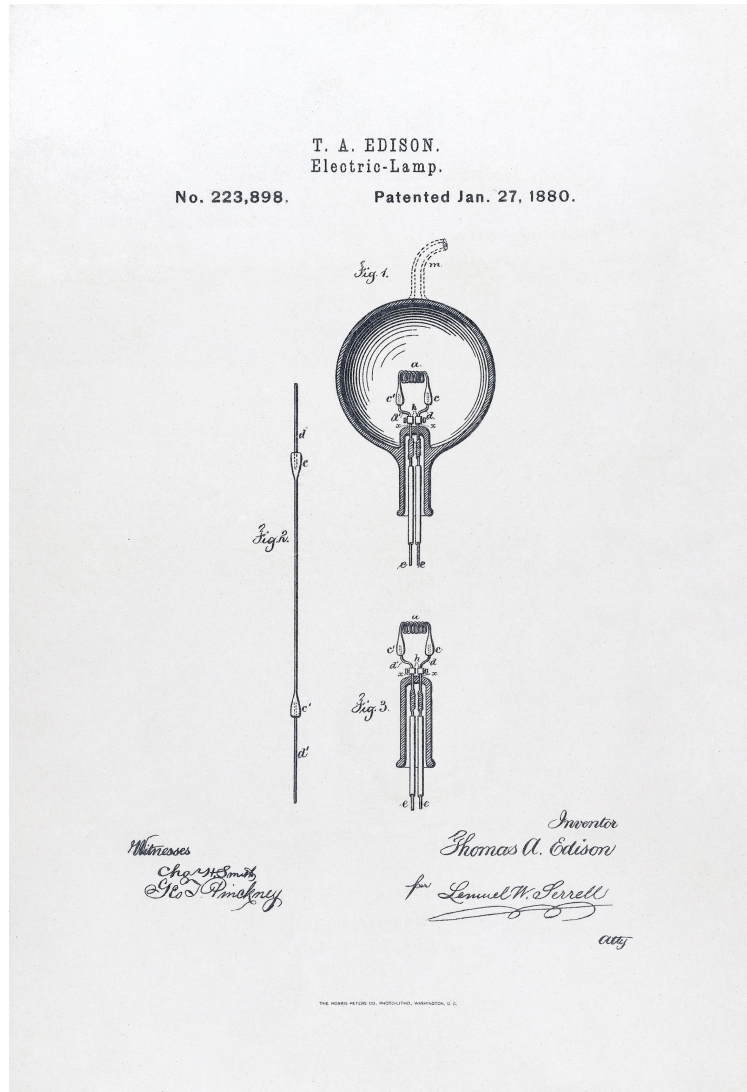


Figure 1.1: Illustration of U.S. Patent No. 233,898 on January 27, 1880.

1.1.1 Environmental concern

Politicians now rank climate change as the world's most important environmental concern. Accordingly, global energy consumption and the use of fossil fuels are often the subjects of debate. Fossil fuels are formed by the anaerobic decomposition of buried dead organisms that lived more than 300 million years ago. Nowadays, over 85 % of the energy demand of modern society worldwide is met by the combustion of fossil fuels. According to statements in the intergovernmental panel on climate change (IPCC) [4] human kind's reliance on fossil fuels is to blame for the average temperature increases of the Earth's atmosphere and oceans.

According to the energy information administration's (EIA) annual energy outlook for 2009, global energy consumption is projected to increase 50 % from 2005 to 2030 [5]. The credit crisis has slowed down predicted growth of the world's energy usage somewhat. The energy demand for lighting plays a significant role to this global environmental issue. World-wide, grid-based electric lighting consumes 19 % of total electricity production. With current economic and lighting trends, it is projected that global demand for artificial light will be 80 % higher by 2030. However, by simply making better use of today's cost-effective efficient-lighting technologies and techniques, global lighting energy demand need not be any higher in 2030 than it is now.

1.1.2 Light pollution

Artificial light at night enables humans to live, work and play for 24 hours a day. However, in the current lighting environment there are enormous sources of waste. Electric light, mostly generated from fossil fuels, is often supplied to spaces that are not used or where no one is present. Moreover, the advent of powerful and affordable artificial lighting has allowed poor architecture to prosper. Uninspired building design has brought us dark boxes where the largest, cleanest and highest-quality source of light, daylight, often cannot reach [6].

In outdoor situations we call misdirected or misused light "light pollution". In general, this pollution results from an inappropriate application of exterior lighting products. Figure 1.2 shows the sheer amount of light that is going up into the sky. This colossal waste of energy merely illuminates our night skies and confuses insects and animals. Breeding patterns are disturbed, food chains disrupted, and vast amounts of carbon dioxide are generated by power stations that create the electricity that lights up the night sky.

The image of Earth's city lights in Fig. 1.2 is based on radiance-calibrated high-resolution defence meteorological satellite program (DMSP) data, and on accurate modelling of light propagation in the atmosphere [7]. It provides a global picture of how mankind is proceeding to envelop itself in a luminous fog [8]. The brightest areas of the Earth are the most urbanised, but these areas are not necessarily the most populated (compare Western Europe with China and India). Cities tend to grow along coastlines, and transportation networks.

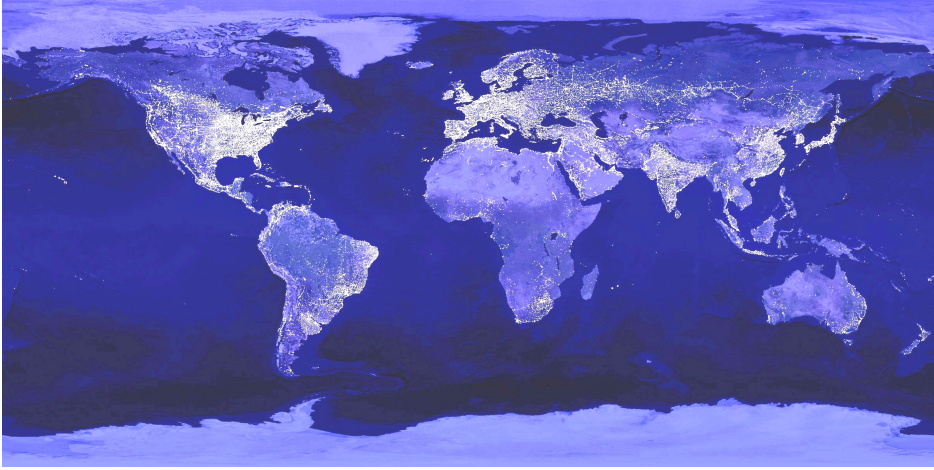


Figure 1.2: Atlas of the zenith artificial night sky brightness (Data courtesy of NASA [7]).

Even without the underlying map, the outlines of many continents would still be visible. Even more than 100 years after the invention of the electric light, some regions remain thinly populated and unlit; for example, Antarctica is entirely dark.

1.1.3 High-intensity-discharge lighting

The energy consumption concerns mentioned above have initiated a transition from classic incandescent lighting to more energy efficient technologies. This transition is being accelerated in many nations by legislation. Most of the energy efficient lighting systems that are currently available can be divided into the following technology categories: fluorescent, high-intensity-discharge (HID), and solid-state lighting (SSL).

This thesis focuses on HID lighting systems. These systems are traditionally widely used in applications where high light levels and a long life time are desired for large areas, such as industrial high-bay spaces, parking areas, and street lighting. Those high power HID lamps are commonly based on high pressure sodium (HPS) vapour, and metal-halide (MH) technology.

In the last ten years the ceramic metal-halide (CMH) lamp technology has expanded the application range of HID lighting, especially in colour critical areas. While still primarily intended for indoor lighting applications, CMH lamps are also becoming popular for high-end outdoor installations, for example in city beautification projects. CMH technology was first introduced in 1994 to solve the problems inherent in older style quartz MH lamps such as high lumen depre-

ciation, low colour rendition, and poor colour consistency [9].

Similar to most energy efficient light solutions, all HID lighting systems require an additional circuit, or “ballast”, to operate. Traditionally, electro-magnetic (EM) ballast designs were the only choice for HID lighting systems. Today, high-efficiency electronic HID ballasts are available that enable system optimisation to improve light technical qualities like colour consistency, and lumen depreciation. Electronic HID operation also opens the door for stable deep dimming of HID lamps. HID lamp dimming has grown in popularity in recent years. Dimming HID lamps can result in energy savings, peak electricity demand reduction, and greater flexibility in multi-use spaces.

1.2 Contribution of the work

The use of HID lamps in critical applications such as shop lighting, city beautification, and projection usage (e.g. beamers), sets both new and stringent requirements on the quality of the light generated by these lamps. For these applications electronic lamp operation is the designated method to enable high-efficiency, advanced control, and continuous dimming. For electronic HID lamp operation, low-frequency-square-wave (LFSW) current is the best option to operate a large variety of the HID lamps in the market.

In LFSW lamp-drivers a number of energy conversion steps are incorporated between the grid connection and the lamp terminals. This power conversion can be realised in two serial connected power electronic stages. In this research this two stage concept is studied and high-efficiency versions are proposed [10–16], including cycle-by-cycle control principles [17–19].

The main aim in HID system design is an optimised lamp-driver interaction, because the system performance depends on both the dynamics of the lamp and the characteristics of the ballast. Therefore, first a simple model that describes the HID lamp’s small-signal electrical behaviour is presented, which is used to study the lamp-driver interaction stability. Secondly, a phase resolved metal-halide lamp model that relies on energy conservation principles is described [20], which is intended for lamp-driver simulations and observer-based control applications.

To optimise the system performance, the results of this ground work are used to study a number of lamp-driver interaction control principles. The first approach presented is based on two control principles integrated in a fuzzy-logic lamp-driver controller that stabilises the HID lamp-current and optimises the LFSW commutation process [21–24].

The second case concerns the application of ultra high performance (UHP) HID lamps in projection systems. Deviations of the lamp-current from the desired modulation scheme translate into artefacts in the projected image. To be able to meet the stringent requirements on the lamp-current performance, a new iterative learning control (ILC) approach [25–28] was explored.

Finally, to create an “intelligent” electronic lamp-driver an observer-based lamp controller was constructed on the basis of the physical lamp modelling efforts. The observer derives physical lamp state signals closely associated with the HID arc discharge physics and the related photometric properties. This new HID lamp control principle enables stable HID lamp dimming by setting a minimum dim-level and monitoring the gas-discharge throughout the lamp’s life [29–31].

1.3 Thesis outline

The importance of high pressure gas-discharge lighting in the transition towards energy efficient lighting is briefly noted in this introduction. In Chapter 2 the HID lamp construction and first principles concerning the lamp operation requirements are presented. These requirements, together with the power utility standards, define the power electronic interface between the mains grid and the lamp terminals. The most commonly applied LFSW topological approaches are discussed in Chapter 4, including the proposed two stage lamp-driver concept. Furthermore, in this chapter the first step of the proposed concept concerning the power-factor-correction (PFC) is addressed and high-efficiency boost converter topologies are explored. Chapter 5 deals with the second lamp-driver stage, which concerns a stacked buck converter topology. Two highly efficient solutions are presented and practical measurements are performed.

The physical properties of metal-halide discharge lamps are researched in more detail in Chapter 3, and a phase resolved metal-halide lamp model, intended for lamp-driver simulation and observer-based control application, is presented. In practice, the HID system performance depends strongly on the lamp-driver interaction (LDI). Therefore, in Chapter 6 the LDI stability and the HID lamp re-ignition are studied, and a fuzzy control approach is presented to optimise those parameters. Accurate lamp-current control becomes increasingly important, especially in critical HID projection applications. This current control problem is analysed, and a repetitive control principle is described and tested in Chapter 7. In Chapter 8 an observer-based LDI control approach is derived based on the physical lamp modelling efforts. Finally, conclusions, contributions and recommendations are given in Chapter 9.

1.4 Publications

The main contributions of the research discussed in this thesis have been published in the following journals, conferences, and patents.

Journal papers

- D. H. J. van Casteren, M. A. M. Hendrix, and J. L. Duarte. Controlled

HID lamp-ballast interaction for low frequency square-wave drivers. *IEEE Transactions on Power Electronics*, vol. 22, no. 3, pp. 780–788, 2007.

- D. H. J. van Casteren, M. A. M. Hendrix, and J. L. Duarte. Transition mode stacked buck converter for HID lamps. *IEEE Transactions on Industry Applications*, vol. 44, no. 1, pp. 68–73, 2008.
- I. Josifović, J. Popović-Gerber, B. Ferreira, and D. H. J. van Casteren. Multi-layer SMT high power density packaging of electronic ballasts for HID lamps. *IEEE Transactions on Industry Applications*. (Accepted for publication in 2012).

Conference papers

- D. H. J. van Casteren and M. A. M. Hendrix. Stacked buck converter for HID lamps. In *Proc. 39th IEEE IAS conf.*, vol. 1, pp. 693–697, 2004. (Conference paper award).
- D. H. J. van Casteren and M. A. M. Hendrix. Improved current control for HID lamp drivers. In *Proc. 40th IEEE IAS conf.*, vol. 2, pp. 1182–1187, 2005.
- D. H. J. van Casteren, M. A. M. Hendrix, and J. L. Duarte. Physics based MATLAB model for ceramic metal halide lamps. In *Proc. 41th IEEE IAS conf.*, vol. 3, pp. 1391–1396, 2006.
- D. H. J. van Casteren and R. L. Tousain. Digital control for improved UHP lamp performance. In *Proc. 11th Int. Symp. on Sci. and Tech. of Light Sources conf.*, vol. 1, no. LL15, pp. 291–292, 2007.
- R. L. Tousain and D. H. J. van Casteren. Iterative learning control in a mass product: Light on demand in DLP projection systems. In *Proc. American control conf.*, vol. 1, pp. 5478–5483, 2007. (Invited paper).
- D. H. J. van Casteren, M. A. M. Hendrix, and J. L. Duarte. Observer-based ceramic HID lamp control. In *Proc. 43th IEEE IAS conf.*, vol. 1, pp. 1–8, 2008.
- I. Josifović, J. Popović-Gerber, B. Ferreira, and D. H. J. van Casteren. Multi-layer SMT high power density packaging of electronic ballasts for HID lamps. In *Proc. 2th IEEE ECCE conf.*, pp. 1275–1282, 2010.

Patents

- D. H. J. van Casteren and O. J. Deurloo. High pressure discharge lamp circuit with successive current phases for operating the lamp in a dimmed state. WO Patent 2002019779-A1, 2002.
- O. J. Deurloo, D. H. J. van Casteren, and M. Krijzer. Switch mode power supply for igniting and operating a high-pressure gas-discharge lamp, comprises ignition sub-circuit with ignition capacitor and switching element having control electrode connected to commutator of lamp circuit. WO Patent 2003009648-A1, 2003.

- D. H. J. van Casteren. Operating device for high-pressure discharge lamp, has controller that regulates on and off condition of switching circuit to control power or current supplied to high-pressure discharge lamp. WO Patent 2003061352-A1, 2003.
- D. H. J. van Casteren and W. D. Couwenberg. Ballast circuit for discharge lamp, has state control circuit to change level of output voltage of dc-dc converter from higher level associated with lamp starting to lower level associated with stationary operation of lamp. WO Patent 2003075619-A1, 2003.
- D. H. J. van Casteren. Gas-discharge lamp-driver, has control unit to generate control signals at low commutation intervals and in high frequency operational phases such that two switches are switched simultaneously in counter-phase. WO Patent 2004010742-A2, 2004.
- T. Oosterbaan, D. H. J. van Casteren, and R. H. A. M. van Zundert. Drive circuit for high pressure discharge lamp for projector, adjusts reference signal for controlling direct current, based on amplitude of periodical voltage across output capacitor caused by commutation of direct current. WO Patent 2004045255-A2, 2004.
- D. H. J. van Casteren. Boost converter used with input stage of full electronic ballast to transform ac mains voltage, for discharge lamp, has RF interference filter connected between ac mains terminals and series connection of boost inductor and switch MOSFETs. WO Patent 2005107054-A1, 2005.
- D. H. J. van Casteren and R. L. Tousain. Lamp-driver for use in projection system, has setpoint signal generator with correctional setpoint signal generator for setpoint signal, and synchronizer for synchronizing generator to principal setpoint signal. WO Patent 2006046199-A1, 2006.
- F. Peeters and D. H. J. van Casteren. Lamp-driver circuit arrangement for operating e.g. high intensity discharge lamp, has control circuit with adaptive feedback controller for adjusting control loops based on variations of actual system behavior. WO Patent 2006056918-A1, 2006.
- D. H. J. van Casteren. Operating method for gas-discharge lamp, involves controlling operating current of gas-discharge lamp based on determined operating state of gas-discharge lamp. WO Patent 2008072158-A2, 2008.
- R. L. Tousain and D. H. J. van Casteren. Driver for driving gas-discharge lamp e.g. metal-halide lamp, has controller for comparing measured characteristic response of lamp with preset reference signal stored in memory. WO Patent 2008093259-A1, 2008.

Chapter 2

High-intensity-discharge lamps

High-intensity-discharge (HID) lamps feature high luminous efficiency, long life time, and high brightness. Application of these lamps in small reflective luminaries creates compact powerful light sources, which are suitable for outdoor flood and indoor spot lighting. From the generation of the first continuous arc discharge in 1810 by Humphry Davy [32], numerous inventions have driven the technical revolution in HID lamps. The first practical HID lamps were developed in the 1930s with hard glass arc tubes [3]. These discharge tubes were dosed with a small amount of mercury which evaporates completely during operation. As a result, the arc discharge between both tungsten electrodes emitted a light spectrum with only a few strong lines. The introduction of quartz discharge vessels in the 1960s enabled the application of metal-halide additives [33] to the mercury, to improve the luminous efficiency and colour rendering.

The next significant development step was the introduction of translucent poly-crystalline alumina (PCA) discharge vessels. These were used for high-pressure sodium (HPS) lamps around 1965 [34] and later metal-halide lamps. The PCA discharge vessel is highly resistant to the aggressive discharge fill compounds and enables operation of the metal-halide compounds at higher temperatures. Metal-halide lamps with ceramic PCA arc tube design were introduced in the 1990s [35] and offer improved colour rendering, colour control and luminous efficiency throughout their lifetime.

This chapter gives a general description of the characteristics of HID lamps and is organised as follows. In Section 2.1 the basics of gas-discharge lamps are briefly presented, together with the elementary differences between low and high-pressure gas-discharge burners. Furthermore, the construction of ceramic HID lamps, their energy conversion, and spectral distribution are discussed. In Section 2.2 a concise description, dealing with the stability of the plasma arc inside the discharge vessel, is given. The HID lamp operation from an electrical point of

view is introduced in Section 2.3. This section also describes the different phases from ignition to stable arc operation, and the influence of the lamp-current wave shape on the operation conditions. Finally, conclusions are drawn in Section 2.4.

2.1 Gas-discharge lamps

The plasma arc, in which electric energy is partly transformed into electromagnetic radiation, is the essence of a gas-discharge lamp. Plasma is a gas in which a certain portion of the particles are ionised, making it electrically conductive. It consists of positive ions, negative electrons, and neutral atoms. Applying an electric field leads to collisions between the electrons and gas atoms. The inelastic collisions that lead to ionisation and excitation are important in this process. Ionisation creates new electrons and ions, where excitation is followed by de-excitation with the emission of electromagnetic radiation.

After ignition, the continuing ionisation process can lead to an increasing number of free electrons and (if no current limiting device is incorporated into the lamp circuit) an unlimited electrical current through the gas-discharge lamp. In other words, the plasma arc has a negative incremental impedance, and the application of a lamp-driver is essential for ignition and failure free operation.

A clear distinction can be made between high and low pressure gas-discharge lamps, based on the temperatures of the particles. For low-pressure gas-discharges there is a low degree of interaction between the electrons and the gas. As a result, the electron temperature is higher than the gas temperature ($T_e \gg T_{\text{ion}} = T_g$), as shown in Fig. 2.1. In high-pressure gas-discharges the number of electron – gas atom collisions is so high that a local thermal equilibrium (LTE) [36] results ($T_e = T_{\text{ion}} = T_g$). As presented in Table 2.1, this difference has many consequences regarding the properties of low and high-pressure gas-discharge lamps.

Table 2.1: General characteristics of high and low-pressure lamps.

Characteristic	Low-pressure	High-pressure
T_e	10000 K	3000 K
T_g	350 K	3000 K
Radiation	“Narrow” lines	“Broad” lines
Envelope	Soft glass	Quartz or ceramic
Size	Large	Compact
Operating pressure	< 1 Bar	> 1 Bar
Power range	4 - 200 W	20 - 6000 W
Luminous flux	0.1 - 35 klm	2 - 600 klm
Luminous efficacy	50 - 200 lm/W	50 - 150 lm/W
Luminance	Low	High

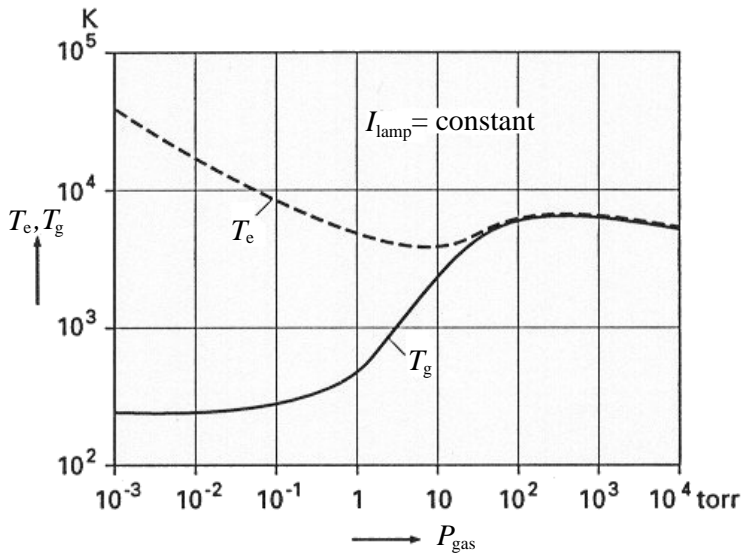


Figure 2.1: The electron temperature T_e and the gas temperature T_g in a mercury discharge as a function of the mercury vapour pressure P_{gas} [37].

2.1.1 High-pressure lamp construction

This research is focused on high-pressure metal-halide lamps and short-arc ultra high performance (UHP) projection lamps. The latter are discussed in more detail in Chapter 7. A detailed view of a compact metal-halide lamp with a ceramic discharge vessel is shown in Fig. 2.2, with a description of the most important elements of the lamp's construction.

The most important part of the high-pressure lamp is the arc tube. The arc tube is the enclosure where light is produced, and can be pictured as a closed cylindrical container with tungsten metal electrodes at each end. The tube is made of a diffuse translucent ceramic material, PCA (poly-crystalline aluminium-oxide, Al_2O_3). The introduction of PCA for HID lamps allows higher wall temperatures (over 1500 K), whereas quartz is limited to 1300 K. This provides the opportunity to operate lamps with higher metal-halide vapour pressures, resulting in improved efficacy and colour rendering.

The projected ceramic discharge vessel in Fig. 2.2 is composed of five PCA pieces. On both sides the tungsten electrode is connected to the lead wire via a Niobium gas-tight ceramic-to-metal seal. The Niobium rod has a coefficient of expansion close to that of sintered alumina and is resistant to the metal-halide compounds at high temperatures. The arc tube is sealed with molten glass made of an oxide mixture, also called sealing frit. Before the tube is sealed during the

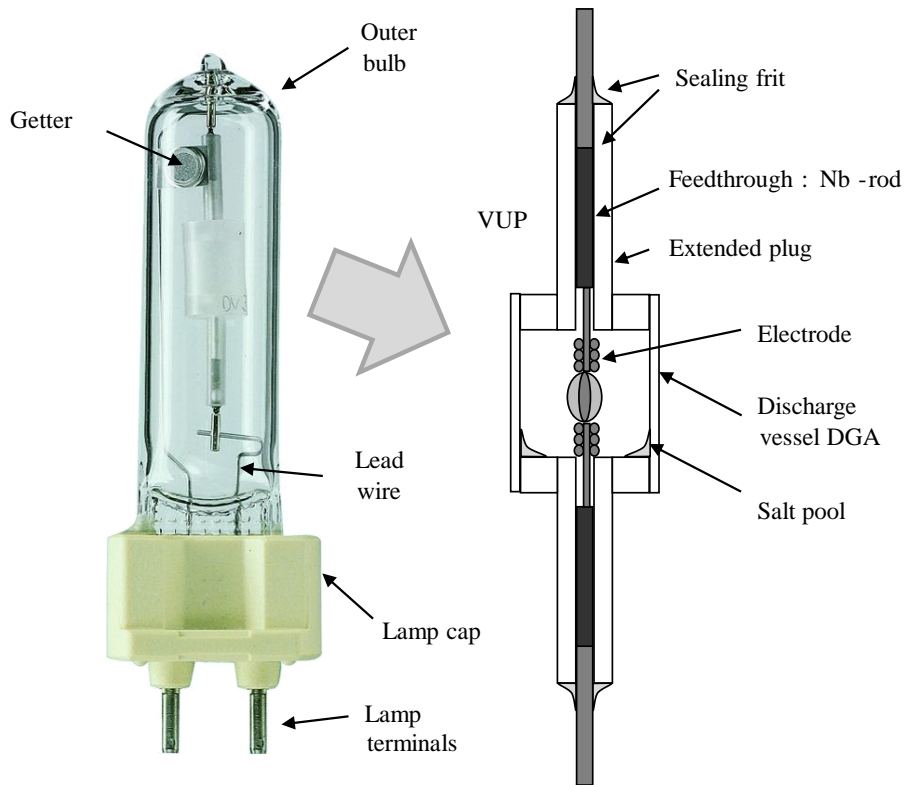


Figure 2.2: A schematic view of the construction of a compact ceramic metal-halide HID lamp (Philips CDM-T 73W).

production process, the filling substances are dosed inside. The filling can be divided into the following main components:

- Start gas
To be able to achieve breakdown with a moderate ignition voltage (ranging between 3 kV and 4 kV), a noble gas at low pressure is present in the cold lamp. In practice, argon and xenon are employed at a pressure of 30 to 100 mbar.
- Buffer gas
The buffer gas determines, together with the distance between the electrodes, the lamp voltage at steady-state. In almost all HID lamps mercury is applied. This element vaporises completely during the warm-up phase and builds up a high-pressure, which results in a high voltage gradient.
- Radiation-emitting substances
In a number of cases, like UHP burners, the buffer gas is also the radiation-emitting substance. In metal-halide lamps additional halides with low partial pressures are brought into a gaseous state during operation. The power radiated in the added metal-halide spectrum exceeds that of the buffer gas. The halides used are bromides and iodides of rare earth metals (e.g. Na, Sc, Tl, Dy and In).

The discharge vessel is encapsulated in the glass outer bulb that protects the arc tube and lead frame from oxidation and heat loss. The outer bulb can be a vacuum or it might be filled with a gas that has a high breakdown voltage. A getter is applied to free the outer bulb from any impurities. Furthermore, the outer bulb blocks short wavelength UV light that is generated by the discharge, and transmitted by the PCA arc tube. The ceramic cap has two functions: mechanical fixation of the lamp in an optical system, and electrical connection to the lamp circuit.

2.1.2 Energy conversion metal-halide lamps

The luminous efficiency of an HID lamp, expressed in lumens per Watt (lm/W), is defined by both the power conversion from electrical input power P_{lamp} to light P_{rad} , and the spectral light distribution correlated to the eye sensitivity curve [38]. The power conversion efficiency of an HID lamp, which depends on the energy loss mechanisms that take place inside the discharge lamp, can be presented in an energy balance diagram. A typical energy balance for a (Na-Ti-In) metal-halide lamp [39] is shown in Fig. 2.3.

The electrical input power, P_{lamp} , is transferred to the plasma arc, P_{arc} , and partially dissipated in the electrodes, P_{ele} , to maintain a sufficient temperature for thermionic electron emission. A considerable part of the power in the plasma column, P_{arc} , is converted to electromagnetic radiation, P_{rad} , where the remaining power is transferred by conduction, P_{cond} , to the arc tube wall. The radiated

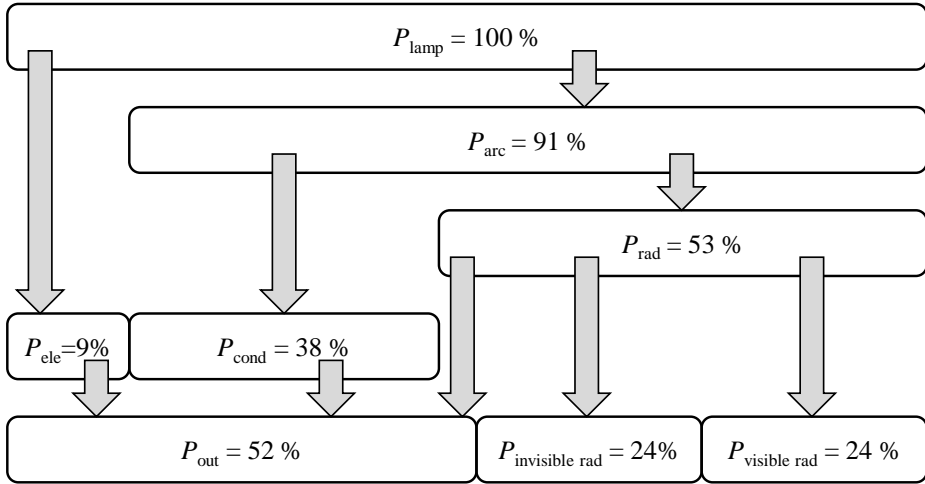


Figure 2.3: Energy balance of a metal-halide discharge lamp.

power consists of light at visible wavelengths, $P_{\text{visible rad}}$, and inevitably a certain amount at invisible wavelengths, $P_{\text{invisible rad}}$. The latter light consists of long-wave radiation (infra-red) and short-wave radiation (ultraviolet). In general, the outer bulb converts almost all the UV radiation into heat (UV block). At the outer bulb the thermal energy of the electrodes, P_{ele} , the discharge tube conduction losses, P_{cond} , and the radiation absorption losses are dissipated. In turn, the outer bulb releases the thermal power P_{out} via thermal radiation, conduction and convection. In Chapter 3 an HID lamp model is presented, based on the discharge energy balance as shown in Fig. 2.3.

2.1.3 Spectral power distribution

High-pressure gas-discharge lamps transform electrical energy into heat and electromagnetic radiation. A considerable part of the radiation is at visible wavelengths. In Fig. 2.4 the spectral energy distribution and light-technical properties for two Philips metal-halide HID lamps with ceramic discharge vessel are shown. This compact 73 W burner is available in two colour temperatures: 3000 K (Fig. 2.4(a)), and 4200 K (Fig. 2.4(b)). The luminous flux Φ , the efficiency η , correlated colour temperature (CCT), and colour rendering index (CRI) are measured. The measurement set-up is discussed in Section 8.3.

Metal-halide lamps are high-pressure mercury lamps with metal-halide additives that enrich the mercury light spectrum and increase the luminous efficiency. In general, these lamps are operated with a saturated metal-halide vapour. Therefore, during operation a condensate salt pool remains at a cold spot on the dis-

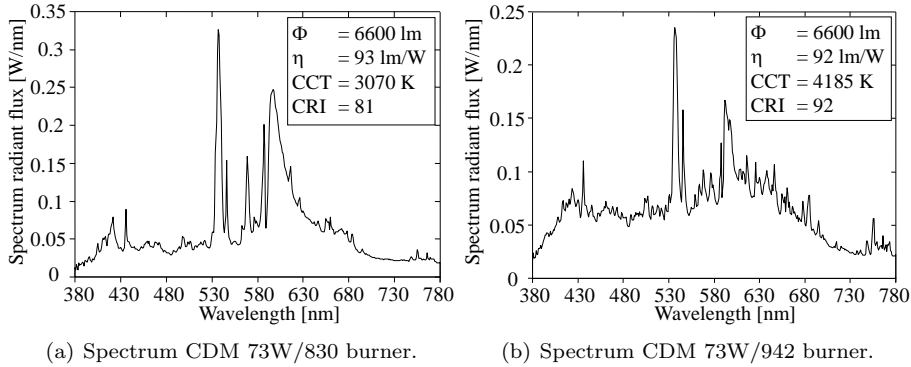


Figure 2.4: Spectral measurements of Philips HID lamps at visible wavelengths.

charge wall, where the cold spot temperature defines the partial vapour pressures of the existing halides. The intensity and spectral distribution greatly depend on the partial pressures of the metal-halide compounds. In turn, the cold spot temperature is strongly related to the electrical input power of the lamp. In Section 8.3 the most important photometric properties are experimentally measured as a function of the lamp power.

2.2 Stability of the arc

To prevent flickering, the plasma arc inside the discharge vessel is stabilised by one of the following mechanisms:

- **Wall-stabilised arcs**
For low pressure discharges (e.g. fluorescent lamps), the arc is diffuse and completely fills the discharge tube; therefore these arcs can be characterised as wall stabilised.
- **Convection dominated arcs**
Most high-pressure discharge lamps, and in particular metal-halide lamps, have some arc constriction. These constricted arcs are less wall stabilised and more dominated by convection flows, and thus have the tendency to become curved and instable as discussed in Section 2.2.1. The arc constriction is strongly related to the dosed metal-halide compounds. Some additives lead to strong arc constriction, while others have exactly the opposite effect [33].
- **Electrode-stabilised arcs**
Ultra short arc lamps like UHP burners have concentrated arcs stabilised between the short electrode gap. In this case the arc attachment to the electrode is extremely important for stable operation.

2.2.1 Transport processes

Transport processes in HID lamps are responsible for effects that are very important to the stable operation of the device. In Fig. 2.5 a schematic view of the convection and diffusion transport processes for vertically and horizontally orientated discharge vessels is given.

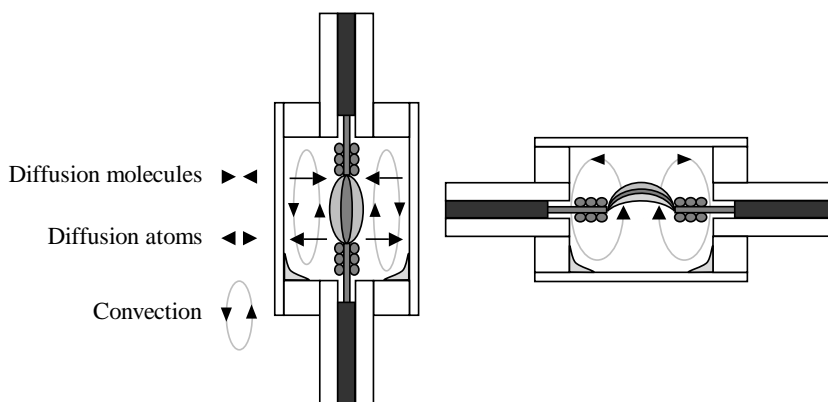


Figure 2.5: A schematic view of the transport processes in HID lamps. For the vertically oriented discharge vessel the convection and diffusion flows are displayed, where for the horizontally oriented vessel only the convection process is given.

Inside the discharge vessel a large temperature gradient between the wall (1200 K) and the plasma core (4500 K) establishes during operation. This temperature gradient leads to mass density differences between the plasma core and the wall region. In turn, the force of gravity will induce convective circulatory motion inside the discharge vessel [40], as shown in Fig. 2.5.

Secondly, metal-halide molecules diffuse to the core of the discharge. There, due to the density and temperature gradient, they decompose and release the metal atoms. These atoms will be excited or ionised and emit visible radiation. The same force causes the metal and iodine atoms to diffuse from the plasma core to the colder wall region, where they recombine again and become less aggressive to the wall.

The diffusion and convection processes in the plasma can lead to radial and axial segregation of the metal-halide additives [41]. Especially in vertically operated HID lamps, the demixing of the metal-halides results in non-uniform light output with colour segregation across the axis, and reduced efficiency and colour rendering ability of the lamp.

2.2.2 Helical instabilities

Helical instabilities have been observed [37] in vertical wall-stabilised arcs. Such instabilities occur when the current induced magnetic force exceeds the wall-stabilising forces [42]. The cylindrical arc column changes to a helical form that rotates around the central axis in the shape of a corkscrew. The strong constriction of the arc increases the self-magnetic force, and therefore the chance of helical instabilities [43]. Although the instability may not have a direct detrimental effect on the efficiency of the lamps, those which are unstable for a prolonged period, may develop a crack in the wall of the burner.

In HID lamps, physical phenomena are severely influenced by the Earth's normal gravity conditions [44]. Therefore, the radial segregation and helical instabilities in metal-halide lamps have been studied under micro-gravity conditions in the international space station (ISS) [45].

2.2.3 Acoustic resonances

Operation of HID lamps on current waveforms that comprise high-frequency components is hampered by the occurrence of standing pressure waves (acoustic resonances) [46]. At certain frequencies, the arc becomes unstable because of standing waves present in the plasma. Such acoustic resonances cause various problems, such as arc instability, light output fluctuations and colour temperature variations. They also increase the lamp's voltage, which may cause arc extinction or, in the worst case scenario, a cracked arc tube. In Fig. 2.6 the arc discharge of a high-pressure sodium lamp is shown for both states, that is, on and off resonance [34]. The discharge vessel's high aspect ratio makes the resonances clearly visible.

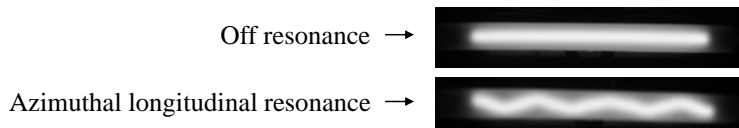


Figure 2.6: Pictures of high-pressure sodium lamp discharge tubes [34]. Showing the occurrence of standing waves in the plasma.

From a theoretical point of view, the acoustic resonance phenomenon is relatively well understood [47]. The frequencies at which the arc distortions occur can be correlated to the eigen-frequencies of standing acoustic pressure waves in the discharge tube (equivalent to an organ pipe). Those periodic pressure oscillations, driven by periodic instantaneous lamp power, behave according to the wave equation [34]

$$\nabla^2 p = \frac{1}{c_s^2} \frac{\partial^2 p}{\partial t^2}, \quad (2.1)$$

where c_s is the velocity of sound, p is the gas pressure, and t is time. To be applicable for high-pressure gas-discharges (2.1) is extended by a damping and excitation term

$$\frac{\partial^2 p}{\partial t^2} + \zeta \frac{\partial p}{\partial t} - c_s^2 \nabla^2 p = \left(\frac{c_p}{c_v} - 1 \right) \frac{\partial P_v}{\partial t}, \quad (2.2)$$

where ζ represents the damping coefficient, P_v is the power input per unit volume of the gas, and c_p, c_v are the specific heat capacities for the gas at constant pressure and constant volume, respectively. This equation can be solved by applying boundary conditions, resulting in radial longitudinal and azimuthal longitudinal modes.

The lamp eigen-frequencies depend on arc vessel geometry and gas filling, i.e. gas thermodynamic state variables (pressure, temperature and density). Both the arc vessel geometry and gas filling vary with manufacturing tolerances, while the thermodynamic state variables will also change as the lamp ages [48]. The occurrence of acoustic resonances can be avoided by choosing the proper discharge tube shape, dimensions, gas filling, and pressure, and by carefully designing the lamp-current wave-shape [49]. The latter will be discussed in more detail in Section 5.3 concerning lamp-driver interaction.

2.3 Electrical lamp operation

2.3.1 High-intensity-discharge lamp operation phases

The process from ignition to stable arc operation involves different phases, each representing a distinct discharge condition. This transition turns the start gas and other elements inside the discharge tube from an insulator into a high-temperature, high-pressure plasma. The different phases of lamp operation are shown in Fig. 2.7 and can be described as follows:

Ignition - Before the lamp is turned on the gas inside the discharge vessel behaves as an insulator. To initiate the starting process, a high voltage (3 kV to 4 kV) is applied across the lamp terminals. An electric field is established in the start gas between both electrodes.

Breakdown - The breakdown process is initiated by primary electrons, which are generated by photo-emission or by (natural) radioactivity. Because the primary electrons depend on the occurrence of this radiation, there can be a time lag before ignition occurs. To reduce the statistical start delay, in most compact HID lamps a low dose of the radioactive component Krypton-85 is present. Additionally, an ultra violet (UV) enhancer is incorporated into UHP projection lamps (Section 7.1) used for photo-emission to reduce the required ignition voltage. After the first electron is produced, in the presence of a strong electric field, an avalanche of new electrons is produced by collisions. This process leads to the breakdown of the start gas.

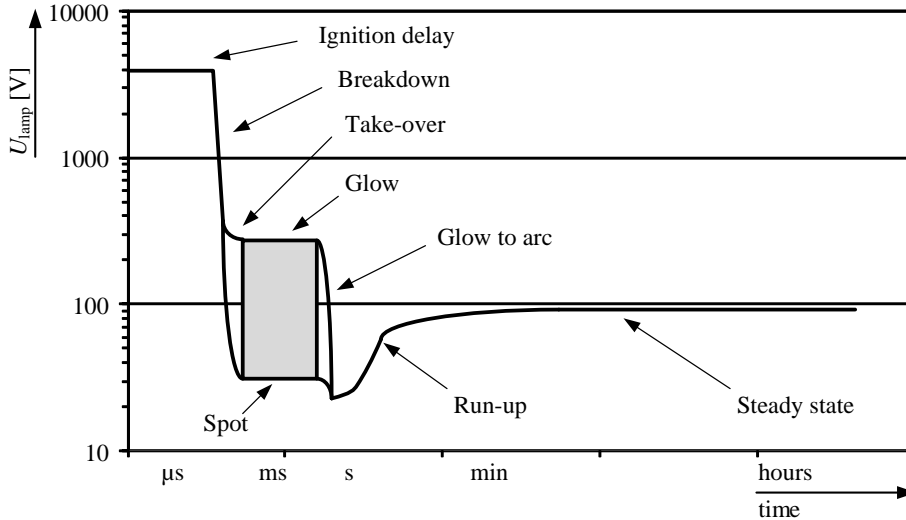


Figure 2.7: Phases of HID lamp operation over time.

Electrode heating - In this phase the electrodes are heated. The temperature of the electrodes increases, and eventually gets high enough to emit the electrons thermionically. Some seconds are necessary to get to such a high temperature. The electrode heating phase can be divided in sub-phases:

- **Take-over** - The breakdown process initiates a conductive channel between both electrodes. This channel has to be sustained to prevent the discharge from extinguishing. Therefore, the lamp-driver needs to deliver energy with a sufficient open circuit voltage (OCV) level. After the very short take-over phase (ms) the HID lamp enters the glow phase.
- **Glow** - In the glow phase the electrodes are heated. The electrode tip temperature is low, therefore electrons are emitted by ion bombardment at the cathode (secondary emission). This mode can be characterised by a high cathode fall and a low current density, resulting in a high glow voltage across the lamp terminals and a low lamp-current (mA). The ion bombardment may cause damage to the electrode through the sputtering of electrode material. This leads to blackening of the discharge tube and a decrease in the luminous flux. To accelerate the glow phase and minimise the lamp degradation the lamp-driver must provide sufficient OCV during the glow phase. During the glow phase a low voltage mode can occur, the so-called spot mode, with a reduced cathode fall. The electrodes have still not reached their nominal operation temperature but at the cathode a local hot spot is created [50]. The resulting impedance is very unstable, and the lamp voltage switches frequently between high and low voltage levels. Particularly if a low frequency

alternating lamp-current is applied, the discharge can easily switch between high and low voltage mode after commutation, or can even extinguish. This behaviour is experimentally observed, as shown in Section 5.4.1.

- **Glow-to-arc transient** - When the electrodes are sufficiently heated in the glow phase, the tip temperature becomes high enough to emit electrons thermionically. At that moment the glow-to-arc transition takes place, and then the cathode fall and related lamp voltage drop significantly with an increasing lamp-current.

Run-up phase - When the electrodes have reached their working temperature, the lamp enters the stable run-up phase. In the beginning of this phase the lamp voltage is low, due to the low burner temperature, and thus low gas pressures. On a time scale of several minutes the energy dissipated in the arc heats the discharge tube, the temperature rises, and the vapour pressure of the fill components increases until a stable level is reached. During this process the lamp resistance continuously increases, and finally the lamp enters steady-state operation. The lamp-driver should limit the current during low voltage operation to a specified maximum level to prevent electrode damage, and it should regulate the lamp power when the burner reaches steady-state operation.

Steady-state operation - In steady-state a total temperature equilibrium is established. The buffer gas pressure and the partial pressures of the metal-halide elements have reached their designed levels, and the HID lamp achieves its optimum light performance. Accurate power control ensures a stable colour point throughout the lamp's life.

2.3.2 Time scales in lamp operation

Several time scales are involved in the operation of HID lamps. The related time constants range from microseconds to thousands of hours. These time constants influence the electrical behaviour of the lamp. Below is an enumeration of the most important phenomena:

Time scale > khour - Throughout lamp life corrosion and erosion processes affect the properties of both the electrodes and the discharge vessel. These processes take place over hundreds or thousands of hours and limit the useful life of the lamp by triggering one of the failure mechanisms, which leads to an end of life (EOL) state.

Sputtering and evaporation of the electrodes can lead to wolfram deposition on the discharge vessel, affecting the thermal energy balance of the discharge. The electrode degradation process can also result in electrode burn-back, increasing arc length between the electrodes. Both effects give rise to a gradually increasing lamp voltage during its life.

Time scale > min - During steady-state operation all parts of the lamp are in a thermal equilibrium state. It takes from a couple of minutes up to an

hour before the lamp reaches this thermal equilibrium. Figure 2.8(a) shows a static HID lamp voltage versus current characteristic that is valid for steady-state operation. The lamp voltage slightly decreases, selecting a lower current set-point of operation. For very low current operation an increased cathode fall contributes to an increased terminal voltage.

s < Time scale < min - During the run-up phase, the discharge vessel is heated and the strongly correlated cold spot temperature reaches a steady-state equilibrium, defining the partial vapour pressures, and therefore the light emitting properties. Input power changes will alter the plasma composition on a time scale ranging from seconds to minutes.

Time scale ms - Phenomena within the plasma and at the electrode surface, which are related to the plasma column and electrode-tip thermal time constants respectively, take place within milliseconds. In particular, the plasma column heat capacity (time constant) and the gas-discharge negative resistive behaviour, as displayed in Fig. 2.8(b), are strongly related to the lamp-driver interaction stability as discussed in Section 5.3.1.

Time scale < μ s - For high-frequency lamp-current operation above the plasma column time constant, the plasma state remains constant, and resistive terminal behaviour results, as shown in Fig. 2.8(c). However, acoustic resonances can be triggered, causing instable operation.

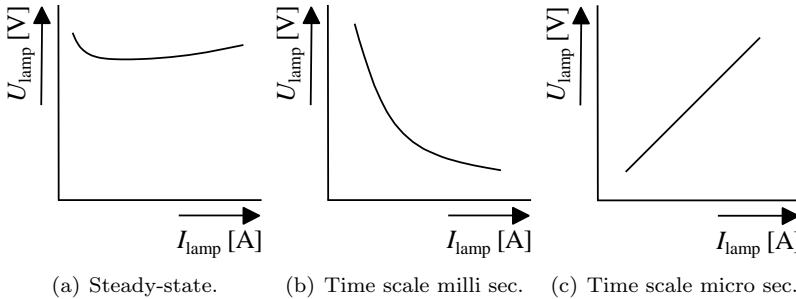


Figure 2.8: Electric behaviour of HID lamp versus time.

The three most important time scales are displayed in Fig. 2.8. When the lamp is forced to change to a certain current value I_{lamp} , the lamp can respond in three different ways depending on the time scale.

2.3.3 Lamp-driver current

To operate HID lamps several lamp-driver approaches are possible. Unlike the conventional sinusoidal 50/60 Hz current operation on an electro-magnetic (EM)

ballast, electronic lamp-drivers make a wide variety of lamp-current wave-shapes possible. Moreover, electronic lamp operation offers additional degrees of freedom to optimise the lamp-driver interaction and system performance [51]. A number of the most important lamp-current wave shapes, found in commercially applied HID drivers, are as follows:

LF sinusoidal wave - The conventional way of operating an HID lamp is by using an EM ballast. Low frequency sinusoidal lamp-current operation can cause light flickering on the 50/60 Hz mains frequency. Moreover, there is no power control to eliminate power shifts caused by the voltage changes of the mains or voltage changes of the burner over the lamp's life. However, EM ballasts are still popular for high power applications ($P_{\text{lamp}} > 400 \text{ W}$) because of their relatively low losses ($< 10 \%$) at these power levels.

HF - Operation of high-pressure discharge lamps at high-frequency (HF), dozen kHz, is very popular for the potential reduction of the size, cost and losses offered by this type of electronic lamp-driver [52]. For fluorescent lamps, HF electronic lamp-drivers are commonly applied [53]. However, the occurrence of acoustic resonances (Section 2.2.3) in HID lamps has hampered general use of HF lamp-drivers for HID lamps.

For compact HID lamps, resonance-free frequency windows exist, in which stable operation is possible in the range of 20 kHz - 150 kHz [54, 55]. However, these windows are either too narrow or too sensitive to changes in the lamp's parameters throughout its lifetime. Frequency modulation of the driving generator can reduce the onset of instabilities [56].

For high power HID lamps ($> 150 \text{ W}$) operated above 150 kHz, the excitation of resonances normally becomes less severe, and resonance-free operation is possible. For frequencies that range from 500 Hz to 20 kHz stable operation is also possible. However, this frequency range is of no practical use because of the resulting audible noise of the ballast and the lamp.

Altogether, these factors exclude the simple and universal HF driver designs for HID lamps.

VHF - Very high-frequency ($> 1 \text{ MHz}$) operation, above the acoustic resonance frequency range of compact HID lamps, is a stable method of operation. However, in this frequency range the lamp-driver design is complicated by radio interference, and increasing losses in the power electronic components.

DC - To operate a high-pressure lamp on direct current (dc) is very attractive from an electronic driver point of view because of the simplicity of this type of lamp-driver, as well as its related low cost and small size. However, there are disadvantages that affect the lamp, such as cataphoretic effects and demixing of the plasma, which make this operation method unsuitable for general lighting purposes.

LF square-wave - Dc operation of the lamps could be a quite suitable basis for electronic ballasts. Symmetry of the discharge can be achieved by periodically reversing the polarity, which would result in a low-frequency-square-wave (LFSW) lamp-current. The square-wave lamp-current spectrum comprises an infinite number of harmonics. However, since the lamp voltage and current are in phase, the power supplied to the lamp, in theory, remains constant. In practice, the lamp voltage and current are non-ideal square-waves, with a limited number of higher harmonics (see also Section 5.3).

2.3.4 Lamp re-ignition

When operating an HID lamp at low frequency sinusoidal or square-wave current, the lamp must re-ignite after every current reversal. During the polarity change the current level is low and momentarily zero, resulting in a decrease in the plasma temperature. As a consequence, the lamp's resistance increases. This creates a re-ignition peak in the voltage when the current starts to flow after the change of polarity. To minimise the voltage peak the current commutation time must be limited.

In Fig. 2.9 the measurement results show the lamp-current and voltage for 50 Hz sinusoidal operation, using an EM ballast. Clear re-ignition peaks are visible in the lamp voltage immediately after the lamp-current passing through zero. These re-ignition voltage peaks after current reversal result from both plasma and electrode effects. First, due to the power modulation during the current reversal process, the plasma cools down. As a result, the electron density drops, so that the electrical conductivity decreases, and the voltage across the column increases. Therefore, the re-ignition peak amplitude is related to the di/dt of the applied lamp-current wave-shape.

Second, when the lamp-current changes direction the electrodes change anode and cathode function. At the start of the cathode mode, the temperature can be too low, which causes the cathode fall to rise, leading to an increased re-ignition peak. When the re-ignition peak amplitude becomes higher than the voltage that can be supplied by the lamp-driver at commutation, the lamp will extinguish.

2.4 Discussion

The technical revolution in gas-discharge lamps has resulted in the high-efficiency lamps currently available. The introduction of metal-halide additives to the discharge fill, and ceramic discharge vessels are milestones in the development of compact HID lamps. These technological steps have improved efficacy and colour rendering ability throughout lamp life.

The performance and stability of the plasma arc rely on stabilisation forces and transport flows. Some of those physical processes are directly related to the terminal operation conditions. In particular, the operation of HID lamps on current waveforms that comprise high-frequency components is hampered by

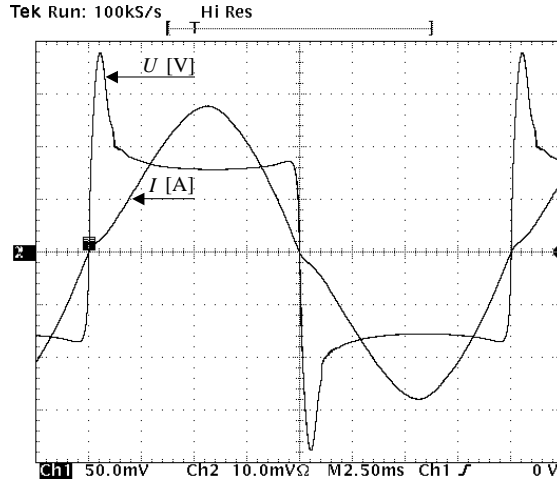


Figure 2.9: Lamp voltage (50 V/div) and current (1 A/div) of Philips CDM-T 73W burner operated on an EM ballast at 50 Hz 230 V mains. Time scale 2.5 ms/div.

the occurrence of standing pressure waves in the plasma (acoustic resonances). The occurrence of acoustic resonances can be avoided by choosing the proper discharge properties and carefully designing the lamp-current wave-shape.

The process from ignition to stable arc operation involves different phases, which each represent a distinct discharge condition. The lamp-driver must provide sufficient open circuit voltage (OCV) and lamp-current control during the different discharge phases to prevent the lamp from overloading or extinguishing. Electronic lamp operation enables additional degrees of freedom in lamp-current wave-shapes compared to the conventional EM ballasts. To operate the large variety of existing HID lamps on the market, the LFSW current is the best option as it creates the smallest risk of malfunction. In chapters 4 and 5 a LFSW lamp-driver concept and related lamp-driver interaction (LDI) are discussed.

Chapter 3

Physics-based lamp model

Lamp modelling is concerned with the mathematical description of physical and electrical phenomena, which evolve in real-time. Selecting which characteristics to take into account and which properties to ignore is an art. The essence is to select only those characteristics, among the many available, that are necessary to accurately describe the gas-discharge lamp with respect to the objectives of the application.

Most gas-discharge lamp related modelling efforts are directed towards the physical processes of the arc discharge with the aim of improving its design. However, for a ballast circuit designer the most interesting characteristic of the gas-discharge is its terminal electrical impedance, although additional physical parameters can also be helpful to optimise the lamp-ballast interaction. Because the lifetime of metal-halide lamps is strongly related to it, the electrode cathode temperature is particularly of great interest [57–59].

The various possibilities for operating metal-halide lamps with conventional or electronic ballasts obviously influence the discharge lamp operation parameters. Accordingly, the resulting system performance depends on both the dynamics of the lamp and on the characteristics of the ballast, a phenomenon known as lamp-driver interaction (LDI) [60]. Therefore, it is important to have numerical tools available that can help the researcher understand and improve metal-halide lamp-driver designs.

In the literature several dynamic models for HID lamps have been proposed [61]. Some of those models are based on heuristics [62, 63], and others on physical principles. Heuristic models can only be used with confidence under the originally prescribed operation conditions. The physical plasma models are mainly based on a one dimensional energy balance [64–67] or a more sophisticated multi-dimensional energy transport representation [40, 68, 69].

Aside from the plasma behaviour, the physical processes in the electrode regions play an important role in the metal-halide lamp behaviour. A literature study on electrodes shows numerous modelling approaches [58, 59, 69–73].

The two- or three-dimensional models presented in the literature require heavy finite-element calculation power. In this chapter a one-dimensional approach for modelling the plasma and the electrode behaviour is presented. This HID lamp model offers appropriate accuracy to simulate the terminal electrical impedance for lamp-driver design with reduced computational effort [20].

In this chapter the physical properties of a metal-halide discharge lamp are studied in more detail. The principal objective is to present a phase resolved metal-halide lamp model intended for lamp-driver simulations and observer-based control application, as presented later in Chapter 8. Metal-halide gas-discharge plasma behaviour based on energy conservation principles is described in Section 3.1. The unknown parameters are identified in Section 3.2, where the exposition includes a measurement set-up and parameter extraction. A physics-based model approach for the voltage that drops across thin sheaths near the electrodes is discussed in Section 3.3. The developed model is validated by the experimental results presented in Section 3.4. Section 3.5 concludes the chapter.

3.1 Energy balance equations

The grey box model developed here is an extension of modelling efforts described in previous papers [66, 73]. In the presented model the metal-halide spectrum lines are incorporated and an additional energy balance equation is introduced to include the dynamics of the arc tube. The result is that a metal-halide discharge can be simulated across a wide range, from run-up to steady-state operation.

The electrical energy supplied to the lamp is dissipated in the lamp electrodes and the arc discharge. From the latter, energy can escape by means of radiation, thermal conduction from the wall of the discharge tube, diffusion of electrons, ions and excited atoms, and convection. Losses caused by the diffusion of particles and by convection are small compared to losses inherent to thermal conduction and radiation; therefore, they can be ignored [39]. Furthermore, for all radiation calculations a two-temperature step profile approximation with homogeneous plasma and wall temperature distribution as displayed in Fig. 3.1 is used [37], where all quantities are cylindrically symmetrical around the axis of the arc tube.

Consequently, the steady-state energy balance equation is given by

$$P_{\text{lamp}} = P_{\text{arc}} + P_{\text{ele}} = P_{\text{rad}} + P_{\text{cond}} + P_{\text{ele}}, \quad (3.1)$$

where, P_{lamp} is the electrical input power, P_{arc} the arc power, P_{rad} the radiated power, P_{cond} the conducted power, and P_{ele} the electrode power.

The power balance at the outer mantle near the wall is composed of three factors. First, heat denoted as P_{out} will escape the discharge tube by thermal radiation. Second, the discharge tube is heated by power conducted by the plasma; and third, the radiated power absorbed by the atoms in this region also causes heating. Consequently, the energy balance equation for the discharge tube is

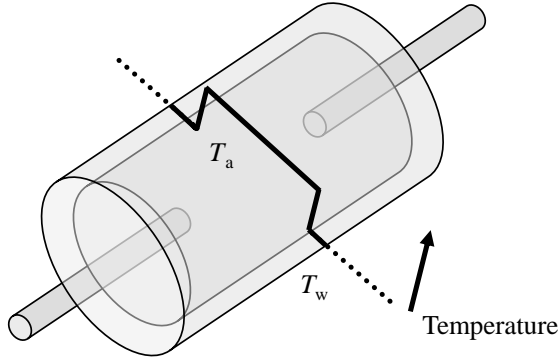


Figure 3.1: HID lamp with two step temperature profile, where T_a is the arc temperature and T_w is the wall temperature.

given by

$$P_{\text{out}} = P_{\text{cond}} + a_1 P_{\text{rad}}, \quad (3.2)$$

where P_{out} is the total thermal power and a_1 is the absorption coefficient of the wall. Assuming the internal energy storage is a linear system, the temperature of the arc column and discharge wall can be approximated by a first order differential equation. The total system can be described by a set of two algebraic non-linear equations, leading to

$$\begin{cases} \frac{dT_a}{dt} = D_1 [P_{\text{lamp}} - P_{\text{rad}}(T_a, T_w) - P_{\text{cond}}(T_a, T_w) - P_{\text{ele}}(\bar{T}_{\text{ele}}, T_w)], \\ \frac{dT_w}{dt} = D_2 [a_1 P_{\text{rad}}(T_a, T_w) + P_{\text{cond}}(T_a, T_w) - P_{\text{out}}(T_w)], \end{cases} \quad (3.3)$$

where D_1 is the arc heat capacity, D_2 is the wall heat capacity, T_a is the homogeneous arc temperature, T_w is the uniform wall temperature (see also Fig. 3.1), and $\bar{T}_{\text{ele}} = (T_{\text{ele}_1}, T_{\text{ele}_2})$ is the tip temperature of each electrode.

The radiated power P_{rad} is related to the Boltzmann law, if the gas temperature is in near local thermal equilibrium (LTE) [33, 34, 36, 74] with the electron gas. Assuming the plasma is optically thin, the total radiation of a metal-halide lamp is a combined radiation spectrum of mercury and metal additives. The radiated power caused by the mercury atoms, which is simplified by taking a constant value b for the energy level, can be described by

$$P_{\text{rad}}(T_a) = n_0 b e^{-\frac{eV}{kT_a}}, \quad (3.4)$$

where n_0 is the concentration of atoms in the ground state, eV is the photon energy, and $k = 1.3806503 \cdot 10^{-23} JK^{-1}$ is Boltzmann's constant. At normal operating conditions, the total amount of mercury inside the arc tube is fully evaporated. However, decreasing the electrical input power will decrease the wall temperature, and the mercury gas may start to condense when the cold-spot temperature [34] approaches the threshold temperature T_{sat} of mercury. Under these circumstances the concentration of the mercury gas decreases [75, 76]. The cold-spot temperature can be assumed to be equal to the wall temperature. Therefore, according to the ideal gas law, it follows that n_0 is given by

$$n_0(T_a, T_w) = \frac{P(T_w)V}{RT_a}, \quad (3.5)$$

where P is the arc tube gas pressure, V is the arc tube volume, and R is the gas constant. Equation (3.5) has been simplified with the approximation that the pressure is an exponential function of the wall temperature T_w (cold spot) when mercury is not fully evaporated [37], and equals a constant temperature otherwise, as follows

$$n_0(T_a, T_w) \approx \frac{e^{\frac{-\alpha_p}{f(T_w)}}}{T_a}, \quad (3.6)$$

$$f(T_w) = \begin{cases} T_{\text{sat}} & T_w > T_{\text{sat}} \\ T_w & T_w \leq T_{\text{sat}}, \end{cases}$$

where α_p is a pressure constant, $f(T_w)$ is a function describing the cold-spot temperature, and $T_{\text{sat}} = 1030$ K, which is the saturation temperature of mercury.

The radiated power for metal-halide lamps result from the combined spectrum of mercury and metal additives, and can be expressed using (3.4) and (3.6)

$$P_{\text{rad}}(T_a, T_w) = \frac{a_5}{T_a} e^{\frac{-a_7}{f(T_w)}} - \frac{eV_{\text{HG}}}{kT_a} + \frac{a_6}{T_a} e^{\frac{-a_8}{T_w}} - \frac{eV_{\text{M}}}{kT_a}, \quad (3.7)$$

where a_5 is the mercury energy level, a_6 is the metal additive's energy level, a_7 is the pressure constant of mercury, a_8 is the pressure constant of the metal additives, $e = 1.602176462 \cdot 10^{-19} C$ is the elementary charge, V_{HG} is the excitation level of mercury, and V_{M} is the excitation level of the metal additives.

The power loss by thermal conduction is determined by

$$P_{\text{cond}} \approx 2\pi L\lambda(T_a - T_w) = a_2(T_a - T_w), \quad (3.8)$$

where L is the length of the discharge, $\lambda(T)$ is the thermal conduction of the vapour, and a_2 is the conductivity of the vapour constant. Thermal radiation loss from the wall, P_{out} , is a fourth-order function of the average wall temperature T_w . The total thermal power can be approximated as

$$P_{\text{out}} = a_3 T_w^4, \quad (3.9)$$

where a_3 is a proportionality constant between the output power and the wall temperature.

The lamp resistance can be deduced using (3.5) and the current density j , yielding

$$j = e\mu n_e E, \quad (3.10)$$

where E is the electric field, μ is the electron mobility, and n_e is the concentration of the plasma electrons. Saha's law [34] can be used to approximate the concentration of the electrons in the plasma, yielding

$$n_e \propto T_a^{\frac{3}{4}} \sqrt{n_{\text{HG}} e^{\frac{-eV_{\text{IHG}}}{kT_a}} + n_{\text{M}} e^{\frac{-eV_{\text{IM}}}{kT_a}}}, \quad (3.11)$$

where n_{HG} is the concentration of mercury atoms, n_{M} is the concentration of metal-halide atoms, V_{IHG} is the ionisation potential of mercury, and V_{IM} is the ionisation potential of the metal-halides. With metal additives added to the discharge the electron mobility is proportional to

$$\mu \propto T_a^{-\frac{1}{2}} \left(n_{\text{HG}} Q_{\text{HG}} + n_{\text{M}} Q_{\text{M}} \right)^{-1}, \quad (3.12)$$

where Q_{HG} is the collision cross-section of mercury, and Q_{M} is the collision cross-section of the metal-halides. For further simplification one can assume that Q_{HG} and Q_{M} are equal, and by applying (3.5) this results in an equivalent lamp resistance

$$R_{\text{model}}(T_a, T_w) = \frac{a_4 T_a^{-\frac{3}{4}} \left(e^{\frac{-a_7}{f(T_w)}} + e^{\frac{-a_8}{T_w}} \right)}{\sqrt{e^{\frac{-a_7}{f(T_w)}} - \frac{eV_{\text{IHG}}}{kT_a} + e^{\frac{-a_8}{T_w}} - \frac{eV_{\text{IM}}}{kT_a}}}, \quad (3.13)$$

where a_4 is a proportionality constant for the lamp resistance.

All together, ten parameters, that is a_1, \dots, a_8 , D_1 and D_2 , have been introduced in Eqs. (3.3), (3.7), (3.8), (3.9) and (3.13), in order to describe the steady-state of the lamp and its dynamic thermal behaviour. The power dissipated in the electrodes, T_{ele} , is modelled in Section 3.3.

The generally applied and commercially available Philips CDM-T 73W/830 HID lamp is selected for these identification procedures and experimental investigations, unless otherwise noted. Some preliminary knowledge regarding the lamp's characteristics is required, including the ionisation potentials and the average excitation potentials of the various elements in the discharge, as well as

the threshold saturation temperature T_{sat} of mercury. In addition to mercury, this type of metal-halide lamp is known to contain sodium iodide, dysprosium, and thallium. Their ionisation potentials and the excitation potentials of the strongest resonance lines are given in Table 3.1. For simplification of the model, the ionisation and excitation potentials of the various metal-halides are averaged to single potentials. The remaining parameter set needs to be identified and this procedure is described in the next Section.

Table 3.1: Lamp constants CDM-T 73W/830.

	Ionisation Potential [eV]		Excitation potential of strongest resonance lines [eV]
Mercury	V_{HG}	10.4	V_{HG} 7.8
Sodium Iodide		5.1	4.57 and 3.27
Dysprosium		6.0	2.91
Thallium		6.0	4.14
Weighted average	V_{IM}	6.0	V_{M} 4.0

3.2 Parameter identification

The applied grey-box model structure relies on two components. One component is based on prior knowledge of the physical principles that govern the system dynamics and the known model parameters, as discussed in the previous Section. The second component involves parameter identification on the basis of input and output data samples of the HID lamp terminal quantities. Using the prior information about the model structure and the relation between the parameters enables the researcher to split the identification procedure into separate sections. This approach provides accurate parameter estimation with reduced data sets of input and output signals. For the proposed HID lamp model the identification procedure can be divided into three separate sections:

1. Steady-state parameter identification (parameters a_1, \dots, a_8 are collected in \bar{a}).
2. Dynamic identification of the plasma heat capacity (parameter D_1).
3. Dynamic identification of the wall heat capacity (parameter D_2).

In the first step of the identification procedure data is compiled during steady-state operation in thermal equilibrium. The heat capacities D_1 , D_2 can be identified following the two-step temperature approximation, as shown in Fig. 3.1. The related time constants are quite different; the plasma time constant is on the order of milli-seconds and the wall time constant is in the second range, as discussed in Section 2.3.2. This wide spread allows the dynamic identification procedure to be separated into two independent parts. Accordingly, during the

separate identification steps appropriate input data sets are applied to excite only the lamp behaviour of concern.

Compared with a data-driven black box strategy, the grey box strategy leads to models with reliable extrapolation properties, so the lamp model is expected to yield better accuracy over a larger range of operating conditions [66, 77].

3.2.1 Experimental set-up

The experimental set-up for determining the steady-state parameters is illustrated in Fig. 3.2. The energy is supplied by an electronic dc source (HP6812A). A series resistor is used to counteract the negative impedance characteristic of the lamp. To provide an alternating current, a full bridge is interposed. The switching frequency is set to 100 Hz, which is very close to the normal operating frequency of square-wave electronic ballast circuits.

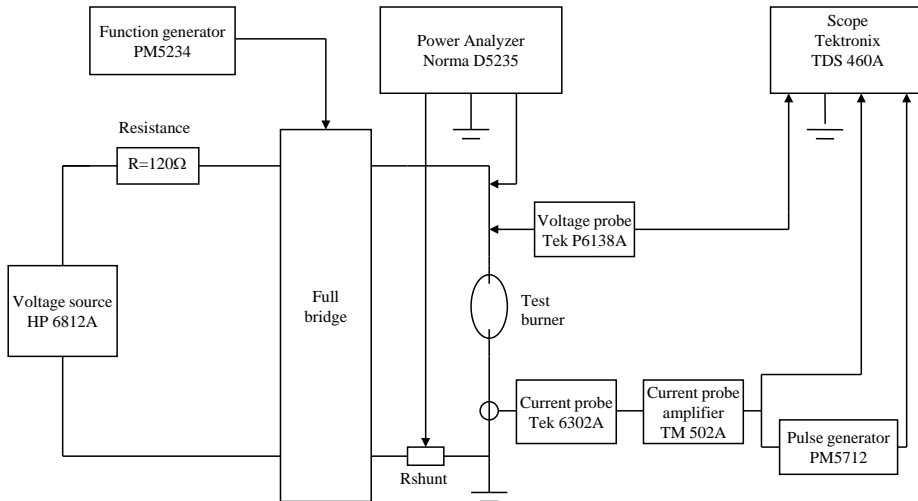


Figure 3.2: Experimental set-up for steady-state identification.

The steady-state lamp power is controlled by varying the voltage source set-point. Further, since the lamp voltages and currents at various power levels are measured experimentally, the lamp power and the lamp resistance can be obtained. The supply voltage is decreased with discrete steps. To ensure that the lamp has reached the quasi-steady-state, a period of two minutes is waited before measuring. The supply voltage is step wise decreased until the lamp extinguishes. To ensure an accurate identification more than 30 steady-state points are needed.

For every power level in quasi-steady-state the HID lamp terminal voltage and current V_{RMS} and I_{RMS} must be determined. Because the lamp voltage and current waveform are almost square-waves, it is sufficient to take one sample

during the whole period. The delay generator (PM5712) in the experimental set-up (Fig. 3.2) is triggered by the commutation process and is used to take a sample in the middle of the positive square-wave period half. A very accurate measurement of the voltage and current can be obtained when taking the average of about 100 samples.

It should be noted that this identification measurement method purposely neglects the dynamic lamp voltage transients during re-ignition, and only the steady-state equilibrium is observed. The transients of the discharge vessel and plasma are captured in the dynamic identification part and the electrode behaviour is captured in the electrode model part. The electrodes significantly influence the lamp behaviour and related terminal properties, particularly during reduced power operation, as addressed in Section 3.3.

3.2.2 Steady-state identification

To identify the steady-state parameters, the lamp voltage and current are examined during steady-state equilibrium for a finite set of discrete supply voltage levels. The corresponding lamp power \bar{P}_{lamp} and resistance \bar{R}_{lamp} arrays, can be computed in a straightforward manner. When the gas-discharge reaches the steady-state, the operating conditions converge to an equilibrium state, at which the plasma temperature, T_a , and the wall temperature, T_w , become constant. This implies $dT_a/dt = 0$ and $dT_w/dt = 0$. Consequently, (3.3) is reduced to a set of non-linear equations as follows:

$$\begin{cases} P_{\text{lamp}} - P_{\text{rad}}(T_a, T_w, \bar{a}) - P_{\text{cond}}(T_a, T_w, a_2) - P_{\text{ele}} &= 0, \\ a_1 P_{\text{rad}}(T_a, T_w, \bar{a}) + P_{\text{cond}}(T_a, T_w, a_2) - P_{\text{out}}(T_w, a_3) &= 0, \end{cases} \quad (3.14)$$

where P_{ele} is fixed to 7 W [39] during the identification procedure. The steady-state parameter computation can be implemented as follows:

1. Compute from the lamp measurements the power and resistance arrays \bar{P}_{lamp} and \bar{R}_{lamp} with N data samples.
2. Select an initial guess for the unknown steady-state array \bar{a} .
3. Minimise lamp temperatures (T_a, T_w) for every given lamp power set-point P_{lamp} using

$$\min_{T_a, T_w} \left(\begin{array}{c} P_{\text{lamp}} - P_{\text{rad}}(T_a, T_w, \bar{a}) - P_{\text{cond}}(T_a, T_w, a_2) - P_{\text{ele}} \\ a_1 P_{\text{rad}}(T_a, T_w, \bar{a}) + P_{\text{cond}}(T_a, T_w, a_2) - P_{\text{out}}(T_w, a_3) \end{array} \right)^2 \quad (3.15)$$

For the N data samples of array \bar{P}_{lamp} , the lamp temperature set $[\bar{T}_a, \bar{T}_w]$ can be estimated by applying the iterative updated steady-state values from \bar{a} .

4. Identify the state array \bar{a} by minimising the error between the experimentally obtained lamp resistance array \bar{R}_{lamp} and the modelled resistance array \bar{R}_{model} using (3.13), given the temperature set $[\bar{T}_a, \bar{T}_w]$.

$$\min_{\bar{a}} \sum_{i=1}^{N_{\text{samples}}} (R_{\text{lamp}}^i - R_{\text{model}}^i(\bar{P}, \bar{a}))^2. \quad (3.16)$$

In this nested multi-dimensional minimisation problem return to step 2 after every iteration. The embedded minimisations (3.13) and (3.15) are updated after every iteration according to the values in \bar{a} .

The algorithm was coded in Matlab using the Optim toolbox facilities. For all the minimisation problems the Gauss-Newton method in combination with a cubic interpolation line search method is selected. If the standard mixed polynomial line search method is used, algorithm instability may occur.

After every iteration of the minimisation in (3.16), the algorithm adjusts the unknown parameters towards convergence to a minimum error. However, this multi-dimensional search may encounter many local minima, thereby preventing convergence to the global minimum. In fact, if the initial guesses for the unknown parameters are not selected properly, quite often the identification will lead to a local minimum instead of the global minimum. To overcome this problem a constrained optimisation is used.

Table 3.2: Identified lamp parameters.

Parameter identified	CDM-T 73W/830
a_1	0.0302
a_2	0.0016
a_3	$3.9609 \cdot 10^{-12}$
a_4	$1.3902 \cdot 10^3$
a_5	$1.4164 \cdot 10^{16}$
a_6	$6.0475 \cdot 10^{14}$
a_7	$1.0121 \cdot 10^4$
a_8	$1.3090 \cdot 10^4$
MAE	0.63 %

The identification procedure results in the following steady-state parameters for the CDM-T 73W/830 burner shown in Table 3.2. The parameters are identified within less than 0.7 % of the mean absolute error (MAE). To verify the accuracy of the identification, the resistance versus power characteristic $R_{\text{model}} = f(P_{\text{lamp}})$ is generated using the identified model (continuous line) and compared against the measured data (dot marks) in Fig. 3.3. This graph shows that there is good agreement between the measured data and the model fitted for the lamp.

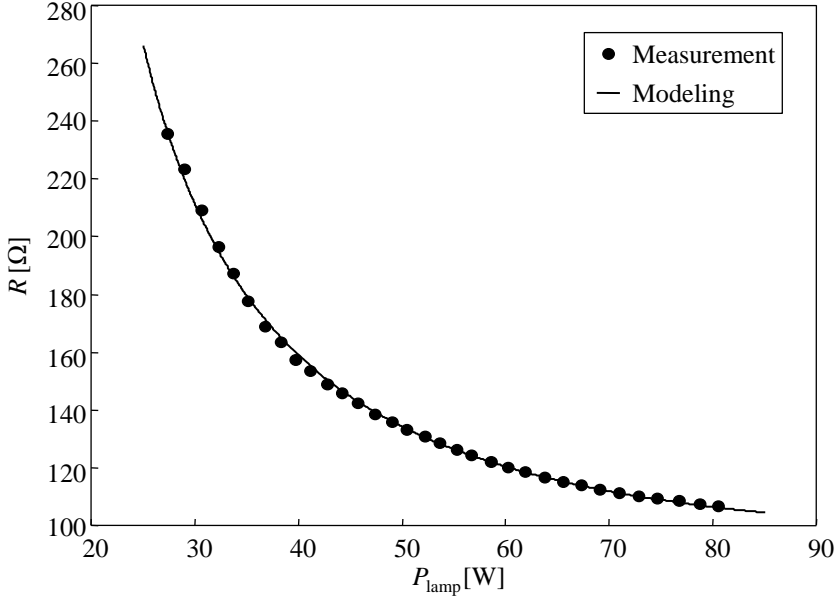


Figure 3.3: Verification of the steady-state identification CDM 73W/830.

In order to make sure that the determined parameters yield a model that makes physical sense, the plasma temperatures T_a and wall temperature T_w are simulated across the power axis, as shown in Fig. 3.4. As the lamp power increases T_w increases, whereas T_a increases and then starts to decrease once the lamp power exceeds the power level of approximately 55 W. The expected decrease in the arc temperature at high power results from the vaporisation of the excess metal-halides due to the increase in the cold spot temperature, which equals the homogenous wall temperature T_w .

3.2.3 Plasma dynamics identification

Once the steady-state parameters are identified, the heat capacity parameters D_1 and D_2 related to the system dynamics can be determined. It's possible to break the dynamics identification process into separate extraction procedures for D_1 and D_2 . Indeed, it is known that the time constant of the wall temperature T_w is in the seconds range and is thus much slower than the time constant of the discharge temperature T_a . It follows that under fast perturbation T_w is essentially constant, whereas under slow perturbations T_a reaches the quasi-steady-state.

In order to determine D_1 , a fast dynamic perturbation must be injected into the system to excite the modes that control the state variable T_a . Since T_w is a slow changing state variable, T_w can be considered constant during the pertur-

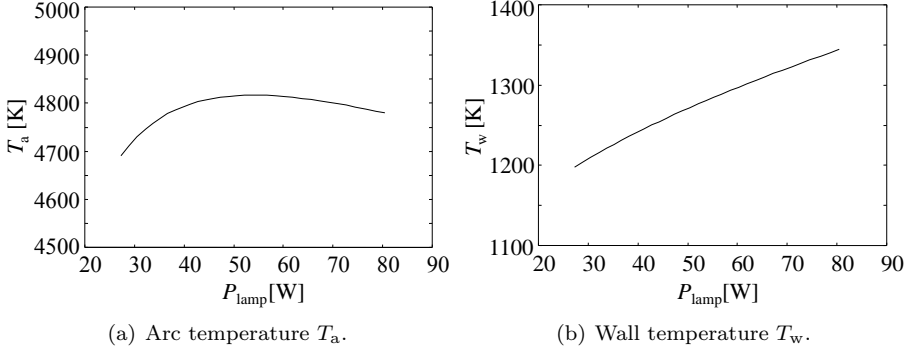


Figure 3.4: Modelled lamp temperatures versus electrical input power P_{lamp} .

bation process. The lamp transfer function (3.14) now becomes

$$\begin{cases} D_1[P_{\text{lamp}} - P_{\text{rad}}(T_a, T_w, \bar{a}) - P_{\text{cond}}(T_a, T_w, a_2) - P_{\text{ele}}] &= \frac{dT_a}{dt}, \\ a_1 P_{\text{rad}}(T_a, T_w, \bar{a}) + P_{\text{cond}}(T_a, T_w, a_2) - P_{\text{out}}(T_w, a_3) &= 0, \end{cases} \quad (3.17)$$

where the slow dynamics parameter D_2 disappears and only D_1 remains as an unknown parameter. The identification procedure for the plasma dynamic parameter D_1 can be implemented as follows:

1. During the fast dynamic perturbation the lamp voltage and current are sampled and a set of $[\bar{P}_{\text{lamp}}, \bar{R}_{\text{lamp}}]$ with N data samples can subsequently be computed.
2. The constant wall temperature T_w is solved using (3.14) with P_{lamp} being the average power input during the dynamic identification measurement. P_{ele} can be considered constant during the fast perturbation process.
3. Compute the plasma temperature array \bar{T}_a using (3.13) for the given input resistance array \bar{R}_{lamp} and constant wall temperature T_w .
4. The first state equation in (3.17) and (3.8) can be equivalently represented by

$$\frac{dT_a}{dt} = D_1[P_u - P_{\text{cond}}(T_a, T_w, a_2)] = D_1[P_u - a_2 T_a], \quad (3.18)$$

where P_u is defined as

$$P_u = P_{\text{lamp}} - P_{\text{rad}}(T_a, T_w, \bar{a}) - P_{\text{cond}}(T_w, a_2) - P_{\text{ele}}. \quad (3.19)$$

5. P_u can be determined using the data set $[\bar{P}_{\text{lamp}}, \bar{T}_a]$ and T_w .
6. Since the system represented in (3.18) equals a continuous-time first order linear model, it can be transformed into an equivalent discrete first order auto-regressive moving average (ARMA) model

$$T_a(k+1) = \theta_1 T_a(k) + \theta_2 [P_u(k+1) + P_u(k)], \quad (3.20)$$

using a bilinear transformation to identify the system on the discrete sample moments, and with the introduction of variable $\bar{\theta} = [\theta_1 \theta_2]^T$. In a more compact notation the dynamic system can be denoted by:

$$\bar{T}_a = \widetilde{M}_a \bar{\theta} + \bar{E}, \quad (3.21)$$

where \bar{E} = error array,

$$\bar{T}_a = \begin{bmatrix} T_a(1) \\ T_a(2) \\ \vdots \\ T_a(N) \end{bmatrix}, \quad \widetilde{M}_a = \begin{bmatrix} T_a(0) & P_u(1) + P_u(0) \\ T_a(1) & P_u(2) + P_u(1) \\ \vdots & \vdots \\ T_a(N-1) & P_u(N) + P_u(N-1) \end{bmatrix}.$$

7. Array $\bar{\theta}$ can be identified by substituting the N sampled data points of set $[\bar{T}_a, \bar{M}_a]$ into the following least square minimisation problem

$$\min_{\bar{\theta}} \sum_{i=1}^{N_{\text{samples}}} \bar{E}^T \bar{E} = \min_{\bar{\theta}} \sum_{i=1}^{N_{\text{samples}}} [\bar{T}_a - \widetilde{M}_a \bar{\theta}]^T [\bar{T}_a - \widetilde{M}_a \bar{\theta}]. \quad (3.22)$$

8. Once the array $\bar{\theta}$ that yields

$$\bar{\theta} = \begin{bmatrix} \frac{2f_s - D_1 a_2}{2f_s + D_1 a_2} \\ \frac{D_1}{2f_s + D_1 a_2} \end{bmatrix}, \quad (3.23)$$

is found, D_1 can be solved by using

$$D_1 = \frac{f_s \theta_2}{1 - a_2 \theta_1}, \quad (3.24)$$

where f_s is the sampling frequency.

3.2.4 Plasma dynamics identification results

As pointed out earlier, fast perturbations must be injected into the system to excite the plasma temperature response which is controlled by D_1 . This is done using the same experimental set-up as is shown in Fig. 3.2, but now with a switched resistor parallel with the voltage source and the ballast resistor. The switching resistor is practically implemented as a series circuit consisting of a power resistor and a MOSFET controlled with a square-wave generator. A single perturbation frequency is chosen because only the exponential behaviour that occurs after a step in the power is of interest. The perturbation frequency is set to 750 Hz to measure a sufficient part of the exponential behaviour that occurs after a step in the supplied power to the lamp.

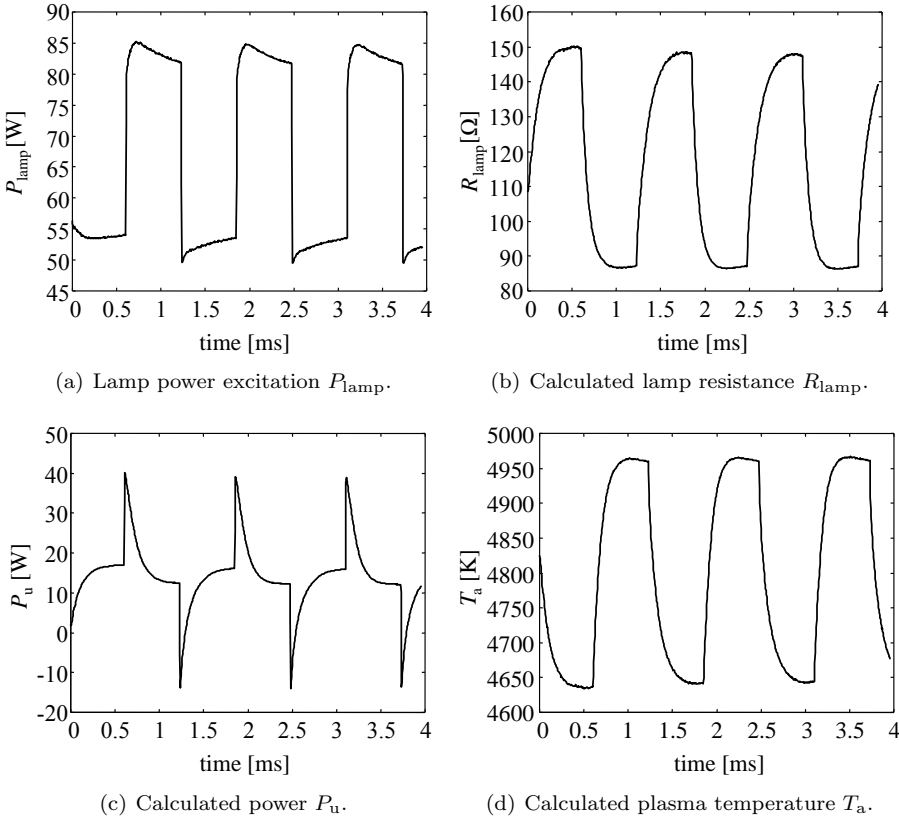


Figure 3.5: Lamp power excitation and calculated values to identify plasma heat capacity parameter D_1 .

Two thousand data points of the set $[\bar{P}_{\text{lamp}}, \bar{R}_{\text{lamp}}]$ are recorded with a sam-

pling rate $f_s = 2$ MHz, and shown in Fig. 3.5(a) and Fig. 3.5(b). Furthermore, the calculated P_u and T_a are plotted in Fig. 3.5(c) and Fig. 3.5(d). P_u shows the characteristic exponential behaviour after a power change like the small signal analysis described in Chapter 6. Fig. 3.5(d) shows the arc temperature versus time. The speed of the temperature change in time is reversed in proportion with the identified fast dynamics parameter D_1 .

Table 3.3: Identified plasma dynamic parameters and corresponding simulated discharge wall temperatures.

P_{lamp} [W]	D_1 [J/K]	T_w [K]
73	$1.501 \cdot 10^5$	1327.27
60	$1.018 \cdot 10^5$	1296.15
50	$0.754 \cdot 10^5$	1270.03
35	$0.453 \cdot 10^5$	1225.10

The CDM 73 W/830 HID burner is dynamically identified for full and reduced power levels. The corresponding identified dynamic parameters are presented in Table 3.3. It becomes clear that the fast dynamics parameter D_1 is not constant over the whole lamp power range. The plasma heat capacity diminishes during reduced power operation. The identified plasma heat capacity is graphically displayed as a function of the discharge wall temperature and the related plasma composition in Fig. 3.6.

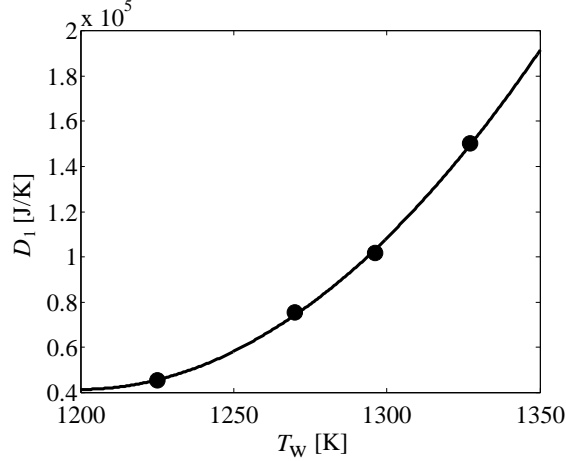


Figure 3.6: Dynamic parameter D_1 versus discharge wall temperature T_w .

A quadratic curve fit is applied to approximate the dynamic plasma behaviour between the measured data points. The quadratic function yields

$$D_1(T_w) = 6.657 T_w^2 - 1.597 \cdot 10^4 T_w + 9.623 \cdot 10^6. \quad (3.25)$$

The first equation of the power balance (3.3) can be extended with the plasma dynamics function as proposed in (3.25). Subsequently, the lamp model implements the fast dynamic behaviour in relation to the wall temperature and coupled time constant as

$$\frac{dT_a}{dt} = D_1(T_w)[P_{\text{lamp}} - P_{\text{rad}}(T_a, T_w) - P_{\text{cond}}(T_a, T_w) - P_{\text{ele}}(\bar{T}_{\text{ele}}, T_w)]. \quad (3.26)$$

3.2.5 Wall dynamics identification

Parameter D_2 impacts the time variations of the wall temperature T_w . Knowing that the run-up period of the lamp is controlled by the wall temperature, the run-up behaviour can be used to identify parameter D_2 . As mentioned earlier, the discharge temperature T_a reaches quasi-steady-state under very slow perturbations, since the time constant of T_a is in the milli-second range. Thus, when the lamp is slowly perturbed, the lamp model can be reduced to the following transfer function

$$\begin{cases} P_{\text{lamp}} - P_{\text{rad}}(T_a, T_w, \bar{a}) - P_{\text{cond}}(T_a, T_w, a_2) - P_{\text{ele}} &= 0, \\ D_2[a_1 P_{\text{rad}}(T_a, T_w, \bar{a}) + P_{\text{cond}}(T_a, T_w, a_2) - P_{\text{out}}(T_w, a_3)] &= \frac{dT_w}{dt}, \end{cases} \quad (3.27)$$

and the identification of the unknown block with the parameter D_2 can be computed as follows:

1. Under slow perturbations, the lamp voltage and current are recorded and a set $[\bar{P}_{\text{lamp}}, \bar{R}_{\text{lamp}}]$ can be defined. Subsequently, the lamp temperatures T_a and T_w for every element of the resistance array can be computed using (3.13), and the first state equation of (3.27).
2. The first state equation of (3.27) can be re-arranged in terms of P_{rad} and substituted into the second state equation using (3.8) as follows

$$\frac{dT_w}{dt} = D_2[P_u + (1 - a_1)P_{\text{cond}}(T_w, a_2)] = D_2[P_u - (1 - a_1)a_2T_w], \quad (3.28)$$

where P_u yields

$$P_u = (1 - a_1)P_{\text{cond}}(T_a, a_2) + a_1(P_{\text{lamp}} - P_{\text{ele}}) - P_{\text{out}}(T_w, a_3). \quad (3.29)$$

3. Finally, P_u can be determined using data set $[\bar{P}_{\text{lamp}}, \bar{T}_a]$ and T_w .

4. In line with the identification procedure for the plasma dynamic parameter, the continuous time first order linear model, as given in (3.28), can be transformed into an equivalent ARMA model

$$T_w(k+1) = \delta_1 T_w(k) + \delta_2 [P_u(k+1) + P_u(k)], \quad (3.30)$$

using the bilinear transformation, and introducing variable $\bar{\delta} = [\delta_1 \delta_2]^T$. In compact notation the dynamic system can be denoted by

$$\bar{T}_w = \widetilde{M}_w \bar{\delta} + \bar{E}, \quad (3.31)$$

where \bar{E} = error array,

$$\bar{T}_w = \begin{bmatrix} T_w(1) \\ T_w(2) \\ \vdots \\ T_w(N) \end{bmatrix}, \quad \widetilde{M}_w = \begin{bmatrix} T_w(0) & P_u(1) + P_u(0) \\ T_w(1) & P_u(2) + P_u(1) \\ \vdots & \vdots \\ T_w(N-1) & P_u(N) + P_u(N-1) \end{bmatrix}.$$

5. Array $\bar{\delta}$ can be identified by substituting the N sampled data points of set $[\bar{T}_w, \widetilde{M}_w]$ into the following least square minimisation problem

$$\min_{\bar{\delta}} \sum_{i=1}^{N_{\text{samples}}} \bar{E}^T \bar{E} = \min_{\bar{\delta}} \sum_{i=1}^{N_{\text{samples}}} [\bar{T}_w - \widetilde{M}_w \bar{\delta}]^T [\bar{T}_w - \widetilde{M}_w \bar{\delta}]. \quad (3.32)$$

6. Once the array $\bar{\delta}$ that yields

$$\bar{\delta} = \begin{bmatrix} \frac{2f_s - D_2(1 - a_1)a_2}{2f_s + D_2(1 - a_1)a_2} \\ \frac{D_2}{2f_s + D_2(1 - a_1)a_2} \end{bmatrix}, \quad (3.33)$$

is found, D_2 can be solved by using

$$D_2 = \frac{f_s \delta_2}{1 - a_1 \delta_1}, \quad (3.34)$$

where f_s is the sampling frequency.

3.2.6 Wall dynamics identification results

The experimental set-up used for measuring the run-up period of the lamp is identical to the one used for the steady-state identification (Fig. 3.2). The voltage source is set at a specified voltage to get a correct nominal power operation

after the run-up period, in combination with the selected series resistance. The acquisition of the lamp voltage and current starts 5 seconds after the ignition of the lamp.

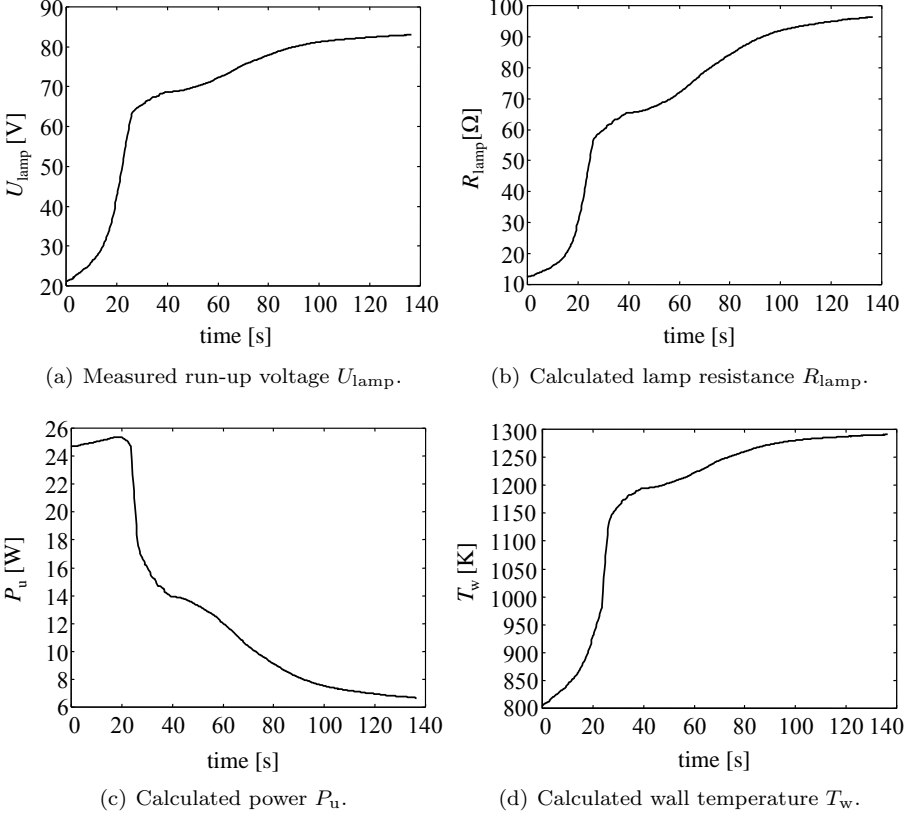


Figure 3.7: Measured lamp run-up voltage and calculated values to identify wall heat capacity parameter D_2 .

It is observed that in the run-up period, directly after the start, voltage and resistance increases exponentially with time, Fig. 3.7(a) and Fig. 3.7(b). This is characteristic for the mercury vaporisation phase. In this phase the pressure is an exponential function of the cold spot temperature (3.6). After the mercury vaporisation phase, the change in the lamp voltage slows down, indicating that all the mercury must have completely volatilised and that the lamp is approaching the steady-state equilibrium condition. In fact, since LTE starts at the very early stage of the run-up period, the model should be valid for most of the run-up phase. Fig. 3.7(d) shows the wall temperature versus time. The speed of the temperature change over time is reversely proportional with the identified slow

dynamics parameter D_2 . Finally, the identification result for the parameter D_2 yields 1.4293 J/K.

3.3 Electrode model

To get insight into the amount the lamp voltage drops across thin sheaths near the electrodes, a one-dimensional model based on [58, 59, 72] is presented. The sum of the cathode and anode fall, the so-called electrode sheath voltage (ESV) [57–59, 70], is added to the plasma column voltage to obtain the lamp terminal voltage. To determine the electric field strength and related ESV for gas-discharges, numerous approaches exist. The classical method is based on experimental measurements of the terminal discharge voltage, using plasma columns of different lengths but with otherwise identical properties [37]. By taking a linear regression of plotted voltage versus length, the field strength can be obtained from the slope of this curve and the ESV from an extrapolation to zero discharge length. However, it is very difficult to determine the cathode and the anode fall separately by using electrical measurements.

A solution to determine the separate cathode and anode falls of HID electrodes may be a measuring method that uses langmuir-probes. The langmuir-probes (fine tungsten wires) are inserted via side arms into the discharge tube of an experimental lamp [78]. A completely different method of determining the ESV uses a one-dimensional time-dependent plasma model [79]. This model describes the column of the ac mercury arc quantitatively and supplies the discharge voltage without the ESV taken into account. Therefore, the difference between the actually measured lamp voltage and the calculated lamp voltage equals the ESV. Although serious efforts have been made to develop electrode voltage measurement methods, it is still quite difficult to perform measurements with practical lamps. Therefore, modelling the electrode behaviour is still a powerful tool for lamp-driver interaction investigations.

In the case of metal-halide lamps, the construction of the electrodes is generally a thin rod over which one or two coil layers are wrapped. In our model a one-dimensional approximation is used to represent the rotationally symmetrical rod-shaped electrode body, as displayed in Fig. 3.1. In fact, the model can only switch discretely between diffuse and spot mode. Both modes have a pre-defined setting, including arc attachment dimensions on the electrode tip surface. This implicates a strong simplification of reality, which may lead to small model deviations. Although, for intended LDI simulations the greatly reduced calculation effort is valuable. Based on these assumptions an electrode sheath voltage model is derived.

The electron current density j_e is given by the Richardson - Dushman equation [58]

$$j_e = A_r T_{\text{ele}}^2 e^{\left(\frac{-e\varphi}{kT_{\text{ele}}}\right)}, \quad (3.35)$$

where A_r is the Richardson constant, T_{ele} is the electrode tip temperature, and φ is the work function. Subsequently, the work function is reduced by the cathode field E according to the Schottky equation [58]

$$\varphi = \varphi_0 - \sqrt{\left(\frac{eE}{4\pi\epsilon_0}\right)}, \quad (3.36)$$

where ϵ_0 is the permittivity of vacuum, and φ_0 is the work function without electric field. In the previous equations the value of φ_0 for pure tungsten electrodes equals 4.5 eV, and A_r is set to the theoretical value of approximately $1.2 \cdot 10^6$ [AK⁻²m⁻²]. Further, the cathode field is related to the cathode fall V_c by the MacKeown equation [58]

$$E \approx \sqrt{\frac{4j_i}{\epsilon_0}} \sqrt{\frac{m_i V_c}{2e}}, \quad (3.37)$$

where j_i is the ion current density, and m_i is the ion mass. Obviously, to ensure the transition of the current from the cathode into the plasma, at the cathode much higher electric field strengths are necessary than in the discharge column itself.

Generally, cathodes operate with a diffuse arc attachment. However, with reduced power spot mode operation can occur. In our electrode model, to overcome the one-dimensional model approach limitations, a discrete transition between diffuse and spot cathode attachment is applied. The electrode arc attachment r in diffuse and spot mode is set to $r_{\text{diff}} = 360 \mu\text{m}$ and $r_{\text{spot}} = 50 \mu\text{m}$ respectively. These values equal practical observed values typical for a Philips CDM 73W/830 burner. In order to predict spot mode operation the ion current is limited [72]. The resulting power balance at the boundary of the cathode region is described by

$$\begin{cases} j_e V_c = j_i V_i & \text{if } j_e V_c < j_{i,\text{max}} V_i \\ j_e V_c = j_{i,\text{max}} V_i + p_{\text{excess}} & \text{otherwise } j_i = j_{i,\text{max}}, \end{cases} \quad (3.38)$$

where p_{excess} is the excess energy density in spot mode operation. Furthermore, the maximum ion current $j_{i,\text{max}}$ equals the ion current $j_i(T_{\text{ipz}})$ when the equation

$$j_i(T_{\text{ipz}}) = e\sqrt{2\pi} \cdot n_i(T_{\text{ipz}}) \sqrt{\frac{kT_{\text{ipz}}}{m_i}}, \quad (3.39)$$

shows a maximum. The ion density n_i is calculated using Dalton's law and the Saha equation [34]. T_{ipz} is assumed to be equal to the electron temperature in the ion-production zone and therefore, T_{ele} . Furthermore, the lamp current at

emitting cathode surface is estimated to be

$$I_{\text{lamp}} = \pi r^2 (j_e + j_i). \quad (3.40)$$

The anode heating power is defined as the evenly distributed current over the anode area times a fixed anode sheath voltage. It is possible to use a fixed value for the anode heating voltage since this voltage is reasonable independent of the current or electrode temperature [59]. The power input into the cathode P_c and anode P_a can now be expressed by

$$\begin{cases} P_c &= I_{\text{lamp}}(V_c - \varphi), \\ P_a &= I_{\text{lamp}}(V_a + \varphi). \end{cases} \quad (3.41)$$

The power output of the rod shaped electrodes, such as those used in this model, can be divided in two terms, which are based on radiation P_{rad_e} and conduction P_{cond_e} power loss

$$\begin{cases} P_{\text{rad}_e} &\approx \varepsilon \sigma T_{\text{ele}}^4, \\ P_{\text{cond}_e} &\approx \lambda \left(\frac{dT_{\text{ele}}}{dx} \right), \end{cases} \quad (3.42)$$

where ε is the emissivity, σ is the Stephan Boltzmann constant, and λ is the heat conduction coefficient. The power balance for both electrodes can be described by a set of two algebraic non-linear equations, leading to

$$\begin{cases} \frac{dT_{\text{ele}_1}}{dt} &= D_3 [P_c - P_{\text{rad}_e}(T_{\text{ele}_1}) - P_{\text{cond}_e}(T_{\text{ele}_1})], \\ \frac{dT_{\text{ele}_2}}{dt} &= D_3 [P_a - P_{\text{rad}_e}(T_{\text{ele}_2}) - P_{\text{cond}_e}(T_{\text{ele}_2})], \end{cases} \quad (3.43)$$

where the electrode input power alternatingly switches between anode P_a and cathode P_c according to the lamps electrical current polarity. In relation to the electrode body mass, the electrode time constant was estimated and yields $D_3 = 0.8 \cdot 10^4$ J/K.

Finally, all the remaining parameters and constants are filled in or estimated for the metal-halide lamp under investigation. Based on the presented physical principles, a Matlab / Simulink model is created, as displayed in Fig. A.4. This model can be used as a circuit design tool for lamp-driver interaction optimisation. The components of the thermo-dynamical energy balance equations, as derived in the previous part of this chapter, are implemented by means of MATLAB functions and positioned on the left side of Fig. A.4. The dynamics of the plasma, wall and electrodes energy storage elements are implemented by first order linear systems on the right side. The electrode function calculates the ESV and the power input for the anode and cathode depending on the polarity of the lamp-current. A logic signal is defined to indicate the electrode mode of operation (diffuse or spot).

3.4 Experimental verification

In this section the identified lamp model is compared to the actual lamp. For verification low frequency (50 Hz) sinusoidal lamp-current operation was selected. The electro-magnetic (EM) ballast used was (type Philips BMH 70L 302 I TS) intended for 73 W metal-halide lamps. First, the lamp voltage for full power operation is shown in Fig. 3.8. There is good agreement between the simulation result and the practical measurement. The height and width of the re-ignition peaks closely agree with the simulation, and the static value of the square-wave plateau is also well predicted. Apparently, the parameters of the lamp model, which were identified with totally different current signals, give good results for 50 Hz excitation.

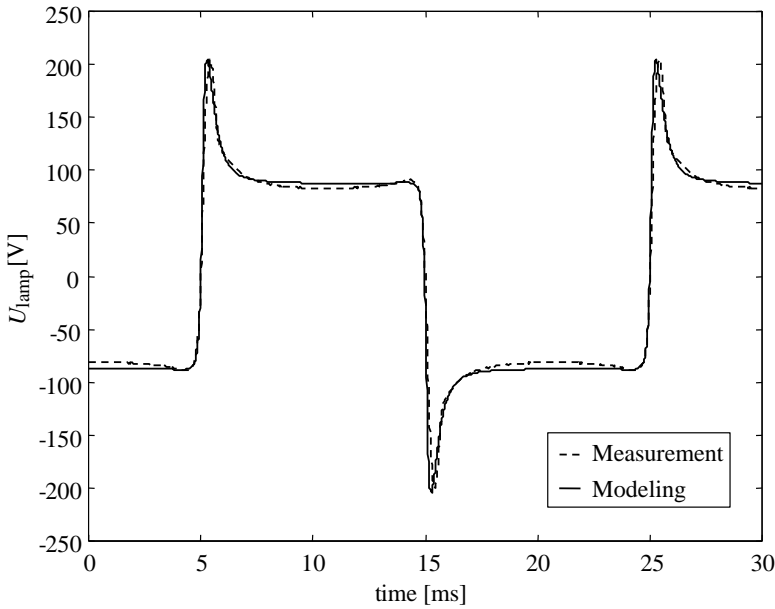


Figure 3.8: Lamp model verification for sinusoidal current operation at full power $P_{\text{lamp}} = 73 \text{ W}$.

Using the same measurement set-up the lamp power level is reduced to 35W. For reduced power operation, the physical lamp temperatures decrease and asymmetrical current operation can occur as shown in Fig. 3.9. With a EM ballast, asymmetrical current operation can occur in practice. Normally the cathode is operated continuously in diffuse mode. However, a sudden drop in the terminal lamp voltage as shown in Fig. 3.9, which indicates a diffuse to spot mode transition. After a current reversal with a too low electrode tip temperature,

the increasing current forces the cathode to switch over to spot mode operation. When the sinusoidal current decreases again towards current reversal the cathode switches back to diffuse mode. The simulation result in Fig. 3.9 shows a good fit to the measured lamp terminal voltage for this asymmetrical reduced power operation mode. However, the selected model structure gives rise to some spread when the electrode model is switching between both modes.

Finally, the average lamp voltage during the run-up phase is tested (Fig. 3.10) and proves to closely agree with the verification measurement and observation in paper [76]. The sharp slope change in Fig. 3.10 indicates the point when the mercury is fully evaporated during the run-up process.

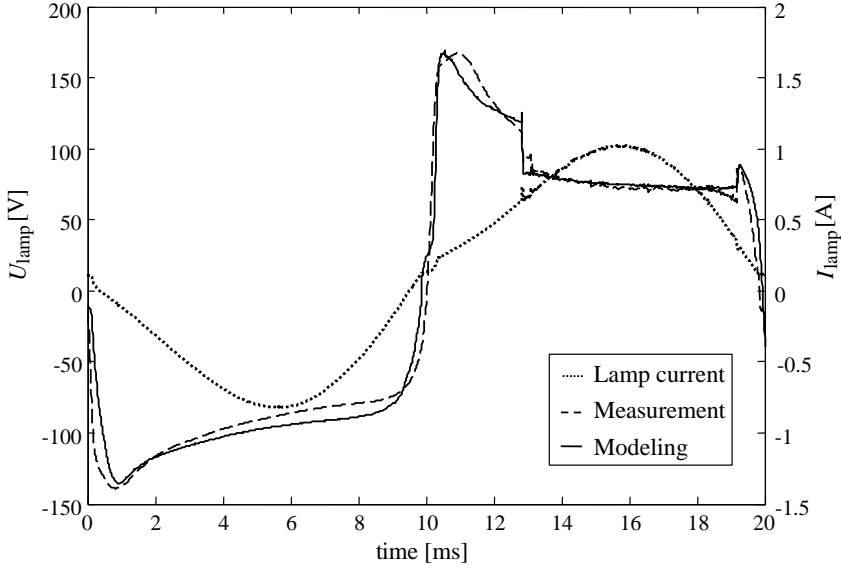


Figure 3.9: Lamp model verification for sinusoidal current operation at reduced power $P_{\text{lamp}} = 35$ W.

3.5 Discussion

A metal-halide HID lamp model has been developed to study the gas-discharge terminal impedance characteristics. In addition physical parameters can provide valuable information, to improve the lamp-driver interaction. This model is intended for use in lamp-driver simulations and observer-based control applications. The approach is based on arc column energy conservation principles, including a metal-halide term for accurate simulation. A two-step temperature approximation is applied assuming both a homogeneous plasma and wall temper-

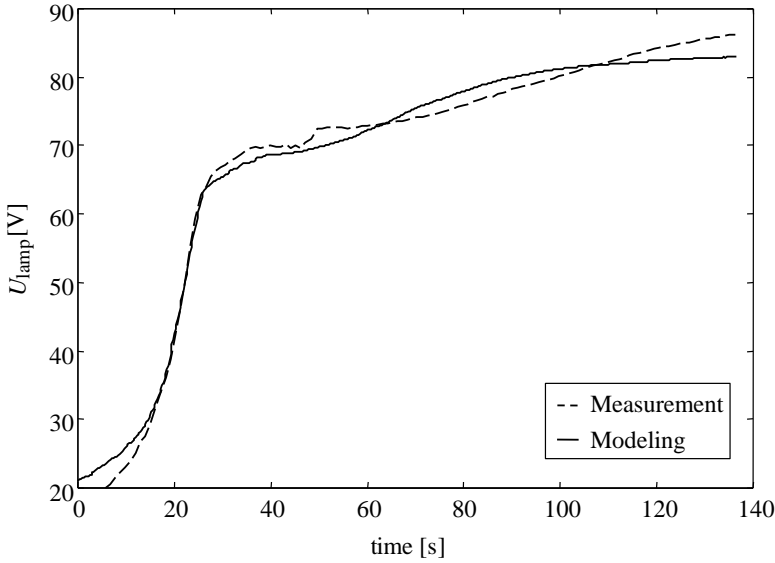


Figure 3.10: Lamp model verification during run-up phase.

ature distribution. To be able to cope with a wide range of operation conditions, the model includes heat capacity constants, and the mercury saturation point is present. The unknown parameters of the grey box model have been identified using static and dynamic identification methods.

The voltage drop across the thin sheaths in front of the electrode tips have been modelled using a one dimensional modelling approach in which the spot and diffuse mode are implemented as separate operation modes. Practical verification measurements have shown that the lamp terminal characteristics are well described over a wide power and frequency range. Besides the electrical behaviour, physical parameters are available to improve lamp-driver understanding and optimisation. In Chapter 8 the plasma part of the model is incorporated into the proposed observer-based control.

Chapter 4

Low-frequency-square-wave drivers

For electronic HID lamp operation, low-frequency-square-wave (LFSW) current, as discussed in Section 2.3.3, is the standard method. From a power electronic point of view, a LFSW current is certainly not the simplest way to drive an HID lamp. But it is surely the best option because it has the smallest risk of malfunctions and the ability to operate a large variety of the HID lamps in the market [80, 81]. The square-wave frequency is preferably above the line frequency (mostly in the range from 70 Hz to 400 Hz).

In LFSW lamp-drivers a number of energy conversion steps are incorporated between the grid connection and the lamp terminals. These steps can be realised in one or more power electronic stages as discussed in Section 4.1. The first conversion step conditions the input-current drawn from the mains grid to meet the power utility standards. This so-called pre-conditioner stage is addressed in Section 4.2, where two high-efficiency boost converter topologies are described. The interaction of the pre-conditioner stage with the HID lamp terminal behaviour is described in Section 4.2.2. Practical measurement results for both boost converter topologies are presented in Section 4.3. Finally, Section 4.4 concludes this chapter.

4.1 Low-frequency-square-wave topologies

Many LFSW HID lamp-driver concepts have been launched on the market or proposed in the literature. In general, these concepts can be categorised according to the number of sequentially coupled stages. The one, two, and three-stage driver concepts will be discussed in reverse order in this section.

4.1.1 Three stage converter

As depicted in Fig. 4.1 the classic topological approach for electronic lamp-drivers typically comprises three-stages [82–84]. For every functional conversion step, this three-stage driver concept (for LFSW current operation) features a separate power electronic circuit. The energy flows from the mains grid to the lamp terminals passing through the series connected power converters.

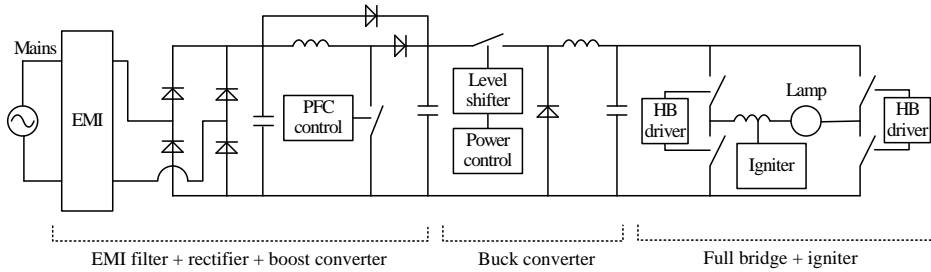


Figure 4.1: Three stage HID lamp-driver topology.

The stages comprise:

1. Pre-conditioner + filter

The first step in this sequence includes an electro-magnetic interference (EMI) filter, full-wave rectifier and a boost converter. The boost converter is operated as a power factor corrector (PFC). This converter controls the input current waveform to be proportional with the sinusoidal mains voltage wave-shape. This is done to attain a high power factor (PF) and guarantee a low total harmonic mains current distortion (THD). On the output side, the dc bus voltage is regulated to a constant level, typically 410 V_{dc}. The electro-magnetic interference (EMI) filter, connected to the mains terminals, attenuates the ballast-generated noise to the desired level.

2. Lamp-current stabiliser

Powered from the pre-conditioner dc bus, the buck converter regulates the lamp-current and thereby the lamp power. The buck controller regulates the cycle-by-cycle switching while an integrated high-voltage level-shift device operates the floating power MOSFET. The output filter, consisting of a capacitor and the igniter transformer series inductance, removes the buck converter switching ripple.

3. Commutator + igniter

The output stage includes a full-bridge circuit to operate the HID lamp with a LFSW current. To achieve an alternating LFSW current, the full-bridge circuit connected to the buck output comprises two half-bridges that commute 180 degrees out of phase with each other. The LFSW current flows

through the HID lamp and series-connected ignition transformer. The ignition circuitry generates current pulses through the primary ignition transformer winding, which in turn induces high-voltage pulses across the lamp terminals, typically between 3 kV and 4 kV. During the non-conductive lamp state the buck output voltage is limited to the open circuit voltage (OCV).

4.1.2 Two stage converter

The existing three-stage (boost, buck, full bridge) electronic driver concept for HID lamps is more than a decade old. Meanwhile, the market, driven by the demand for compactness and cheaper electronic ballasts, has initiated a race between competitors in the lighting electronics business. Although the three-stage converter is still commercially available, it is mostly used for special lighting applications; the main stream market is being supplied with power topologies with a reduced component count.

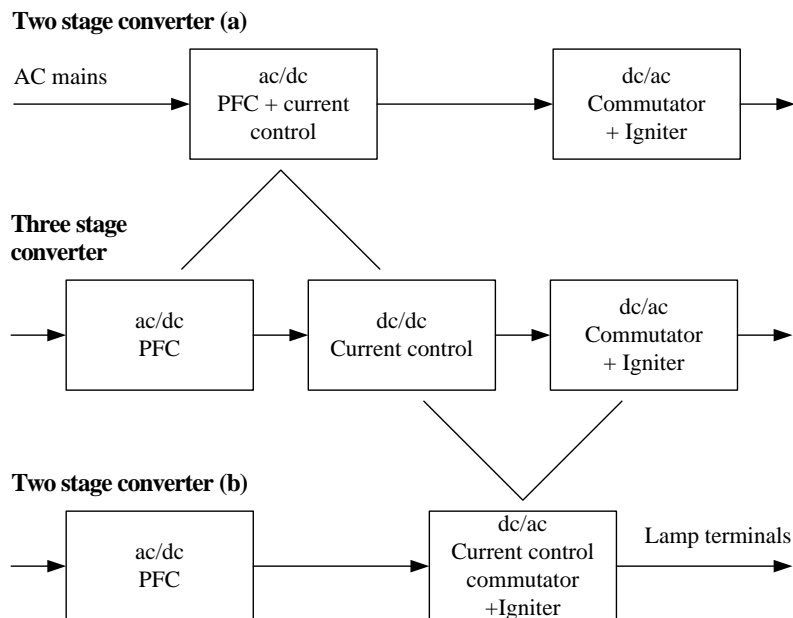


Figure 4.2: Two stage HID driver concepts.

Nowadays, most HID drivers consist of two series connected power stages that control the energy flow from the mains grid downstream to the lamp terminals. In this case one of the converters features combined functionality, in contrast with the classic three-stage concept that comprises a power stage for every functional conversion step. In Fig. 4.2 two possible concepts are described. Concept

(a) combines the PFC ac-dc stage and dc-dc current control stage into a single current controlled ac-dc front-end stage, followed by a dc-ac commutator stage that includes an igniter. Concept (b) combines the dc-dc current control stage with the commutation stage and precedes it with a PFC front-end stage.

In general the first group (a) is based on a flyback or derivative topology [85–88] followed by a low frequency half or full bridge commutator. Those in the second group (b) normally consist of a boost converter pre-conditioner coupled with a half or full bridge buck converter topology [89–92].

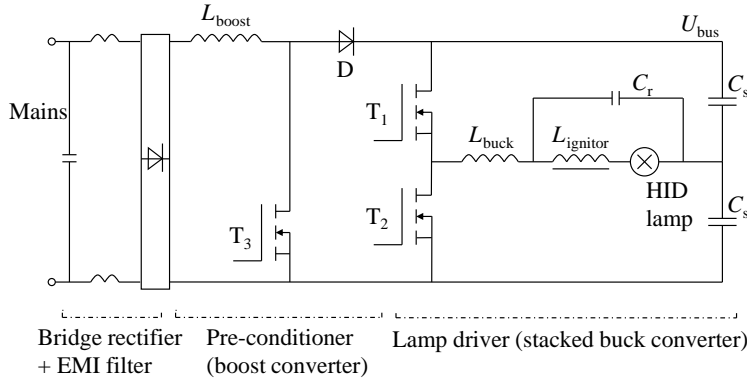


Figure 4.3: Preferred two-stage HID driver consisting of a boost and stacked buck converter.

It is shown in this research that the two-stage configuration, consisting of a boost converter PFC stage and a stacked buck converter, is best suited to replace the three stage converter (Fig. 4.3). The reduced component count and high efficiency enables miniaturisation and cost effective lamp-driver designs. Therefore, this concept is analysed in detail and high-efficiency versions of the boost and stacked buck converter are proposed in Chapter 4 and 5 respectively. The contributions presented in this research have accelerated the market introduction of two-stage topologies by large HID-system manufacturers.

4.1.3 Other lamp-driver concepts

Total integration of all power conversion steps leads to a one stage converter. In this concept the PFC functionality is often based on power feedback schemes [93]. Although this sounds very promising in terms of reduced component count, size, and price, in practice the component stresses, efficiency, and LDI configurability are critical [94]. Therefore, this configuration is hardly ever used in commercial lamp-driver designs.

Another class of lamp-driver topologies is presented in [95]; in this class, HID driver approaches that synchronise the lamp-current with the mains frequency

are discussed. Here the goal is to minimise the energy buffer size and driver losses. However, lamp LFSW current frequencies above the mains frequency are desirable in order to avoid visible light flickering.

4.1.4 Power integration

Topology and circuit optimisation can be used to reduce the component count and maximise the system efficiency. However, the power density of the lamp-driver is limited by the passive components construction technologies, thermal management issues, and power converter manufacturing methods [96]. Mainstream passive power components have non-standard form factors (i.e. different profiles) and poor thermal properties. The assembly of these components on a single PCB results in poor three-dimensional (3D) volume utilisation. To reduce the size and cost of HID lamp ballasts, and therefore make them more attractive for lighting applications, new system integration and packaging technologies were investigated. In [97, 98] the power density of a two-stage LFSW HID ballast is increased by a factor of 1.7 (volume reduced by 41 %), using 3D passive integration technologies.

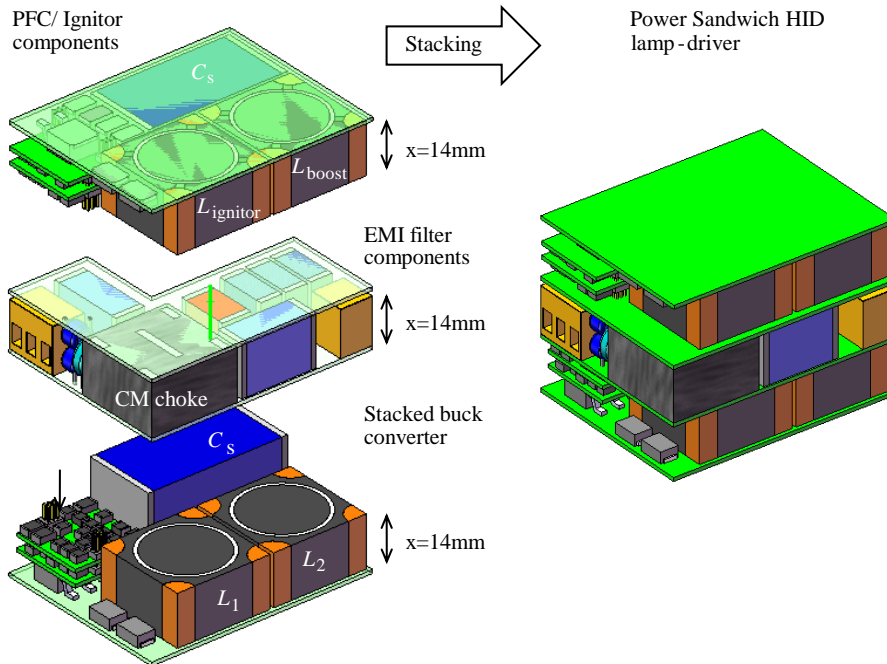


Figure 4.4: High power density packaging (power sandwich) of two-stage HID lamp-driver implemented in three stacked layers [12].

A proposed two-stage HID lamp-driver configuration, consisting of a PFC stage (Section 4.2), and a dual branch stacked buck converter (Section 5.1.3) is implemented using a power sandwich construction method in [12, 13]. These publications present a multilayer high power density packaging of the proposed electronic lamp-driver as shown in Fig. 4.4. The electrical and thermal properties of this sandwich construction, including the thermal models and simulation of the proposed heat removal method, are experimentally investigated.

4.2 Power-factor-correction

To eliminate the stroboscopic effect of light flicker associated with magnetic HID ballasts, almost all electronically operated gas-discharge lamps are driven decoupled from the mains frequency. Therefore, the power from the utility grid flows via an energy buffer to the lamp terminals. Conventionally, lamp-drivers have used simple input circuits consisting of a rectifier bridge followed by a large buffer capacitor. As a consequence, the line current is non-sinusoidal, meaning that it contains a significant amount of harmonics and pollutes the utility grid.

Table 4.1: IEC 61000-3-2 class C standard for lighting equipment.

Harmonic order $[n]$	Limit [%]
2	2
3	$30PF^*$
5	10
7	7
9	5
$11 \leq n \leq 39$ (odd harmonics only)	3
* PF is the circuit power factor	

Governmental legislation and energy standards prohibit this simple and low cost approach for lighting equipment when the active power level is greater than 25 W. In fact, the IEC 61000-3-2 class C (European) standard [99] for lighting equipment (with rated current below 16 A_{RMS} per phase) limits the maximum value of each mains current harmonic separately up to the 39th order. (Table 4.1). For a sinusoidal voltage and non-sinusoidal current, the power factor (PF) can be expressed as

$$PF = \frac{I_{1,\text{RMS}}}{\sqrt{I_{1,\text{RMS}}^2 + I_{2,\text{RMS}}^2 + \cdots + I_{n,\text{RMS}}^2}} \cos \varphi, \quad (4.1)$$

in terms of the RMS value of each contributing harmonic and the phase shift of the fundamental φ . The relation between the PF and the total harmonic

distortion (THD) can be denoted as

$$PF = \frac{1}{\sqrt{1 + \text{THD}^2}} \cos \varphi. \quad (4.2)$$

In order to comply with the lighting regulations, PFC functionality is necessary. In terms of miniaturisation and performance [100, 101] an active switch mode power supply (SMPS) approach is most suitable for lighting applications, although passive approaches [102, 103] do exist. In this case a dc/dc converter with an integrated or separate rectifier stage with a switching frequency far above the mains frequency is applied to shape the input current. Commonly, electronically operated HID lamp-drivers consist of a non-insulated boost converter front-end stage as depicted in Fig. 4.3.

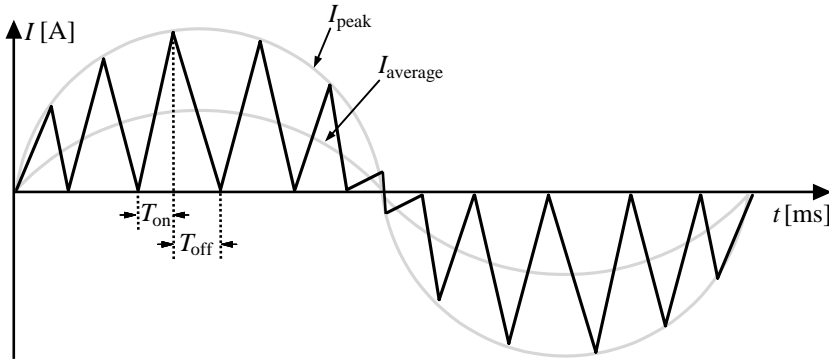


Figure 4.5: Transition mode pre-conditioner inductor current I_{peak} and MOSFET timing (T_{on} , T_{off}). The mains current equals the averaged triangular shaped inductor current I_{average} .

Among the several possible PFC topologies, the boost converter features low component-stress and high efficiency [104–106]. The PFC stage converts the ac grid voltage into a regulated dc bus voltage and shapes the input current to a sinusoidal waveform. For the application under consideration, with a power level ranging between 25 W and 150 W, operation on the border between continuous and discontinuous mode is desirable (Fig. 4.5). The so-called transition mode (TM) of operation improves the converter efficiency by lowering the reverse recovery losses of diode D (Fig. 4.7) and enabling zero voltage switching (ZVS) or at least valley switching [107], as is later detailed in Fig. 4.6. However, the TM mode gives rise to a high input current ripple. Those current harmonics require additional input electromagnetic interference (EMI) filter effort to comply with the standards [108]. However, the EMI issue of the inductor current ripple is reduced by the frequency modulation effect of the TM operation [109].

A wide range of integrated circuit (IC) PFC controllers exist that can operate

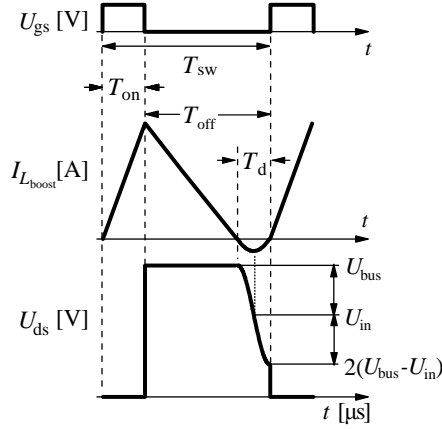


Figure 4.6: Switching waveforms transition mode operation.

the boost converter in the proposed cycle-by-cycle mode. For the experimental set-up an 8-pin device (L6561) is selected [110]. This peak current PFC controller can achieve a PF typically above 0.98, with low enough harmonic current to comply with the regulations.

In Fig. 4.7 the boost converter and its control section are depicted. The HF cycle starts at the moment the boost-inductor current reaches zero and the zero current detection (ZCD) circuit triggers the SR latch to enable the power MOSFET driver GD. At start-up the “starter” sub-circuit provides pulses on the “set” input to enable the MOSFET in the absence of ZCD signals.

The current comparator senses the voltage across the current sense resistor R_s and, by comparing it with the outer control loop signal delivered by the error amplifier, determines the exact time when the external MOSFET is to be switched “off”. The inner loop defines the peak current level to be proportional to the rectified sinusoidal input voltage (R_1 , R_2) and the outer control loop level. The low bandwidth outer control loop regulates the output voltage. It consists of a voltage divider (R_3 , R_4), reference voltage source, and differential error amplifier with compensation network.

Operating the boost converter topology in TM mode allows for a significant reduction in switching losses. In Fig. 4.6 the most important waveforms during TM operation are provided [111]. After the gate drive signal U_{gs} is disabled the inductor current $I_{L_{boost}}$ ramps down until zero current. At that point the boost inductor resonates together with the parasitic circuit capacitance. The zero current detection circuit based on the boost inductor voltage features an inherent delay (T_d) that enables the turn-on of the power MOSFET exactly at zero voltage or in the valley of the drain voltage U_{ds} oscillation. As a result, the turn-on losses are strongly reduced. Depending on the momentary input voltage

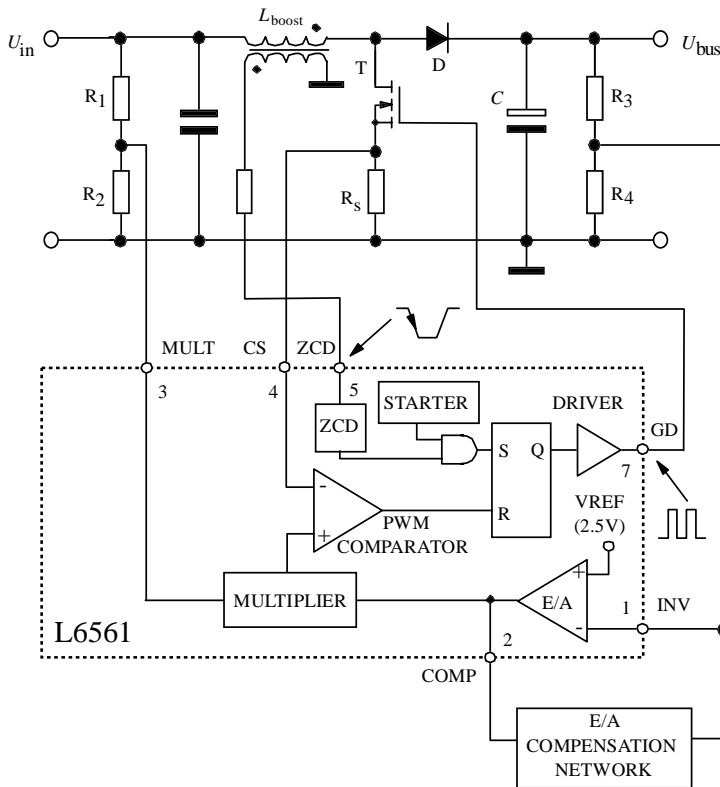


Figure 4.7: Schematic PFC converter including control section.

level and the selected output voltage, the zero voltage criterion is defined as

$$\text{ZVS} \Rightarrow \left[0 \leq \sqrt{2}U_{\text{in RMS}} \leq \frac{U_{\text{bus}}}{2} \right]. \quad (4.3)$$

In practice, at 230 V line voltage and an output voltage that equals 410 V, the ZVS criterion is satisfied for approximately 156° of the sinusoidal mains voltage period.

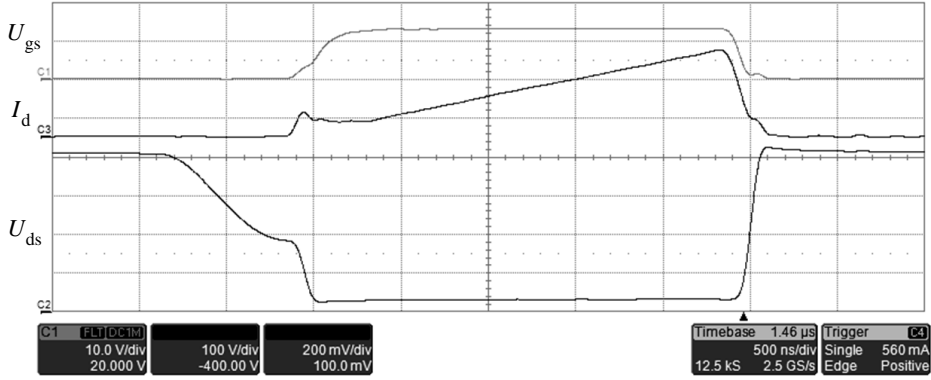


Figure 4.8: Measurement transition mode operation. Gate drive voltage U_{gs} (10 V/div), MOSFET channel current I_{d} (0.2 A/div), MOSFET drain source voltage U_{ds} with small offset to make it distinguishable (100 V/div), time scale (500 ns/div).

The switching behaviour of the boost converter, as shown in Fig. 4.6, was studied in practice. The most important signals were captured (Fig. 4.8) when operating a practical measurement set-up at 230 V mains, with output voltage U_{bus} equal to 410 V. After zero current, the voltage U_{ds} across the MOSFET resonates down to a valley level when the MOSFET gate U_{gs} is enabled. At that moment a small current peak arises in the MOSFET channel current I_{d} , indicating the discharge of the total parasitic capacitance that is present on the MOSFET drain node. Thereafter, the MOSFET current is equal to the boost inductor current and increases linearly, until the programmed maximum peak current level is reached.

4.2.1 Voltage doubler topology

In North America, Japan, and other countries the bulk of the domestic electricity consumption is drawn from 120 V_{ac} mains. In line with the European Union, where 230 V_{ac} mains is the norm, lamp-driver systems suited for 120 V_{RMS} mains operation are commonly equipped with a so-called universal mains pre-

conditioner, which copes with high-line (180 - 264 V_{RMS}) as well as low line (90 - 130 V_{RMS}) mains grid voltage. This coping function is mostly accomplished using a boost converter designed for a wide range of ac line voltages. The penalty for this universal mains approach is increased stress on the power components, which necessitates larger and more expensive components [112].

In this section a voltage doubler boost converter topology [113, 114] is discussed, which aims to overcome the problems introduced by the universal mains approach. This boost converter derivative is intended for low line mains operation. The proposed topology is shown in Fig. 4.9, where the sub-figures illustrate the operating modes. This boost converter is directly connected to the ac mains terminals without a diode bridge [115]. This approach leads to a reduced number of power components in the current path. The differences found during the “on” and “off” state of the power MOSFETs are given in Table 4.2.

Table 4.2: Comparison of boost converter topologies.

	Normal boost	Voltage doubler boost
T_{on}	2×Diode (V_{F}), 1×FET ($R_{\text{ds(on)}}$)	2×FET ($R_{\text{ds(on)}}$)
T_{off}	3×Diode (V_{F})	1×Diode (V_{F})

The conduction losses can be divided into a diode forward voltage drop component V_{F} , and a resistive component $R_{\text{ds(on)}}$. The conduction losses play an important role especially in low line (90 - 130 V_{RMS}) operation where high current stresses occurs. This is in contrast with a reduced voltage stress on the power semiconductors. Therefore, MOSFETs can be applied with lower voltage rating, resulting in a significant reduction in the $R_{\text{ds(on)}}$ resistance for the same die size.

The control section features an exceptional solution that reduces the component count [19]. Both MOSFET gates are operated synchronously without level-shifter circuitry from the floating ground potential GNDA. The cycle-by-cycle control circuitry is designed around the previously introduced IC L6561 (see Section 4.2). Application of a bi-directional MOSFET switch hampers the implementation of the normal peak current control, and consequently the cycle-by-cycle switching is based on a T_{on} timing circuit. The output voltage feedback loop is coupled to the timing circuit that sets the T_{on} time. The output voltage regulation is based on a feedback arrangement, which includes an optocoupler that transfers the control signal from the output voltage ground GND to the floating ground GNDA. The ZCD input of the control IC is connected to the ZCD capacitive divider C_{ZCD} as displayed in Fig. 4.9.

Transition mode cycle-by-cycle operation is favourable for the voltage doubler boost converter with power levels ranging between 25 W and 150 W. This is in line with the normal boost converter preferred operation range discussed in the previous section. The topological modes of operation are displayed in Fig. 4.9 and the related voltage and current wave-shape plots are given in Fig. 4.10. The

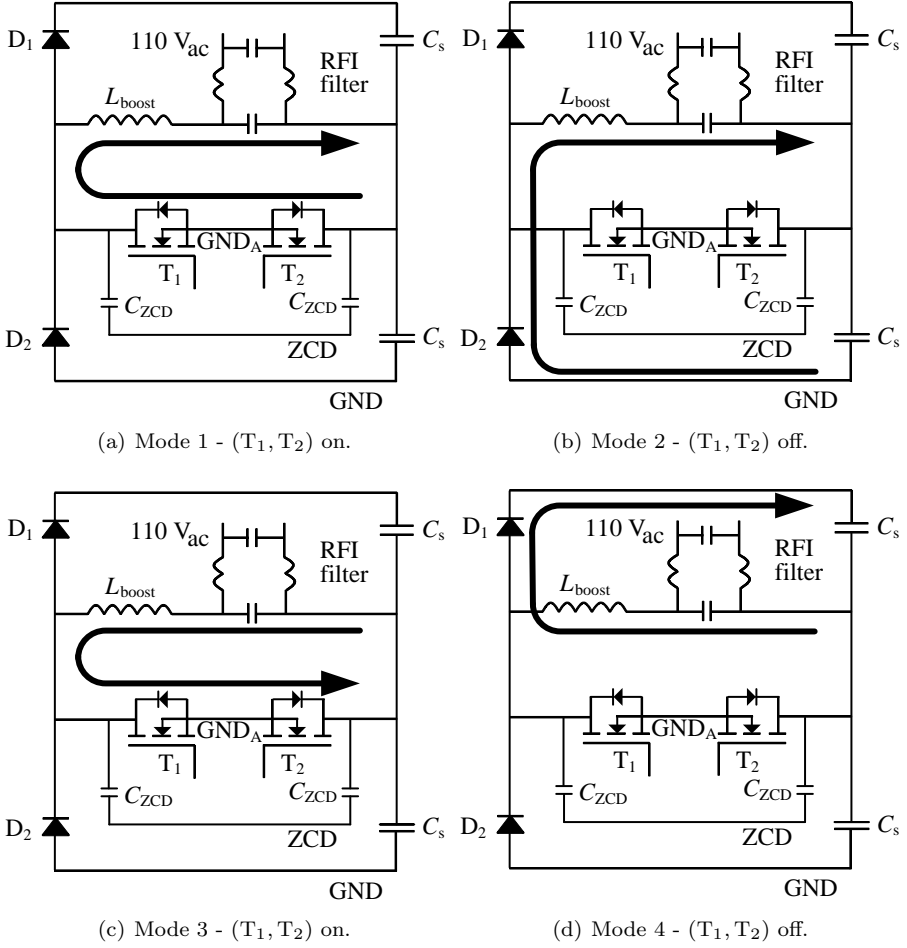


Figure 4.9: Topological modes of the transition mode voltage doubler within one mains cycle.

current flow during a full mains period is defined as follows:

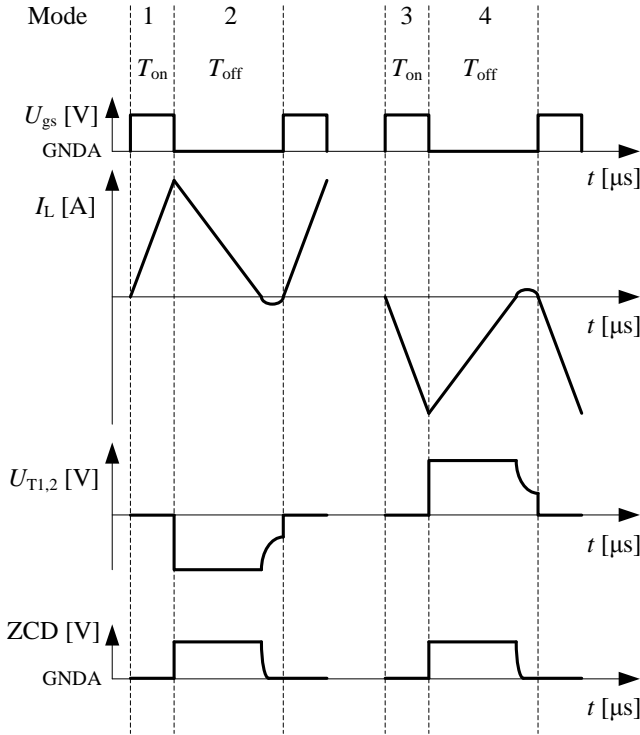


Figure 4.10: Voltage and current wave shapes for voltage doubler topology for the positive and negative part of a mains period.

Mode 1: The bi-directional MOSFET configuration T_1 , T_2 starts conducting at zero current. The inductor current increases until the T_{on} time is expired and T_1 , T_2 are switched off. At that moment the C_{ZCD} and the MOSFET parasitic drain source C_{ds} capacitors take over the current and the voltage across the bi-directional MOSFET switch increases very quickly.

ZCD: During the switch off transition, GND_A falls to GND potential and the zero current detection (ZCD) (ZCD capacitive divider midpoint node) drops to half U_{C_s} . As a result, a positive edge appears on the ZCD logic input.

Mode 2: Diode D_2 takes over the inductor current and ramps down to zero. The inductor current reverses and the voltage across the reverse biased diode D_2 rises. The zero current detection delays (T_d) the turn-on of the bi-directional power MOSFET switch until the voltage across the bi-directional switch resonates

($L_{\text{boost}}, C_{\text{ZCD}} \parallel C_{\text{ds}}$) down to a valley or zero as shown in Fig. 4.10, and Mode 1 starts again.

ZCD: The two nodes of importance (ZCD, GNDA) are capacitively coupled with the rising voltage across diode D_2 . Two capacitive voltage dividers C_{ZCD1} , C_{ZCD2} and $C_{\text{ds(T1)}}$, $C_{\text{ds(T2)}}$ define the voltage between the nodes (ZCD, GNDA). The voltage over the ZCD capacitive divider is equally distributed, which is in contrast with the asymmetric voltage distribution over the MOSFETs C_{ds} series circuit. The voltage dependent behaviour of the parasitic MOSFET device capacitor C_{ds} can be described by

$$C_{\text{ds}} = \sqrt{\frac{qk_s\epsilon_0 C_B}{2(U_{\text{ds}} + \phi_B)}}, \quad (4.4)$$

according to [116, 117], where k_s is the silicon dielectric constant, C_B is the epitaxial layer background concentration [atoms/cm³], and ϕ_B equals the diode potential. If $U_{\text{ds}} \gg \phi_B$, (4.4) can be simplified and yields

$$C_{\text{ds}} \propto \sqrt{\frac{1}{U_{\text{ds}}}}. \quad (4.5)$$

When the voltage across diode D_2 rises, the parasitic divider yields $C_{\text{ds}}(U_{\text{ds}} = 0\text{V}) > C_{\text{ds}}(U_{\text{ds}} = U_{C_s})$ using (4.5). In turn, this leads to a negative edge trigger on the logic ZCD input that triggers the SR latch.

Mode 3: This mode is similar to Mode 1, only the current direction is inverted and is valid for the opposite mains period-half.

ZCD: After the bi-directional switch is turned off the voltage over D_2 rises to bus voltage level and the capacitively coupled node ZCD lifts accordingly. However, node GNDA is connected to U_{C_s} via a body-diode of T_2 , and remains constant, leading to a positive edge on ZCD logic input.

Mode 4: This mode equals Mode 2 in the opposite mains period-half, where D_2 conducts the inductor current.

ZCD: After the inductor current crosses zero, the voltage across D_1 increases. Accordingly, the voltage on the capacitively coupled ZCD node decreases, while node GNDA remains equal to U_{C_s} . Consequently, a negative edge appears on the ZCD input that triggers the SR latch.

4.2.2 Power-factor-correction and lamp-driver interaction

The proposed two-stage HID driver topology consists of a boost converter and a half bridge lamp-driver stage as shown in Fig. 4.3. For this topology the open circuit voltage (OCV) across the lamp terminals equals only half the pre-conditioner

output voltage. In practice, when applying normal (600 V) power components and severe safety margins are taken into account the maximum bus voltage is limited to 520 V, and therefore the OCV level to 260 V. This restricted OCV level is sufficient to operate compact ceramic metal-halide lamps according to the ANSI C 78.43 standard [118]. To optimise the two-stage converter performance with respect to both the LDI and circuit efficiency, the bus voltage level is switched between two set-points according to the lamp operating conditions as follows:

High voltage mode ($U_{\text{bus}} = 520 \text{ V}$).

Preceding the lamp start, the high voltage mode is enabled to provide a sufficient OCV level during the take-over phase. Inadequate OCV levels can lead to start problems and lamp degradation. To prevent the lamp from extinguishing when high re-ignition peaks occur, this mode is also active during reduced power conditions or when the lamp is instable.

Low voltage mode ($U_{\text{bus}} = 410 \text{ V}$).

The low voltage mode can be enabled during the run-up phase and normal steady-state operation to increase the driver efficiency.

The lamp-driver's efficiency dependency on the pre-conditioner bus voltage U_{bus} can be explained by the step-up and step-down ratio of the boost and buck converter respectively when it is operated at a higher bus voltage level. An increased conversion ratio of both converters results in lower circuit efficiency when other system parameters remain constant [119].

The PFC control, as discussed in Section 4.2, includes a low bandwidth outer loop to keep the output voltage of the PFC stage constant, and a cycle-by-cycle inner loop to control the boost inductor peak current. The outer loop characteristic affects both the output voltage regulation and the power factor. This feedback loop consists of an error amplifier and a compensation network as depicted in Fig. 4.7. To achieve a high PF and to avoid input current distortion, the loop gain of the PFC regulator must have a crossover frequency below the mains frequency ($< 25 \text{ Hz}$). However, the dc gain and phase margin must be sufficient to ensure stability over a large variety of operating conditions. Especially during the take-over lamp phase, fast load changes between no-load and near full power can occur (see also Section 2.3.1).

The PFC powers the stacked buck converter connected downstream. The stacked buck converter is operated in transition mode with a constant T_{on} timing of the MOSFETs. Therefore, this converter can be seen as an uncomplicated resistive load (Section 5.2) and the compensation network can be designed in a straightforward way [110, 120, 121].

4.3 Experimental measurements

This section discusses the experimental results for both the normal boost converter for high mains and the voltage doubler for low mains operation. The

Table 4.3: List of the most important components used in the experimental set-up.

Component	Normal boost (Voltage doubler boost)
EMI filter	Vogt RK17 $1\ \Omega$ (RK23 $0.45\ \Omega$)
Control IC	ST L6561
MOSFET(s)	ST 6NC60 $R_{ds(on)} = 0.75\ \Omega$
Bridge diodes	1N4007 $V_F = 1.1\ \text{V}$
Fast diode(s)	MUR160 $V_F = 1.1\ \text{V}$
Electrolytic capacitors	BXA $68\ \mu\text{F}$ $350\ \text{V}$
Boost inductor	$1.2\ \text{mH}$ ($0.6\ \text{mH}$)

prototypes are built with commonly available components, as listed in Table 4.3.

The performance of the boost converter was measured while it was powered from an ac power supply HP 6812A at 230 V, 50 Hz. The converter output is connected with a resistive load and regulated at 410 V. About 78 W output power is delivered, which is comparable to a two-stage 73 W HID lamp-driver configuration. The mains voltage and current were measured with a LeCroy WaveRunner 6030A oscilloscope that included current probe LeCroy AP015. In Fig. 4.11 the resulting waveforms are displayed. In contrast to the pure sinusoidal input voltage, the ac current drawn from the supply shows crossover distortion near the zero-crossings of the line voltage, increasing the mains current THD. To overcome this issue, an additional control loop can be implemented to boost the existing peak current level near the zero crossings [110]. Secondly, the current wave-shape maxima are slightly out of phase with the mains voltage. This skewing is caused by the small output voltage ripple caused by the rectified mains frequency, where the error amplifier links the output voltage with the momentary input current level. The design compromise between the load regulation and input current THD defines the compensation network configuration.

The second boost converter configuration in this section is operated at 110 V, 60 Hz. In line with the previous evaluation, the output terminals are connected with a resistive load regulated at 410 V resulting in approximately 78 W output power. In Fig. 4.12 the line voltage and input current for the voltage doubler boost converter are given. Here also, some crossover distortion appears near the zero crossings. For both pre-conditioner configurations the measured operation conditions are summarised in Table 4.4. The corresponding harmonic line current components and international standard IEC 61000-3-2 limits are presented in Table 4.14, and graphically displayed in Fig. 4.14. The measured efficiency for both experimental pre-conditioners at maximum output power $P = 78\ \text{W}$ as a function of the line voltage is shown in Fig. 4.13. The performance of the voltage doubler converter at low line voltages illustrates the advantages of the reduced conduction losses for this configuration. The switching losses are minimised through the TM mode of operation.

Table 4.4: Measured performance pre-conditioners.

Version	230 V PFC	110 V PFC
f	50 Hz	60 Hz
P	82.10 W	81.1 W
S	84.5 VA	82.1 VA
Q	19.9 VAR	13.3 VAR
PF	0.972	0.986
CF	1.53	1.61
V_{THD}	0.03 %	0.03 %
I_{THD}	9.8 %	14.88 %
η	96.5 %	95.7 %
U_{output}	410 V	410 V
P_{output}	79.2 W	77.4 W

Table 4.5: Measured line current harmonics.

Harmonic order [n]	Limit [%]	230V PFC [%]	110V PFC
2	2	0.047	1.86
3	$30\lambda^* \approx 29.4$	7.281	13.523
5	10	4.776	4.815
7	7	3.861	2.925
9	5	1.822	1.570
$11 \leq n \leq 39$ (odd harmonics only)	3	≤ 0.832	≤ 0.729
* λ is the circuit power factor			

4.4 Discussion

Electronic low-frequency-square-wave (LFSW) lamp-drivers control the power flow from the utility grid to the lamp terminals. This power conversion consists of three functional steps which can be realised using one or more sequentially coupled power converters. The first step comprises a power factor corrector (PFC) to condition the input-current drawn from the mains grid to meet the power utility standards. To implement the PFC functionality, two non-isolated boost converters are discussed. Both are operated in transition mode to reduce the switching losses.

The standard boost converter is perfectly suited for high mains applications, while the voltage doubler boosts the system efficiency at low mains grids. In the proposed voltage doubler topology the diode bridge is omitted to minimise the conduction losses. In addition, the control section features a floating control solution, which serves to reduce the component count. From a lamp-driver interaction (LDI) perspective it is essential to regulate the dc bus voltage to achieve both sufficient open circuit voltage (OCV) during the start phase and optimal efficacy at steady-state.

In the proposed lamp-driver configuration the two remaining functional conversion steps can be combined in a stacked buck converter configuration that will be discussed further in Chapter 5. The resulting two-stage lamp-driver is desirable for its controllability, high efficiency, and high power density. To reduce the size and cost of this HID lamp-driver concept even further, the application of power sandwich packaging is researched.

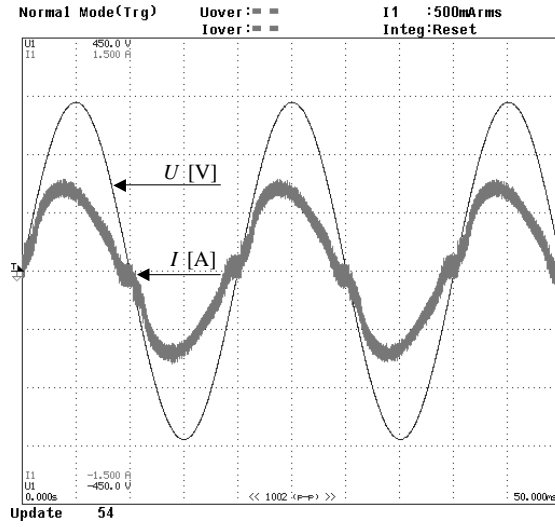


Figure 4.11: Measurement of the normal boost converter mains voltage (112.5 V/div) and mains current (0.375 A/div). Time scale (5 ms/div).

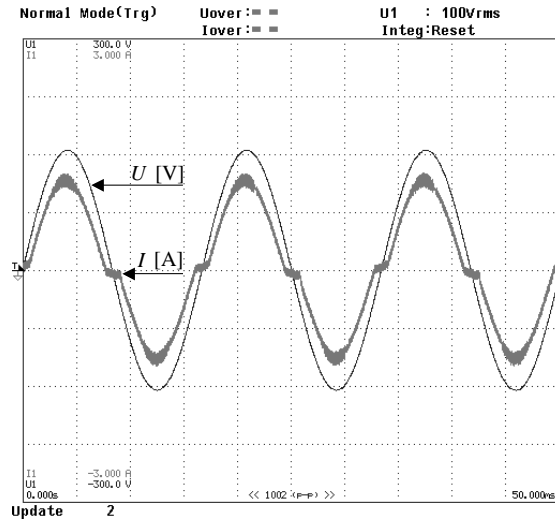


Figure 4.12: Measurement of the voltage doubler boost converter mains voltage (75 V/div) and mains current (0.75 A/div). Time scale (5 ms/div).

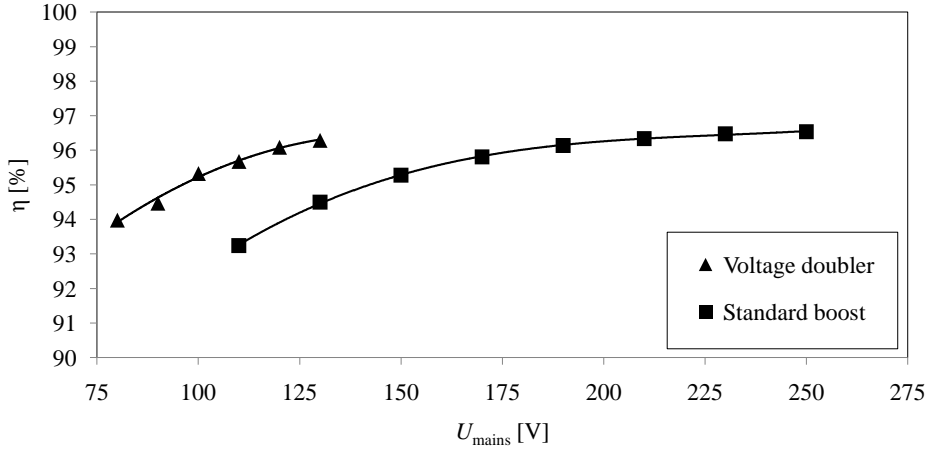


Figure 4.13: Measured pre-conditioner efficiency for voltage doubler (110 V) and standard boost converter (230 V) configuration.

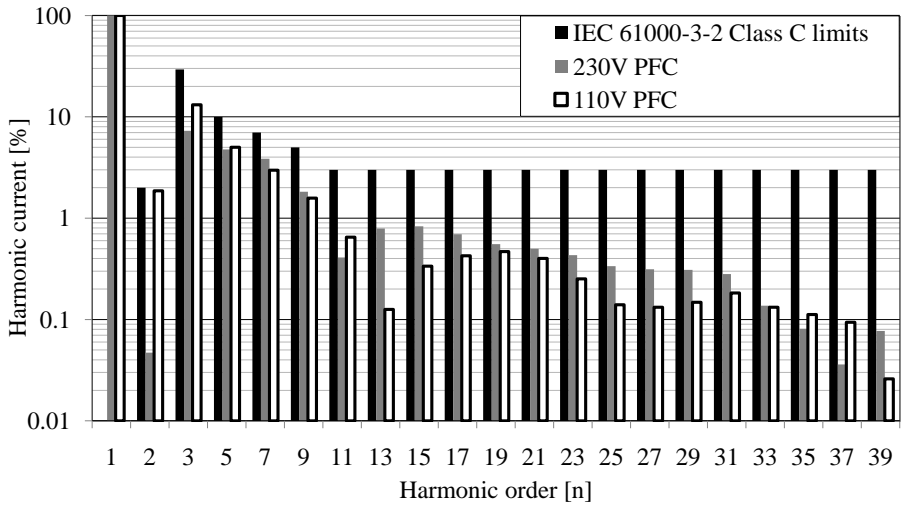


Figure 4.14: Pre-conditioner conformity to EN 61000-3-2 standard.

Chapter 5

Stacked buck converter

Electronic lamp-drivers are becoming increasingly popular for indoor HID applications (e.g. shop lighting), and high-end outdoor HID applications (e.g. city beautification). They offer power saving, flicker free operation, and reduced weight and size. Cost-effective designs that feature continuous dimming and digital addressable lighting interface (DALI) [122] have further accelerated their market share. Numerous lamp-driver topology concepts have been described in the literature and implemented in commercial designs. Low-frequency-square-wave (LFSW) HID lamp-driver topologies in general can be categorised based on whether they have one, two, or three-stage converters, as discussed in Chapter 4.

This chapter addresses the second part of the proposed two-stage converter, the stacked buck topology [123]. Two high-efficiency zero voltage switching (ZVS) stacked buck topologies are proposed in Section 5.1. The cycle-by-cycle control that enables ZVS operation is described in Section 5.2. The impact of the driver control on the gas-discharge during the different phases of operation is discussed in Section 5.3. Practical implementation and measurements are given in Section 5.4. The chapter is concluded with a discussion in Section 5.5.

5.1 Stacked buck topology

Among the several possible LFSW topologies, two-stage drivers [92] can provide excellent performance with high-efficiency. The two-stage approach comprises a pre-conditioner section followed by a stacked buck converter that includes an igniter, as shown in Fig. 5.1. The stacked buck configuration consists of a MOSFET half bridge in one half and two large buffer capacitors C_s in the other half of the bridge. On average, the buffer capacitors are equally charged, therefore during operation the capacitive divider midpoint equals half the bus voltage U_{bus} .

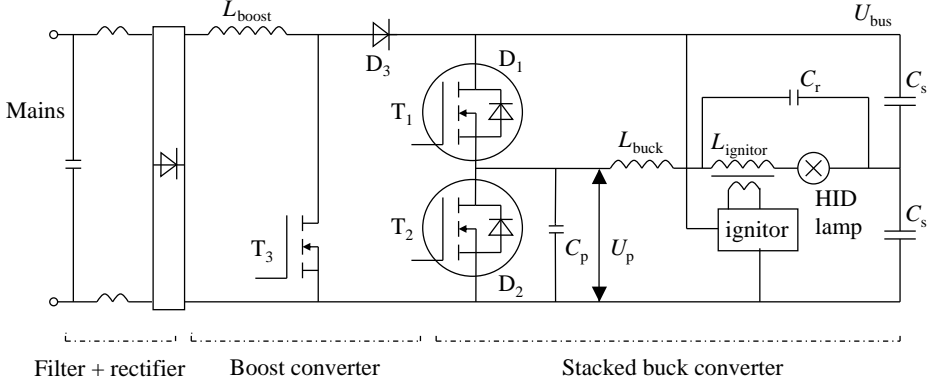


Figure 5.1: Two-stage lamp-driver topology.

5.1.1 Zero voltage switching

There is a need for improved efficiency in HID drivers. Improving the LFSW lamp-driver efficiency requires reduction of both conduction and switching losses. Due to their extremely low switching losses during each switching transition, ZVS topologies are of great interest [91, 124]. Power converters based on mainstream power components that can be operated at high switching frequencies are favourable. In practice the switching frequency is designed between 100 kHz and 400 kHz. In line with the boost converter design considerations, to allow ZVS, the stacked buck topology is operated in critical discontinuous, so-called transition mode (TM). In this case the ZVS condition is defined as follows

$$\text{ZVS} \Rightarrow [0 \leq U_{\text{lamp}} \leq \frac{1}{2}U_{\text{bus}}], \quad (5.1)$$

where U_{bus} represents the pre-conditioner output voltage, which in practice equals 410 V. Thus, ZVS can be achieved within a lamp voltage range between zero and half the bus voltage. In general, this is always the case for compact HID lamps, with a nominal terminal voltage ranging between 80 V and 120 V.

The classic stacked buck converter topology [123], as displayed in Fig. 5.1, consists of two integrated (stacked) buck converters in a half bridge topology. In this configuration MOSFET T_1 is operated in combination with body-diode D_2 and MOSFET T_2 with body-diode D_1 . To produce a LFSW current through the lamp terminals, the role of the two switches must be changed every low frequency half period. The triangular shaped buck converter current, I_{buck} , that flows between the MOSFET half bridge and the buffer capacitors is shown in Fig. 5.2 for both parts of a low frequency period. The output filter formed by C_r and L_{ignitor} diminishes the high-frequency components of the triangular buck converter current, to avoid the occurrence of acoustic resonances inside the

discharge vessel.

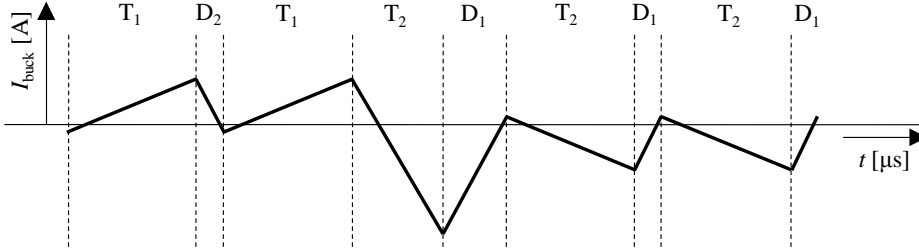


Figure 5.2: Stacked buck converter inductor current I_{buck} .

To ensure ZVS during the low-frequency commutation, this process is synchronised with the high-frequency cycle-by-cycle switching action. This eliminates hard switching and makes the current reversal as fast as possible, without creating additional commutation dead time [91].

In this quasi-resonant converter the LC resonant circuit, associated with the power switch, consists of the buck converter inductor L_{buck} and the total parasitic capacitance C_p as present on the MOSFET half bridge midpoint node. Between the zero-current-detection (ZCD) time instants and the actual switching action, a small control delay enables ZVS operation. This small delay allows the MOSFET half bridge node to resonate to the other rail. In the classic stacked buck converter configuration the negative current at the end of a high-frequency cycle (Fig. 5.2) is mainly caused by the slow body-diode reverse-recovery. Despite ZVS, in practice the slow reverse-recovery of the MOSFET internal body-diode plays a dominant role in the total losses. This phenomenon is described in more detail in the following Section 5.1.2.

5.1.2 Switching losses

The ZVS mode appears to be the perfect solution until the stresses are examined [125]. The power MOSFET in a high-voltage high-frequency ZVS converter will experience different dv/dt and di/dt dynamic stresses compared to a standard PWM circuit. The body-diode is especially troublesome. There are two points of concern: the body-diode ruggedness and its reverse recovery charge.

The body-diode losses can be divided into conduction losses, which are proportional to the forward voltage V_F multiplied by the current through the diode, and reverse recovery losses. Reverse recovery results when the forward conducting diode is taken from forward to reverse bias. Figure 5.3 shows typical reverse recovery waveforms for an inductively loaded diode. Interval I of the diode conduction characteristics shows a diode conducting current I_F in the forward direction with forward voltage drop of V_F . When the diode is reverse biased in interval II, the series inductance within the circuit continues to force current through the

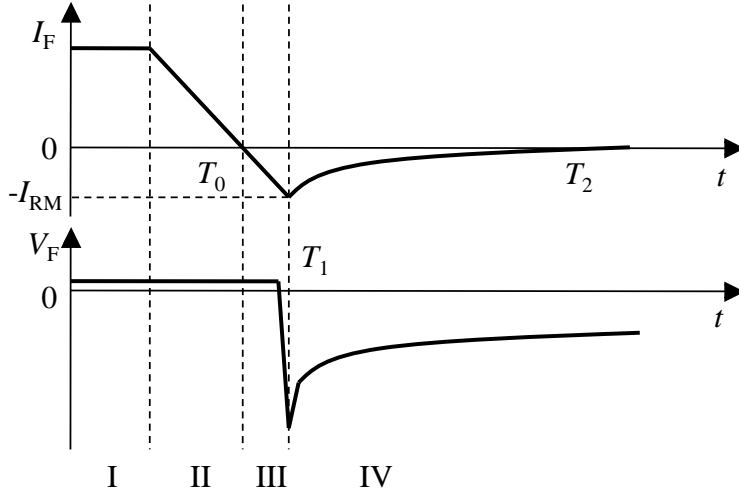


Figure 5.3: Diode current I_F and voltage V_F during reverse recovery.

diode. The voltage V_F will remain approximately constant as the current reaches zero at time T_0 . In interval III the stored charges within the diode PN junction are depleted, resulting in a negative current which peaks at a value of I_{RM} at time T_1 . When the stored charge is depleted, the voltage drop across the diode snaps in the direction of the reverse bias. After a brief overshoot it will settle at the steady-state reverse biased value in interval IV. In the reverse recovery case, power is dissipated during interval III and IV until equilibrium is restored within the PN junction, and the diode current drops to zero.

Table 5.1: Reverse recovery time versus voltage [126].

Reverse voltage [V]	t_{rr} [μs]	Comment
1	3.73	Estimated
20	1.09	Measured
100	0.57	Measured
400	0.32	Measured

The effect of voltage across the body-diode on the reverse recovery process is examined in [126]. In Table 5.1 the reverse recovery time t_{rr} at 100 A/ μs versus the applied reverse voltage are given for a standard 500 V IR power MOSFET. This data shows that for these MOSFETs the reverse recovery time, t_{rr} , increases when the applied reverse voltage decreases. Furthermore, the reverse recovery time is dependent on the forward current, di/dt , and the junction temperature.

In a ZVS half bridge circuit the power MOSFET is turned “on” at zero voltage when its body-diode is conducting and clamps the drain-source to approximately

-0.7 V. The body-diode is under reverse recovery while the MOSFET starts to carry forward current. No dynamic voltage stress is imposed on the drain of the power MOSFET when the body-diode is in reverse recovery. Theoretically, due to ZVS the reverse recovery of the body-diode will not be subjected to the turn-off dv/dt stress that usually happens in a hard-switching converter. But as shown in Table 5.1, it will take longer for the body-diode to sweep the charges out from the drift region and for the depletion region to re-combine under low voltage conditions.

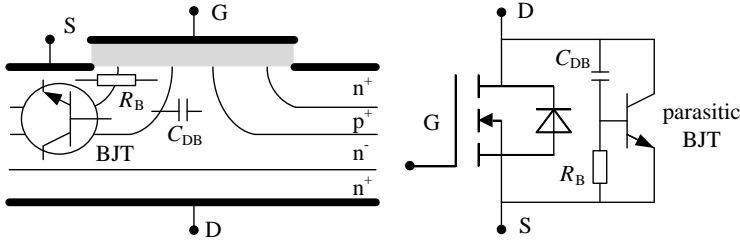


Figure 5.4: Simplified cross-section and equivalent circuit of a standard MOSFET.

At the moment the power MOSFET turns “off”, the body-diode is not yet fully recovered, and thus it may not be able to block reverse voltage. If the remaining charges are still in the junction when the opposite power MOSFET is turned “on”, the resulting high dv/dt may trigger the parasitic bipolar junction transistor (BJT) shown in Fig. 5.4 and might destroy the power MOSFET. Once the body-diode is in reverse recovery, two conditions could trigger the failure mode. The first is due to the peak reverse recovery current I_{RRM} . This current flows from drift region n^- into p^+ implant, and when this current produces a voltage drop on the p^+ implant resistance R_B , the parasitic BJT might turn “on”. Secondly, turn-off dv/dt induces a current through C_{DB} and R_B , and might turn “on” the parasitic BJT.

The classic way to overcome the problems encountered in the basic ZVS topology, is to apply a power MOSFET with a series-connected diode, to prevent forward-bias of the body-diode, and a parallel ultra-fast diode to carry the free-wheel current. However, this solution has a negative impact on cost, circuit complexity, and system efficiency. In the following sections two high-efficiency stacked buck converter variants are presented.

5.1.3 Dual branch stacked buck converter

In this section a topology solution of the stacked buck converter is presented, based on the principle of disabling the MOSFET slow internal body-diodes. In this configuration the stacked buck converter topology is split up into two in-

dependent buck converter sections (dual branch topology) [14] with fast free-wheeling diodes and separated inductors, as shown in Fig. 5.5.

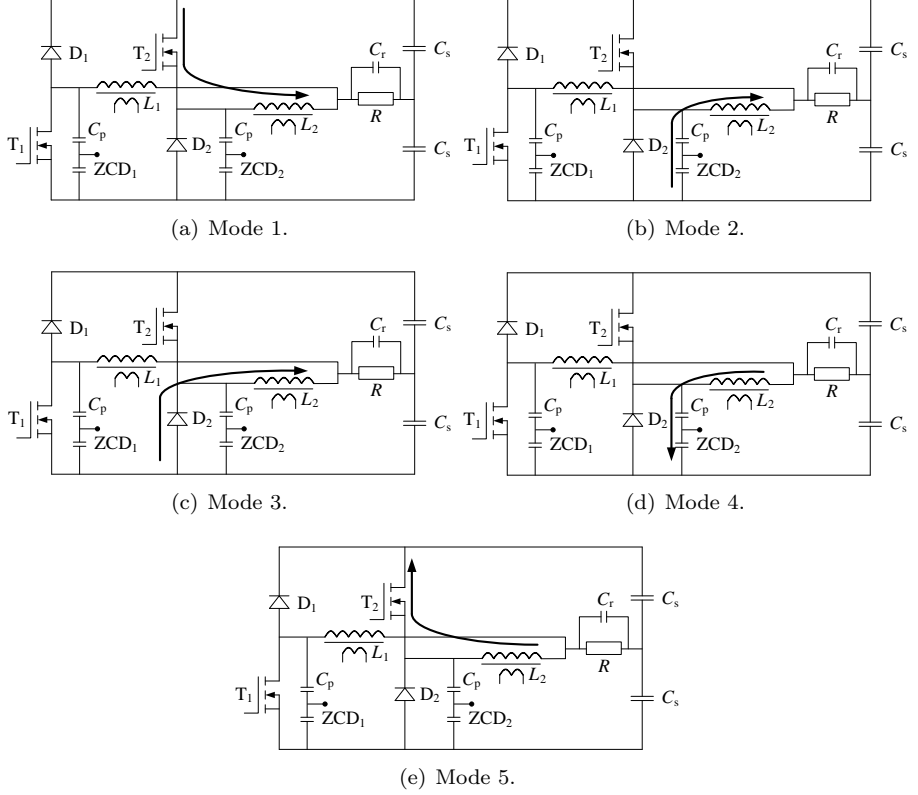


Figure 5.5: Topological modes of the dual branch stacked buck converter within one switching cycle.

The topological modes of the proposed ZVS converter are shown in Fig. 5.5. In this analysis the total parasitic capacitance of the MOSFET, diode, and inductor is lumped together with the capacitive divider C_p that is placed between the lower bus and the centre point. The tap points of these capacitive dividers (ZCD_1, ZCD_2) are coupled with the zero current detection cycle-by-cycle control logic (Section 5.2.2). Typical cycle-by-cycle converter voltage and current waveforms are displayed in Fig. 5.6. The stages within one switching cycle are described as follows:

Mode 1: MOSFET T_2 starts conducting at zero voltage and the inductor current increases.

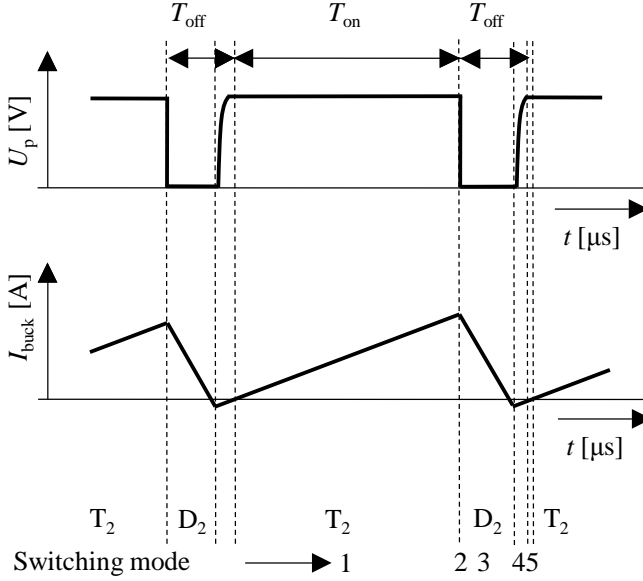


Figure 5.6: Dual branch stacked buck converter current I_{buck} and voltage U_p across capacitive divider C_p .

Mode 2: When the T_{on} time expires, or the peak current limit is reached, T_2 is switched “off” and the parallel capacitor C_p takes over the inductor current. The capacitor’s voltage decreases very quickly.

Mode 3: Freewheel-diode D_2 takes over the inductor current when the capacitor voltage U_p reaches the lower bus voltage level. In this phase, the inductor current continues to decrease until it reaches zero, after which the diode is operated in reverse biased mode and a reverse voltage builds up.

Mode 4: When diode D_2 is switched “off”, the capacitor C_p takes over the inductor current. The capacitor C_p charges and the voltage across it increases rapidly.

Mode 5: When the capacitor C_p voltage equals the bus voltage level the body-diode D_2 takes over the small resonant current. Now MOSFET T_2 can be switched “on” again in ZVS condition and Mode 1 starts again.

This explanation shows that the freewheel current is conducted by the external fast diodes. During operation there is no reverse recovery of the internal slow body diodes, preventing high switching losses.

The proposed dual branch topology has proven to be very robust. In this configuration with separate inductors cross conduction of the MOSFET half bridge

is almost impossible. Therefore, the timing of the level-shifter circuitry is uncritical. This makes this topology perfectly suited for mass production with multiple component suppliers.

5.1.4 Synchronous stacked buck converter

The classic stacked buck converter topology (Fig. 5.1) can be controlled in such a way that the low-ohmic MOSFET channel is used bi-directionally. As a result the MOSFET channel replaces the body-diode function, allowing the stacked buck converter to be operated in synchronous switching mode [15]. The border condition for this operation mode can be defined as

$$R_{ds(on)}I_{ds} < V_F, \quad (5.2)$$

where V_F equals the body diode forward voltage. Consequently, the switching losses are almost eliminated, because the MOSFET channel can be switched “off” much faster than the internal body-diode. In contrast with a normal synchronous buck converter, this topology doesn’t need a forced negative current to provide ZVS as defined in (5.1). Therefore, for optimum efficiency the control delay and its related negative current must be as small as possible.

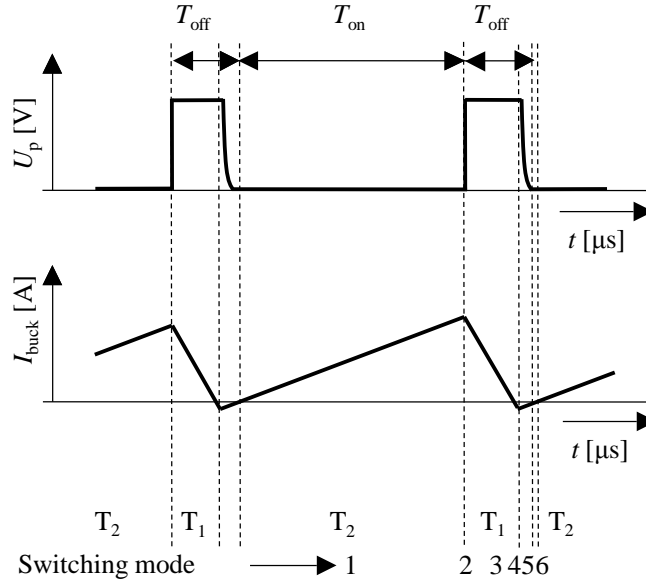


Figure 5.7: Synchronous stacked buck converter current I_{buck} and voltage U_p across capacitor C_p .

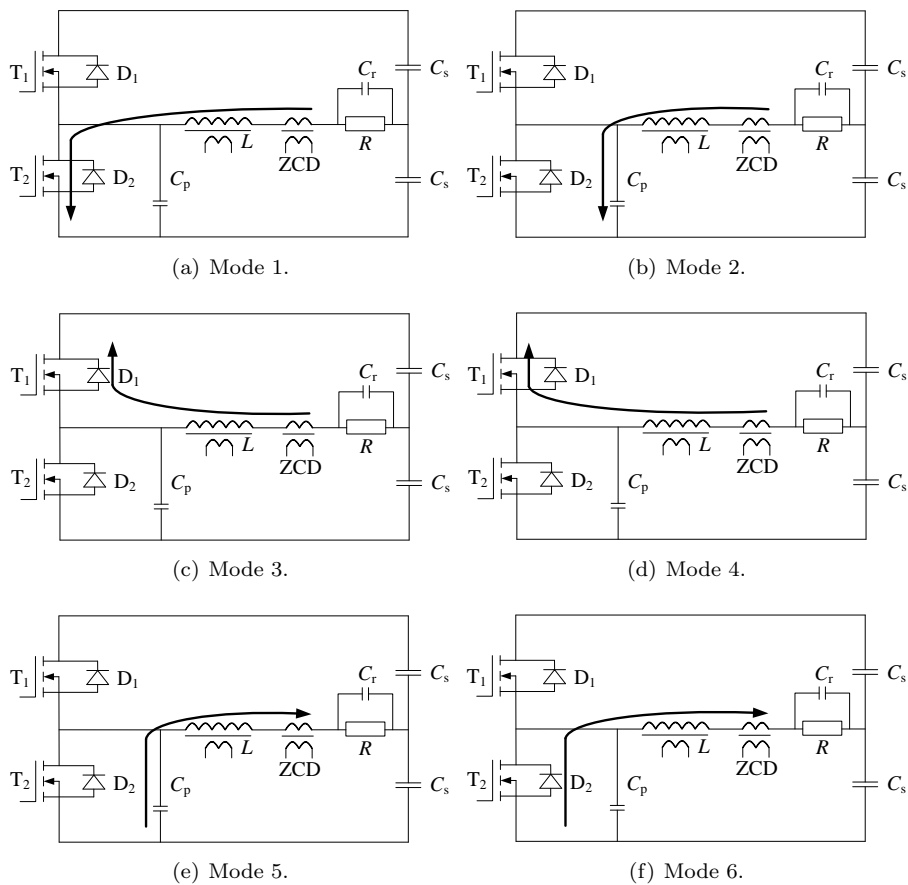


Figure 5.8: Topological modes of the synchronous stacked buck converter within one switching cycle.

The topological modes of the proposed ZVS converter are explained using the simplified schematics in Fig. 5.8. Here the total parasitic capacitance of the MOSFET and buck inductor are lumped together and represented by capacitor C_p , placed between the lower bus and the centre point. The voltage across this capacitor and the corresponding converter current are displayed in Fig. 5.7. The sequential converter stages within one switching cycle are defined as follows:

Mode 1: MOSFET T_2 starts conducting at zero voltage and the inductor current increases.

Mode 2: When the T_{on} interval expires, or the peak current limit is reached, T_2 is switched “off” and the parallel capacitor C_p takes over the inductor current. The capacitor’s voltage rises very quickly.

Mode 3: Body-diode D_1 takes over the inductor current when the capacitor C_p voltage equals the bus voltage.

Mode 4: MOSFET T_1 can be switched “on” (ZVS) while the body-diode is conducting. In this phase, the inductor current decreases further and reaches zero. The control circuitry detects zero current and switches “off” MOSFET T_1 . However, an inherent time delay causes a small negative current.

Mode 5: When MOSFET T_1 is switched “off”, the capacitor C_p takes over the inductor current. The capacitor C_p discharges and the voltage across it decreases rapidly.

Mode 6: When the capacitor C_p voltage equals zero the body-diode D_2 takes over the negative current. Now MOSFET T_2 can be switched “on” again in ZVS condition and Mode 1 starts again.

The previous explanation shows that body diode operation is almost excluded. In the practical situation the dead time in mode 3 and 6 must be implemented to avoid cross conduction. The short body diode conduction time that is followed by MOSFET channel conduction (5.2) enables the diode to fully recover. The synchronous switching mode principle is experimentally verified in Section 5.4.1. Those practical measurements show the proposed operation mode is much more efficient than the classic approach (Section 5.1).

The stacked topology operated in synchronous mode is highly efficient [10], and therefore is perfectly suited for miniaturised designs. Moreover, it features only one buck inductor, compared to the dual branch converter which has two. However, MOSFET timing is critical to minimise the negative current and related circuit losses.

5.2 Cycle-by-cycle switching control

In full electronic HID ballasts both the power level during steady-state and the run-up current must be controlled. More precisely, in steady-state the power

must be held in a narrow band within the nominal lamp voltage range. In the run-up phase the current must be limited to fulfil a given lamp specification. Normally a feedback loop is used to control the lamp power and run-up current [127]. In the approach applied here, a power control loop can be omitted. The stacked buck converter topology consists of an active switch with a fixed on time (T_{on}) setting. The lamp power is then defined as

$$P_{\text{lamp}} = \left(\frac{1}{2}U_{\text{bus}}U_{\text{lamp}} - U_{\text{lamp}}^2\right) \left(\frac{T_{\text{on}}}{2L}\right), \quad (5.3)$$

which results in a parabolic lamp power curve [127]. There is a maximum where

$$P_{\text{lamp}} = P_{\text{max}} \rightarrow U_{\text{lamp}} = \frac{1}{4}U_{\text{bus}}. \quad (5.4)$$

This results in an acceptably flat power level over the nominal lamp voltage range. In Table 5.2 the power regulation is shown for a supply voltage U_{bus} that equals 410 V and a lamp voltage range between 75 - 115 V.

Table 5.2: Lamp power regulation over lamp voltage range.

Lamp voltage [V]	Lamp power [W]	Power regulation [%]
75	69.78	-4.41
80	71.57	-1.96
85	73	0
90	74.04	1.47
102.5	75.19	3.00
115	74.07	1.47

According to the American national standard (ANSI) C 82.14-2006 [128], which concerns LFSW electronic ballasts for metal-halide lamps, a lamp-driver shall deliver power to the lamp within 5 % of its nominal value over the lamp voltage range specified in the lamp standard ANSI C 78.43 [118]. Power excursions greater than ± 5 % increase the risk of noticeable lamp-colour variations. According to the ANSI C 78.43 lamp standard for 73 W single-ended ceramic metal-halide lamps, the lamp voltage at 100 hours ranges between 80 V and 100 V. Practical measurements in Section 5.4.1 show the parabolic lamp power curve and validate this behaviour.

On the input terminals, the stacked buck converter operated in T_{on} mode can be characterised as a resistive load using (5.3)-(5.4) and the simplification $P_{\text{circuit}} = P_{\text{lamp}}$, with

$$P_{\text{circuit}} = U_{\text{bus}}^2 \left(\frac{T_{\text{on}}}{32L}\right) = U_{\text{bus}}^2 \left(\frac{1}{R_{\text{circuit}}}\right), \quad (5.5)$$

where R_{circuit} equals the equivalent circuit load resistance.

5.2.1 Peak current limitation

To operate the proposed topology in T_{on} controlled transition mode (TM), theoretically one, but in practice two input signals are necessary. First, to achieve TM operation an accurate ZCD signal is essential. Secondly, a peak current measurement is required. Directly after commutation, the recharging of the output filter capacitor C_r causes very high current flow through the coil L_{buck} (Fig. 5.1). To avoid saturation of the buck coil, an additional peak current limitation is required. Moreover, as a protection measure, the lamp-current I_{lamp} must be limited to I_{max} in the run-up phase and during a short-circuit situation. In practical implementations the I_{max} current limitation is set to 1.5 A for the operation of 73 W HID burners. To avoid differential current measurements the buck current is sensed indirectly, with an auxiliary winding(s) on the buck inductor(s) L_{buck} (Fig. 5.5, 5.8). The auxiliary winding voltage is integrated to get a measure for the converter current, which is used by the control circuitry.

5.2.2 Zero current detection

Detection of the zero current occurrence in the dual branch configuration (Section 5.1.3) is implemented in a straightforward way. After the MOSFET stops conducting, the freewheel diode takes over the inductor current. Then the inductor current decreases and finally reaches zero. At that moment the fast freewheel diode switches from forward biased mode to reverse biased mode and a reverse voltage builds up. This voltage across the diode terminals can be reduced to logic voltage levels by means of a capacitive divider C_p (Fig. 5.5), assisted by two small-signal clamping diodes. The proposed detection circuit is displayed in Fig. 5.9, including the control logic to select the appropriate ZCD capacitive divider (see $\text{ZCD}_1, \text{ZCD}_2$ in Fig. 5.5) during a LFSW period according to the HI/LO logic level. The HI/LO signal is given in Fig. 5.12, and follows the polarity of the constrained buck converter current I_{buck} .

For the synchronous buck converter configuration, detection of the zero current moment is more complicated. In fact, in this configuration the freewheeling current is conducted by the MOSFET channel without rectifying properties. Therefore, an additional current sensor in series with the inductor is incorporated to sense the zero current occurrences.

In series with the buck converter inductor (Fig. 5.8) a fast-saturating ferrite “toroid” ZCD transformer delivers pulses for the control logic. By doing so, the detection signal can be galvanically isolated from the control circuitry. The auxiliary winding on the core induces one voltage peak per zero crossing (Fig. 5.10(b)). One benefit of this method is the presence of the rising edge before zero is actually reached. The timing can be influenced by the moment of core saturation, which is defined by the number of primary windings, and by the magnetic core material permeability μ . This can be used to eliminate most of the inherent control delay, and thereby it minimises the amount of negative current allowing for the highest possible circuit efficiency.

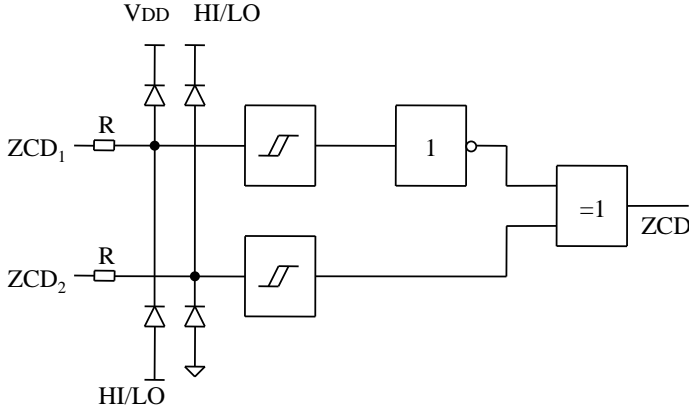


Figure 5.9: Zero current detection (ZCD) circuit.

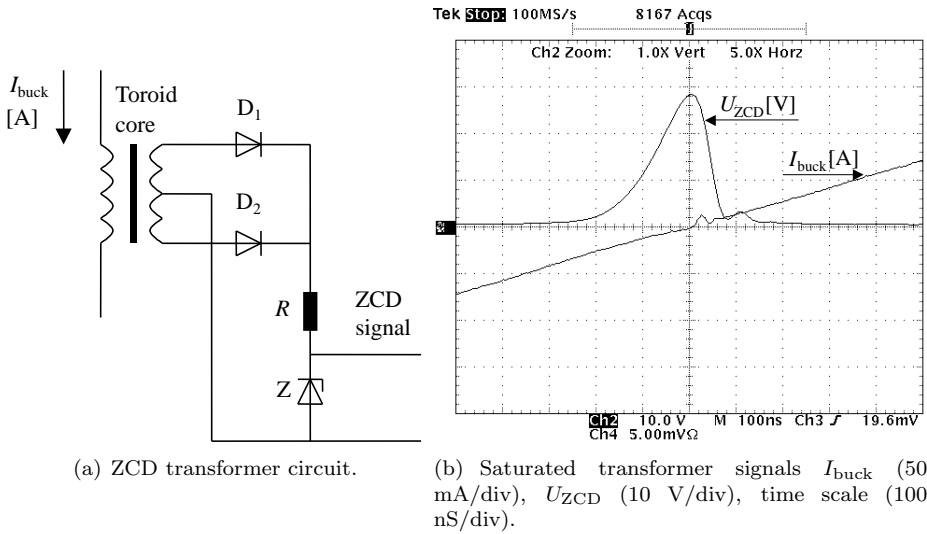


Figure 5.10: ZCD circuit and operation signals that include transformer output pulse voltage and buck inductor current primary transformer current.

The ZCD signal must be present for both the positive and the negative part of a low frequency commutation period. An additional circuit is needed to create a positive edge independent of the buck inductor current direction, as showed in Fig. 5.10(a), where the maximum voltage is clamped by means of a zener diode to protect the control input against excessively high input voltages.

5.2.3 Control circuit implementation

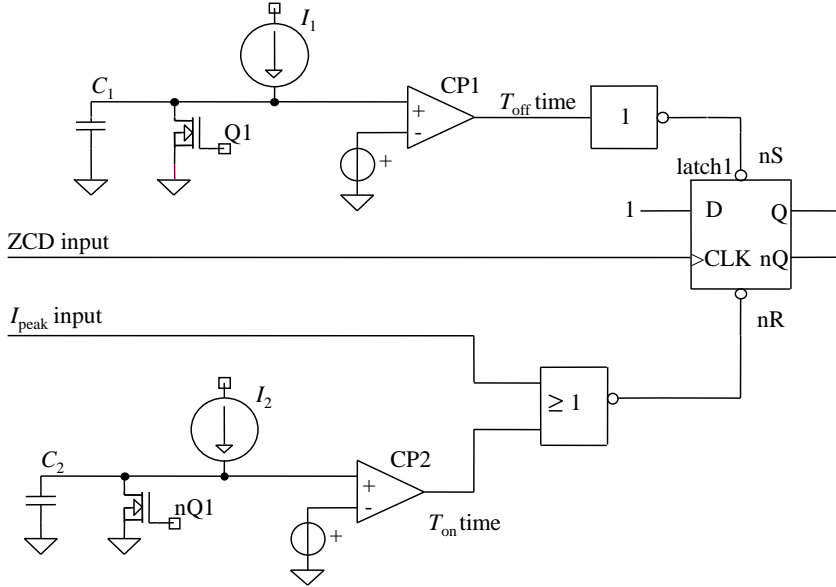


Figure 5.11: Control circuit input section of the stacked buck converter.

The control part that achieves TM operation is built around a standard flip-flop (latch1), as displayed in Fig. 5.11. The ZCD signal (as defined in the previous Section 5.2.2) is connected to the positive edge triggered clock input. The rising edge of a ZCD pulse combined with the static logic “1” on the D input results in a set signal. The maximum T_{off} timer is connected with the asynchronous set input. Finally, the T_{on} timer and the current peak input are combined with a logic OR function and linked with the asynchronous dominant reset pin. The T_{on} timer is built around a comparator, as is the T_{off} timer. The timing principle is straightforward: a fixed current source charges the connected capacitor until the capacitor voltage equals the reference voltage on the inverting comparator input. At that moment the comparator triggers the flip-flop (latch-1), and as a result, the corresponding small-signal discharge MOSFET is enabled.

The second part of the control logic is displayed in Fig. 5.12, where the input

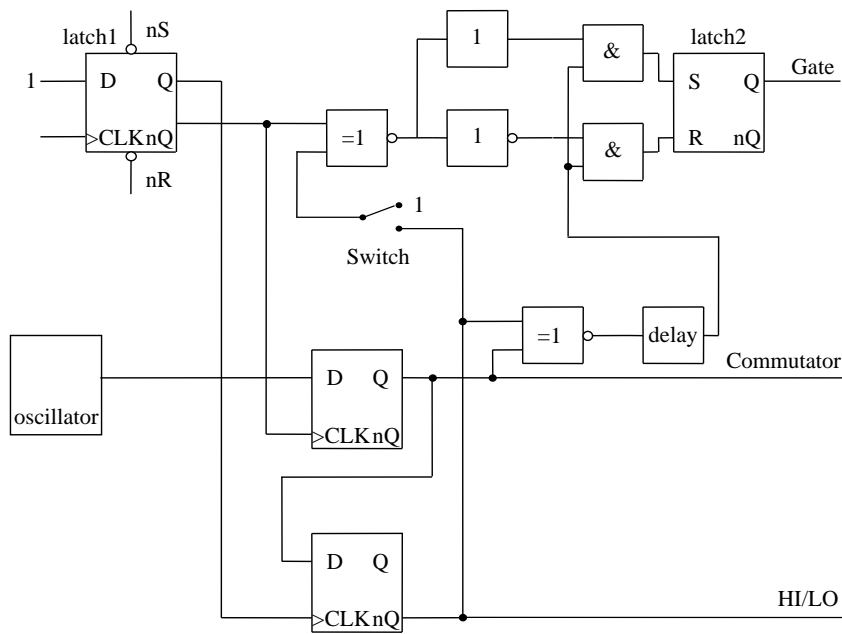


Figure 5.12: Control circuit output section of the stacked buck converter.

part of latch-1, comprising the peak current and ZCD input and timers, are not displayed. The low-frequency oscillator for the commutation is synchronised with the switching process to ensure an impeccable low-frequency commutation, by means of two additional D-flip-flops. Those flip-flops are triggered by the positive and negative edge of latch-1, generating the output signals Commutation and HI/LO respectively. Finally, the input of latch-2 is temporarily locked during the commutation process for a brief moment to prevent a glitch from appearing on the output. This is only the case for the synchronous stacked buck converter control configuration, as discussed in Section 5.2.5.

5.2.4 Control signals of the dual branch converter

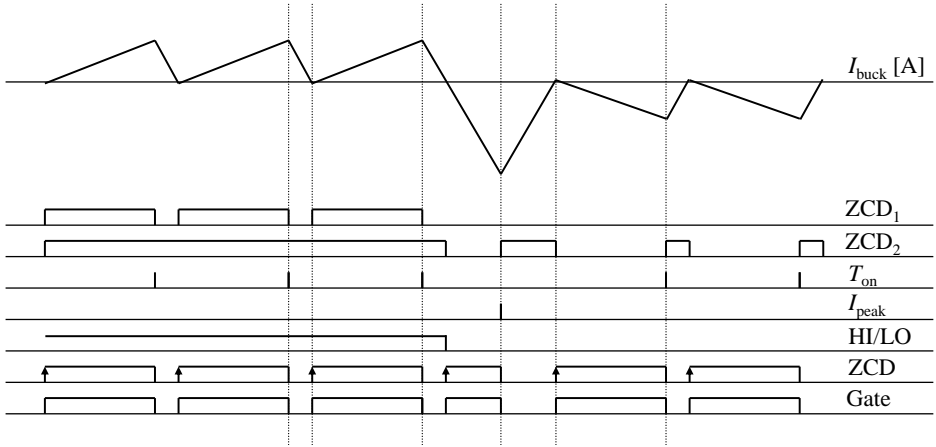


Figure 5.13: Timing diagram of the dual branch stacked buck converter (Section 5.1.3).

For the dual branch buck converter topology, the switch in the control circuit (Fig. 5.12) is set to the static logic “1” and, as a result, latch-1 is directly coupled with latch-2. In the timing diagram displayed in Fig. 5.13, the logic signal flow is explained in more detail for this topology. The top signal represents the combined buck converter current $I_{\text{buck}} = I_{L_1} + I_{L_2}$. Accordingly, for both branches the capacitive divider signals ZCD_1 and ZCD_2 are displayed. The signals, coupled with the ZCD circuitry given in Fig. 5.9, result in a logic ZCD signal. Furthermore, the logic input signals T_{on} and I_{peak} are displayed. The result on the output side is a synchronised commutation signal HI/LO, selecting one of the buck converters that is controlled by the Gate signal.

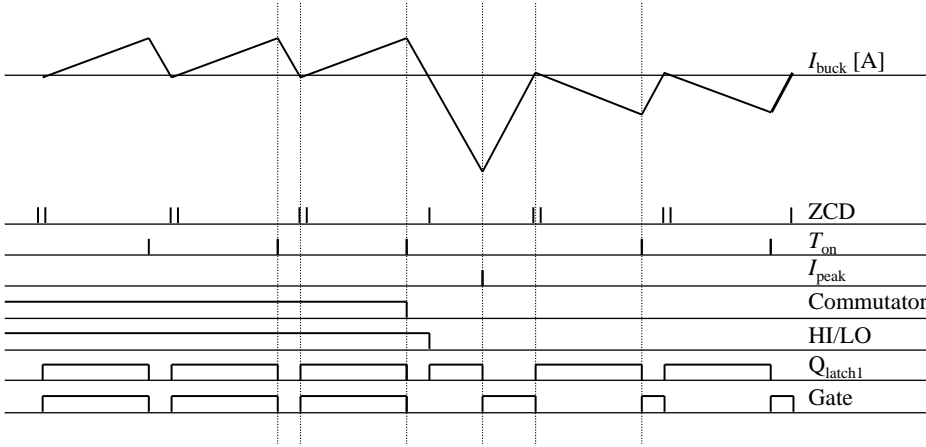


Figure 5.14: Timing diagram of the synchronous stacked buck converter (Section 5.1.4).

5.2.5 Control signals of the synchronous converter

For the synchronous stacked buck converter the logic signals are presented in Fig. 5.14. Besides the buck converter current I_{buck} , the saturated ZCD transformer pulses, T_{on} , and I_{peak} signals are displayed. The resulting logic output signal Q_{latch1} is given, as well as the signals Commutator and HI/LO, which are synchronised with the output signal Q_{latch1} . Finally, the switch in the control circuit (Fig. 5.12) couples the HI/LO signal with the XNOR and inverts the Q_{latch1} for half a LFSW period. The resulting Gate signal controls the level-shift circuitry by selecting the upper or lower MOSFET.

The commutation process for the synchronous stacked buck converter is presented in more detail in Fig. 5.15. It starts the moment the logic oscillator signal toggles state. When the T_{on} time expires, latch-1 resets and the Gate output changes state (Fig. 5.12). In turn the edge triggered Commutator signal toggles on $\overline{Q_{\text{latch1}}}$. During the time when the Commutator signal and HI/LO differ in logical state, the input of latch-2 is locked.

At the moment the buck inductor current reaches zero, a ZCD pulse is generated. As a result, latch1 is clocked and accordingly the HI/LO signal toggles. The logic signal sequence of Q_{latch1} and HI/LO on the input of the XNOR generates a glitch on the XNOR output state that is blocked on the input side of latch-2, therefore the output state that equals the Gate signal remains well defined.

The power MOSFETs are operated with a half bridge level-shifter that toggles between its outputs with an inherent transfer delay and a non-overlap protection delay as displayed in the lower traces of Fig. 5.15.

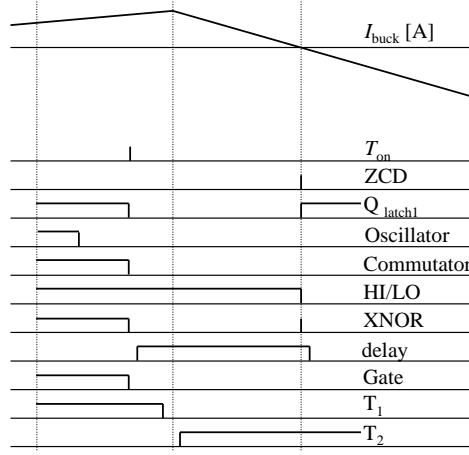


Figure 5.15: Timing diagram of the synchronous stacked buck converter in detail.

5.3 Lamp-driver interaction

For impeccable HID lamp operation the lamp-driver output characteristic has to comply with the gas-discharge operation conditions. The HID lamp operation has been defined in Chapter 2 as a sequence of gas-discharge phases, each representing a distinct discharge condition. In this section the LDI for the proposed highly-efficient stacked buck converters is reported for each of the different lamp phases.

Ignition - The HID lamp operation starts when a high terminal voltage is applied to electrically breakdown the noble gas, changing it from a non-conductive state into a conductive state. The igniter circuitry provides high voltage ignition pulses superimposed onto the LFSW OCV. Preferably, the ignition pulses are synchronised with the beginning of each LFSW period-half, to maximise the initial lamp conduction time before the next current reversal. The igniter circuit (Section 5.4) is active as long as high OCV modes occur.

Electrode heating phase - In this thesis the electrode heating phase is defined as being between the initial breakdown and the run-up phase. During the take-over phase several sub-phases take place, characterised by frequent switching between both high and low voltage modes. The lamp-driver must be able to deliver limited current during the low voltage modes and sufficient power to prevent the lamp from extinguishing when high voltage modes occur. In particular when the lamp switches instantaneously from a low to a high voltage mode, the lamp-driver must be able to restore the output voltage rapidly.

The T_{on} based cycle-by-cycle control enables fast switching between set-points on the parabolic power curve. To optimise the LDI in this phase, the smallest

possible output filter capacitor C_r (Fig. 5.1) must be selected, without sacrificing the lamp-current filter function that is needed for steady-state operation.

The PFC is operated at the high bus voltage mode (520 V) during the start and take-over phase as discussed in Section 4.2.2.

Run-up - Unlike the irregular take-over phase, the run-up phase, which is when the discharge vessel is heated, is characterised by stable lamp behaviour. This phase starts with low impedance and high lamp-current, and ends in the steady-state with nominal lamp impedance. Active limitation of the converter current is required to prevent over-loading of the lamp electrodes, according to the lamp specifications. Therefore, the peak current limitation circuit, as discussed in Section 5.2.1, regulates the lamp-current during the first part of the run-up phase.

Steady-state - During steady-state operation, the stability of the gas-discharge is the most important factor. In general, from an LDI perspective the HID lamp operation can be affected by acoustic resonances and the negative incremental lamp impedance.

The acoustic behaviour of an HID lamp depends on the power waveform supplied to the lamp. High frequency spectral power components can generate acoustic waves inside the discharge vessel. Therefore, the buck converter induced high frequency ripple superimposed on the LFSW lamp-current must be limited to a level that will not cause serious perturbations.

Conventionally, a maximum lamp-current modulation depth ($< 10\%$) [81] is specified to prevent triggering of the fundamental resonances [55]. However, with this approach the frequency modulation effect of a transition mode buck converter and the quality factor Q (the ratio of damping time to oscillation period) of the lamp plasma are not taken into account. Therefore, a new measurement technique is proposed [129, 130] based on the spectral power density (SPD).

Secondly, the proposed stacked buck converter must stabilise the negative incremental resistance behaviour of an HID lamp. The static stability criterion is addressed in Section 5.3.1 and the dynamic LDI stability is discussed in Section 6.1.

EOL - Lamp degradation after many hours of operation and thousands of “on/off” cycles finally results in an end of life (EOL) state. Physical and chemical processes inside the HID lamp trigger one of the EOL mechanisms. EOL behaviour has proven to be a difficult phase to handle. The way lamps reach EOL can differ depending on whether they have an electronic ballast or an electro-magnetic ballast. The EOL behaviour of the burner can even damage the ballast.

Broken burners can often still be operated in low or high voltage modes that mimic the run-up or take-over phase respectively. When those modes persist for a long time, and are therefore outside the nominal burner specifications, the lamp must be switched “off”, to avoid detrimental operation that can lead to lamp-base over-temperature situations. However, the reduced power setting for high voltage

modes inherent to the parabolic power curve, as implemented in the stacked buck converter, is generally a sufficient measure to avoid detrimental EOL behaviour.

5.3.1 Lamp-driver interaction damping

A basic problem when operating gas-discharge lamps is the negative incremental resistance that is seen at the lamp terminals. In general, a high impedance ballast is applied to offset the negative incremental impedance of the lamp. Therefore, most electronic lamp-drivers feature a current-source characteristic to stabilise the LDI. The open loop may include a low bandwidth feedback for an accurate power setting.

As denoted in Section 5.2 the proposed stacked-buck converter concepts have a power-source characteristic on the output side over the normal lamp voltage range. This behaviour can be modelled by a current-source in parallel with a resistor. To analyse the LDI stability in this case a small-signal equivalent circuit is given in Fig. 5.16.

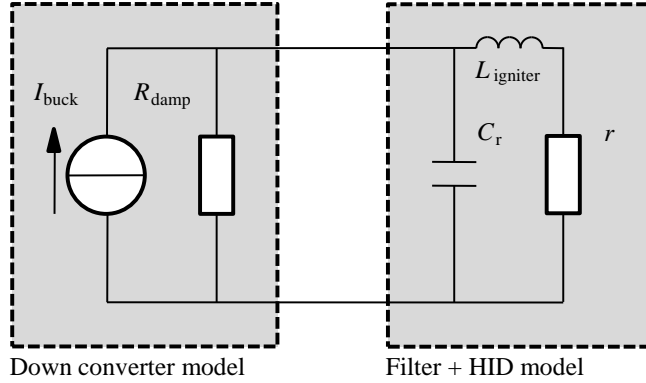


Figure 5.16: Equivalent small-signal LDI circuit.

In this equivalent circuit the power source is connected to the output filter (L_{igniter} , C_r), as given in Fig. 5.1. In turn, the filter is connected to the small-signal negative lamp resistance r . The damping resistance can be defined as

$$R_{\text{damp}} = \frac{1}{2} U_{\text{bus}} / I_{\text{max}}, \quad (5.6)$$

where, for normal operation, R_{damp} equals approximately $137 \, \Omega$, ($U_{\text{bus}} = 410 \, \text{V}$, $I_{\text{max}} = 1.5 \, \text{A}$, see Section 5.2.1). The static stability criterion [131, 132] states $R_{\text{damp}} > |r|$ and says that the operation point of the lamp is stable if the lamp's negative incremental impedance is smaller in magnitude than the ballast resistance. According to experimental measurements, as given in Table 6.1, in practice r ranges between -4 and $-30 \, \Omega$ for compact metal-halide lamps. Thus, it

can be concluded that the LDI is stable according to the static stability criterion. The dynamic stability is analysed in Section 6.1.

5.4 Experimental set-up

For reliable ignition, which overcomes the breakdown phase of an HID lamp, the ignition transformer and accompanying circuitry must provide voltage peaks ranging between 3 kV and 4 kV [118]. Pulse igniters are very common in electronic HID ballasts. In such igniter designs the ignition energy is drawn from the OCV [133]. Unfortunately, this results in a reduced OCV level directly after an ignition pulse, hampering the take-over phase. In an improved version [16], given in Fig. 5.17, the ignition energy is drawn directly from the rail voltage.

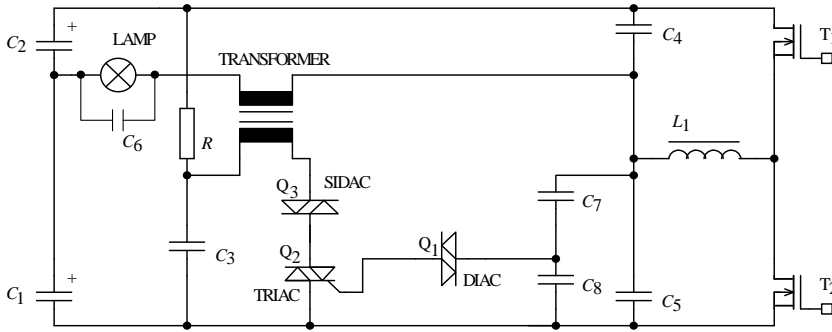


Figure 5.17: Igniter circuit.

In the igniter circuit, as shown in Fig. 5.17, the (TRIAC, SIDAC) series circuit conducts only when capacitor C_3 is sufficiently charged to trigger the TRIAC. The TRIAC gate is coupled via a DIAC with a capacitive divider (C_7, C_8) that triggers only at full OCV commutations of the half bridge. As a result, the ignition pulses are generated automatically during high OCV modes and are always synchronised with the low-frequency-square-wave current. The ignition pulse coincides with the beginning of each period-half to maximise the initial discharge conduction time.

To cope with a wide range of cable capacitances between the igniter and the lamp terminals [134], the ignition transformer and the high voltage capacitor C_6 must be carefully designed [135, 136].

5.4.1 Experimental measurements

In Fig. 5.18 the proposed two stage dual branch HID lamp-driver is shown. As can be seen, this topology configuration enables compact printed circuit board

(PCB) designs. The front-end PFC, as presented in Chapter 4, operates in critical mode with a 100 kHz average switching frequency. The same average switching frequency is chosen for the stacked buck converter, and the LFSW current frequency was set to 130 Hz. In Table 5.3 the applied power components and system settings are listed. The over-all efficiency, cycle-by-cycle switching, and lamp-driver interaction are measured.

Table 5.3: Stacked buck converter components and settings.

Preconditioner output voltage	
U_{bus}	410 V, start phase 520 V
Capacitors	68 μF 350 V Rubicon BXA
Stacked buck converter components	
MOSFETs	ST 7NB60
Buck Inductor	0.8 mH
Levelshifter	ST L6384
Filter capacitors	47 nF
Igniter inductor	1.2 mH

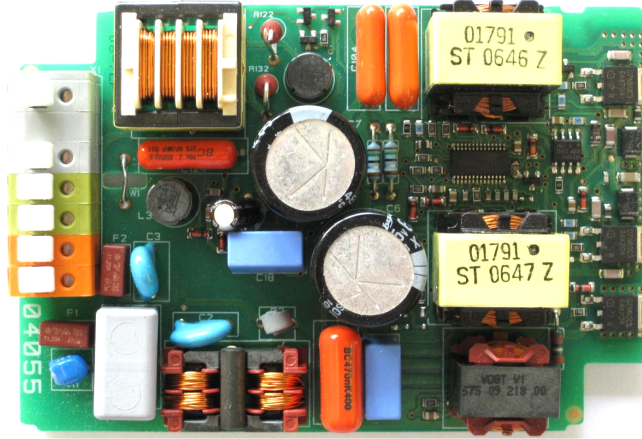


Figure 5.18: Photo of HID lamp driver (Philips HID PrimaVision).

The control section of the synchronous stacked buck converter was monitored and the most important signals are displayed in Fig. 5.19. At zero current the saturated toroid transformer generates a pulse voltage U_{ZCD} . Therefore, the double zero crossing of the buck inductor results in two pulses. However, the edge-triggered latch-1 (Fig. 5.11) only responds to the first rising edge. This rising edge sets latch-1, which results in an increasing inductor L_{buck} current and

consequently during the commutation signal HI/LO toggles. After the T_{on} time is expired, the current decreases during the T_{off} time until the ZCD signal appears and the cycle starts over again. The synchronised commutation process shows a smooth transition between both buck converters, without any hard switching.

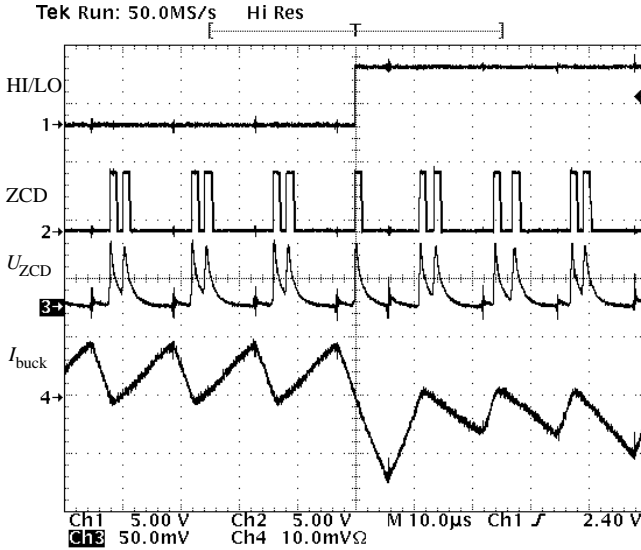


Figure 5.19: Measured control signals: synchronised commutation signal HI/LO (5 V/div), logical ZCD signal (5 V/div), rectified input ZCD transformer signal U_{ZCD} (5 V/div), and buck inductor current I_{buck} (2 A/div). Time scale (10 $\mu\text{s}/\text{div}$).

An experimental prototype of the dual branch converter coupled with a new CDM 73W/830 burner was examined while the circuit was powering up until the lamp entered the run-up phase. In this experiment the bus voltage, lamp voltage, and current are measured as shown in Fig. 5.20. The lamp voltage probe is coupled in front of the ignition transformer to prevent it from overloading. Therefore, the ignition pulses are not visible in the scope plot.

After the mains switch is closed, the bus voltage ramps up and thereafter the PFC boosts the bus voltage towards the 520 V level. The lamp voltage shows a number of full OCV commutations before an initial breakdown takes place in the burner. The moment of breakdown can be seen in the current trace. Thereafter, frequent changes between high and low voltage modes are apparent. The cycle-by-cycle based T_{on} control switches rapidly between set-points on the parabolic power curve. When the irregular electrode heating phase ends, the burner enters the run-up phase. This phase is characterised by a stable low lamp voltage and a high lamp-current.

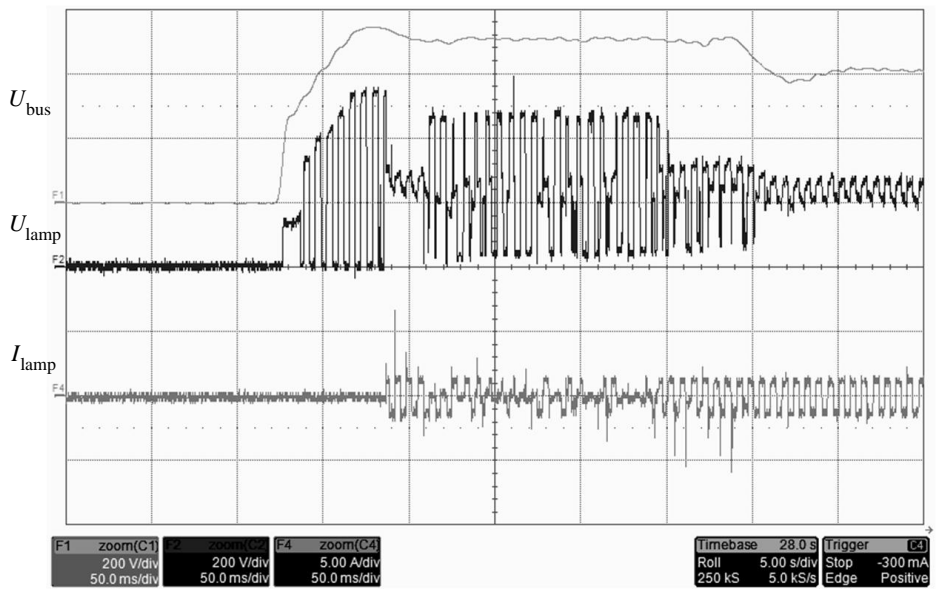


Figure 5.20: Measurement of the lamp start behaviour: pre-conditioner voltage U_{bus} (200 V/div), lamp voltage U_{lamp} (200 V/div), lamp-current I_{lamp} (5 A/div), time scale (50 ms/div).

The same experimental set-up and burner as were used in the previous experiment were also used to study steady-state operation. The lamp voltage and current are captured and displayed in Fig. 5.21. The lamp-current shows a slight decay over every half cycle caused by the midpoint voltage fluctuation of the series-connected electrolytic buffer capacitors C_s (in Fig. 5.1). Furthermore, the effect of the filter circuit comprised of C_r and L_{igniter} , illustrated in the same figure, virtually eliminates the critical discontinuous buck converter ripple component in the lamp-current. For the selected configuration in the experimental set-up, the lamp burns stable and the measured lamp voltage shows a stable commutation process, where re-ignition spikes are almost absent.

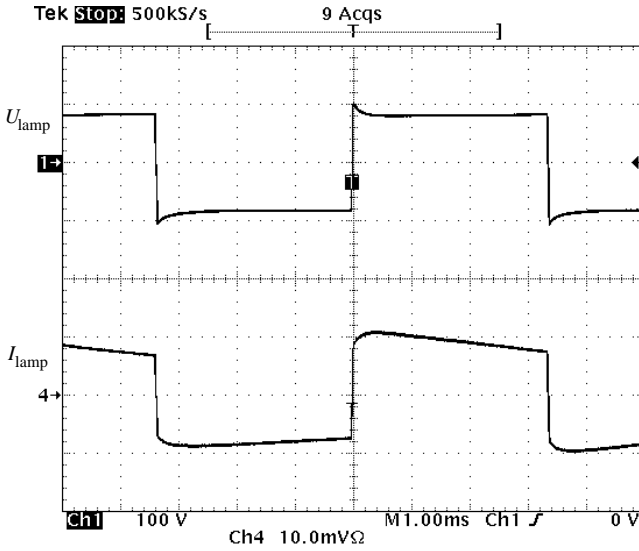


Figure 5.21: Measurement steady state lamp voltage U_{lamp} (100 V/div) and current I_{lamp} (1 A/div), time scale (1 ms/div).

The T_{on} cycle-by-cycle control parabolic characteristic stated in (5.3) was verified in practice. The output current as a function of the output voltage was measured with the dual branch experimental set-up and a variable resistive load, as displayed in Fig. 5.22. The parabolic power curve results from the linearly decreasing output current for increasing output voltage. To overcome problems with EOL lamp operation outside the nominal specification, for high lamp voltages the power level is automatically reduced. Furthermore, for very low output voltages, which normally occur during take-over and run-up phase or abnormal short-circuit situations, the output current is limited by means of the cycle-by-cycle peak current limiter.

Practical efficiency measurements with the experimental prototypes were per-

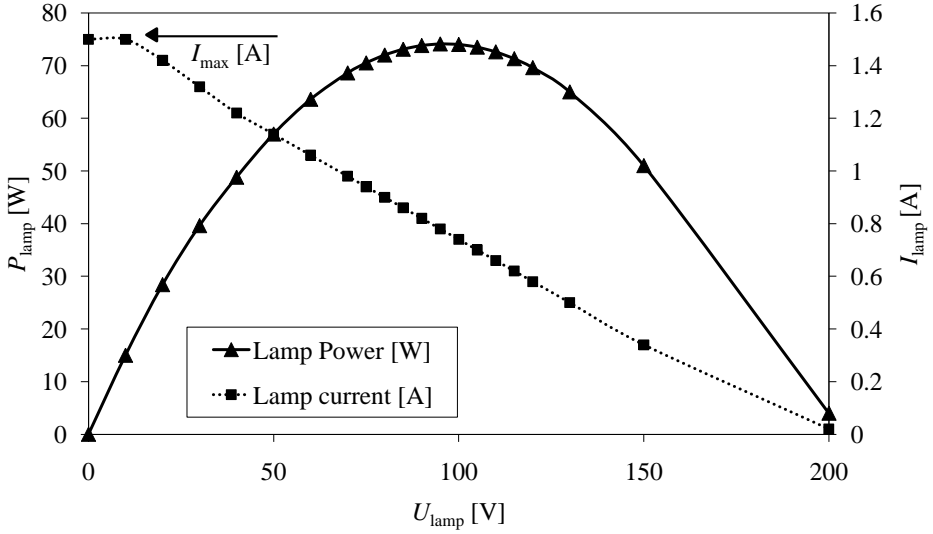


Figure 5.22: Lamp-driver output power P_{lamp} and current I_{lamp} measurement as a function of the lamp voltage U_{lamp} .

formed with the classic, dual branch, and synchronous topology configurations. The reverse recovery losses that were discussed in Section 5.1.2 are studied in the proposed topology configurations. In order to present realistic efficiency results these measurements include the pre-conditioner stage operated at 230 V_{ac}. Furthermore, a resistive load was applied that represents a nominal lamp load at 90 V. In Table 5.4 the topology configurations, including the selected power switches and the measured system efficiencies, are presented.

Table 5.4: Measured stacked buck converter efficiencies.

η [%]	Topology configuration
	Classic buck converter
87.0	MOSFET ST 7NB60
90.4	IGBT IRG4BC20W + MUR160
90.7	FREDFETS PHP8ND50
	Dual branch stacked buck converter
92.0	MOSFET ST 7NB60 + MUR160
	Synchronous stacked buck converter
92.5	MOSFET ST 7NB60

The classic stacked buck converter (Fig. 5.1) is operated with a number of

different semiconductor devices. At first, standard MOSFETs are applied where the free-wheeling diode function is represented by the internal body-diode. This resulted in relatively high losses and correspondingly low system efficiency. Next, fast recovery epitaxial diode (FRED) FETs were applied. These devices feature a low $R_{ds(on)}$ and fast body diodes with a recovery speed of less than 200 ns. As a result, the circuit efficiency is improved. Alternatively, fast IGBT devices were applied, in combination with external fast anti-parallel diodes. Despite the fast anti-parallel diodes, the configuration could not improve upon the FREDFET performance. Two power loss mechanisms are important here: The IGBT switch off current tail and the voltage drop U_{ce} in conduction mode [137]. For the applied fast IGBTs, the latter is dominant in the total loss figure.

Secondly, the dual branch and synchronous stacked buck converter experimental set-ups were evaluated. In contrast with the classic stacked buck converter configuration, here the power MOSFET characteristics are not critical regarding the system efficiency. In essence, only the $R_{ds(on)}$ is important in the system losses. This fact makes these topology configurations suitable for mass-production, where parameter spread and multiple component suppliers are common.

5.5 Discussion

Based on the principle of disabling the MOSFET slow internal body-diodes, two high-efficiency zero voltage switching (ZVS) stacked buck converter variants were explored. The diode reverse recovery losses are prevalent in ZVS stacked buck converters. A first variant comprises two independent buck converter sections (dual branch topology) with fast free-wheeling diodes and separate inductors. The second configuration is operated in synchronous switching mode, in which the MOSFET channel replaces the body-diode function.

The stacked buck converters feature a cycle-by-cycle control based on a fixed T_{on} time. This results in a parabolic relationship between lamp power and lamp voltage, matching the discharge requirements during the different lamp phases. The proposed topologies are operated in transition mode with only two control signals, ZCD and I_{peak} . An indirect peak current measurement is used to limit the current during commutation, in the run-up phase, and during a short-circuit situation. The MOSFET control logic synchronises the high-frequency cycle-by-cycle switching with the low-frequency commutation process, ensuring permanent zero voltage switching. To maximise the initial discharge conduction time during the start phase, the ignition pulses coincide with the beginning of each LFSW period-half. Practical efficiency measurements with the proposed two-stage lamp-driver prototypes have shown an overall efficiency of 92.5 %.

Additional control measures are required for optimal system performance of the lamp-driver system over its life-time and during several operation conditions, including dimming. In the remaining chapters the lamp-driver interaction is stud-

ied in more detail, and control algorithms to improve the HID system performance are presented.

Chapter 6

Lamp-driver interaction control

To ensure failure-free operation and to obtain optimal light performance throughout the rated lifetime of the burner, the main concern in driver design is an optimised lamp-driver interaction (LDI). Therefore, the relations between both the physical processes inside the discharge vessel and the electrical lamp terminal properties are of great interest. Therefore, when attempting to improve driver design, the physical lamp processes can be linked to electronic circuit parameters.

LDI simulation is a strong tool for optimisation. In addition to the physical modelling efforts described in Chapter 3, a simple lamp-model is derived in this chapter to describe the essence of the electric terminal behaviour for control purposes. A linearised representation that models the HID lamp small-signal negative incremental impedance behaviour is generally sufficient for lamp-driver stability analysis.

Power electronics-based HID drivers do not act as ideal current sources. Accordingly, the resulting system performance depends on both the dynamics of the lamp and the driver [51, 138]. Some combinations tend to be poorly damped, resulting in an oscillatory lamp-current, as shown later in Fig. 6.15. Other combinations exhibit large re-ignition peaks, especially when operated at reduced power or after numerous operating hours (Fig. 6.18).

To optimise the LDI for a broad range of HID lamps operated at normal or reduced power, active control of the lamp-driver set-points can be applied [139–145]. The approach presented here is based on two control principles integrated in a fuzzy-logic lamp-driver controller that stabilises the lamp-current and optimises the commutation process. The first principle consists of an adaptive feedback loop that achieves over-critical damping. The second principle uses an adaptive lamp-current pulse ahead of the commutation event to reduce the re-ignition spike.

This chapter is organised as follows. In Section 6.1 a small-signal model is used to study the terminal behaviour of a gas-discharge plasma. Based on this small-

signal behaviour, an LDI simulation model is proposed and verified in Section 6.2. The electrode behaviour and its impact on the LDI properties are discussed in Section 6.3. In Section 6.4 a fuzzy-logic controller that copes with non-linear LDI behaviour is presented. Experimental results with fuzzy-logic controlled LDI are presented in Section 6.5. Finally, a discussion about the achieved results can be found in Section 6.6.

6.1 Small-signal modelling

In this section the plasma physics induced terminal behaviour is analysed. A simple representation is used to experimentally model the HID lamp plasma's small-signal properties. In order to identify the dynamic parameters, the burner is excited with a small step on the lamp-current [146].

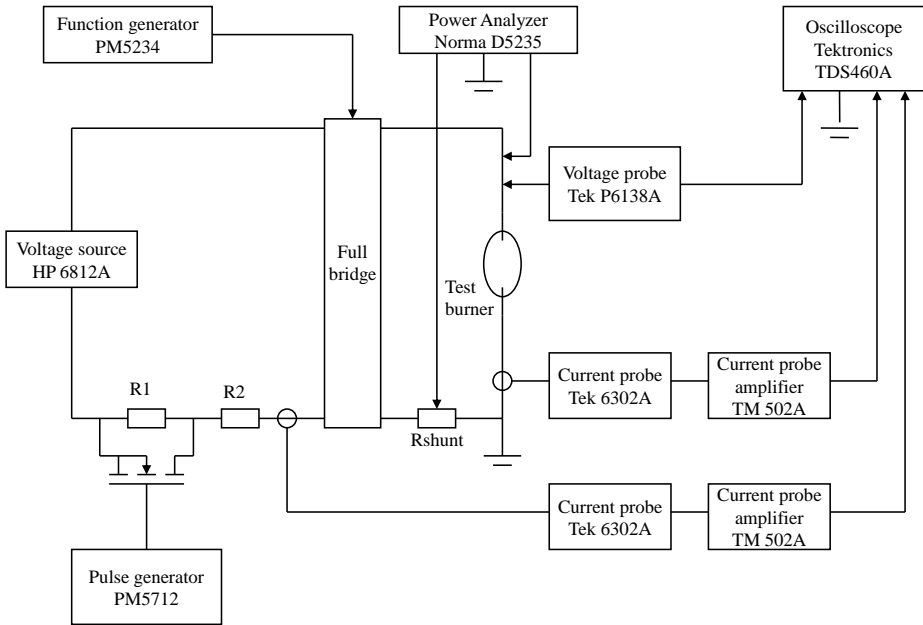


Figure 6.1: Small-signal measurement set-up.

The measurement set-up to derive the small-signal lamp parameters is shown in Fig. 6.1. The ballast resistor is split into two parts, one of which can be short-circuited by means of an electronic switch that is driven by a pulse generator. The resulting instantaneous decrease in total ballast resistance gives rise to a small superimposed step on the normal LFSW lamp-current. This current step and the resulting lamp voltage are measured with an oscilloscope, which is triggered by

the current step. The resulting burner voltage response is displayed in Fig. 6.2. In the same figure an idealised current step and burner voltage response are sketched. In these sketches parameters are assigned to analyse the response.

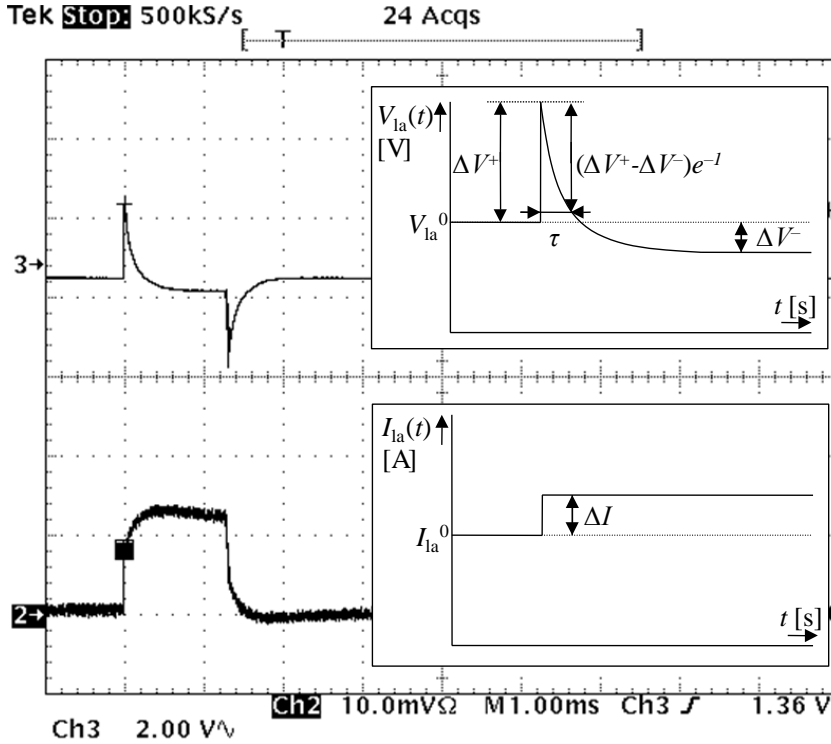


Figure 6.2: Small-signal measurement with lamp voltage above (offset, 2 V/div, upper trace) and lamp-current (offset, 20 mA/div, lower trace), time scale 1 ms/div. The current step and resulting burner voltage response are sketched in the same figure.

The response can be translated to the Laplace domain, leading to a transfer function of the burner. Based on the idealised response given in Fig. 6.2, the following definitions are of importance for the derivation

$$R_{la}^0 = \frac{V_{la}^0}{I_{la}^0} = \frac{\Delta V^+}{\Delta I}, \quad (6.1)$$

where R_{la}^0 is the nominal lamp-impedance and the other parameters are defined in Fig. 6.2. Since the plasma conductivity cannot change instantaneously, an increase in current also means a proportional increase in lamp voltage, resulting in resistive behaviour. However, within some milliseconds the lamp voltage de-

creases as the plasma temperature changes. In the following equation we assume that this voltage decreases according to an exponential curve, characterised by the plasma time constant τ [s]. Note that since ΔV^- in Fig. 6.2 is negative, the plasma resistance r [Ω] is also negative as follows

$$r = \frac{\Delta V^-}{\Delta I}. \quad (6.2)$$

On a time scale of seconds to minutes, the lamp voltage increases again to a higher value than prior to the current step. This slow voltage change is related to the thermal time constant of the discharge vessel and is ignored here in our small-signal analysis, but it is addressed later in Section 6.2. Referring to Fig. 6.2, it is possible to describe the time response of the burner as

$$V_{\text{la}}(t) = V_{\text{la}}^0 + V(t), \quad (6.3)$$

where

$$\begin{aligned} V(t) &= 0 & t < 0, \\ V(t) &= \Delta V^+ - (\Delta V^+ - \Delta V^-) \left(1 - e^{\frac{-t}{\tau}} \right) & t \geq 0. \end{aligned} \quad (6.4)$$

According to (6.4), this response can be translated to the Laplace domain, leading to the transfer function $H(s)$ of the burner (considering only small-signal effects). The Laplace transform of the voltage variation, incorporating the current step, is found to be

$$H(s) = \frac{V(s)}{I(s)} = \frac{sR_{\text{la}}^0 + \frac{r}{\tau}}{s + \frac{1}{\tau}}. \quad (6.5)$$

This type of transfer function is also found to be a good fit in frequency domain lamp analysis [132, 147]. In a first attempt to explain the LDI stability, a commonly used parallel capacitor C_r (see Fig. 4.1) is included, resulting in an impedance $Z(s)$ given by

$$Z(s) = \frac{sR_{\text{la}}^0 + \frac{r}{\tau}}{s^2 R_{\text{la}}^0 C_r + s \left(1 + \frac{rC_r}{\tau} \right) + \frac{1}{\tau}}. \quad (6.6)$$

Stability, according to the Routh-Hurwitz criterion for this second order polynomial, requires that all coefficients of the denominator be positive. Obviously, this is always the case for $R_{\text{la}}^0 C_r$ and $\frac{1}{\tau}$, so the criterion for stability becomes

Table 6.1: Identified lamp parameters.

Lamp type	V_{la}^0 [V]	P_{lamp} [W]	R_{la}^0 [Ω]	τ [μ s]	r [Ω]	C_{max} [μ F]
Sylvania Britespot ES50 35W	113.0	35.3	350.9	63	-30	2.1
Philips CDM-T 73W/830	90.0	73.4	110.1	85	-9.7	8.8
Philips CDM-TD 150W/942 (aged)	103.7	157.4	67.6	48	-4	12

$$1 + \frac{rC_r}{\tau} > 0 \Rightarrow \frac{|r|C_r}{\tau} < 1 \Rightarrow \text{stability border} \Rightarrow C_{max} = \frac{\tau}{|r|}. \quad (6.7)$$

For three different compact HID lamps the small-signal parameters are identified as shown in Table 6.1. Before the measurement procedure, the lamps were operated for 10 minutes at rated power to allow the gas-discharge, to reach steady-state operation. For the Britespot HID lamp operated on an electronic lamp-driver with an output capacitor equal to 1 μ F, stability problems may occur. The margin with the calculated critical parallel capacitor, $C_{max} = 2.1$ μ F, is rather small.

6.1.1 Plasma dynamical behaviour

In the previous experiment the small-signal parameters are deduced after the gas-discharge operation has converged to an equilibrium state at full power. To study LDI stability for HID systems operated in dimmed mode, measurements are performed in equilibrium state at reduced power levels. Observing dimmable HID lamp-driver systems shows that with some lamp-driver combinations the burner tends to extinguish during the transition to a lower power set-point. Therefore, additional small-signal identifications were conducted directly after step-wise changes from full to reduced power operation and visa-versa. In contrast to a steady-state identification, these experiments probe the lamp dynamics before a new thermal equilibrium is established.

In Table 6.2 the small-signal identification results and the calculated critical capacitance C_{max} are shown. The identification results for C_{max} are plotted in Fig 6.3. For reduced power operation under steady-state conditions the graph shows that no instability is to be expected. However, a descending power step results in a reduced stability margin. Step-wise increase of the power is again uncritical.

The small-signal property C_{max} gives only an indication of the LDI stability. This is because, in practice, a diminished LDI damping leads to large-signal non-linear lamp-current oscillations (as shown in Fig. 6.15). These oscillations are

Table 6.2: HID lamp small-signal analysis Philips CDM-T 73W/830.

	P_{lamp} [W]	τ [μs]	r [Ω]	C_{max} [μF]
Steady-state (Identification at thermal equilibrium)	73	85	-9.65	8.8
	60	100	-9.69	10.3
	50	155	-18.02	8.6
Power step (Identification before thermal equilibrium)	73 \rightarrow 60	90	-14.33	6.3
	73 \rightarrow 50	122	-21.07	5.8
	60 \rightarrow 73	95	-7.95	11.9
	50 \rightarrow 73	125	-6.23	20.0

triggered by the lamp-current commutation process, and therefore they depend on the driver's properties. In turn, these lamp-current fluctuations give rise to large lamp power fluctuations and lamp extinguishing can occur.

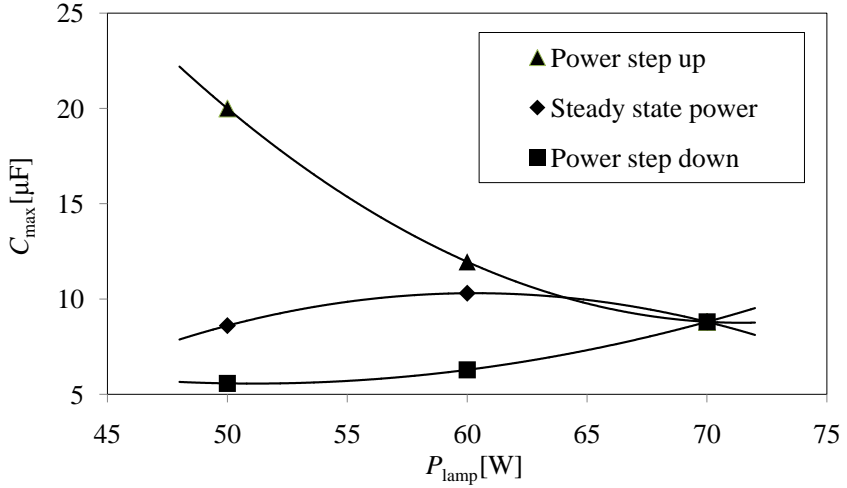


Figure 6.3: Static and transient small-signal behaviour.

6.2 Lamp-driver interaction simulation

First, to study the LDI in more detail, a lamp model is built based on the small-signal analysis as derived in (6.5). In Fig. 6.4 a block diagram of the proposed lamp is shown, and a capture of the original Simulink model is attached in Fig. A.1. The negative resistive impedance characteristic is constructed in a straightforward way from (6.5) by using an integrator to represent the time constant τ . This small-signal transfer function is extended in order to perform

large-signal simulations.

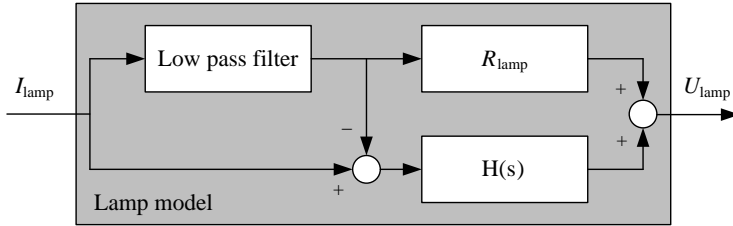


Figure 6.4: HID lamp model.

In the block diagram (Fig. 6.4) the nominal lamp voltage is calculated as the nominal lamp resistance R_{lamp} times the average lamp-current, where a first order low pass filter averages the (rectified) lamp-current. Lamp physics relates the average voltage drop across the plasma column with the discharge vessel temperature. Therefore, the filter's time constant represents a first order approximation of the discharge vessel's heat capacity, as derived in Section 3.2.5. The lamp voltage U_{lamp} in Fig. 6.4 results from the nominal lamp voltage plus the transient current times the negative impedance transfer function, where the transient current equals the lamp-current minus the average lamp-current.

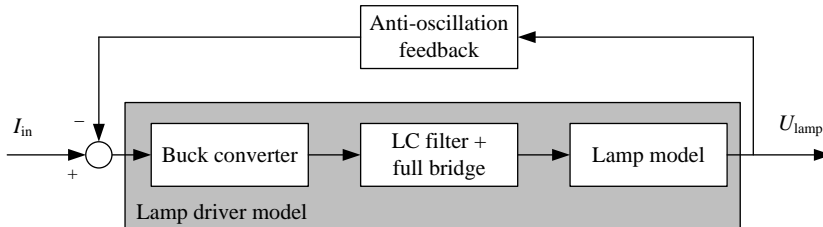


Figure 6.5: Lamp-driver model plus voltage feedback loop.

Subsequently, the simple lamp model proposed in Fig. 6.4 is embedded in a block called “Lamp model”. This block consists of two nodes (I_{lamp} , U_{lamp}), and is connected to the most important driver components as shown in Fig. 6.5. Starting from the input node I_{in} , which represents the current set-point, the buck converter block represents a zero order hold and saturation function [148, 149] (see also Fig. A.2). This mimics the peak current controlled transition mode buck converter applied in the experimental set-up. The zero order hold time equals the cycle time of the average buck converter switching frequency (100 kHz), and the saturation limits the current range. In the “LC filter + full bridge” block the filter capacitor is modelled in a straightforward way by means of a simple

integration action. The capacitor voltage is coupled with a switch and signal generator combo, which together act as the low frequency full bridge commutator. After the commutation switch, a series circuit consisting of the igniter inductance, modelled by means of a simple integration action, and the previously presented HID lamp model.

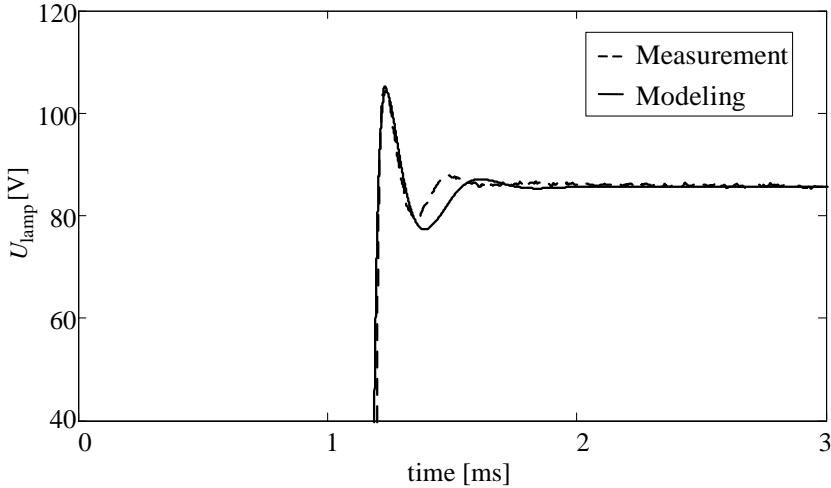


Figure 6.6: Lamp model verification.

The LDI simulation model is verified using a three-stage driver (Section 4.1.1) with the following output filter component values: $C_r = 1 \mu\text{F}$; $L_{\text{igniter}} = 0.3 \text{ mH}$. This configuration is applied for all experiments unless otherwise noted. The lamp-driver is coupled with a Philips CDM-T 73W/830 burner and the lamp parameters are selected accordingly, see Table 6.1. A time domain simulation is performed and plotted together with the corresponding time domain measurement in Fig. 6.6. It can be concluded that the model predicts LFSW operation with adequate accuracy. As stated before, this simulation model is a linearised representation of the non-linear HID lamp terminal behaviour, and therefore is only valid for small variations around the selected operation point.

Some lamp-driver combinations tend to be under-damped. In order to damp the LDI responses, an anti-oscillation feedback is proposed as displayed in Fig. 6.5. This feedback loop is coupled from the buck converter output voltage U_c towards the input current set-point I_{in} . The feedback loop consists of a gain and an un-critical band pass filter ($10 \text{ Hz} < f < 20 \text{ kHz}$). The low pass section rejects the dc lamp voltage component and the high pass section attenuates the switching frequency ripple. The presented Simulink lamp-driver model is used to analyse the proposed feedback loop. For this simulation the BriteSpot lamp parameters are selected (Table 6.1).

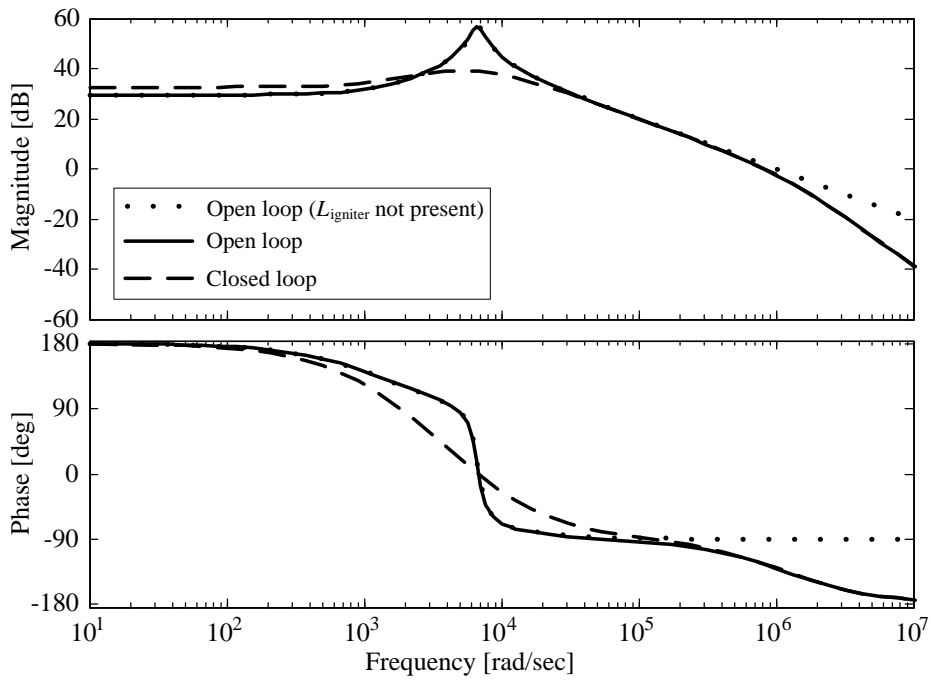


Figure 6.7: Bode diagram transfer function $I_{\text{in}}/U_{\text{lamp}}$ for open and closed loop configurations.

The LDI simulation model shown in Fig. 6.5 is used to study the anti-oscillation feedback in open and closed loop configurations. In Fig. 6.7 the transfer function $I_{\text{in}}/U_{\text{lamp}}$ is analysed in the frequency domain. The open loop transfer function, displayed with the solid and dotted line, shows a clear magnitude resonance peak that represents the under damped system mode. To study the impact of the igniter inductance on this under-damped mode, the open loop configuration was simulated with (solid line), and without (dotted line), this inductance. When the anti-oscillation feedback loop is closed the resonance peak is strongly reduced in magnitude, as shown in the same figure. As can be seen, for common output filter capacitance and inductance values the parallel capacitor dominates the LDI stability. Therefore, the stability criterion in terms of the critical parallel capacitor C_{max} , as deduced in (6.7), gives a good indication for the LDI stability.

6.3 Electrode behaviour

In general, a high-pressure gas-discharge is situated between two electrodes. The electrodes electrically connect the power supply and the gas-discharge. The terminal lamp voltage includes the voltage drop in the arc column and the drops across the two electrode regions [69, 73]. The latter are also known as the electrode-sheath voltages (ESV) [57, 79]. In the remainder of this section the electrodes behaviour and related impact on the LDI are discussed.

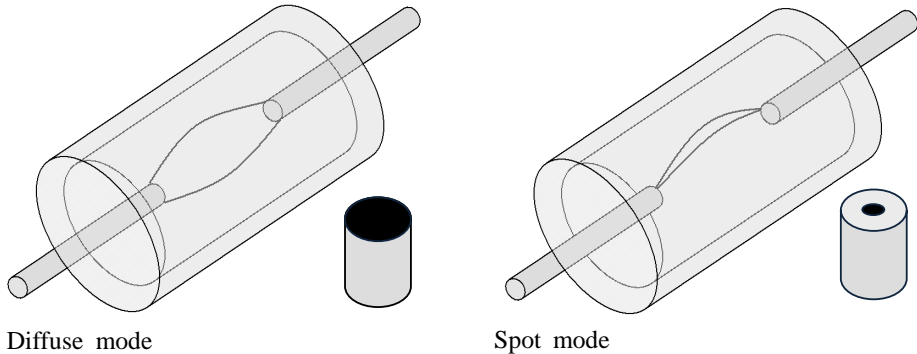


Figure 6.8: Sketched HID lamps for diffuse and spot mode operation.

During full power operation the electrodes affect the LDI properties only marginally, and the previously described plasma behaviour dominates the process. However, for older lamps and reduced power mode operation the electrodes play an important role. Conventionally, it is accepted that the value of the voltage drop across the electrode sheaths is a constant value. However, experimental

results have shown that the electrode drop voltage is non-linear and strongly dependent on ac operating conditions [79]. The most important electrode operation conditions are the absolute value and surface gradient of the tip temperature, which define the mode of operation. The temperature distribution and the directly related arc attachment mode range from a diffuse spread over the entire electrode tip surface, to a contracted arc attachment, to a hot spot somewhere on the tip's surface or its edge.

To describe the mode of operation, several names are used for the same phenomena in the literature. During normal full power operation we can assume that the entire electrode tip, or at least a considerable part of it, has an appropriate temperature for thermionic emission: the so-called low-field mode. On the border of designed performance the electrode tends to switch over from diffuse-mode (low-field) to spot mode (high-field), obeying the principle of minimum energy [69]. In this mode the electrode rod cools down and only a tiny spot on the tip surface is heated to the appropriate temperature to emit electrons. Both modes are sketched in Fig. 6.8 and observed in practice, as displayed in Fig. 8.16.

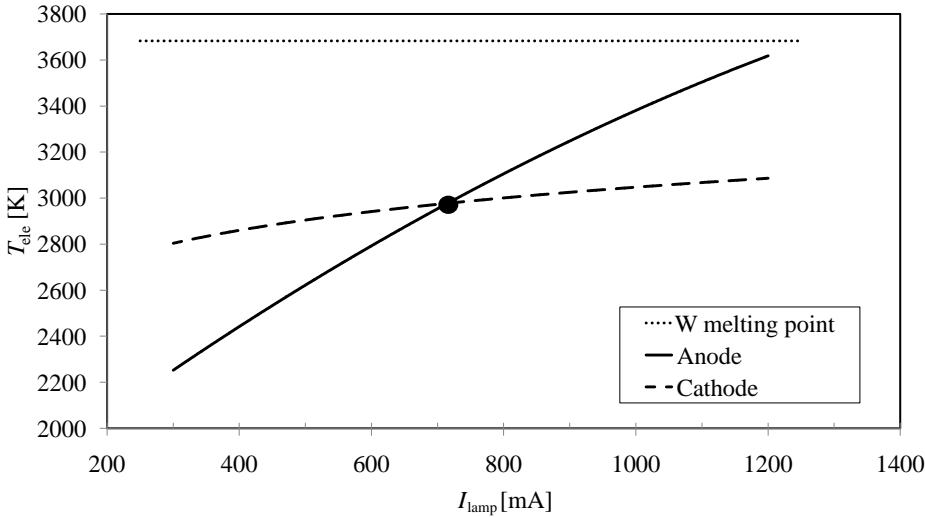


Figure 6.9: Calculated electrode tip temperature for direct current operation (diffuse mode).

The electrode model presented in Section 3.3 is applied to estimate tip temperatures at different current set-points. In Fig. 6.9, the anode and diffuse cathode mode temperature lines are plotted as a function of the lamp current. The dotted line in this plot represents the melting point for tungsten electrodes. The intersection point of both tip temperature lines, the cross-over point, has special significance. For LFSW operation at a lamp-current coinciding with the cross-

over point, a constant electrode tip temperature results. However, for a LFSW current at a different set-point the electrode function jumps between both lines and the tip temperature follows, according to the thermal balance dynamics. For the modelled 73 W HID lamp electrodes the nominal lamp-current equals approximately 800 mA. At this nominal lamp-current set-point the electrode tip temperature increases during the anode phase, and the hand-over tip temperature is more than sufficient to start the cathode phase. This can be contrasted with LFSW operation below the cross-over point, where the electrode tip must be heated up to reach an appropriate temperature at the start of the cathode phase.

From an LDI perspective, a tip temperature that is too low in the cathode phase leads to a momentary increase in cathode fall voltage, and therefore to a voltage spike across the lamp terminals. The re-ignition voltage during commutation is the sum of both the voltage fall over the electrode sheaths (ESV) and the voltage drop across the plasma impedance. The latter drop becomes visible at slow commutation speeds (e.g. at sinusoidal operation), when the plasma column cools down and an increased plasma E-field is needed to restore the plasma column temperature, resulting in a wide re-ignition peak. In general, the re-ignition voltage should be as low as possible. It can never exceed the ballast open circuit voltage (OCV), which is equal to the PFC output voltage (Fig. 4.1).

Due to tungsten deposition on the discharge vessel wall, the cathode mode of operation has a great influence on the lifetime of the cathode and the related wall darkening. The tungsten deposition during life consists of two components: one is caused by sputtering during start-up [150, 151], and the other results from evaporation during continuous operation [152]. Electrode temperatures that are too high will cause evaporation and thus a blackening of the lamp wall. Otherwise, an electrode tip temperature that is too low will lead to sputtering, which also has a negative effect on the life of the electrode. During normal operation an appropriate electrode temperature, related to the so-called low field mode, has to prevail. Besides physical parameters (electrode dimensions, material, metal-halide filling, etc. [152]), reduced power operation, and worn-out electrodes affect the electrode temperature and operation mode. Even the burning orientation affects the individual electrode temperatures. For example, in the vertical burning position, the upper electrode usually has a higher temperature than the lower electrode.

To prevent an insufficient hand-over cathode temperature at the start of each period-half, the total amount of current can be increased by means of a current pulse (Fig. 6.10). The pulses raise the temperature of the electrode in order to secure a stable cathode phase [153]. This patented principle can also be used for a limited extension of diffuse mode operation at reduced power. In this way, lamp extinguishing can be prevented in a wide power range where spot mode operation can occur.

The electrode tip temperature modulation for 50 Hz sinusoidal current operation at rated power was simulated using the electrode model in Section 3.3. The

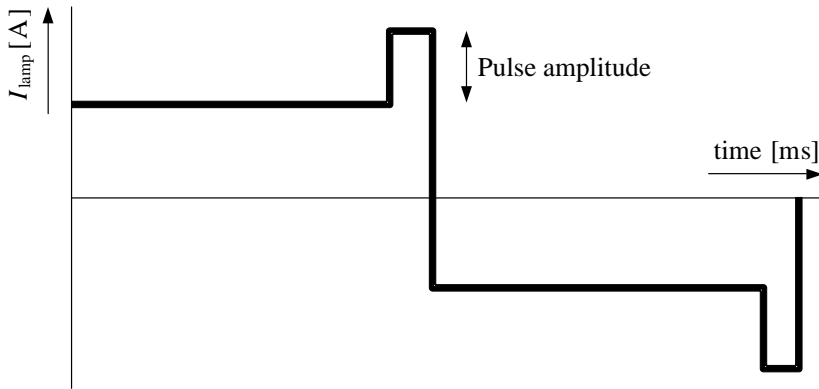


Figure 6.10: LFSW lamp-current with superimposed pulse versus time.

plot visualises (Fig. 6.11) the strong influence of the momentary lamp-current on the tip temperature. For operation at rated power, the electrode tips heats up during the anode phase and cools down in the cathode phase, during operation above the cross-over point shown in Fig. 6.9.

6.4 Fuzzy-logic control

In this section a fuzzy-logic controller is proposed that optimises the non-linear lamp-driver interaction [21] in the presence of a wide spread in lamp and driver dynamic parameters. Fuzzy-logic control is derived from the mathematical theory of fuzzy sets first defined by Zadeh in 1965 [154]. It is based on heuristic rules, and can effectively express highly non-linear functional relationships. Therefore, it allows easier application of the non-linear control laws needed to address the non-linear nature of HID lamp-ballast interaction. However, fuzzy-logic controllers generally cannot provide a better small-signal response than standard regulators [155].

The purpose of the lamp-driver controller is to stabilise the lamp-current and optimise the lamp behaviour in the presence of parametric variations and disturbances. The fuzzy-logic controller adapts both the anti-oscillation feedback loop, presented in Section 6.2, to achieve over-critical LDI damping, as well as the current pulse ahead of the commutation, as described in Section 6.3 to stabilise the re-ignition process. On the input side, the lamp voltage fluctuation after commutation is sensed. The overshoot amplitude is a measure to correct the re-ignition behaviour and the undershoot amplitude is used to control the system damping. The LDI properties and corresponding input and output signals are summarised in Table 6.3.

The closed loop fuzzy control block diagram that is shown in Fig. 6.12 com-

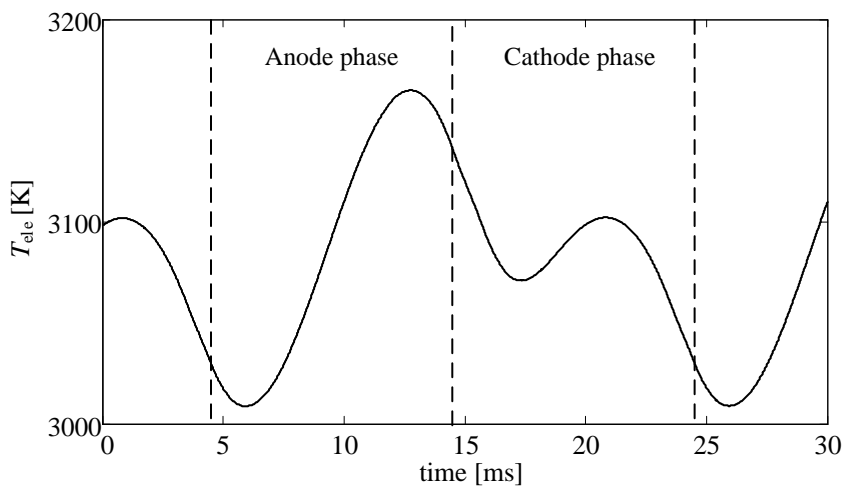


Figure 6.11: Calculated electrode tip temperature during 50 Hz sinusoidal lamp-current operation.

Table 6.3: LDI control principle.

LDI property	Input parameter (sense)	Output parameter (actuate)
Re-ignition behaviour	Overshoot (U_{over}) lamp voltage	Pulse amplitude (ΔP) lamp-current
System damping	Undershoot (U_{under}) lamp voltage	Gain feedback loop (ΔD)

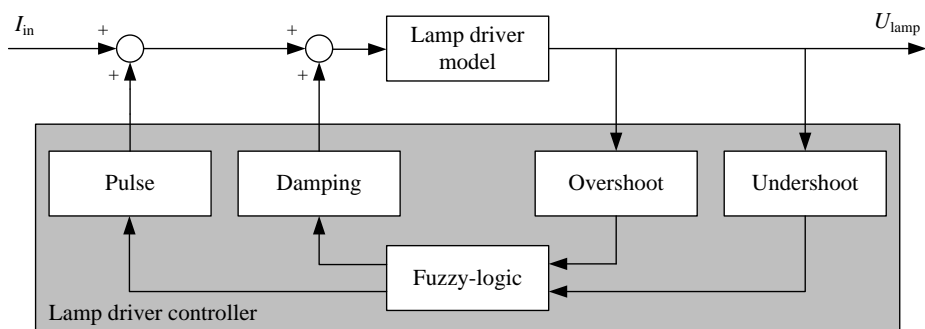


Figure 6.12: Lamp-ballast system and fuzzy-logic controller.

Table 6.4: Fuzzy rules and definition of fuzzy levels.

1	IF U_{under} is <i>PB</i> AND U_{over} is <i>PB</i>	THEN ΔD is <i>PB</i> AND ΔP is <i>ZE</i>
2	IF U_{under} is <i>PS</i> AND U_{over} is <i>ZE</i>	THEN ΔD is <i>ZE</i> AND ΔP is <i>NS</i>
3	IF U_{under} is <i>ZE</i> AND U_{over} is <i>PS</i>	THEN ΔD is <i>NS</i> AND ΔP is <i>ZE</i>
4	IF U_{under} is <i>ZE</i> AND U_{over} is <i>PB</i>	THEN ΔD is <i>ZE</i> AND ΔP is <i>PB</i>
-	<i>PB</i> = Positive Big	<i>ZE</i> = Zero
-	<i>PS</i> = Positive Small	<i>NS</i> = Negative small

prises both proposed control methods. The lamp-driver model block is previously described in Section 6.2. The lamp voltage is observed and during the commutation the overshoot (U_{over}) and undershoot (U_{under}) are calculated. These parameters are normalised to $[-1,1]$ with suitable scaling factors and are then used as input for the fuzzy-logic controller. On the output side of the fuzzy-logic controller the relative voltage feedback gain (ΔD) and relative pulse amplitude (ΔP) are present. The absolute values are defined in the “Pulse” and “Damping” blocks, which contains a memory function.

The proposed fuzzy logic control loop is implemented in Simulink as shown in Fig. A.3. In practice the input signals (U_{over}) and (U_{under}) results from the filtered lamp voltage signal U_{ac} . The lamp voltage before the commutator U_{c} is coupled via a band-pass filter, which is identical to the anti-oscillation feedback filter that is described in Section 6.2.

The fuzzy-logic controller block in Fig. 6.12 comprises three main components: the fuzzification stage, the rule base, and the defuzzification stage. The fuzzification stage is used to transform the so called crisp values of the input variables into fuzzy membership values. Then, these membership values are processed using fuzzy rules, as stated in Table 6.4, based on conditional “if-then” statements.

The fuzzified values for the outputs of the rules were classified into triangular shaped membership sets that are similar to the input values. In turn, the outputs of the rules are summed and defuzzified into a crisp analogue output value. The control surfaces in Fig. 6.13 show the value of the delta damping (ΔD) (relative voltage feedback gain) and delta pulse (ΔP) (relative pulse amplitude) at different combinations of the positive overshoot (U_{over}) and undershoot (U_{under}), using the fuzzy-logic model. The surface plot visualises the input – output relation, which is determined by the design of fuzzy sets, rule-base and membership functions.

The function of the fuzzy controller is to find a minimum for the positive and negative overshoot. The fuzzy controller will increase the damping and pulse amplitude in small steps (*PS*) until the system settles down at a stable operation point where the positive and negative overshoots are minimised. However, if the HID lamp tends to extinguish, which is sensed by large positive and negative voltage overshoots, one output parameter is strongly increased (*PB*) to stabilise the system. If the positive or negative overshoot tends to become zero (*ZE*), the

damping and pulse amplitude are decreased again in small steps (NS). Large negative steps are not necessary in a stable situation. This behaviour is embedded in the fuzzy rules given in Table 6.4.

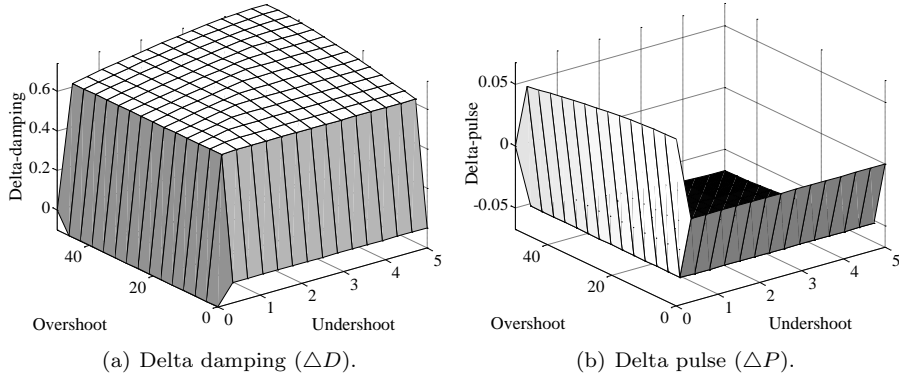


Figure 6.13: Surface plots showing relationship between input and output parameters.

6.4.1 Fuzzy-logic controlled lamp-driver stability

The stability of the LDI system comprising the proposed fuzzy-logic controller is analysed in this section. Both embedded control principles are discussed individually including their limitations and border conditions.

During operation the anti-oscillation feedback gain will be adapted within a pre-defined interval to stabilise the lamp-current. This interval ranges from zero to maximum gain, where zero gain equals the open loop configuration. In open loop configuration the LDI stability mainly depends on the cycle-by-cycle damping of the applied converter (Section 5.3.1). On the other hand, the maximum gain of the anti-oscillation feedback must be limited to prevent an instable system. The LDI stability was studied using the HID lamp small-signal analysis discussed in Section 6.1. The anti-oscillation feedback loop can be represented by an additional impedance R_f [Ω] placed parallel to the circuit capacitor C in (6.6), and this yields

$$R_f = \frac{1}{\Gamma} = \frac{U_{ac}}{I_{in}}, \quad (6.8)$$

where Γ represents the anti-oscillation feedback loop gain. Similar to the previous stability analysis in (6.7), it is found that the Routh-Hurwitz criterion for stability in this case becomes

$$\begin{aligned}
C_{\max} &= \frac{\tau}{|r|} \left(\frac{R_f}{R_f + R_{\text{la}}^0} \right), \\
\Gamma_{\max} &= \frac{1}{|r|}.
\end{aligned} \tag{6.9}$$

The first coefficient, C_{\max} , shows an increased stability margin because the anti-oscillation feedback loop introduces the virtual impedance R_f . The second coefficient, Γ_{\max} , limits the maximum feedback gain.

For the adaptive current pulse the border conditions concerning the system stability are less complicated. In this case the maximum permissible pulse current equals the maximum run-up current noted in the lamp specifications. The additional electrode heating current pulse ahead of the commutation process cannot destabilise the LDI system. However, additional heating of a sufficiently heated electrode can lead to extra wolfram deposition and lamp degradation. Therefore, pulse amplitude adaptation that depends on the operation conditions is required.

6.5 Experimental results

In this section the results of an experimental investigation of the proposed fuzzy logic control is presented using two driver concepts. The first set-up consists of a three-stage electronic driver, which is discussed in Section 4.1. The applied three stage converter shown in Fig. 6.14 consists of an output capacitor of $C = 1 \mu\text{F}$ and a series igniter of $L = 0.3 \text{ mH}$. The second driver set-up is based on the stacked buck converter topology, which is presented in Chapter 5, with $C = 100 \text{ nF}$ and $L = 1.2 \text{ mH}$. The Simulink fuzzy control algorithm runs on a dSPACE system with a sampling frequency of 30 kHz, connected to the in- and outputs of the electronic lamp-driver.

Using the first practical set-up the LDI stability is studied operating the BriteSpot HID lamp at the rated power level (35 W). The small-signal analysis in Section 6.2 for this lamp-driver combination shows an under-damped system mode. The effectiveness of the fuzzy-logic control is examined in the presence of this under-damped LDI. During steady-state operation in open loop configuration the lamp voltage and current are measured (Fig. 6.15) and show an oscillatory LDI. Every commutation initiates an almost undamped non-linear oscillation, and the resulting large lamp power modulation, eventually causes the lamp extinguish.

By adjusting the voltage feedback gain, and therefore the damping ratio, the fuzzy-logic control loop stabilises the lamp-driver interaction, as shown in Fig. 6.16. This eliminates the high current peaks and prevents the lamp from extinguishing. In the lamp voltage a small ripple remains, however, the undershoot is reduced to almost zero. Note, that this undershoot is used as the input

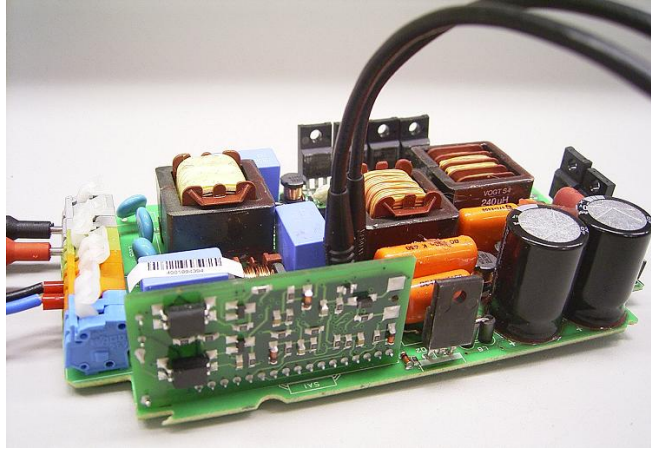


Figure 6.14: Photo of modified three stage lamp-driver with additional inputs.

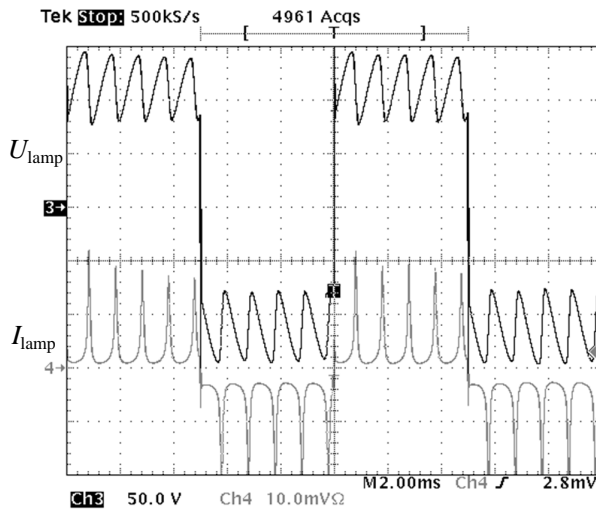


Figure 6.15: Open loop LFSW operation of the BriteSpot HID burner in set-up 1. Lamp voltage (50 V/div, upper trace), lamp-current (1 A/div, lower trace), time scale 2 ms/div.

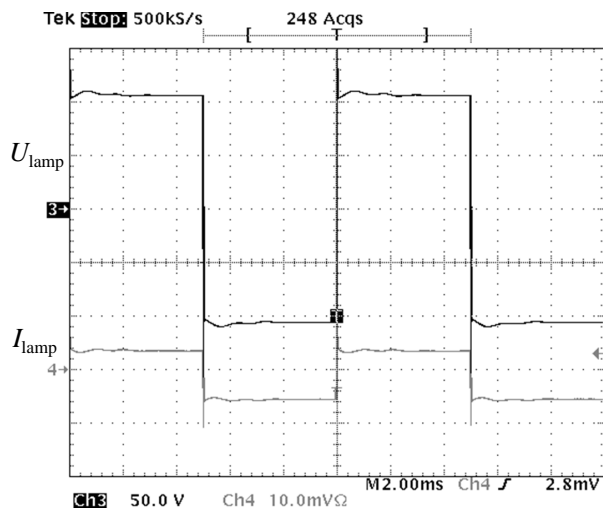


Figure 6.16: Closed loop LFSW operation of the BriteSpot HID burner in set-up 1. Lamp voltage (50 V/div, upper trace), lamp-current (1 A/div, lower trace), time scale 2 ms/div.

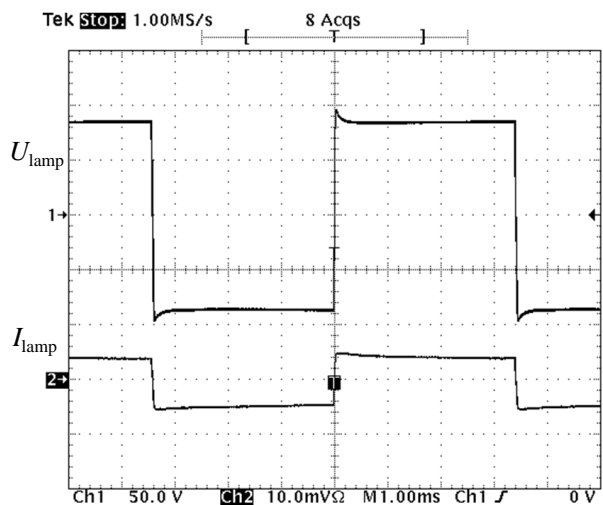


Figure 6.17: Open loop LFSW operation of the BriteSpot HID burner in set-up 2. Lamp voltage (50 V/div, upper trace), lamp-current (1 A/div, lower trace), time scale 1 ms/div.

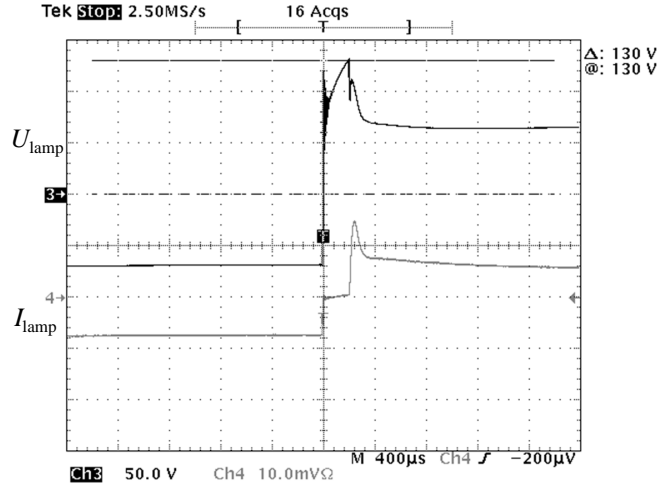


Figure 6.18: Detailed view of the commutation process of the CDM-TD 150W HID burner in set-up 1 in open loop operation. Note the large re-ignition peak. Lamp voltage (50 V/div, upper trace), lamp-current (1 A/div, lower trace), time scale 400 $\mu\text{s}/\text{div}$.

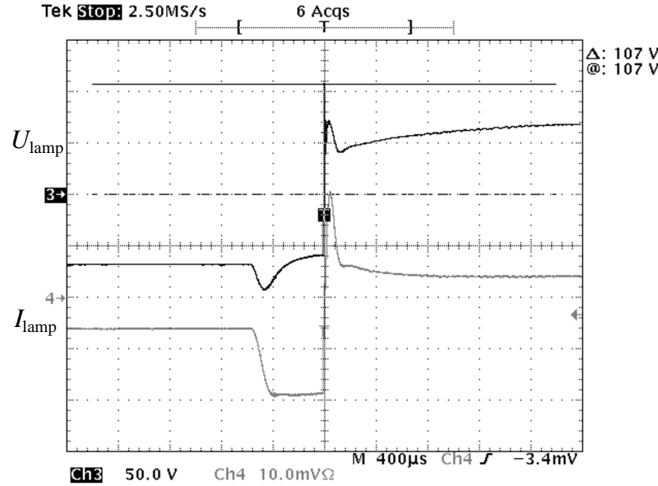


Figure 6.19: Detailed view of the commutation process of the CDM-TD 150W HID burner in set-up 1 in closed loop operation. Note the current pulse before commutation and small re-ignition peak. Lamp voltage (50 V/div, upper trace), lamp-current (1 A/div, lower trace), time scale 400 $\mu\text{s}/\text{div}$.

measure for the system damping control. On the other hand, the small re-ignition spike does not give rise to an increase of the pulse amplitude.

The second measurement set-up (Fig. 6.17) is used to operate the BriteSpot HID lamp at the rated power level (35W). The system appears to be perfectly stable in open loop configuration. Besides the fact that the output capacitor is ten times smaller than it is in the three-stage configuration, the stacked buck converter features standard cycle-by-cycle damping (Section 5.3.1), and both these characteristics are advantageous for the LDI stability. Therefore, in this case, enabling the fuzzy-logic control does not improve the LDI performance any further.

To study the commutation process and related electrode effects, the first measurement set-up is used to operate a Philips CDM-TD 150W / 942 burner at 50 W dim level. A detailed view of the negative to positive current transition is displayed in Fig. 6.18. During the transition electrode effects are apparent. When the current goes to zero the voltage across the output capacitor builds up until the lamp re-ignites. In the same time interval the lamp-current stays at a very low level. If this re-ignition time lasts too long the lamp extinguishes.

In line with the previous experiment, the LDI is examined in an open loop and in a closed loop, with the fuzzy-logic control activated. To heat up the electrode tip before the cathodic phase starts, the controller adjusts the pulse magnitude before commutation (Fig. 6.19). As a result, the re-ignition peak is strongly reduced. As can be seen, the final lamp voltage still includes a positive and negative overshoot. But the low current phase during the commutation has disappeared. During the pulse amplitude adaptation process it was observed that the re-ignition peak suddenly disappeared almost completely. When exceeding a certain threshold level, a linear increasing pulse amplitude results in a discrete step decrease in the measured re-ignition voltage, confirming the non-linear electrode behaviour.

The second measurement set-up (with a stacked-buck converter) is used to operate a CDM-T 73W/830 burner at 35 W dim level. As shown in Fig. 6.20 the voltage rises quickly after commutation and settles on a level dictated by the converter's power curve shown in Fig. 5.22. If this phase takes too long, the lamp extinguishes due to plasma cooling, and because the actual lamp-current is far too low for proper electrode heating.

For this lamp-driver combination operating at reduced power, enabling the fuzzy-logic control regulates the pulse amplitude before commutation. A relatively small amplitude is sufficient to overcome the glow mode after commutation, as shown in Fig. 6.21.

6.6 Discussion

In practice the lamp-driver performance depends on both the dynamics of the lamp and the driver. Some combinations tend to be poorly damped, resulting in an oscillatory lamp-current and even lamp extinguishing. To study the

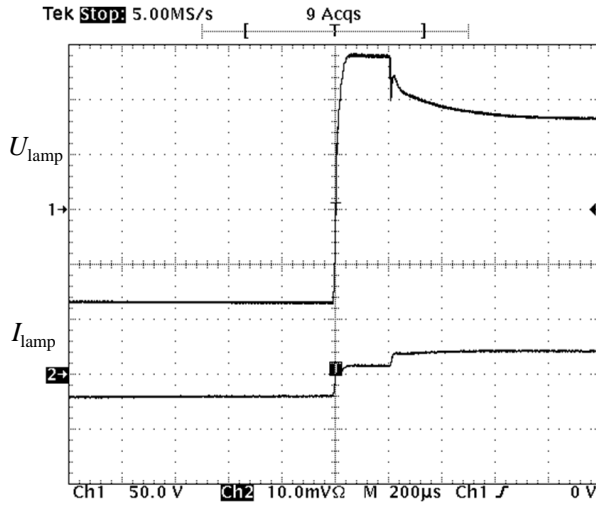


Figure 6.20: Detailed view of the commutation process of the CDM-T 73W HID burner in set-up 2 in open loop configuration. Lamp voltage (50 V/div, upper trace), lamp-current (1 A/div, lower trace), time scale 200 $\mu\text{s}/\text{div}$.

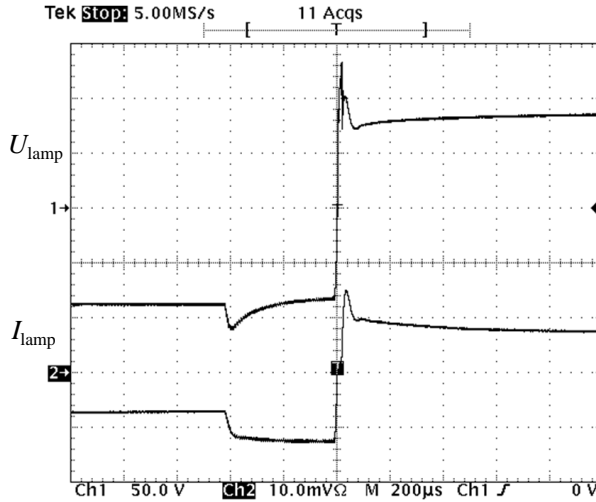


Figure 6.21: Detailed view of the commutation process of the CDM-T 73W HID burner in set-up 2 in closed loop configuration. Note the current pulse before commutation. Lamp voltage (50 V/div, upper trace), lamp-current (1 A/div, lower trace), time scale 200 $\mu\text{s}/\text{div}$.

lamp-driver interaction stability, a simple lamp model has been described that represents an HID lamp's small-signal electrical behaviour. The necessary parameters can be easily obtained from step response measurements. Using this lamp model the small-signal LDI behaviour is simulated and a feedback loop to stabilise the system is explored.

During normal operation we can assume that the electrodes have an appropriate temperature for thermionic emission. However, for older lamps or reduced power operation the electrode temperature can become too low, resulting in large re-ignition peaks. When a current pulse is applied at the end of each LFSW period-half, the temperature of the electrode can be sufficiently raised to secure stable re-ignition.

These two control principles are integrated in a fuzzy-logic controller to cope with lamp-driver parameter variations and non-linearity. The pulse current amplitude and feedback loop gain are adapted by heuristic rules to influence the re-ignition behaviour and lamp-ballast interaction stability. Experimental measurements with different LDI combinations operated at full and reduced power have shown that active LDI control is able to extend the range of stable operation.

Chapter 7

Light on demand in projection systems

The preferred light source for projection systems is the ultra high performance (UHP) HID lamp. Application of UHP lamps in rear and front projection systems sets new and more stringent requirements on the quality of the light generated by these lamps. This is especially the case with digital light processing (DLP) projection systems where light modulation is applied in synchronisation with the colour sequence. Deviations of the lamp-current from the desired modulation scheme translate to deviations in the light modulation of the lamp, which may lead to artefacts in the projected image.

The lamp-current control problem is subject to widely varying burner dynamics. The small-signal properties, as defined in Section 6.1, of the UHP lamp are known to vary significantly over time. In order to meet the stringent lamp-current requirements in the presence of poorly damped and varying LDI dynamics, in this chapter a control strategy is proposed that consists of two control loops. Firstly, the analogue anti-oscillation feedback loop, as defined in Section 6.2, is applied to stabilise the under-damped mode of the LDI system. Secondly, a new iterative learning control (ILC) approach [25] that compensates for the repetitive lamp-current disturbances is explored.

This chapter is organised as follows. The UHP lamp, which is intended for projection applications, is briefly introduced in Section 7.1. The projection system requirements regarding the lamp-current control are described in Section 7.2. The variation of the lamp-driver system dynamics throughout burner life is analysed in Section 7.3, and models are generated to be used in the ILC design. Subsequently, the ILC design strategy is described in Section 7.4, taking the time-varying behaviour of the system into account. Experimental results are shown in Section 7.5. Finally, a discussion of the achieved results can be found in Section 7.6.

7.1 Ultra high performance burner

The UHP lamp, which was introduced in 1995 [156], has an ultra short arc burner with an electrode distance of approximately 1 mm, mounted in a reflector (Fig. 7.1). This short arc lamp is a key component of projection systems that achieve the highest efficiency for small projection display sizes, in terms of luminance and etendue [157]. The etendue E [mm^2 SRad] describes the propagation of light through an optical system. For a beam with ray directions within a small solid angle Ω passing through a cross sectional area A , the etendue is defined as $E = A\Omega$. The etendue relates to the throughput of an optical system, and can never become smaller by transmitting a beam through a passive optical system.

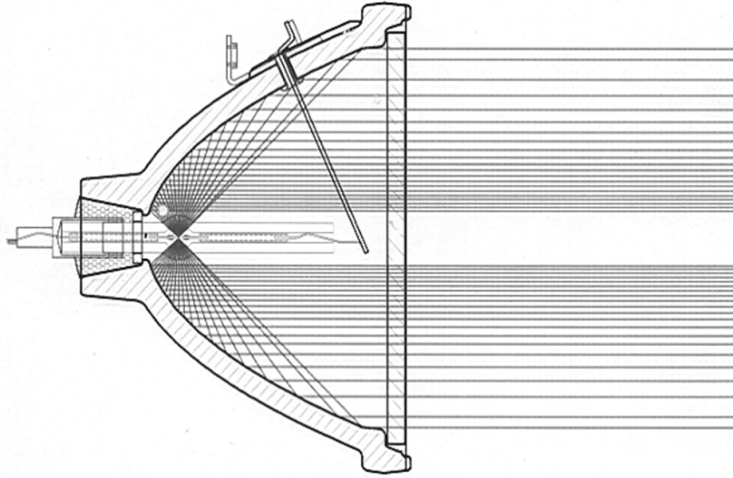


Figure 7.1: Sketched UHP lamp and light distribution.

In order to reach sufficient brightness, the light source should be point-like. This is because the light from the lamp has to be collected into the small etendue of currently available display systems, which are usually based on liquid crystal display (LCD) or digital mirror device (DMD) technology. Depending on the optical system, parabolic or elliptical reflectors are applied. In the focal point of these reflectors the ultra-short arc burner should provide extremely high brightness and a white spectrum throughout its lifetime.

The main components of the UHP burner (Fig. 7.2) are: a quartz tube, tungsten electrodes, and a mercury fill. In the stationary situation the mercury filling is completely evaporated, and the gas inside the lamp attains a pressure of more than 200 bar. The electrodes are placed opposite to each other and are relatively large, since they have to sustain high heat loads during operation of the lamp. The electrodes are heated to such high temperatures that tungsten atoms evaporate and enter the plasma state. Particles that are transported in the direction

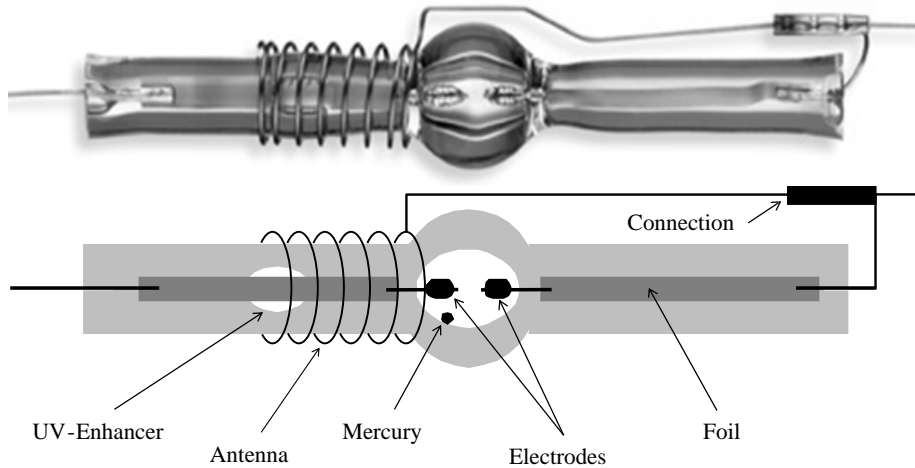


Figure 7.2: A schematic view of the construction of a UHP burner.

of the cold wall will deposit there and form a black solid layer, reducing the light output of the lamp. This process is similar to normal HID lamps. However, the reduced heat load of the normal HID electrodes leads to an acceptable deposition rate of tungsten on the wall. To overcome the wall blackening problem in UHP burners, a so-called regenerative chemical transport cycle is applied using a halogen filling [158], a technique also used with tungsten halogen lamps. As a result, the UHP lamp lifetime can exceed 10000 hours, depending on the power level and related heat load [159].

To create a gas-discharge primary electrons are needed. After switching off a lamp all charge carriers will have been neutralised after some hours. Some primary electrons are produced by natural radioactivity but many more primary electrons have to be created via field emission at the electrodes. In practice, 20 kV has to be applied to the lamp to guarantee ignition within an acceptable time delay. However, electrons can also be produced via photo-emission. For photo-emission the photon energy should be above the threshold frequency of the metal. Therefore, ultraviolet (UV) radiation with a short wavelength ($\lambda < 270$ nm) is needed, due to the work function of the tungsten electrodes (4.54 eV). In practice, for reliable ignition at voltages below 5 kV, a UV enhancer is incorporated into the electrode seal of the UHP burner [160], as shown in Fig. 7.2. A small cavity filled with an argon mercury mixture is ignited by an external wire (antenna). Subsequently, a capacitive discharge between the foil and the antenna produces UV light, which is conducted along the sealing towards the main burner. Secondly, the antenna construction modifies the electric field distribution inside the burner and helps to reduce the hot re-strike time.

7.1.1 Electrode stabilisation

In the UHP lamp the electrode tips are operated at temperatures usually above the melting point of tungsten (3500 K). During the lamp's lifetime the resulting large electrode surface modifications will alter any initial electrode surface into a rough and sometimes flat structure. The stability of arc attachment depends on the actual structure of the electrode tip. Therefore, after the first 10 to 100 hours the initial stable arc changes its attachment point on the rough surface frequently, no matter how perfect the electrode shape was initially. Such arc movement affects the light distribution on the display and causes disturbing brightness variations on the screen [161, 162]. With typical jump frequencies of 0.01 – 10 Hz they severely distract the audience.

An electronic drive scheme that stabilises the arc throughout its total lifetime was invented by Philips [153]. The application of extra current pulses superimposed on the LFSW current at the end of each half-wave (Fig. 6.10) results in a strong reduction in arc instability, in terms of probability and arc jump width. Measurements have shown that arc instability is suppressed by more than a factor of 1000 [161] and that any remaining disturbing visual effects are negligible.

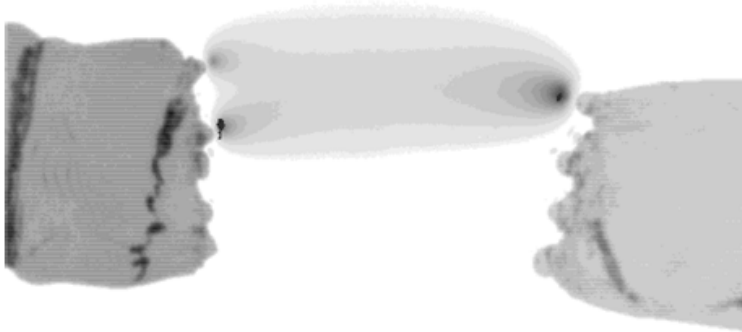


Figure 7.3: UHP burner operation with a LFSW of 1000 Hz.

Using a CCD camera set-up, the electrode surface conditions and arc attachments of UHP burners operated under different conditions are captured at the Philips research laboratories in Aachen. Typical pictures of the electrodes after approximately ten hours are shown in Fig. 7.3 and Fig. 7.4. The shape of the electrodes is shown and their contours indicate the brightness distribution of the arc at the same time. In the first picture the arc and electrodes are shown for a lamp operated on LFSW current at a frequency of 1000 Hz (Fig. 7.3). As a result of the strong material evaporation and back transport at the electrode surface [163], a more or less flat electrode front surface develops with multiple tips. The arc plasma jumps between the attachment points on this surface frequently. With LFSW pulse operation at 100 Hz (Fig. 7.4), single electrode tips develop

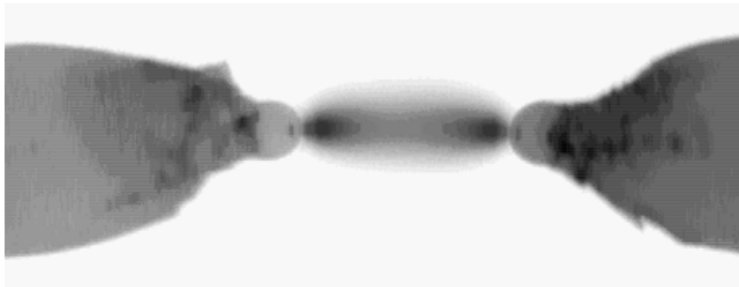


Figure 7.4: UHP burner operation with a LFSW of 100 Hz with additional current pulse.

and define a clear start point for the cathode phase after current reversal, thereby improving the stability of the arc.

In the long term, electrode material is transferred from the front of the electrode to the back, so called burn-back. Therefore, the distance between the electrodes grows and the plasma column length increases accordingly. First, this causes a voltage drop across the plasma column that increases proportional to its length. Secondly, the plasma's dynamic properties are affected because the parameters τ and r defined in Section 6.1 change. The lamp-current control problem discussed in this chapter is strongly related to the variation in burner dynamics throughout the burner's lifetime.

7.2 Projection application

Digital light processing (DLP) technology from Texas Instruments has made significant inroads in the projection display market, enabling small data and video projectors, HDTVs, and digital cinema. At the heart of these display solutions sits a digital micro mirror device (DMD), a semiconductor-based “light switch” array of thousands of individually addressable, tiltable, mirror-pixels [164, 165]. In a one-chip DLP projection system (Fig. 7.5) white light (from a UHP lamp) is focused down onto a spinning colour-wheel filter system. The wheel spins, illuminating the DMD sequentially with red, green, and blue light. At the same time an RGB video signal is being sent to the DMD mirror-pixels. Each mirror modulates the light intensity during each colour segment by switching very quickly between the “on” and “off” state to make the many shades of grey, according to a pulse-width modulation scheme called dithering. The human eye integrates the sequential images and a full colour image is seen.

The application of UHP lamps in DLP projection system sets new and more stringent requirements on the quality of the light generated by these lamps. Developments to enhance the video quality of DLP systems in terms of brightness

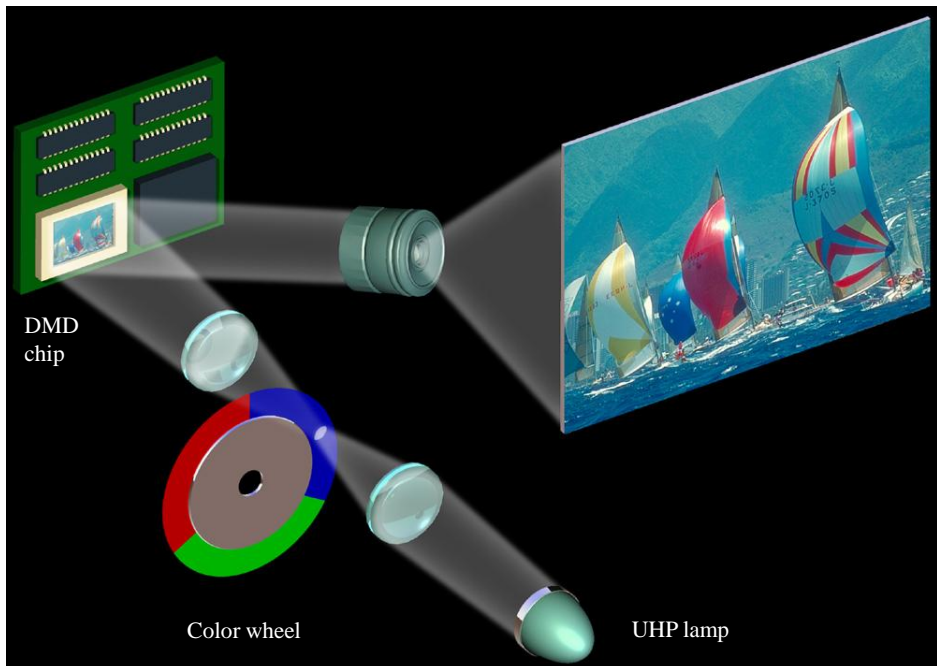


Figure 7.5: DLP based projection system (picture courtesy of Texas Instruments [166]).

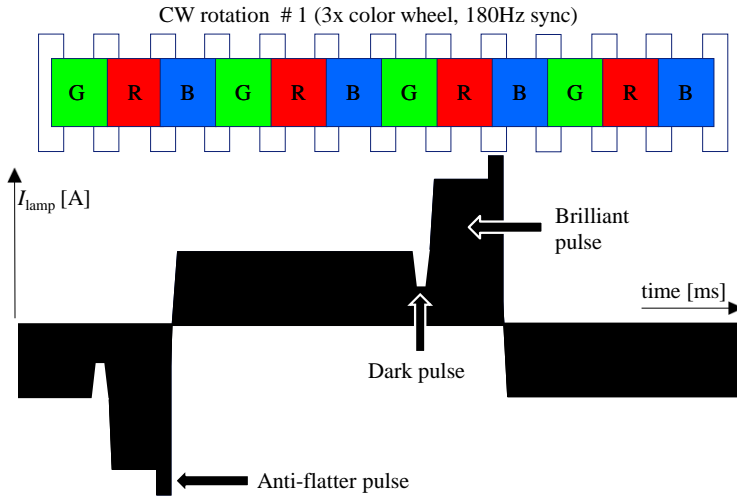


Figure 7.6: Lamp reference current profile and colour-wheel position where B = Blue, G = Green, R = Red.

and contrast require an accurate and stable light output level. To enhance the picture or video performance of DLP projection systems, amplitude modulation of the light by two types of pulses was introduced. The first pulse, called the dark pulse, lowers the light output in the green segment by 75 % for a very short time. This enables the creation of up to 2 extra bits in the grey scale resolution, and results in an enhanced contrast ratio and a strong reduction in visible dither noise. With the second pulse, called the brilliant pulse, the UHP light output is boosted up to 200 % during the red or blue segment of the colour-wheel sequence. This will increase the screen brightness by 30 % and enable adaptation of the colour temperature to a lower or higher level, according to the user's preferences.

In order to fulfil the light modulation demands of modern DLP projection systems, accurate control of the light source is required. From a control perspective, accurate regulation of the total luminous flux is quite cumbersome. Feedback principles based on optical measurements are hampered by the practical limitations of light sensor(s). Light sensors are expensive, sensitive to dust and contamination throughout life, and can be disturbed by arc instabilities. Fortunately, measurements have shown a strong correlation between the total light flux and the lamp-current, as displayed in Fig. 7.15.

In Fig. 7.6 the relation between the desired lamp-current (and related light) and colour-wheel position is given. To avoid picture artefacts, the light (and hence the lamp-current) must obey these setpoint specifications very accurately. In Table 7.1 the lamp-current performance specifications are shown.

In the past, the lamp-current performance had been realised by means of

Table 7.1: Lamp-current performance specifications.

Performance item	Limit
Overshoot pulse and commutation $\left(\frac{I_{\text{overshoot}}}{I_{\text{reference}}} - 1\right) \times 100 \%$	8 %
Rise and fall time from 10 % to 90 % of its final value	100 μs

empirically tuned feed-forward tables. To cope with the changes in the lamp behaviour over time, different tables had to be programmed to achieve a satisfactory performance. There are several reasons why this strategy was no longer considered to be attractive. First, manual tuning does not result in optimal behaviour. Second, the manual tuning procedure is very difficult and time-consuming. Third, the manual tuning approach is rather inflexible with regards to changes in the lamp-current profiles. The current profile, as shown in Fig. 7.6, is a basic profile, but for specific projection systems more complex profiles are required. For these reasons, a new control strategy for UHP lamps was desired. ILC is believed to be a good candidate for reasons described in the following sections.

7.3 Lamp-driver control strategy

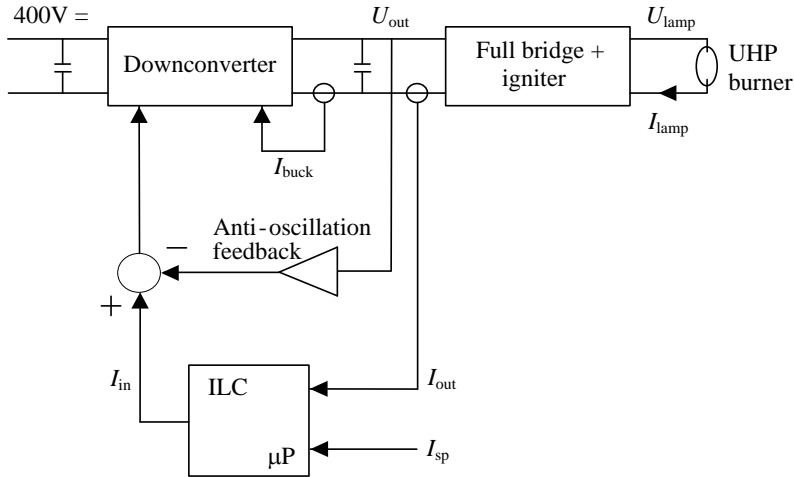


Figure 7.7: Lamp-driver control configuration.

In order to meet the stringent lamp-current requirements in the presence of varying system dynamics, the control strategy sketched in Fig. 7.7 is proposed. First, an analogue inner feedback loop stabilises the under-damped mode of the LDI system. As described in Section 6.2, this anti-oscillation feedback provides

additional damping. Practical measurements with UHP lamp 5 (Table 7.2) in an open loop configuration, as shown in Fig. 7.8(a), results in a rather undamped lamp-current response. Closing the loop in Fig. 7.8(b) shows the additional damping effect. For this system a conservative gain setting is selected for the anti-oscillation feedback loop. This is because a high gain setting can degrade the lamp-current transient response during commutation and pulse events.

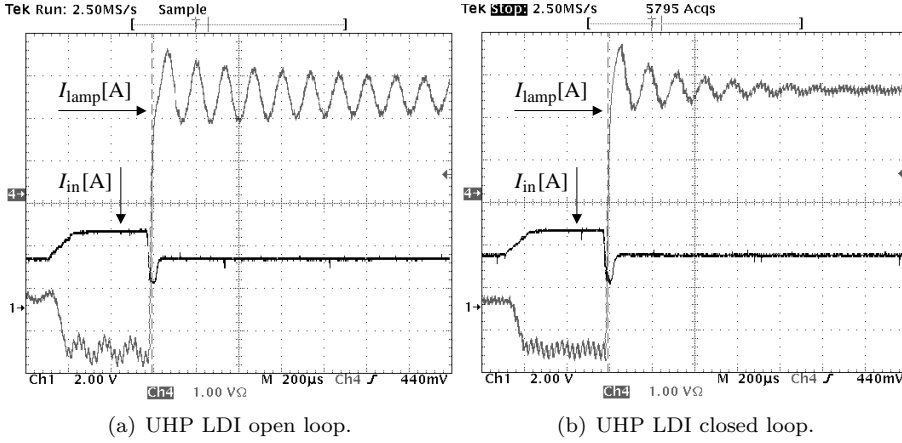


Figure 7.8: Measurement lamp-current I_{lamp} (0.5 A/div) and down converter set-point I_{in} (1 A/div), time scale 200 $\mu\text{s}/\text{div}$.

Secondly, the outer loop accurately controls the lamp-current according to the reference current profile, as shown in Fig. 7.6. The system to be controlled includes both the lamp-driver system and the anti-oscillation feedback. The software-based ILC loop updates the buck converter set-point sequence iteratively in such a way that the difference between the reference and the actual lamp-current diminishes after a couple of iterations. The repeating tasks are defined within one half of the symmetrical lamp-current commutation period. ILC acts only in control windows designed around the current transitions within the reference current profile, as shown in Fig 7.14.

7.3.1 System description and varying dynamics

The system to be controlled consists of a three-stage driver circuit (Section 4.1.1) connected to an UHP burner. In order to enable high bandwidth lamp-current control, the lamp-driver buck converter is operated in transition mode (TM), with an average switching frequency of 100 kHz. The buck converter current is controlled cycle-by-cycle in a peak current mode, as depicted in Fig. 7.7, with the I_{buck} feedback loop. In the practical set-up the Philips EUC 132 DP Power-Pack driver is applied, where the output filter capacitor and series igniter equal,

Table 7.2: Identified lamp parameters (UHP 120W 1mm).

Lamp	V_{la}^0 [V]	I [A]	r [Ω]	τ [μ s]	R_{la}^0 [Ω]	C_{max} [μ F]
1	71.7	1.75	-1.22	12	41.0	9.8
2	75.4	1.62	-2	12	46.5	6.0
3	79.3	1.62	-1.9	12	49.0	6.3
4	84.3	1.43	-3.41	19	59.0	5.6
5	97.0	1.27	-4.92	27	76.4	5.5
6	107.7	1.13	-5.7	32	95.3	5.6
7	115.8	1.07	-5.84	29	108.2	5.0
8	136.6	0.92	-8.92	44	148.5	4.9
9	146.3	0.86	-9.45	50	170.1	5.3

respectively, $C = 1.4 \mu\text{F}$; $L = 0.56 \text{ mH}$.

The dynamics of UHP lamps are known to vary significantly over time. This variation is caused by the increasing plasma column length throughout life, as discussed in Section 7.1.1. This time-varying behaviour has been studied using the practical set-up given in Fig. 6.1. For this investigation, a set of nine UHP lamps (type 120 W 1 mm) was selected representing nine instances almost equally distributed throughout the lamp's entire lifetime. The measurement results are denoted in Table 7.2. Analysing these measurements shows an increasing lamp voltage during life.

Next, these identification results were analysed using the lamp-driver interaction model, as derived in Section 6.2. The parameters of lamp 1 and 9 are applied in combination with the "PowerPack" driver parameters. In Fig. 7.9 the transfer function I_{in} / I_{out} is displayed in the frequency domain. The dominant resonance frequency varies from 7500 Hz for lamp 1 to 2000 Hz for lamp 9. The damping also varies by a significant amount.

7.3.2 System modelling

To generate accurate impulse response models that can be used in the ILC design, the transfer from current setpoint I_{in} to the output current I_{out} is experimentally modelled. The first experiments are conducted on a practical set-up (Fig. 7.10), consisting of a "PowerPack" lamp-driver including an anti-oscillation feedback loop, a dSPACE rti1103 processor board, and the set of nine UHP lamps described in Section 7.3.1. The dSPACE application runs at a sampling frequency of 30 kHz, which is the minimum sample frequency required for the intended performance. The following identification strategy was used:

1. Measure the nominal lamp-current in an interval within a LFSW period-half. The effect of noise is attenuated by averaging the lamp-current profiles over 10 successive periods. The nominal lamp-current profile is denoted \bar{Y} and consists of N_y samples.

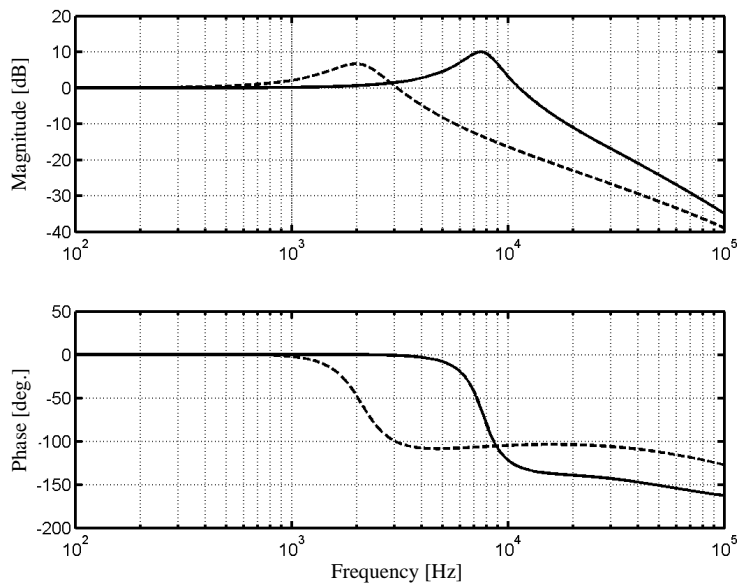


Figure 7.9: Varying dynamics of UHP lamps throughout life. Bode diagrams of the transfer function I_{in} / I_{out} using lamp 1 (solid line) and lamp 9 (dashed line).

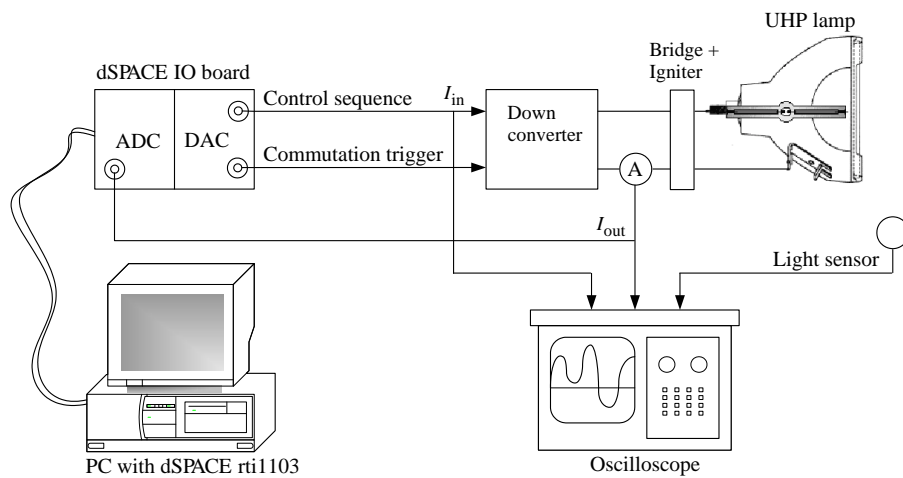
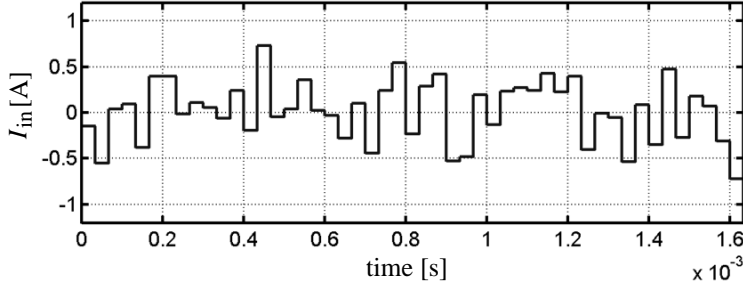
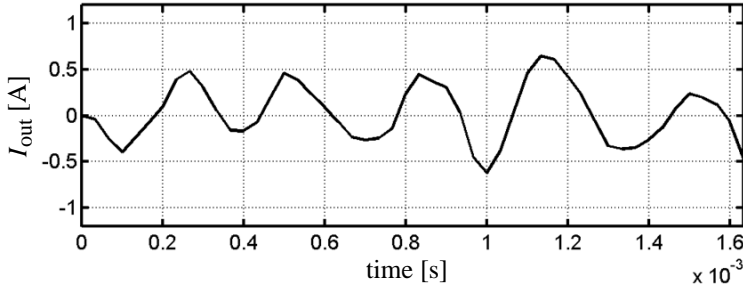


Figure 7.10: System identification measurement set-up.

Figure 7.11: Injected noise signal \bar{V} .

2. Add a pseudo random noise sequence (PRNS) signal \bar{V} (Fig. 7.11) of length N_y to the nominal current set-point signal, and measure the periodically disturbed lamp-current by averaging lamp-current profiles over 10 successive periods of length N_y . The disturbed current profile is denoted by \hat{Y} and the change in the output due to \bar{V} can be computed by subtracting the nominal current profile.

$$\Delta\bar{Y} = \hat{Y} - \bar{Y}. \quad (7.1)$$

Figure 7.12: Lamp-current response $\Delta\bar{Y}$.

3. From \bar{V} and $\Delta\bar{Y}$ (Fig. 7.12) compute the N_v leading impulse response parameters of the system, $\bar{G} = [G_0, G_1, \dots, G_{N_v-1}]^T$. The coefficients of \bar{G} are the values that minimise the difference between the measured and predicted output values, and can be computed by a least squares optimisation as follows

$$\min_{\bar{G}} \|\Delta\bar{Y} - \widetilde{M}_v \bar{G}\|^2, \quad (7.2)$$

where \widetilde{M}_v yields

$$\widetilde{M}_v = \begin{bmatrix} V_1 & 0 & \cdots & 0 \\ V_2 & V_1 & \cdots & 0 \\ \vdots & \vdots & \ddots & \vdots \\ V_{N_v} & V_{N_v-1} & \cdots & V_1 \\ \vdots & \vdots & \ddots & \vdots \\ V_{N_y} & V_{N_y-1} & \cdots & V_{N_y-N_v+1} \end{bmatrix}.$$

Solving for \overline{G} gives

$$\overline{G} = (\widetilde{M}_v^T \widetilde{M}_v)^{-1} \widetilde{M}_v^T \Delta \overline{Y}, \quad (7.3)$$

where $(\widetilde{M}_v^T \widetilde{M}_v)^{-1} \widetilde{M}_v^T$ is constructed from the noise sequence. If the same noise sequence is reused, it needs to be computed only once.

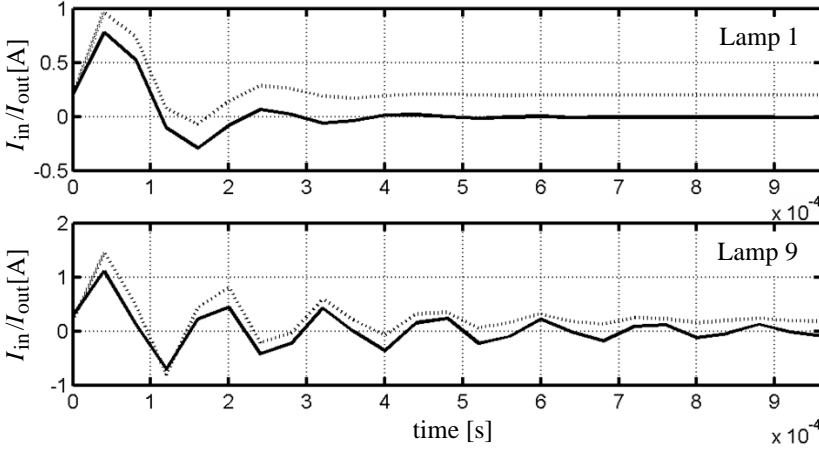


Figure 7.13: Impulse responses of lamps 1 and 9. Solid line is the identified pulse response. Dotted line is the LDI simulation model response, shifted upwards by 0.2 A.

The resulting identified impulse responses of lamp 1 and lamp 9 of the representative set of different UHP devices are shown in Fig. 7.13. The black dotted lines (shifted up by 0.2 A to make them distinguishable from the solid lines) represent corresponding impulse responses from the lamp-driver interaction model. These responses are obtained by fitting the equivalent lamp and driver parameters in the LDI model, as applied in Section 7.3.1. It can be concluded that the model structure is adequate for describing the dynamic effect of lamp-ballast interaction on the lamp-current.

7.4 Robust iterative learning control design

Iterative learning control (ILC) has received a lot of attention in the literature over the past decades. This is probably because the performance gained with ILC in systems executing repeated tasks is so spectacular compared to alternative control approaches. Early publications on ILC focussed on fairly simple design techniques using the frequency domain [167, 168]. Thereafter, a more adequate and accurate finite time description of ILC was introduced [169], showing that convergence of ILC is similar to the stability of a multi-variable difference equation describing the cycle to cycle behaviour of the learned system. The same finite time description was used to show [170] that the update law can be designed using different optimal control strategies, for example, to find an optimal balance between noise amplification and convergence speed.

The ILC has also been studied in the mathematical context of 2-d systems theory, where the dynamics in time and trial domain are studied simultaneously [171]. This mathematical framework enables e.g. the simultaneous optimisation of feedback control and cycle to cycle learning, however this is at the cost of a significant increase in complexity. Research on ILC was first and foremost considered in the context of high precision positioning applications, mainly wafer stages used in semiconductor lithography tools [172–174].

7.4.1 Lifted iterative learning control theory

The ILC design used in this work is based on the so-called “lifted systems” ILC design methodology [170]. In this “lifted systems” approach, the system behaviour is described over a finite horizon by a static mapping from an input sequence to an output sequence. The ILC is designed by considering the “convergence” dynamics in the trial-domain. Let the input to the buck converter (the current set-point) be defined as u and the output (the lamp-current) as y . Then, we define an input sequence $\bar{U} = [u_1, u_2, \dots, u_{N_u}]^T$, and an output sequence $\bar{Y} = [y_1, y_2, \dots, y_{N_y}]^T$, where $(\cdot)_k = (\cdot)(kT_s)$. T_s is the sample time and $N_u \leq N_y$. The relation between \bar{Y} and \bar{U} is causal and given by the following matrix expression

$$\begin{bmatrix} y_1 \\ y_2 \\ \vdots \\ y_{N_u} \\ \vdots \\ y_{N_y} \end{bmatrix} = \begin{bmatrix} P_0 & 0 & \cdots & 0 \\ P_1 & P_0 & \cdots & 0 \\ \vdots & \vdots & \ddots & \vdots \\ P_{N_u-1} & P_{N_u-2} & \cdots & P_0 \\ \vdots & \vdots & \cdots & \vdots \\ P_{N_y-1} & P_{N_y-2} & \cdots & P_{N_y-N_u-2} \end{bmatrix} \begin{bmatrix} u_1 \\ u_2 \\ \vdots \\ u_{N_u} \end{bmatrix} \quad (7.4)$$

where P_{N_y} is the N_y^{th} impulse response coefficient of the plant. In short notation we can formulate this as

$$\bar{Y} = \widetilde{M_p} \bar{U}. \quad (7.5)$$

The error sequence, $\bar{E} = [e_1, e_2, \dots, e_{N_y}]^T$, can be defined using the reference set-point sequence, $\bar{R} = [r_1, r_2, \dots, r_{N_y}]^T$, and the lamp-current \bar{Y} , as follows

$$\bar{E}_l = \bar{R} - \bar{Y}_l, \quad (7.6)$$

where l is the trial index, and \bar{Y}_l and \bar{E}_l represent the output and error in the l^{th} , trial respectively. Then, the iterative shaped input in the $(l+1)^{th}$ trial can be computed as

$$\bar{U}_{l+1} = \bar{U}_l + \Delta \bar{U}_l, \quad (7.7)$$

where $\Delta \bar{U}_l$ is the solution to the following minimisation problem

$$\min_{\Delta \bar{U}_l} \left[\bar{E}_l - \widetilde{M}_p \Delta \bar{U}_l \right]^T \left[\bar{E}_l - \widetilde{M}_p \Delta \bar{U}_l \right] + \alpha \left[\bar{U}_l + \Delta \bar{U}_l \right]^T \left[\bar{U}_l + \Delta \bar{U}_l \right] + \beta \Delta \bar{U}_l^T \Delta \bar{U}_l, \quad (7.8)$$

where α weighs the contribution of the sum of the squared control action to the objective, and β weighs the contribution of the sum of the squared change to the control action. The asymptotically converged solution is a trade-off between the error and the control effort using the α -term, and a trade-off between convergence speed and disturbance sensitivity using the β -term. The solution to this minimisation problem can be expressed in \bar{E}_l and \bar{U}_l

$$\Delta \bar{U}_l = (\widetilde{M}_p^T \widetilde{M}_p + (\alpha + \beta) \tilde{I})^{-1} (\widetilde{M}_p^T \tilde{I} \bar{E}_l - \alpha \bar{U}_l), \quad (7.9)$$

where \tilde{I} is the identity matrix. In compact notation, the ILC update law is given by

$$\Delta \bar{U}_l = \tilde{L}_u \bar{U}_l + \tilde{L}_e \bar{E}_l, \quad (7.10)$$

with learning matrices

$$\begin{aligned} \tilde{L}_e &= (\widetilde{M}_p^T \widetilde{M}_p + (\alpha + \beta) \tilde{I})^{-1} \widetilde{M}_p^T \tilde{I}, \\ \tilde{L}_u &= \tilde{I} - (\widetilde{M}_p^T \widetilde{M}_p + (\alpha + \beta) \tilde{I})^{-1} \alpha. \end{aligned} \quad (7.11)$$

$\tilde{L}_e \in \mathbb{R}^{N_u \times N_u}$ and $\tilde{L}_u \in \mathbb{R}^{N_u \times N_y}$ can be constructed off-line from the pulse response sequence.

7.4.2 Window selection

In the lifted ILC framework, the control and observation windows can be selected individually. To make implementation of the ILC in a low-cost micro-processor actually feasible, the computation and memory requirements should be limited.

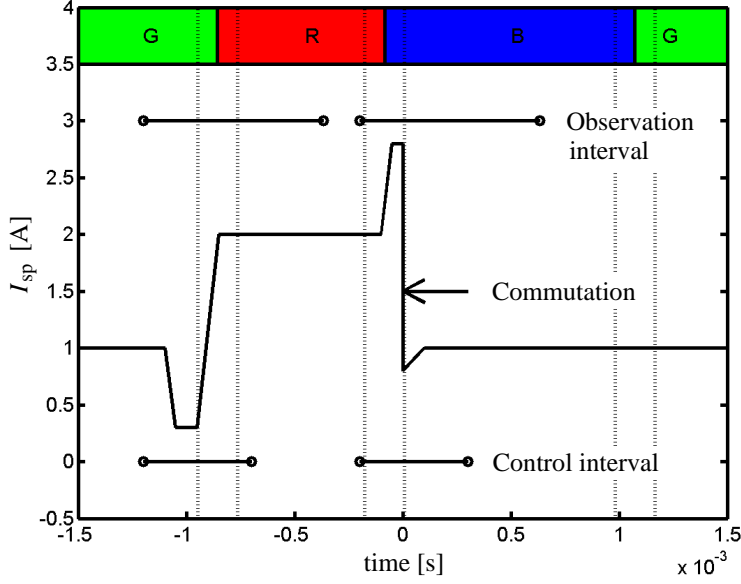


Figure 7.14: Typical DVE lamp-current set-point, I_{sp} , with control and observation intervals.

Therefore, the ILC is allowed to act on only a small section of the entire commutation period and very short observation windows and even shorter control windows have been selected. The rationale for choosing an observation window that is larger than the control window is that the specifications on the lamp-current after the control window are as stringent as those that apply during the control interval. In the reference current profile, two control and two observation intervals are selected, as displayed in Fig. 7.14. The first control interval is located around the dark pulse in the current profile at the end of the green section, the second control interval is around the anti-flutter pulse and commutation event.

7.4.3 Lifted iterative learning control convergence

In the lifted ILC approach, we consider the following learning law

$$\bar{U}_{l+1} = \tilde{L}_u \bar{U}_l + \tilde{L}_e \bar{E}_l. \quad (7.12)$$

If we substitute in the learning law, the expression for the system dynamics (7.5) and the error definition (7.6), we get the following expression for the convergence dynamics in the trail domain

$$\bar{U}_{l+1} = (\tilde{L}_u - \tilde{L}_e \tilde{M}_p) \bar{U}_l + \tilde{L}_e \bar{R}. \quad (7.13)$$

Hence, the ILC is convergent if all eigenvalues of $(\tilde{L}_u - \tilde{L}_e \tilde{M}_p)$ are inside the unit disk of lamp-current.

7.4.4 Robust learning gain design

The control problem entails finding matrices \tilde{L}_u and \tilde{L}_e such that fast convergence to a desired steady-state is obtained while all eigenvalues of $(\tilde{L}_u - \tilde{L}_e \tilde{M}_p)$ are inside the unit disk for all expected lamp behaviours \tilde{M}_p throughout life. This, in fact, is a robust control problem, considering the infinite possible variations of the system dynamics. This robust ILC design problem has so-far received little attention in literature. When the possible variations of the system dynamics are limited to a finite set of lamp behaviours, the robust design problem boils down to a simpler, so-called simultaneous stabilisation problem [175]. A conservative solution to this problem can be found using linear matrix inequalities. This approach was not pursued here. Instead, an alternative design approach has been taken where convergence was checked afterwards. This approach is based on least squares minimisation of an objective function consisting of the sum of the squared error in the observation interval and the sum of the squared control action in the control interval, summed over a set of representative lamps N_{lamps} . The solution of $\Delta \bar{U}_l$ then boils down to the following minimisation problem

$$\min_{\Delta \bar{U}_l} \sum_{i=1}^{N_{lamps}} \left[\bar{E}_l - \tilde{M}_p^i \Delta \bar{U}_l \right]^T \left[\bar{E}_l - \tilde{M}_p^i \Delta \bar{U}_l \right] + \alpha [\bar{U}_l + \Delta \bar{U}_l]^T [\bar{U}_l + \Delta \bar{U}_l] + \beta \Delta \bar{U}_l^T \Delta \bar{U}_l. \quad (7.14)$$

The objective function is constructed by taking the sum of the error over all N_{lamps} lamp models to take into account the variation in the lamp dynamics. The solution to this minimisation problem can be expressed in \bar{E}_l and \bar{U}_l

$$\begin{aligned} \Delta \bar{U}_l &= (\tilde{M}_s^T \tilde{M}_s + (\alpha + \beta) \tilde{I})^{-1} (\tilde{M}_s^T \tilde{M}_I \bar{E}_l - \alpha \bar{U}_l), \\ \text{with } \tilde{M}_s &= [M_p^{1T}, M_p^{2T}, \dots, M_p^{N_{lamps}T}]^T, \\ \text{and } \tilde{M}_I &= [\tilde{I}^{N_y}, \tilde{I}^{N_y}, \dots, \tilde{I}^{N_y}]^T, \end{aligned} \quad (7.15)$$

where $\tilde{M}_I \in \mathbb{R}^{N_y \times N_{lamps} N_y}$, and \tilde{I}^{N_y} is an identity matrix of dimension N_y . This leads to the following learning matrices

$$\begin{aligned}
\tilde{L}_e &= (\tilde{M}_s^T \tilde{M}_s + (\alpha + \beta) \tilde{I})^{-1} \tilde{M}_s^T \tilde{M}_I, \\
\tilde{L}_u &= \tilde{I}^N - (\tilde{M}_s^T \tilde{M}_s + (\alpha + \beta) \tilde{I})^{-1} \alpha.
\end{aligned} \tag{7.16}$$

In (7.16) the learning matrices for a multi-model approach are defined. Using the impulse response identification method described in Section 7.3.2 for a representative set of UHP burners, the robust learning matrices \tilde{L}_e and \tilde{L}_u can be computed.

7.5 Measurement results

The ILC principle has been tested together with various UHP lamps using the experimental set-up defined in Section 7.3.2. Photos of the experimental set-up are displayed in Fig. 7.16. The ILC control algorithm is coded in MATLAB and run on a dSPACE rti1103 processor board at 30 kHz, using the robust learning matrices \tilde{L}_e and \tilde{L}_u computed in Section 7.4.4.

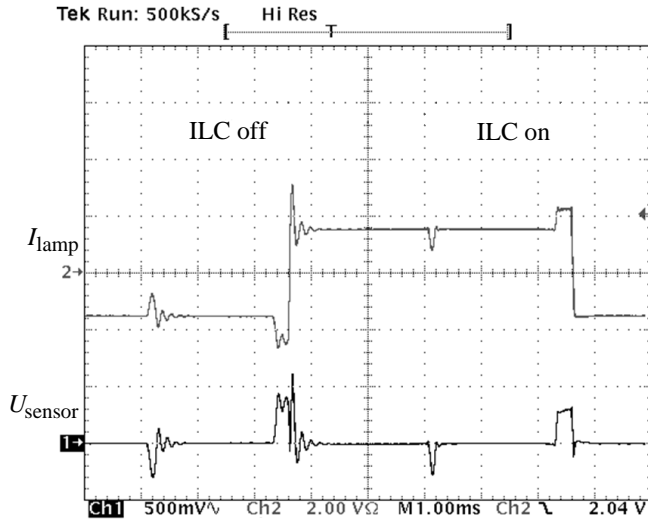


Figure 7.15: ILC enabled for one half period. lamp-current (2 A/div, upper trace), response light sensor (0.5 V/div, lower trace), time scale 1 ms/div.

In a first experiment, with UHP lamp 1 (Table 7.2), the ILC is enabled only for one half period and the brilliant pulse is omitted in the current set-point. In open loop mode the set-point transitions lead to overshoots and damped oscillations in the lamp-current as shown in Fig. 7.15. In the second period-half ILC is enabled

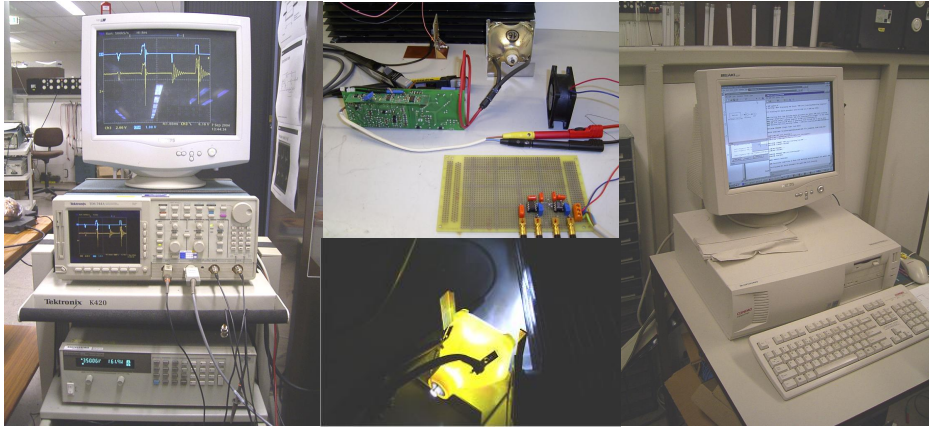


Figure 7.16: Photos of practical measurement set-up.

and corrects the deviation between the set-point and the actual lamp-current. The applied damping is sufficient to enable ILC to operate within the defined small control and observation windows. In the same graph the ac response of the light sensor is displayed. It can be concluded that the lamp physics strongly connects the lamp-current and the emitted light flux.

To prove that the ILC performance is robust, tests are performed using the dSPACE set-up (Fig. 7.10), for two 132 W UHP lamps that were excluded from the identification procedure. One UHP lamp is almost new and had an average lamp voltage that equals 57 V, and a correspondingly high lamp-current of approximately 2.2 A in the LFSW plateau. The other UHP lamp is of the same type, but had used for about 5000 hours of operation. This older lamp has a voltage of 117 V, and consequently has a much lower current of about 1 A. The current setpoint for this old lamp includes an anti-flatter pulse prior to the commutation. This anti-flatter pulse, with a height of 2.8 A, ensures arc stability. The two lamps represent the extremes of the rather wide range of variations in lamp dynamics. Both lamps are tested on the “Powerpack” driver, which includes the anti-oscillation feedback control loop. The lamp-current profile of the 57 V lamp without ILC, is plotted in Fig. 7.17. With ILC as shown in Fig. 7.18, excellent tracking of the lamp-current reference profile is obtained. Spectacular improvements are visible after commutation: the resonant response completely disappears. The dotted lines indicate the spokes of the colour-wheel, where the lamp current performance is less critical. The control signal after convergence is shown in the same figure.

In Fig. 7.19 the lamp-current without ILC for the old 117 V lamp is shown. The large difference in the response to the dip between the 57 V lamp (Fig. 7.17) and the 117 V lamp can easily be seen. Nevertheless, the same ILC manages

to achieve excellent tracking of the current setpoint, also for the 117 V lamp (Fig. 7.20). Based on the successful results from the test set-up, it was decided to make ILC part of the newest UHP lamp-driver technology.

7.6 Discussion

The application of ultra high performance (UHP) HID lamps in projection systems sets new and stringent requirements on the quality of the light generated by these lamps. These systems are subject to periodic disturbances synchronous with the LFSW commutation period. Iterative learning control (ILC) has been explored to compensate for the repetitive disturbances by means of a feed-forward signal. ILC updates the setpoint of the lamp-current continuously, making use of the internal model principle to achieve asymptotic tracking and disturbance rejection. As a result, the actual lamp-current converges to the required lamp-current profile, and strongly related emitted luminous flux, even in the face of the inevitable changes in the lamp dynamics over time.

The robustness of ILC during lamp life has been improved by taking a multi-model approach in the design of the ILC update law. The excellent performance of the UHP lamp driver with ILC is demonstrated experimentally. Care has been taken to end up with a simple and computationally cheap algorithm.

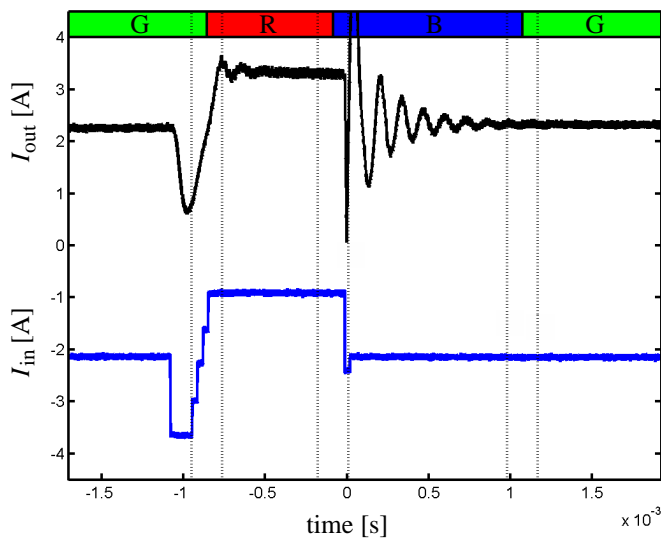


Figure 7.17: Performance without ILC for 57 [V] UHP 132 W lamp. Down converter set-point $I_{in} = I_{sp}$ is shifted down to make it distinguishable.

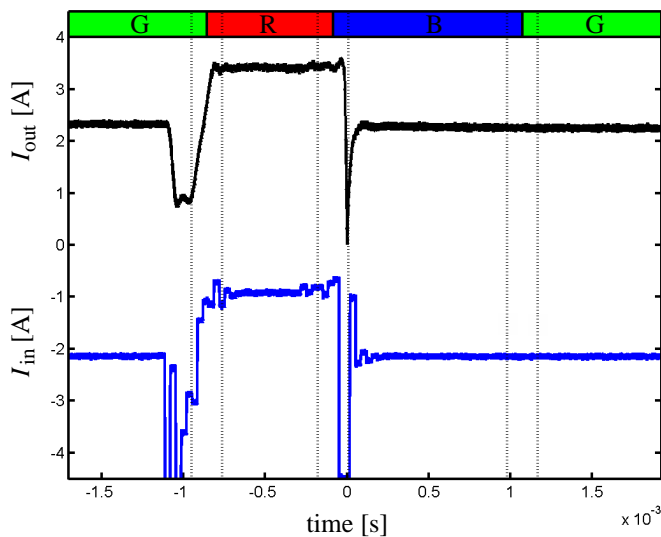


Figure 7.18: Performance with ILC for 57 [V] UHP 132 W lamp. Down converter set-point I_{in} is shifted down to make it distinguishable.

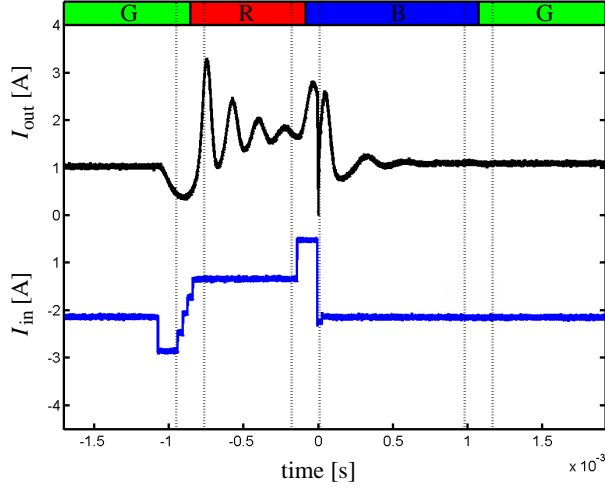


Figure 7.19: Performance without ILC for 117 [V] UHP 132 W lamp. Down converter set-point $I_{in} = I_{sp}$ is shifted down to make it distinguishable.

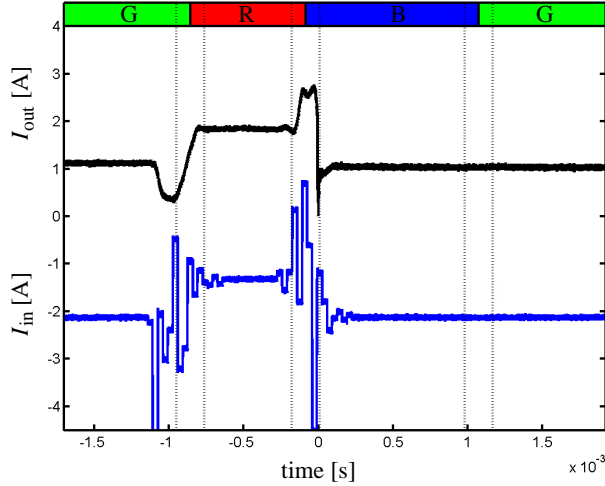


Figure 7.20: Performance with ILC for 117 [V] UHP 132 W lamp. Down converter set-point I_{in} is shifted down over to make it distinguishable.

Chapter 8

Observer-based lamp control

HID lighting systems are now widely used in a broad range of interior and exterior applications to provide energy efficient and cost effective illumination. Enabling HID lamp dimming provides a significant opportunity to reduce the energy consumption even further. HID lamps can be dimmed using step-level or continuous-dimming systems. Step-level dimming can be used to save energy during periods when the illuminated area is unoccupied but needs to stay lighted for safety and security reasons. Continuous dimming is ideally suited for applications where it is advantageous to adapt the lighting system to a wide range of light-levels.

Continuous dimming is also well suited for daylight harvesting because it allows the HID lamp output to be tuned to maintain a constant light-level in the room of concern. Electronic lamp-drivers for HID burners can provide continuous dimming, typically from 100 to 50 % light output for metal-halide, and from 100 to 30 % light output for high-pressure sodium lamps. Metal-halide lamps operated below the rated power may experience degradation in service life, efficacy, and lumen maintenance, or they may even extinguish. Furthermore, HID lamps can experience a colour shift during dimming as well as a reduction in their colour rendering ability [176].

The application of HID lamps in critical indoor settings (e.g. shop lighting) and high-end outdoor areas (e.g. city beautification projects), sets high standards for the light generated by these lamps in terms of operation stability, luminous flux, colour temperature, and colour rendering. In these systems, dimming is also utilised to create dynamic lighting and light scene settings. To be able to meet the stringent light quality requirements and the increasing demand for stable HID lamp dimming, new control principles are investigated.

In this chapter an “intelligent” electronic lamp-driver [146] is proposed that sets a stable minimum dim-level and monitors the gas-discharge throughout life. An HID lamp observer derives physical lamp state signals closely associated with the HID arc discharge physics and the related photometric properties. These improvements are meant to be used conjointly with the more conventional control

principles discussed in Chapter 6.

This chapter is organised as follows. The HID lamp observer and control principle are briefly introduced in Section 8.1. The observer model, which includes a reduced parameter identification method to track the lamp behaviour over life, is discussed in Section 8.2. Integrating sphere measurements were performed to study the photometric and colorimetric performance for new and old ceramic HID lamps and are presented in Section 8.3. Electrode behaviour during operation at full and reduced power was studied using the proposed lamp observer and verified with optical measurements in Section 8.4. An observer-based HID lamp controller that enhances the system performance is discussed in Section 8.5. Finally, the conclusions are presented in Section 8.6.

8.1 High-intensity-discharge lamp observer

The feedback principle is an essential concept in control theory. Many different control strategies are based on the assumption that all internal states of the controlled object are available for feedback. In most cases, however, only a few of the states or some functions of the states can be measured, due to either economic or physical constraints. These circumstances give rise to the need for techniques which make it possible to estimate states and create a “state observer” [177].

Observer-based techniques are well known from their use in sensorless motor control [178]. Sensorless control refers to a special type of motor control where the rotor position and velocity sensors have been replaced by a mathematical algorithm. These rotor sensors were expensive, prone to fail, and increased the mechanical complexity. The observer algorithm estimates the rotor position and velocity based on voltage and current measurements. These voltage and current sensors are less expensive and more reliable than the rotor sensors. On the other hand, the mathematical algorithm that is used to replace the sensors can be quite complex and may require heavy computational effort. However, this is hardly an issue today due to the increasing availability of powerful, cost effective microprocessors.

In this chapter an observer-based control approach is applied to ceramic metal-halide lamp systems. The lamp state observer constructs unmeasured system states from a known set of system states and parameters. The lamp observer directly enhances system performance because it allows more sophisticated control schemes that make use of physical quantities, for example the electrode sheath voltage (ESV), which heretofore was unavailable. Measured terminal quantities are used to calculate unmeasured states using a mathematical description of the physical lamp processes. Implementation of the proposed lamp observer in real-time is possible with the powerful microprocessors that are available nowadays.

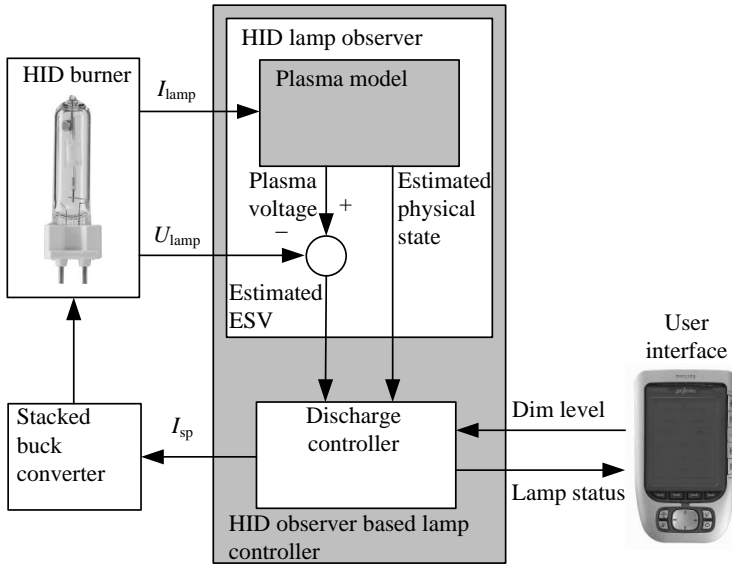


Figure 8.1: Observer-based HID lamp controller.

8.1.1 Observer-based control

In Fig. 8.1 the principle of an observer-based HID lamp-driver is sketched. This set-up includes an HID lamp and driver (Stacked buck converter) connected to a control section that comprises the proposed HID lamp observer and discharge controller. The latter provides a lamp-current control I_{sp} action according to user preferences and the actual HID lamp states.

In the realisation phase the grey box phase resolved plasma model described in Section 3.1 is implemented. In this model the elementary mathematical rules of the physical lamp processes are embedded, including the known model constants. The remaining parameters can be considered as unknown and need to be identified.

For the ESV observer part, the most interesting characteristic of the plasma model is its terminal voltage; although the discharge model can also provide physical parameters for a plasma observer part. The latter parameters can include an ageing factor containing essential information about the actual discharge condition. The ESV is determined taking the difference between the actually measured lamp voltage and the calculated plasma column voltage, as discussed in Section 3.3. Finally, based on the terminal lamp properties, the proposed lamp observer estimates both electrode and plasma state variables.

Table 8.1: Nominal lamp resistance measurements $P_{\text{lamp}} = 71$ W.

New lamps	R_{lamp} [Ω]	Old lamps	R_{lamp} [Ω]
N1	92.68	O1	111.30
N2	82.91	O2	112.36
N3	92.96	O3	115.03
N4	95.62	O4	102.88

Table 8.2: Identified lamp parameters.

Parameter identified	New lamp (N2)	Old lamp (O3)
a_1	0.0331	0.1720
a_2	0.0026	0.0049
a_3	$5.6962 \cdot 10^{-12}$	$1.1292 \cdot 10^{-11}$
a_4	$1.0543 \cdot 10^3$	$1.0562 \cdot 10^3$
a_5	$1.3669 \cdot 10^{16}$	$1.3669 \cdot 10^{16}$
a_6	$6.0475 \cdot 10^{14}$	$6.0475 \cdot 10^{14}$
a_7	$1.0122 \cdot 10^4$	$1.0122 \cdot 10^4$
a_8	$1.3093 \cdot 10^4$	$1.3093 \cdot 10^4$
MAE	1.29 %	3.04 %

8.2 Plasma model identification

To study the lamp's behaviour throughout life, eight Philips CDM-T 73W/830 lamps are selected for the identification procedure. This batch consists of four new lamps with (100 – 1000) hours of burn-in time, and four old lamps ranging between 8000 and 9000 hours of service. Operated at full power, the nominal lamp resistance increases throughout life according to Table 8.1, where the lamps (N2) and (O3) represent respectively the lowest and highest resistance.

For all lamps the steady-state parameters are identified using the power resistance response obtained during steady-state equilibrium, at defined power levels ranging between rated power and minimum dim level. A constrained minimisation was performed for the selected batch of lamps, in line with the procedure in Section 3.2.2. Analysing the results show that the parameters $a_{(1-4)}$ have a strong correlation with the increasing nominal lamp resistance over life as given in Table 8.1, and the parameters $a_{(5-8)}$ are almost identical for all lamps in the identified batch. The proposition here is that the steady-state identification parameters can be split up into two sets: a parameter set $a_{(1-4)}$ related to the lamp degradation during life and a parameter set $a_{(5-8)}$ that is related to the lamp type.

To prove this theorem, first a reduced parameter set $a_{(1-4)}$ identification was performed for lamp (N2) and (O3). In this identification procedure the parameters $a_{(5-8)}$ are constants and equal the accurate identification result that was given in Section 3.2.2 for the same lamp type. The reduced identification results

are presented in Table 8.2 and verified in Fig. 8.2, where the modelled resistance versus power characteristics (continuous lines) and measured data points are displayed. This graph demonstrates that the reduced parameter set identification procedure is able to fit both measured data sets adequately concerning lamps of the same type.

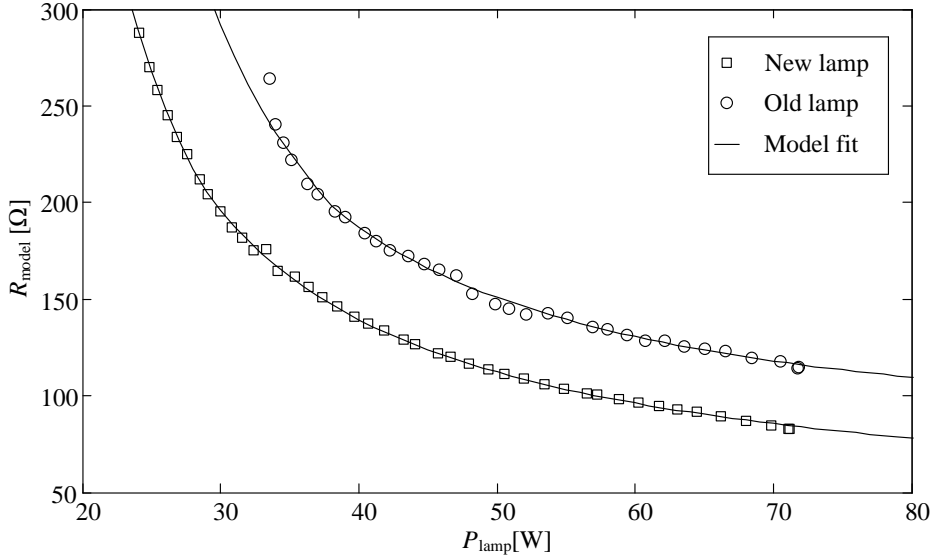


Figure 8.2: Identification verification new (N2) and old (O3) burner.

During life the lamp resistance curve shifts upward as shown in Fig. 8.2. Analysing the measured data points in the same figure in more detail shows some small discrepancies in the curve. These small steps are more apparent for the old lamp and can be explained by changes in the electrode function when reducing the lamp-current. In turn this gives rise to a slightly increased mean averaged error (MAE) for the old lamp identification (Table 8.2).

To prove the split identification theorem in a second way, a batch of four new (100 hr.) Philips CDM-T 73W/942 lamps was identified. Those lamps contained a different salt mix, and therefore emitted light with a different colour temperature, as shown in Section 2.1.3. The impact on the lamp constants is small, and therefore treated indifferent in this experiment. The identification results were compared with the four previously identified new CDM-T 73W/830 lamps. The parameters $a_{(1-4)}$ show a small spread between the individual lamps, while parameters $a_{(5-8)}$ clearly differ according to the lamp type. This difference is graphically displayed in Fig. 8.3, showing the simulated resistance versus power characteristic averaged over the four lamps of each type.

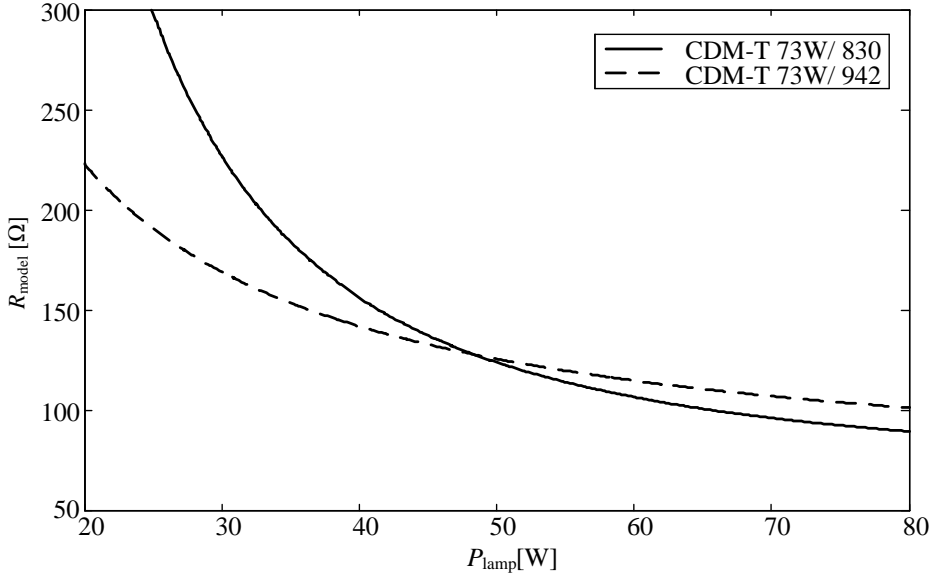


Figure 8.3: Simulation resistance versus power characteristic for CDM-T 73W/830 lamps and CDM-T 73W/942 lamps.

8.2.1 High-intensity-discharge lamp degradation

The time dependent degradation of metal-halide lamps equipped with a ceramic envelope can be explained by two main effects [179, 180]. First, there is tungsten deposition on the discharge vessel wall as a result of sputtering at lamp start and also from electrode evaporation during continuous operation. Second, there are chemical reactions between the aggressive metal-halide compounds and the polycrystalline alumina discharge vessel wall. Discharge tubes made of transparent alumina have better durability against high temperatures and corrosion than quartz glass envelopes.

Chemical interaction between the salt fill and ceramic envelope takes place in the gas phase as well as in the liquid phase. For some metal-halide filling compounds, formation of a garnet structure on the discharge vessel wall indicates corrosion during a gas phase. In the liquid phase, corrosion under the salt pool is a commonly observed phenomenon [179, 180]. This is one of the end-of-life mechanisms for ceramic burners, leading to leakage of the discharge tube.

The wall blackening phenomena, which leads to light flux reduction, is a valid indicator that can be utilised to evaluate the degree of the degradation of an HID lamp. Figure 8.4 displays photos of the identified HID burners (N2, O3). Comparing both lamps shows the reduced optical transparency of the old burner, caused by blackening and corrosion. Leaching of the ceramic tube by corrosion

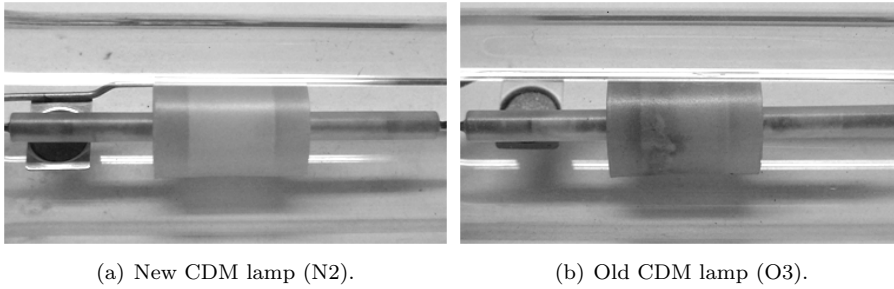


Figure 8.4: Photos of CDM discharge vessel blackening over time.

Table 8.3: Average wall temperature measurements.

New lamp	P_{lamp} [W]	T_w [K]	Old lamp	P_{lamp} [W]	T_w [K]
N2	73	1205	O3	73	1320
N2	40	1160	O3	40	1225

processes is visible at the left side of the old burner; the position is related to the salt pool location during vertical operation. The increased absorption coefficient of the discharge wall caused by arc tube wall blackening leads to a higher salt pool (cold spot) temperature.

The wall temperature versus lamp power for a new (N2) and old burner (O3) are simulated and plotted in Fig. 8.5. To verify the simulation results, wall temperature measurements were performed at the Philips lighting laboratory using a calibrated infrared pyrometer (FLIR CS 4000) set-up. The discharge vessel of a lamp has been taken out the outer bulb and installed into a vacuum environment identical to the original lamp. During steady-state operation the discharge tube is imaged in the far infrared region, i.e. $8 \sim 12 \mu\text{m}$, where the PCA envelope material is not transparent anymore. Therefore, the intensity of the signal can be related to the temperature of the wall, using the emissivity coefficient of the PCA material.

Wall temperature verification measurements were performed for both burners (N2, O3) operated at full and reduced power. The resulting temperature profiles were averaged, as given in Table 8.3, and displayed with markers in Fig. 8.5. Analyses of the result shows a good fit between the simulated and the measured wall temperature. Although the assumption of a uniform wall temperature, that equals the cold spot temperature, is a strong simplification of reality, it provides a good indication. In practice, convection flow and arc bending, especially in a horizontal position, affect the temperature distribution, and therefore the cold spot temperature.

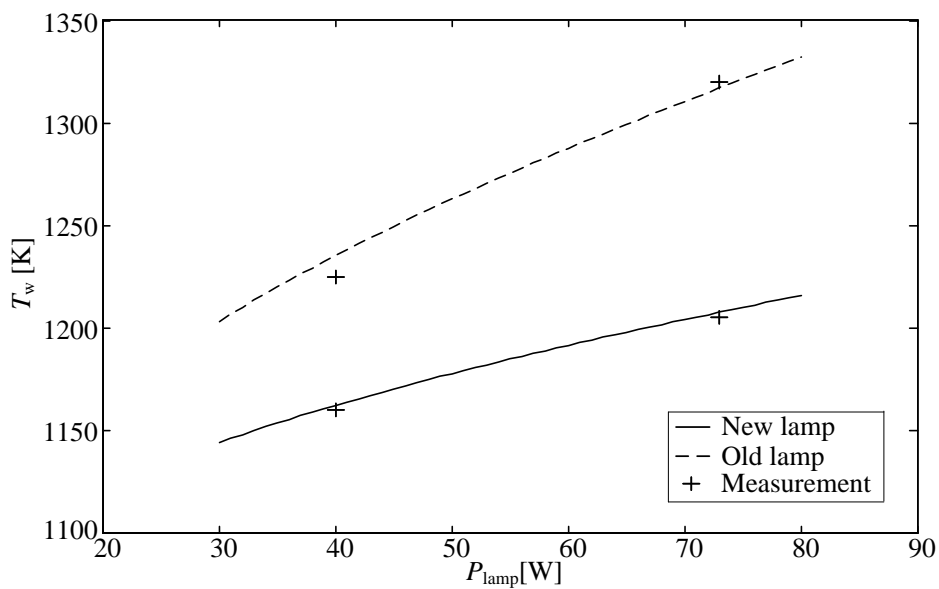


Figure 8.5: Simulated wall temperature as a function of the lamp power for new lamp (N2) and old lamp (O3). Verification measurements are displayed with markers.

8.2.2 Parameter adaptation throughout lamp life

Deviations between the identified parameters and actual process parameters can be expected due to lifetime effects and production spread. Throughout lamp life, reduced arc tube transparency and chemical reactions alter the physical plasma states. In turn, the terminal behaviour and correlated static and dynamic lamp model parameters shift over life. To enable the proposed observer-based HID lamp control principle, accurate prediction of the voltage drop across the gas-discharge is essential.

The state-of-the-art solution comprises an embedded identification procedure for ten parameters that are based on static and dynamic lamp-current excitations. Online identification enhances the accuracy and enables the tracking of the lamp ageing process. However, implementation of this feature requires massive calculation efforts and is, therefore, not feasible for practical cost effective lamp-driver designs. Therefore, a less complicated solution is proposed that comprises a linear adaption of the lamp model parameters between two off-line identified parameter sets. In this case the reduced steady-state parameter set applied in observer model \bar{a}_{model} becomes

$$\bar{a}_{model} = \bar{a}_{new(1-4)} - (\bar{a}_{new(1-4)} - \bar{a}_{old(1-4)})m_{age}, \quad (8.1)$$

where \bar{a}_{new} and \bar{a}_{old} represent lamp parameter sets on both sides of the lifetime spectrum, and $0 \leq m_{age} \leq 1$ is a variable that characterises the lamp condition (ageing factor). In the experimental phase, $\bar{a}_{new} = \bar{a}_{N2}$ and $\bar{a}_{old} = \bar{a}_{O3}$ are applied as denoted in Table 8.2.

Below, the dynamic model parameters D_1 and D_2 represent respectively the plasma and discharge vessel thermal heat capacity, and are adapted to match the dynamics of the selected lamps. The quadratic curve fit for D_1 in (3.25) is modified to approximate the dynamic response over lamp life and equals

$$D_1 = 6.657 (T_w - 96.2m_{age})^2 - 1.597 \cdot 10^4 (T_w - 96.2m_{age}) + 9.623 \cdot 10^6. \quad (8.2)$$

Parameter D_2 is adapted in line with the method applied for the static parameters (8.1) and yields

$$D_2 = 1.569 - (1.569 - 1.308)m_{age}. \quad (8.3)$$

For the proposed method the online identification procedure boils down to fitting just one parameter, m_{age} , and this scalar needs to be identified for the actual lamp terminal conditions.

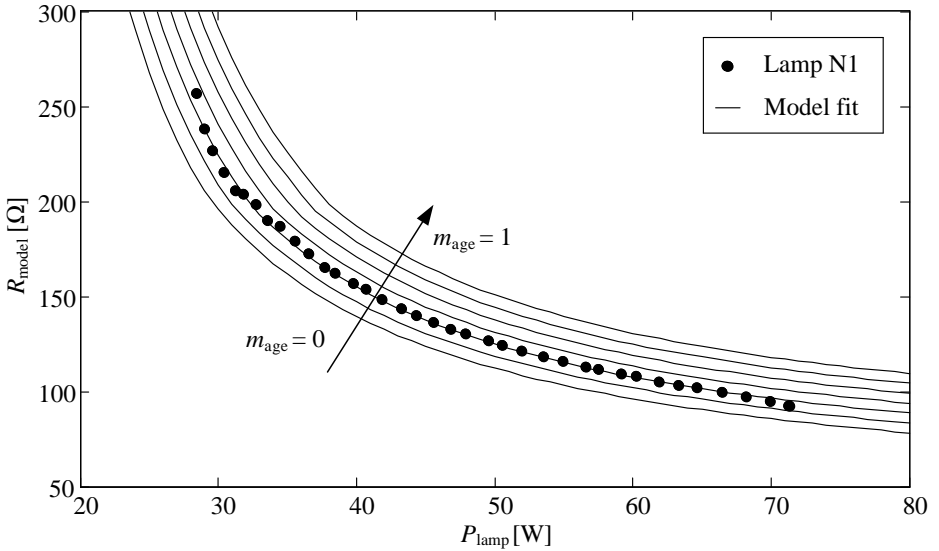
8.2.3 Lamp ageing factor

To enable an accurate HID state observer, the internal plasma model parameters need to be adapted during lamp life to compensate for ageing effects. In the

Table 8.4: Results one parameter identification (m_{age}).

New lamps	m_{age}	MAE [%]	Old lamps	m_{age}	MAE [%]
N1	0.2949	2.01	O1	0.7279	2.69
N2	0	1.29	O2	0.8863	4.66
N3	0.2852	2.69	O3	1	3.04
N4	0.3093	3.55	O4	0.4765	1.31

previous Section 8.2.2, a linear adaption method is described that alters the static and dynamic grey box model parameters.

Figure 8.6: Lamp resistive behaviour versus m_{age} .

To proof this principle, all old and new lamps of the test batch (Table 8.1) are identified. In Table 8.4 the resulting m_{age} parameters are displayed. Lamp N2 ($m_{\text{age}} = 0$) and lamp O3 ($m_{\text{age}} = 1$) correspond to the edges of the ageing spectrum. The ageing factor reduces throughout lamp life according to the lamp degradation. The lamp degradation (wall blackening is accelerated by not only the operation hours, but also by the number of on-off cycles (cq. lamp starts). This explains the relatively larger differences in m_{age} , in particular, for the batch of old lamps. The effect of the ageing factor on the lamp terminal quantities is given in Fig. 8.6. In this graph, simulated resistance curves are displayed corresponding to six m_{age} instances equidistantly distributed between $[0 \rightarrow 1]$. Lamps of the same type as identified can be characterised throughout life. As an example, the measured lamp resistance data points over power for lamp N1

are displayed too. These data points coincide perfectly with one of the simulated resistance lines.

8.3 Optical measurements

In the lamp industry, integrating sphere systems are widely used for measurement of the photometric properties of different lamps. Because the original form was invented by R. Ulbricht at the turn of the 20th century, they are called Ulbricht spheres. An integrating sphere is used to measure the total light output of a lamp independent of the light's spatial distribution. The lamp being tested is placed in the centre of the integrating sphere. At one side of the sphere light sensors are placed, which measure the light output of the lamp. Between the lamp and the light sensors is a baffle to prevent the sensors from seeing any direct light from the lamp. The inside of the sphere (including the baffle) is coated with a white paint that diffuses all wavelengths equally. This allows the researcher to get very accurate measurements. The light bounces around the sphere until it reaches the light sensors.

The applied measurement set-up includes the LMT Colormeter C1200 and Ocean optics HR4000 for respectively photometric and colorimetric characterisation of the light sources. The lamp terminal properties are measured with a Yokogawa PZ4000 power analyser. Finally, software on a PC automates the measurement set-up, including lamp-driver control and data acquisition. For the selected batch of HID lamps denoted in Table 8.1 the luminous flux, correlated colour temperature (CCT), and colour rendering index (CRI) are measured. Analysing these results shows the consequences of reduced power operation regarding new and old ceramic metal-halide lamps [176].

The photometric property luminous flux measures the total spectral power output from a light source, scaled to the visual response of the human eye [38]. The luminous flux of the HID lamps, as depicted in Fig. 8.7, decreases almost linearly with the reduction of power. However, the ratio of reduction in wattage to reduction in light output is not proportional. The light output will be reduced more than the wattage reduction. The group of older lamps shows a lumen maintenance loss mainly due to tungsten deposition on the discharge vessel wall.

The colorimetric property CCT expresses the position of any white light source close to the black body line defined by its colour temperature. Low temperatures (2700 – 3000 K) represent a reddish, “warm” light, high temperatures (5000 K or more) represent a bluish, “cool” light. All tested lamps shift to higher colour temperatures when reducing the power level, as shown in Fig. 8.8. The old HID lamps are less colour-sensitive to power reduction. This can be explained by the higher cold spot temperatures for the aged lamps and related salt composition. The spread on the colour point is larger in the dimmed state.

The CRI defines how well colours are rendered by the measured source of illumination. This index is based on the average of eight standard colour tiles;

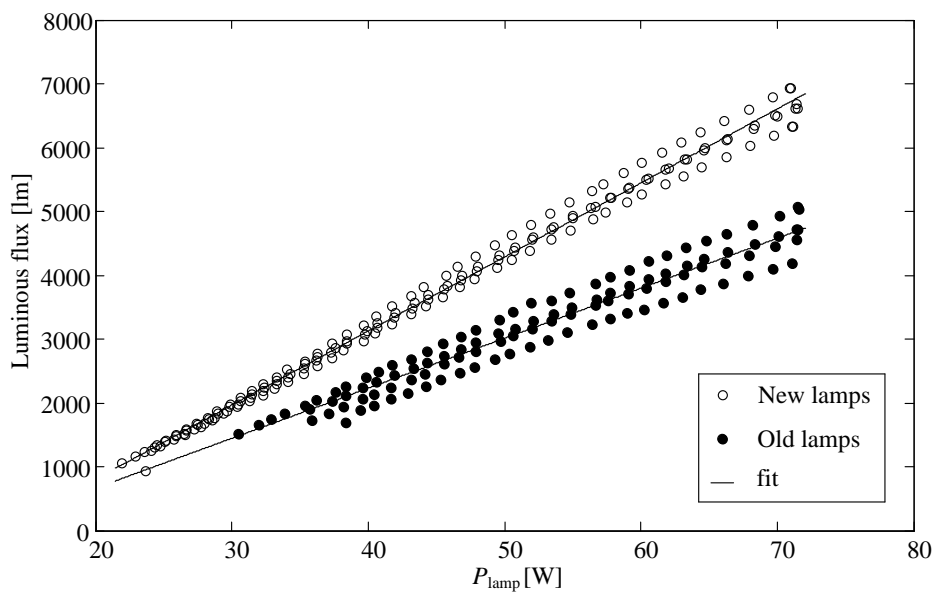


Figure 8.7: Luminous flux for new and old CDM 73W / 830 burners.

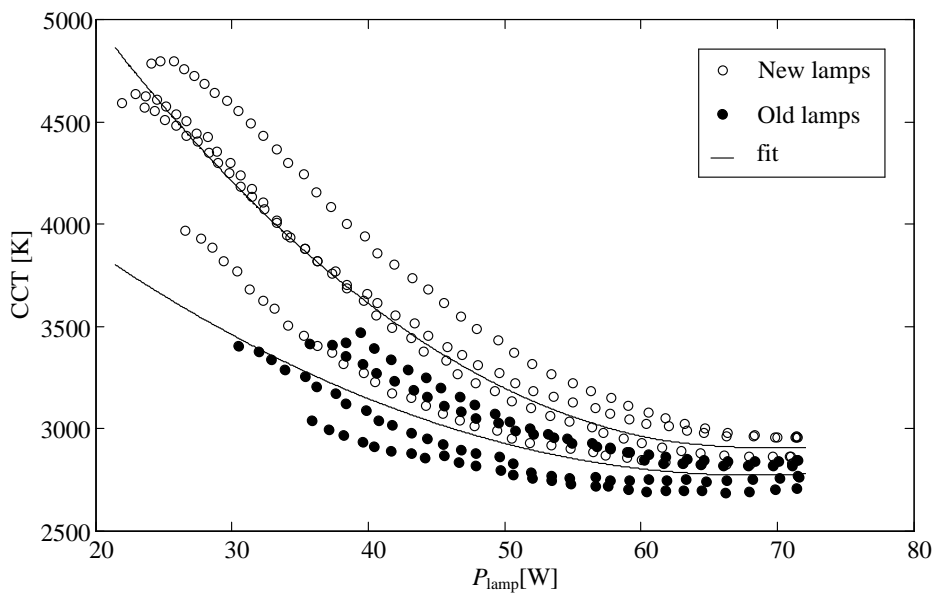


Figure 8.8: CCT for new and old CDM 73 W / 830 burners.

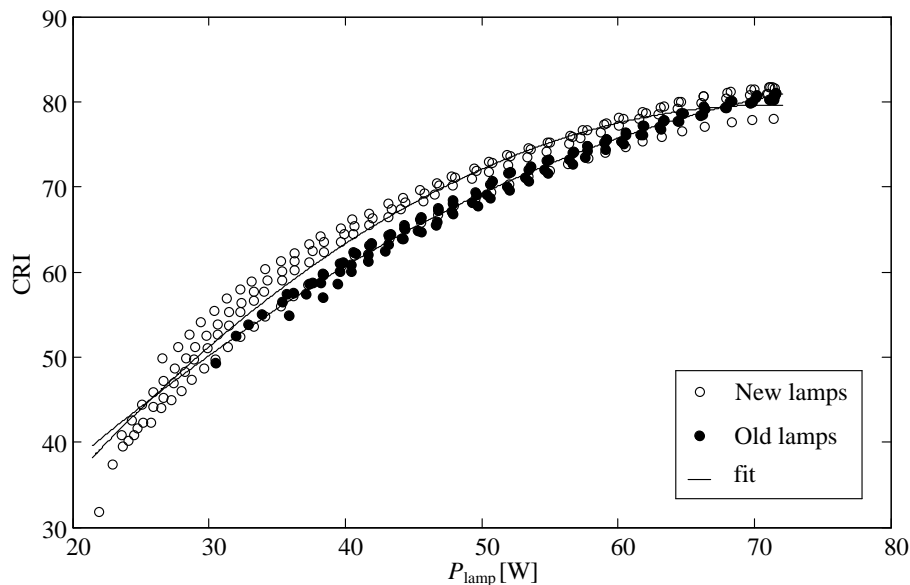


Figure 8.9: CRI for new and old CDM 73 W / 830 burners.

the smaller the difference in perceived colour, the better the colour rendering. The CRI is a dimensionless quantity. The higher the value of CRI, the closer the source approximates white light, with a maximum value of 100. In practice, when reducing the power level all HID lamps in the batch being tested show a decreasing CRI, and the difference between the new and old lamps is small.

Earlier studies [181] have reported the possible consequences of reduced power operation regarding quartz metal-halide lamps and metal-halide lamps in ceramic envelopes. Those explorations have shown that both the decrease in luminous flux and the change in colorimetric properties (CCT, CRI) are considerably less for the ceramic types of lamps. The explanation for this reduced sensitivity for the reduction of the lamp power can be found in the fact that the metal-halide vapour pressures are considerably higher in the ceramic lamps compared to the quartz lamps. Regarding the electrode operation related aspects of dimmed operation, the concerns and limitations for ceramic and quartz metal-halide lamps are similar.

Curve fitting of the measured series of data was used to provide an average prediction of the photometric and colorimetric properties over the applicable lamp power range. For each optical property two polynomial functions are fitted regarding the new and old lamp data series. The resulting parameters are denoted in Table 8.5, and are the coefficients of the following polynomial function

Table 8.5: Optical measurement fitting parameters.

	Luminous flux [lm]		CCT [K]		CRI	
Lamps	N(1-4)	O(1-4)	N(1-4)	O(1-4)	N(1-4)	O(1-4)
c_1	0	0	0.9037	0.4706	-0.01667	-0.01002
c_2	116.0	78.34	-122.9	-64.25	2.378	1.754
c_3	-1517	-906.0	7085	4964	-5.142	6.543

$$y = c_1 P_{in}^2 + c_2 P_{in} + c_3, \quad (8.4)$$

where y represents the optical property of concern (luminous flux, CCT, CRI) in line with the parameters c_{1-3} applied. Although the measured data series shows a large spread, in particular for the photometric CCT, the identified polynomial functions fit the sets of measured data points accurately.

8.4 Electrode sheath voltage

In this section the electrode work function and the related ESV [57, 79] is investigated. Especially for aged lamps or reduced power mode operation, the electrode-induced phenomena play an important role in lamp-driver interaction. These phenomena can cause re-ignition voltage spikes, light intensity fluctuations (flickering), or even cause the lamp to extinguish. The most important aspect of the electrode operation is the tip temperature, because the cathode mode of operation is strongly related to it [57–59]. In Section 6.3 the electrode tip temperature is discussed in more detail. The current transfer at the cathode side, where principally two modes can occur (diffuse mode and spot mode), is much more complicated than on the anode side. During the diffuse mode, a stable arc attachment covers the entire electrode tip or a sizeable fraction thereof. In contrast, the less stable spot mode is characterised by an arc attachment that is constricted to a very small area. Reduced power operation or old electrodes with deformed surfaces can affect the diffuse mode of operation. At the border of designed performance, the cathode tends to switch over from diffuse mode to spot mode, obeying the principle of minimum energy [69]. Spot mode attachment is less favourable to lamp operation because the electrode can become locally overheated, which causes excessive erosion and accelerates arc tube blackening.

In terms of lamp-driver interaction the re-ignition voltage during commutation depends on the voltage drop across the plasma column plus the actual ESV interacting with the ballast. The ESV will be strongly influenced by the actual electrode-operating mode [152]. In general, the re-ignition voltage should be as low as possible. It should never reach the maximum output voltage of the lamp-driver OCV because then the lamp will extinguish. Therefore, in the remainder of this section the ESV is observed during operation to avoid deleterious lamp operation and to improve the lamp-driver system performance over life.

8.4.1 Electrode sheath voltage observation

In this section the ESV is studied as a characteristic property of the electrode behaviour, and for this purpose the proposed HID lamp observer is applied. Practical measurements were performed using the stacked buck converter, as presented in Chapter 5, to test the HID lamps in full and reduced power mode. In the proposed measurement set-up (Fig. 8.10) the converter current set-point and commutation trigger are controlled with dSPACE. The dSPACE input channels capture the time-resolved values of voltage and current on the lamp terminals. Subsequently, signal processing is carried out by means of MATLAB functions.

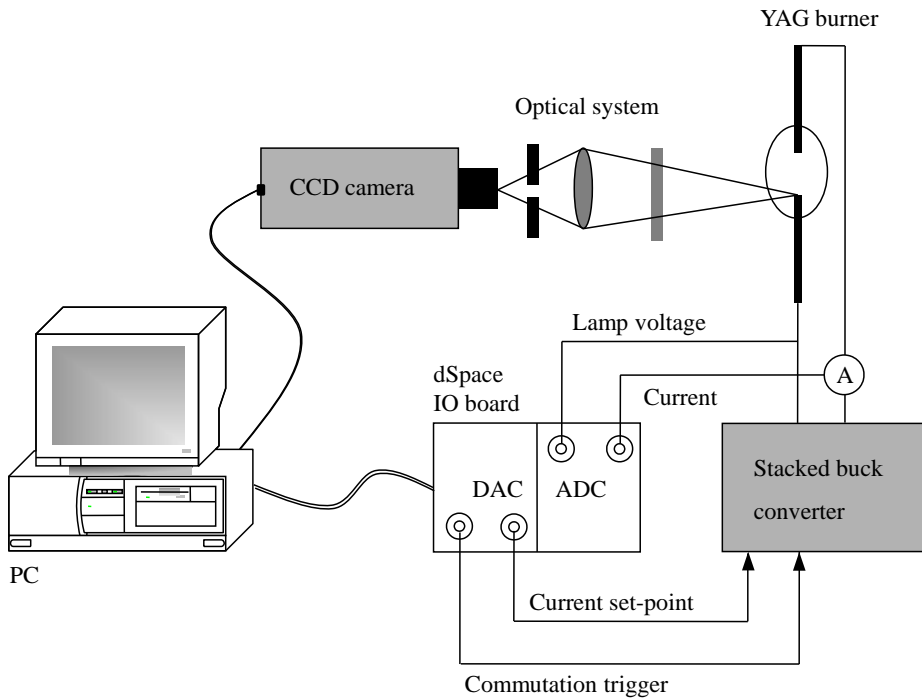


Figure 8.10: Experimental set-up shown as the arrangement for electrical and optical measurements.

All lamps of the test batch (Table 8.1) were operated in this experimental set-up in vertical orientation similar to the position during aging. In this burning position, the individual electrode temperatures can be influenced by both cathophoresis and convection. Most of the time the upper electrode tip temperature exceeds that of the lower electrode because of convection heating of the top electrode and convection cooling of the bottom one. The cathophoresis effect vanishes for LFSW operation above 100 Hz [182]. The first measurement is performed

with burner (N4) operated at the rated power level. The measured lamp voltage and current were processed and the resulting ESV estimation is presented in Fig. 8.11. The sheath voltage shows a smooth behaviour. At the start of each period-half the electrode voltage drop is slightly increased, similar to the findings for sinusoidal 50 Hz current operation [57]. Finally, it can be stated that both the voltage drop across the plasma column and the electrode sheaths undergo distinct changes during a current cycle and strongly depend on the operation conditions.

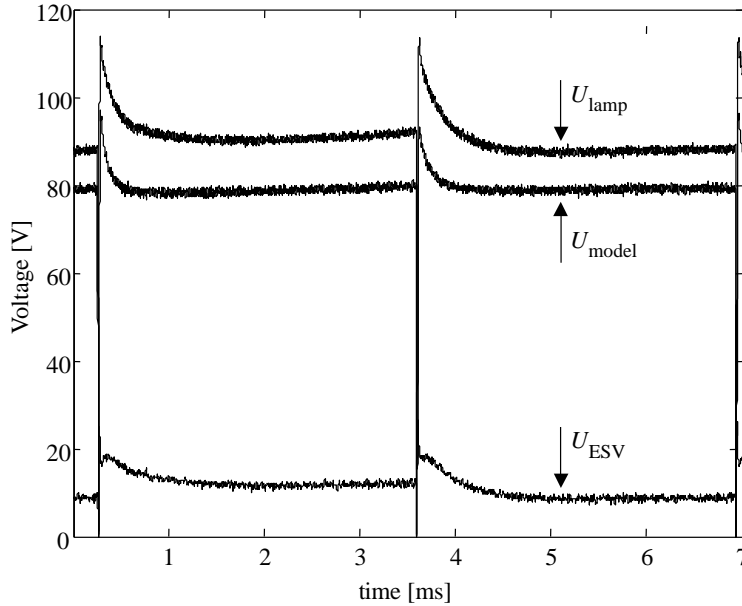


Figure 8.11: Upper trace: terminal lamp voltage [V], middle trace: simulated plasma voltage [V], lower trace: estimated ESV [V] of vertically operated burner (N4) ($P_{\text{lamp}} = 73 \text{ W}$).

Reducing the power level ($P_{\text{lamp}} = 35 \text{ W}$) for the same burner used previously results in a quite different phase-resolved ESV behaviour, which is displayed in Fig. 8.12. The first half period shows a raised electrode voltage drop amplitude and a small re-ignition spike. In this case, the increased cathode-fall voltage strongly contributes to the raised ESV level. In contrast, the second period part has a large re-ignition spike preceded by a folding-back start of a lowered ESV plateau with a minimum directly after the spike. Very low ESV values, especially during the current rise, are ascribed to the anode fall [183] and also observed for sinusoidal 50Hz metal-halide lamp operation [57].

The observed increased sheath voltage results from the reduced power setting,

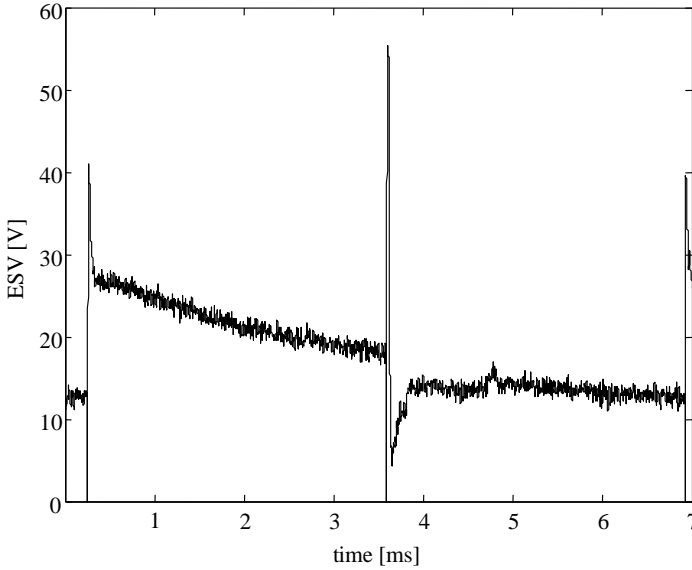


Figure 8.12: Estimated ESV [V] of vertically operated burner (N4) ($P_{\text{lamp}} = 35$ W).

and therefore lower lamp-current. To get insight into the correlation between the electrode sheath voltage and lamp-current, the sheath power is calculated and displayed in Fig. 8.13. Obviously, the average power in the first period-half exceeds the second part by several watts. The difference indicates a change in cathode mode for the successive period parts. This hypothesis is verified with optical observations in Section 8.4.2.

To study the lifetime effects and in particular the electrode performance degradation caused by erosion and deformation, the reduced power mode measurement is repeated with an aged burner (O3). The resulting ESV is plotted in Fig. 8.14. For this aged lamp under reduced power ($P_{\text{lamp}} = 35$ W) large re-ignition spikes in the ESV amplitude are dominant. Those peaks can be ascribed to an increased cathode voltage drop. An insufficient cathode temperature for thermionic electron emission at the start of the cathode phase give rises to glow mode operation with a strong increase in cathode fall voltage. In this case the amplitude and duration of the cathode fall induced re-ignition spike are critical. During this high voltage and low current mode the re-ignition peak amplitude is limited by the OCV level, where the duration gives rise to plasma cooling. Therefore, excessive re-ignition peaks can lead to light flickering and lamp extinguishing. The lamp under test (O3) extinguishes after some time when it is operated at reduced power ($P_{\text{lamp}} = 35$ W). Furthermore, here also the large re-ignition spike precedes a folding-back start for both period parts.

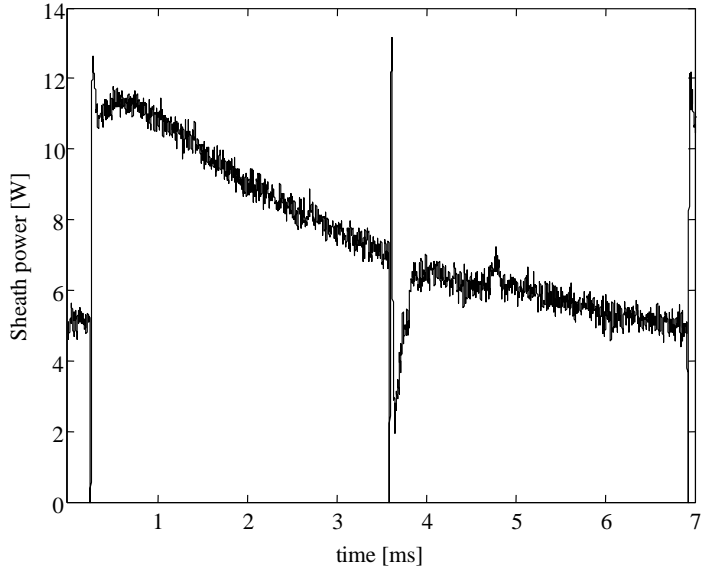


Figure 8.13: Calculated electrode sheath power [W] of vertically operated burner (N4) ($P_{\text{lamp}} = 35$ W).

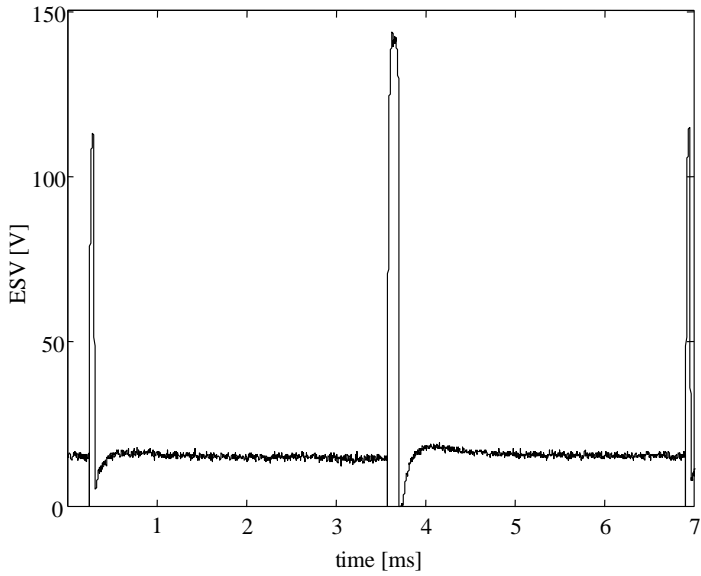


Figure 8.14: Estimated ESV [V] of vertically operated burner (O3) ($P_{\text{lamp}} = 35$ W).

8.4.2 Optical electrode observation

In order to analyse the HID observer state signals, the practical measurement set-up was extended with a CCD camera, as shown in Fig. 8.10. However, the standard polycrystalline alumina discharge wall is optically diffuse (Fig 8.4). Therefore, a ceramic discharge lamp with a transparent discharge wall made of yttrium aluminium garnet (YAG) was applied [184] as shown in Fig. 8.15. This enables the researcher to study the arc attachment and the related electrode operation mode. Apart from its transparent wall, this YAG lamp has otherwise identical properties to the standard CDM 73W/830 burner design in terms of arc tube fill and electrode dimensions.

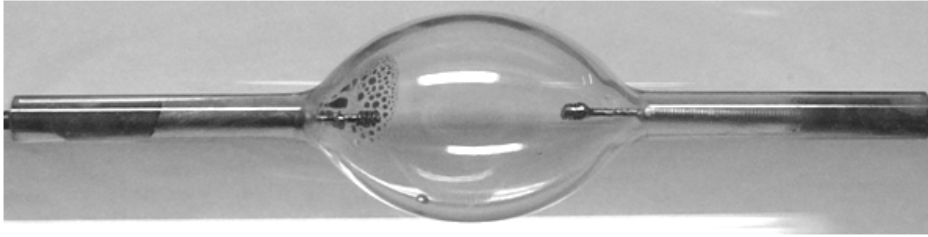


Figure 8.15: Photo of new YAG burner.

The arc attachment was observed with a triggered CCD camera with an exposure time of $960 \mu s$ and a resolution of 1280×1024 pixels. The selected magnification factor leads to a spatial resolution of $2.4 \mu m$. Furthermore, the optical system consist of a diaphragm and a RG630 filter that only passes light of wavelengths greater than about 630 nm. The recorded intensity distribution was transferred to a PC for further processing of the images. The time of registration was determined by an electronic trigger signal and could be placed anywhere in the lamp-current cycle.

In line with previous experiments with HID lamp (N4), the YAG burner was operated in vertical orientation. For about half of the rated power level ($P_{\text{lamp}} = 35 \text{ W}$) both electrodes were optically and electrically observed. Electrode attachment pictures for both electrodes were captured synchronously with the phase resolved ESV estimation. These camera observations of the arc attachment during the cathode phase show diffuse and spot mode operation.

The appearance of the diffuse mode in the cathode phase occurs at the upper electrode as shown in Fig. 8.16 on the left. The arc footprint is spread over the appropriately heated electrode tip surface, in contrast with the lower electrode displayed in the same figure on the right side, where the spot mode is clearly observed. In this case the electrode body has a significantly lower temperature and the arc contracts to a very small region, where the cathode temperature under the attachment point is very high and can reach the melting point of tungsten.

A bright plasma ball covering the attachment region characterises the contracted arc.

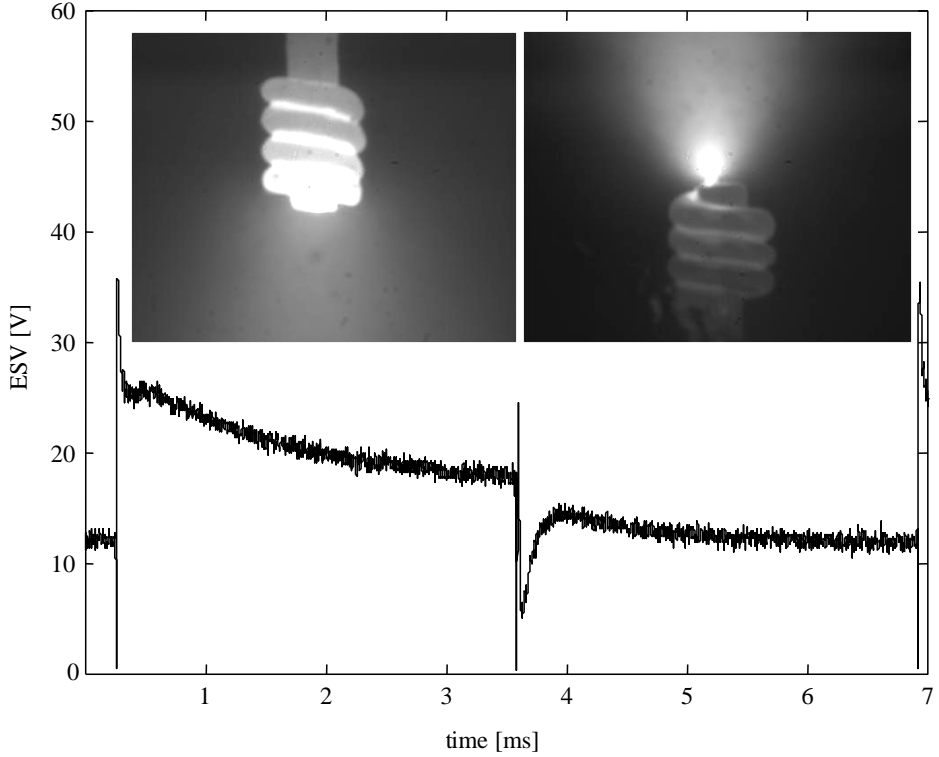


Figure 8.16: Estimated ESV [V] of vertically operated YAG burner ($P_{\text{lamp}} = 35$ W) and related electrode pictures.

The accompanying ESV estimation for the optical measurements with the YAG burner is given in the same Fig. 8.16. In this plot the first period-half corresponds with the diffuse cathode mode of the upper electrode, while the second period part is in phase with a spot cathode mode of the lower electrode. The increased ESV correlates with diffuse mode and the subsequent decrease reflects the formation of the observed spot mode. It becomes clear that the estimated ESV in spot mode is about 10V lower than in diffuse mode, which is in accordance with other experimental findings [57]. From these results it can be stated that the estimated ESV and the sheath power derived signals provide valuable information concerning the electrode mode of operation, in terms of absolute values for minimum sheath power and re-ignition amplitude.

8.5 Observer and control

In this last section the HID lamp state observer is combined with a digital control algorithm to construct an “intelligent” lamp-driver [146]. The control algorithm monitors the estimated lamp state and controls the lamp-current and power with respect to the end-user’s preferences. Furthermore, the lamp status, in terms of an aging factor and an indication of the photometric properties, can be reported back to the end-user interface [29].

Digital controllers facilitate the application of advanced control techniques even in cost critical mass products. The digital controllers that are available nowadays offer the possibility of embedding both the proposed lamp observer and the control loop.

8.5.1 Accurate state observation

In the observer-based control configuration a fixed set of parameters is embedded with the lamp model equations. Some parameters are fixed, while others result from off-line identification. To cope with deviations between the identified parameters and actual process parameters, a linear interpolation of the lamp model parameters between two off-line identified parameter sets is applied (Section 8.2.2). As a result, the online identification procedure boils down to a one parameter fitting procedure, the aging factor m_{age} . In order to enable accurate ESV estimation during life, this parameter m_{age} is iteratively updated with a very low frequency (e.g. after every 100 hour of service) to track the lamp degradation process. The parameter m_{age} is altered in such a way that the following criterion is satisfied

$$U_{\text{plasma}} = U_{\text{lamp}} - \frac{P_{\text{ESV}}}{I_{\text{lamp}}}, \quad (8.5)$$

where U_{plasma} equals the simulated average plasma column voltage and U_{lamp} , I_{lamp} are the averaged measured terminal properties. The sheath power, P_{ESV} , is selected according to the energy balance of HID lamps [39] and equals $P_{\text{ele}} = 7 \text{ W}$ during the steady-state identification (Section 3.2.2).

8.5.2 Lamp controller

The operation of the HID lamp controller has two parts. In the first part, the controller regulates the lamp-current setting, and thereby the lamp power, according to the user preferences and state observations. To guarantee stable lamp operation, an active limitation of the minimum dim level is important. Subsequently, feedback of the actual lamp operation conditions, including lifetime degradation factor m_{age} , is provided.

Operational stability of the HID lamp-driver system is mainly affected by the electrode function. The observed ESV is strongly correlated with the actual elec-

trode function, as discussed in Section 8.4.1. To safeguard stable gas-discharge operation and enable lamp dimming, the ESV properties are monitored continuously. Empirically selected constraints are observed during the re-ignition process. In particular the height and width of the ESV peak at the start of the cathode phase after the lamp-current reversal are a key concern for stable lamp operation. In the experimental phase the following constraints were found: ESV peak = 125 V, ESV width = 50 μs .

If the lamp is operated within these limits while dimming, it will prevent the lamp from flickering and/or extinguishing. These constraints correspond to a minimum power level for stable operation depending on the actual operational conditions and lamp condition (age, electrode degradation, lamp orientation, production spread, etc.). The lamp controller prevents any attempt to lower the lamp power even further.

The second part of the lamp controller enables user interface feedback regarding the actual operation conditions. This feedback is based on the m_{age} parameter that provides valuable information regarding the actual lamp degradation state. Secondly, in line with the method applied to adapt the plasma model parameter sets, the optical function parameters can be adapted

$$\bar{c} = \bar{c}_{\text{new}} - (\bar{c}_{\text{new}} - \bar{c}_{\text{old}})m_{\text{age}}, \quad (8.6)$$

where $\bar{c} = [c_1, c_2, c_3]^T$ can be applied to (8.4). As a result, an indication of the luminous flux, CCT, and CRI are available as functions of actual lamp power P_{lamp} and m_{age} .

8.5.3 Controller operation

To operate the HID observer-based control, the sequence starts with data acquisition of the terminal lamp properties as given in Fig. 8.17. The lamp voltage and current are sampled simultaneously over one complete LFSW period. Subsequently, the HID lamp observer calculates the plasma column voltage and related ESV data arrays for the same period. In the background the sampled lamp voltage and estimated plasma voltage are averaged when operating at constant power. Using this data and (8.5) enables adaptation of the lamp aging factor m_{age} , to cope with lamp spread and deviations over life.

The lamp controller validates the actual ESV vector according to defined limits, and raises the minimum dim level flag if limit values are reached. The power controller regulates the lamp-current set-point, and thereby lamp power in harmony with the requested dim level and minimum dim level flag. If this flag is raised the lamp power is increased by a small step when reducing the lamp power or during operation at minimum power. This process raises the power level and defines the minimum dim level in accordance with the actual lamp operation conditions. In the last step, the actual lamp properties are updated and can be provided to the user in terms of a minimum dim level P_{limit} , life time prediction

m_{age} , luminous flux, and colorimetric properties CCT and CRI. Finally, the cycle starts over again, and the next iteration starts with the data acquisition process.

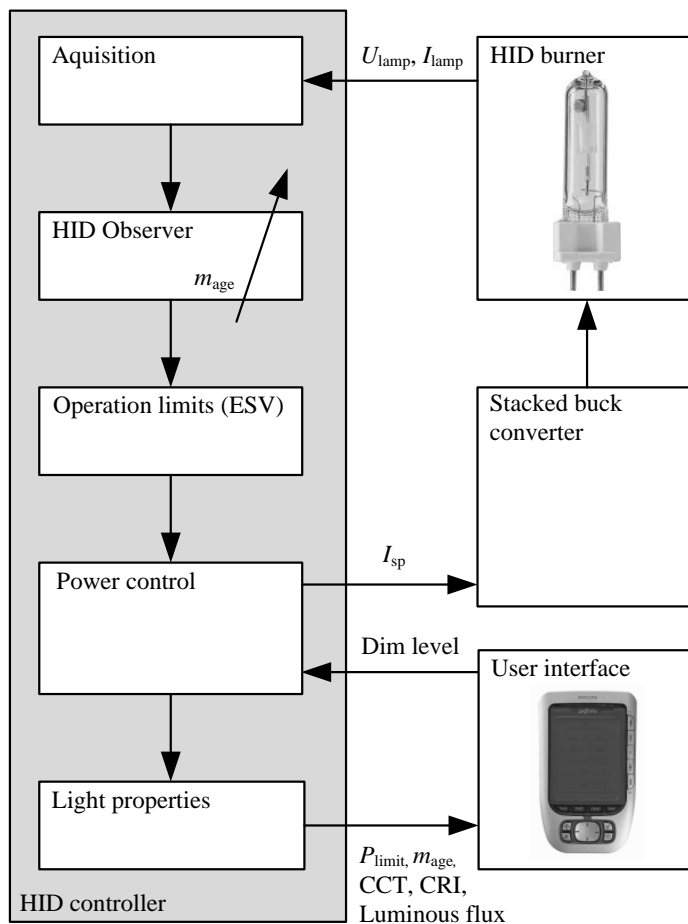


Figure 8.17: Flowchart of the digital lamp power control.

The identified CDM 73W/830 burners (Table 8.1) are operated with the proposed measurement set-up consisting of a stacked buck converter and a dSPACE controller (Fig. 8.10). After ignition, all lamps were operated at rated power for about 10 min. Thereafter, the dim level was set to minimum, and the power stabilised to the minimum dim level P_{limit} . At this power level the optical properties were calculated. The limiting factors are given in terms of ESV-width and ESV-peak in Table 8.6. When the minimum dim level flag is overruled, the power can be lowered but the lamp then extinguishes at P_{off} . This experiment is a proof

Table 8.6: Observer-based dimming.

Lamp	P_{off} [W]	P_{limit} [W]	ESV width	ESV peak	Flux [lm]	CCT [K]	CRI
N1	26.57	31.34	✓		2118	4121	53.0
N2	21.97	26.66	✓		1575	4451	46.4
N3	23.58	27.48	✓		1670	4390	47.6
N4	24.07	34.10	✓		2438	3945	56.5
O1	35.70	41.92		✓	2378	3097	62.2
O2	35.85	44.14		✓	2552	3045	64.1
O3	30.50	39.83		✓	2214	3151	60.1
O4	38.35	41.67		✓	2358	3104	61.9

of the principles behind the observer-based HID lamp controller. Independent of ageing all lamps can be dimmed between rated power and a minimum dim level defined by the lamp controller.

8.6 Discussion

HID lamp dimming provides a significant opportunity to reduce energy consumption and adapt light-levels according to user requirements. Important issues when operating ceramic metal-halide lamps at reduced power are the photometric properties and electrode related operation stability. These states cannot easily be measured due to economic and physical constraints, and are not available for control strategies. Therefore, an observer-based control approach is proposed.

The HID lamp observer estimates physical lamp state signals closely associated with the electrode operation conditions and arc discharge physics. Based on these state signals the lamp controller regulates the lamp power according to user preferences, and limits the minimum dim level to guarantee stable operation. Secondly, the actual photometric properties and lifetime degradation factor are available for the user-interface.

A reduced on-line identification procedure is implemented to enable an accurate HID state estimation, robust with respect to lamp ageing and spread. The process parameters result from a linear interpolation between two off-line identified parameter sets, according to the identified lamp aging factor. Finally, practical measurements prove that the proposed HID lamp control principle enhances the lamp-driver system performance.

Chapter 9

Conclusions

Highly-efficient HID lighting systems are important in the transition towards energy efficient lighting. The application of electronic gas-discharge operation offers additional degrees of freedom to optimise the lamp-driver interaction and system performance. In this thesis highly-efficient lamp-drivers, lamp models and control algorithms have been designed and verified. The major contributions of this thesis are summarised in Section 9.2. They have resulted in a number of patents that have contributed to innovative technology.

9.1 Concluding remarks

9.1.1 Highly-efficient electronic lamp-drivers

The technical revolution in gas-discharge lamps has resulted in the highly-efficient lamps currently available. The introduction of metal-halide additives to the discharge fill and ceramic discharge vessels are milestones in the development of compact HID lamps. These technological steps have resulted in improved efficacy and colour rendering ability throughout lamp life, and opened the door for the use of these lamps in critical indoor and outdoor applications. For these applications electronic lamp operation is the optimal method as it allows for high-efficiency, advanced control, and continuous dimming. To operate the large variety of HID lamps in the market, low frequency square-wave (LFSW) current is the best option as it has the smallest risk of malfunctions.

The proposed topological approach for an electronic lamp-driver consists of a power factor corrector (PFC) stage and a stacked buck converter. The PFC conditions the input-current drawn from the mains grid to meet the power utility standards. On the output side the dc bus voltage is regulated to achieve both sufficient open circuit voltage (OCV) during the start phase and optimal efficiency at steady-state. To implement the PFC functionality two non-isolated boost converters are discussed. Both are operated in transition mode to reduce the

switching losses. The standard boost converter is perfectly suited for high mains applications (230 V), while the voltage doubler boosts the system efficiency at low mains grids (110 V). In the proposed voltage doubler topology the diode bridge is omitted in order to minimise the conduction losses, and the control section features a floating control solution that reduces the component count.

To enable highly-efficient lamp-drivers two zero voltage switching (ZVS) stacked buck converter variants have been designed. To overcome the reverse recovery losses that are common in ZVS stacked buck converters, the MOSFETs slow internal body-diodes are disabled. The first variant is comprised of two independent buck converter sections (dual branch topology) with fast free-wheeling diodes and separate inductors. The second configuration is operated in synchronous switching mode, where the MOSFET channel replaces the body-diode function. The stacked buck converter features a cycle-by-cycle control based on a fixed T_{on} time. This results in a parabolic relationship between lamp power and lamp voltage, which matches the discharge requirements during the different lamp phases. The MOSFET control logic synchronises the cycle-by-cycle switching with the low-frequency commutation process, ensuring permanent ZVS. The ignition circuitry is synchronised with the LFSW period to optimise the starting process.

The resulting two-stage lamp-driver demonstrates controllability, high efficiency and high power density suitable for power sandwich packaging. Practical efficiency measurements with the proposed two-stage lamp-driver prototypes have shown an overall efficiency of 92.5 %.

9.1.2 Lamp modelling

To study the metal-halide lamp characteristics two HID lamp models have been developed. The first model describes the HID lamp's small-signal electrical behaviour, and it is intended to be used for studying the lamp-driver interaction stability.

Secondly, a metal-halide HID lamp model has been developed. This model is based on physical equations for the arc column and electrode regions and is intended to be used for lamp-driver simulations and observer-based control applications. The gas-discharge behaviour is based on the energy conservation principles, and it uses a two temperature profile approximations with a homogeneous plasma and wall temperature distribution. The unknown parameters of the grey box model have been identified using static and dynamic identification methods. The voltage drop across the thin sheet in front of the electrode tip is modelled using a one dimensional approach that includes the diffuse and spot arc attachment mode. Verification measurements have shown that the lamp terminal characteristics are present over a wide power and frequency range.

9.1.3 Lamp-driver interaction control

Active measures have been investigated that aim to stabilise the lamp-driver interaction, optimise the light performance, and enable stable HID lamp dimming. Three control principles have been explored and experimentally verified.

The main concern in driver design is optimising lamp-driver interaction (LDI) to ensure failure free operation and to obtain optimal light performance throughout the rated lifetime of the burner. The first principle involves a fuzzy-logic controller to stabilise the LDI and optimise the commutation process. A feedback loop to achieve over-critical LDI damping, and a lamp-current pulse ahead of the commutation event to pre-heat the cathode to stabilise the re-ignition process are adapted by heuristic rules. Experimental measurements with different LDI combinations, operated at full and reduced power, have shown the ability of active LDI control to extend the range of stable operation.

Secondly, the application of ultra high performance (UHP) HID lamps in projection systems sets new and stringent requirements on the quality of the light generated by these lamps. This is especially important in projection systems where light modulation is applied in synchronisation with the colour sequence. Deviations of the light modulation of the lamp may lead to artefacts in the projected image. These systems are subject to periodic disturbances synchronous with the LFSW commutation period. Iterative learning control (ILC) has been explored to compensate for the repetitive disturbances. As a result of ILC, the actual lamp-current converges to the required lamp-current profile and its strongly related emitted luminous flux, even in the face of the inevitable changes in the lamp dynamics over time. The robustness of ILC against these changes has been improved by using a multi-model pseudo random noise sequence (PRNS) identification method for the ILC design. The excellent performance of the lamp-driver with ILC is demonstrated experimentally.

Thirdly, HID lamp dimming provides a significant opportunity to reduce energy consumption and adapt light-levels according to user requirements. Important issues that arise when operating ceramic metal-halide lamps at reduced power are the photometric properties and electrode-related operation stability. An “intelligent” electronic lamp-driver is proposed that monitors the HID burner operation conditions and enables stable lamp dimming. This control principle is based on an HID lamp observer that derives physical lamp state signals that are closely associated with the electrode operation conditions and arc discharge physics. A reduced on-line identification procedure is implemented to enable an accurate HID state estimation, robust with respect to lamp ageing and spread. Finally, practical measurements prove that the proposed HID lamp control techniques enhance the lamp-driver system performance.

9.2 Thesis contributions

- *HID lamp models.* To study the metal-halide lamp characteristic, two HID lamp models have been developed. The first model describes the lamp's small-signal electrical behaviour. Secondly, a metal-halide lamp model has been developed based on physics equations for the arc column and electrode regions. The model is implemented in MATLAB, and the unknown parameters of the grey box model have been identified using static and dynamic identification methods.
- *Highly-efficient electronic HID lamp-drivers.* To enable highly-efficient electronic HID lamp operation, two-stage LFSW converters have been explored. These drivers consist of a boost converter PFC stage and a stacked buck converter. The proposed voltage doubler PFC topology features reduce switching and conduction losses and reduce component count [19]. The dc bus voltage is controlled to optimise both the LDI and the system efficiency [17].

Two highly-efficient ZVS stacked buck converter topologies have been designed: The dual branch [14] and the synchronous stacked buck converter [15]. Their cycle-by-cycle control is based on a fixed T_{on} time [18] with a synchronised commutation process.

- *Lamp-driver interaction control algorithms.* Three LDI control algorithms have been investigated. The first of which is a fuzzy-logic controller, which has been designed to stabilise the LDI [23] and optimise the commutation process [24]. Secondly, to meet the light requirements in UHP projection systems, the ILC has been explored [27]. A multi-model PRNS identification method for the ILC design is used [28]. Thirdly, an HID lamp observer-based control [30] has been investigated. The controller monitors the HID burner operation conditions and enables stable lamp dimming [31].

9.3 Recommendations

The transition to energy efficient lighting technologies invites further research on electronic operation and control of gas-discharge lamps. In line with the contributions of this thesis, the following recommendations for future developments can be given.

The HID lamp models that have been developed for lamp-driver interaction optimisation are focussed on the run-up and steady-state HID lamp operation phases. Other interesting fields of investigation related to lamp modelling are the electrode heating phase and the EOL phase. While the electrode heating phase is strongly related to lamp maintenance, the EOL phase is mainly associated with driver robustness and system specifications.

The principles of a highly-efficient stacked buck converter have been described. In particular, the control circuitry implementation and the ignition method can

be subject of further investigation. These modifications affect both the electronic concept and the lamp-driver's interaction performance.

A fuzzy-logic control principle has been presented and implemented in an electronic HID lamp-driver. This control method enhances the system stability and commutation process, and enables stable operation for a wide range of commercially available HID lamps. Most of these HID lamps are designed for universal operation on both conventional electro-magnetic and electronic lamp-drivers. Therefore, an interesting research area is dedicated to systems consisting of an electronic driver perfectly matched to an HID lamp that is especially designed for electronically controlled operation.

Iterative learning control has been investigated to meet the stringent requirements on the quality of the light generated by UHP lamps in projection systems. The on-going rapid progress in these systems requires new and more complicated light patterns and an extension of the lamp-current control range. Further investigation of the ILC approach will enable more flexibility and more complicated light patterns, while preserving the high current control accuracy that has been presented.

An observer-based control approach has been proposed for HID lamp-driver systems applications. This method enables the observation of photometric properties and electrode stability during operation. Continuing the research on this topic and performing statistical system tests with large lighting systems (e.g. street lighting) would enhance the predictability and reliability of new HID systems.

Appendix A

Simulink figures

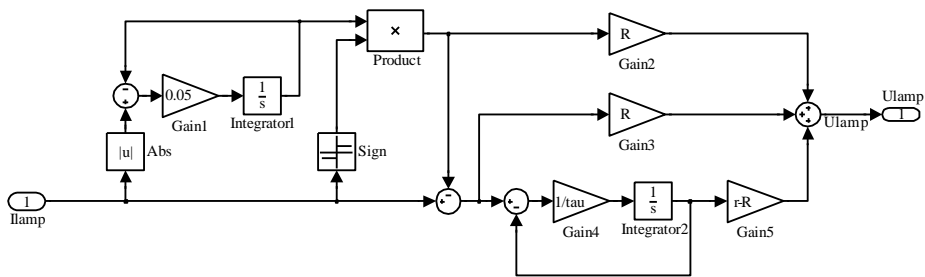


Figure A.1: HID lamp model Simulink block (Input is lamp-current I_{lamp} ; Output is lamp voltage U_{lamp}).

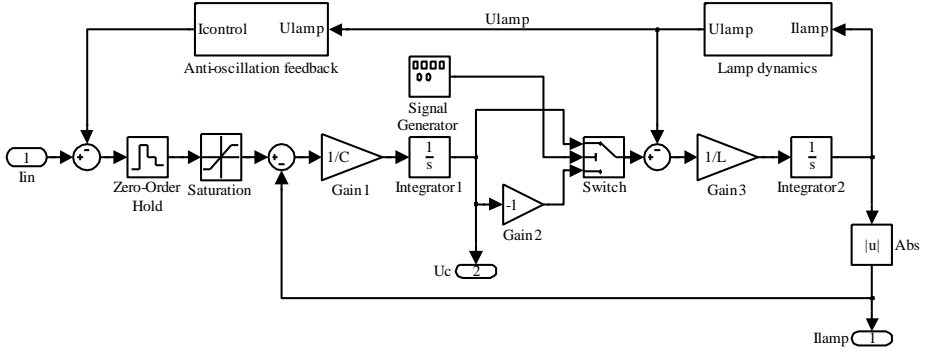


Figure A.2: Simulink lamp-driver model plus voltage feedback loop (I_{in} is the lamp-current set-point; I_{lamp} is the rectified lamp-current; U_c is the buck converter output voltage).

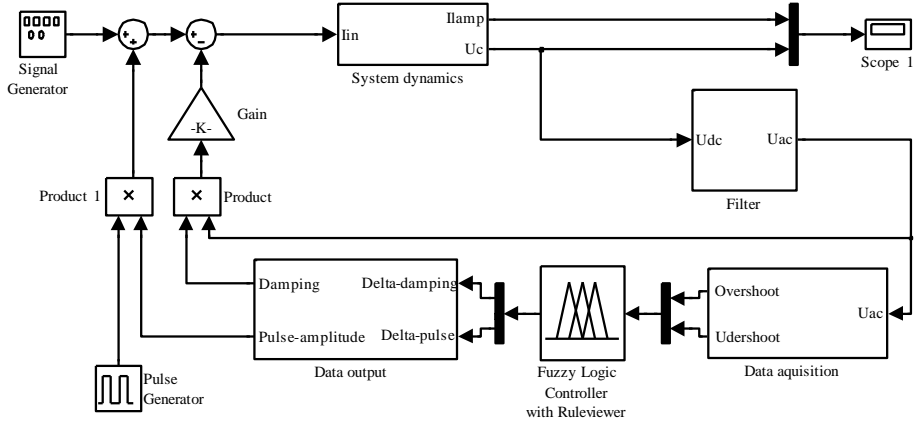


Figure A.3: Simulink model of lamp-ballast system and fuzzy-logic controller.

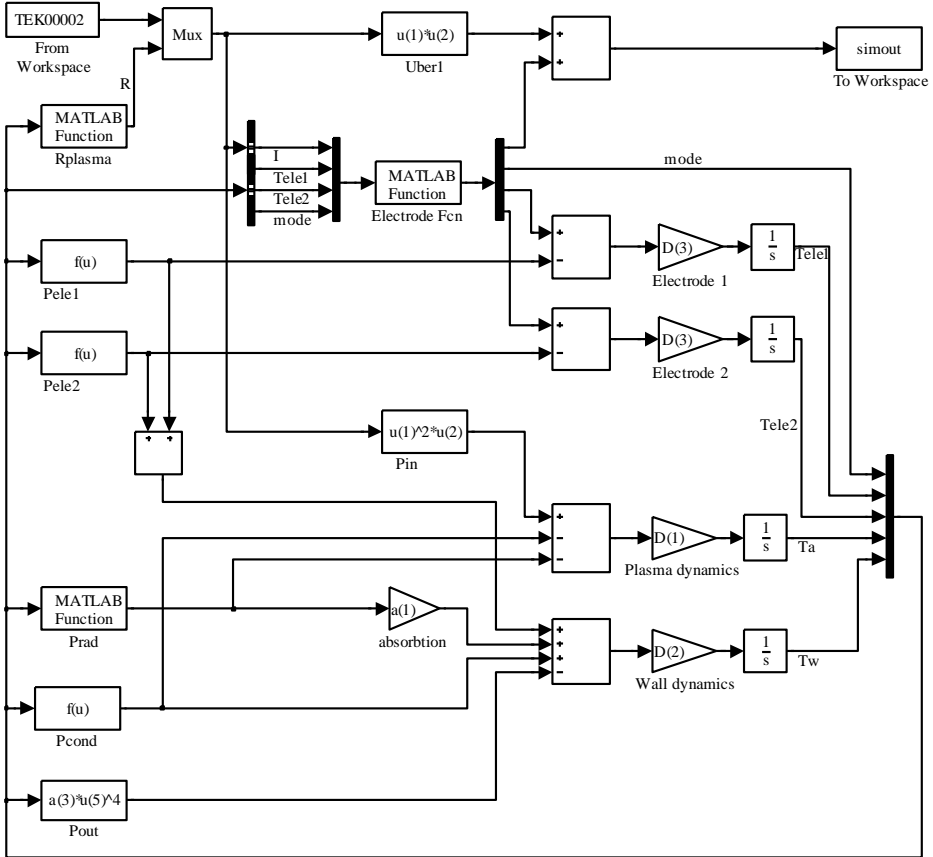


Figure A.4: Simulink implementation of proposed HID lamp model.

Bibliography

- [1] R. Friedel, P. Israel, and B. S. Finn. *Edison's Electric Light*. Number ISBN 0813511186. Rutgers University Press, United States, 1986.
- [2] R. W. Home. Francis Hauksbees theory of electricity. *Arch. Hist. Exact Sci.*, (4):203, 1967.
- [3] M. F. Gendre. Two centuries of electric light source innovations. http://www.einlightred.tue.nl/lightsources/history/light_history.pdf, 2005.
- [4] Climate change 2007 synthesis report. Fourth assessment report, IPCC, Geneva, Switzerland, November 2007.
- [5] Annual energy outlook. Report DOE/EIA-0383, EIA, March 2009.
- [6] Light's labour's lost; policies for energy-efficient lighting. Technical report, The International Energy Agency (IEA), 2006.
- [7] C. Mayhew and R. Simmon. Image of Earths city lights, NASA GSFC. <http://earthobservatory.nasa.gov>, 1994.
- [8] P. Cinzano, F. Falchi, and C. D. Elvidge. The first World Atlas of the artificial night sky brightness. *Mon. Not. R. Astron. Soc.*, (328):689–707, 2001.
- [9] S. A. Mucklejohn and B. Preston. Developments in low wattage high intensity discharge lamps. In *Proc. 35th IEEE IAS conf.*, volume 5, pages 3326–3329, 2000.
- [10] D. H. J. van Casteren, M. A. M. Hendrix, and J. L. Duarte. Transition mode stacked buck converter for HID lamps. *IEEE Transactions on Industry Applications*, 44(1):68–73, 2008.
- [11] D. H. J. van Casteren and M. A. M. Hendrix. Stacked buck converter for HID lamps. In *Proc. 39th IEEE IAS conf.*, volume 1, pages 693–697, 2004.

- [12] I. Josifović, J. Popović-Gerber, B. Ferreira, and D. H. J. van Casteren. Multilayer SMT high power density packaging of electronic ballasts for HID lamps. In *Proc. 2th IEEE ECCE conf.*, pages 1275–1282, 2010.
- [13] I. Josifović, J. Popović-Gerber, B. Ferreira, and D. H. J. van Casteren. Multilayer SMT high power density packaging of electronic ballasts for HID lamps. *IEEE Transactions on Industry Applications*, (Accepted for publication in 2012).
- [14] D. H. J. van Casteren. Drive circuit of high-intensity discharge lamp, has arrangement comprising mosfet coupled between input terminal and node to which diode is connected, designed to allow voltage over MOSFET to return to zero before MOSFET is closed. WO Patent 2004066688-A1, 2004.
- [15] D. H. J. van Casteren. Gas-discharge lamp-driver, has control unit to generate control signals at low commutation intervals and in high frequency operational phases such that two switches are switched simultaneously in counter-phase. WO Patent 2004010742-A2, 2004.
- [16] O. J. Deurloo, D. H. J. van Casteren, and M. Krijzer. Switch mode power supply for igniting and operating a high-pressure gas-discharge lamp, comprises ignition sub-circuit with ignition capacitor and switching element having control electrode connected to commutator of lamp circuit. WO Patent 2003009648-A1, 2003.
- [17] D. H. J. van Casteren and W. D. Couwenberg. Ballast circuit for discharge lamp, has state control circuit to change level of output voltage of dc-dc converter from higher level associated with lamp starting to lower level associated with stationary operation of lamp. WO Patent 2003075619-A1, 2003.
- [18] D. H. J. van Casteren. Operating device for high-pressure discharge lamp, has controller that regulates on and off condition of switching circuit to control power or current supplied to high-pressure discharge lamp. WO Patent 2003061352-A1, 2003.
- [19] D. H. J. van Casteren. Boost converter used with input stage of full electronic ballast to transform ac mains voltage, for discharge lamp, has RF interference filter connected between ac mains terminals and series connection of boost inductor and switch MOSFETs. WO Patent 2005107054-A1, 2005.
- [20] D. H. J. van Casteren, M. A. M. Hendrix, and J. L. Duarte. Physics based MATLAB model for ceramic metal halide lamps. In *Proc. 41th IEEE IAS conf.*, volume 3, pages 1391–1396, 2006.

- [21] D. H. J. van Casteren, M. A. M. Hendrix, and J. L. Duarte. Controlled HID lamp-ballast interaction for low frequency square-wave drivers. *IEEE Transactions on Power Electronics*, 22(3):780–788, 2007.
- [22] D. H. J. van Casteren and M. A. M. Hendrix. Improved current control for HID lamp drivers. In *Proc. 40th IEEE IAS conf.*, volume 2, pages 1182–1187, 2005.
- [23] T. Oosterbaan, D. H. J. van Casteren, and R. H. A. M. van Zundert. Drive circuit for high pressure discharge lamp for projector, adjusts reference signal for controlling direct current, based on amplitude of periodical voltage across output capacitor caused by commutation of direct current. WO Patent 2004045255-A2, 2004.
- [24] F. Peeters and D. H. J. van Casteren. Lamp-driver circuit arrangement for operating e.g. high intensity discharge lamp, has control circuit with adaptive feedback controller for adjusting control loops based on variations of actual system behavior. WO Patent 2006056918-A1, 2006.
- [25] D. H. J. van Casteren and R. L. Tousain. Digital control for improved UHP lamp performance. In *Proc. 11th Int. Symp. Sci. Tech. Light Sources*, volume 1, pages 291–292, 2007.
- [26] R. L. Tousain and D. H. J. van Casteren. Iterative learning control in a mass product: Light on demand in DLP projection systems. In *Proc. American control conf.*, volume 1, pages 5478–5483, 2007.
- [27] D. H. J. van Casteren and R. L. Tousain. Lamp-driver for use in projection system, has setpoint signal generator with correctional setpoint signal generator for setpoint signal, and synchronizer for synchronizing generator to principal setpoint signal. WO Patent 2006046199-A1, 2006.
- [28] R. L. Tousain and D. H. J. van Casteren. Driver for driving gas-discharge lamp e.g. metal-halide lamp, has controller for comparing measured characteristic response of lamp with preset reference signal stored in memory. WO Patent 2008093259-A1, 2008.
- [29] D. H. J. van Casteren, M. A. M. Hendrix, and J. L. Duarte. Observer-based ceramic HID lamp control. In *Proc. 43th IEEE IAS conf.*, volume 1, pages 1–8, 2008.
- [30] D. H. J. van Casteren. Operating method for gas-discharge lamp, involves controlling operating current of gas-discharge lamp based on determined operating state of gas-discharge lamp. WO Patent 2008072158-A2, 2008.
- [31] D. H. J. van Casteren and O. J. Deurloo. High pressure discharge lamp circuit with successive current phases for operating the lamp in a dimmed state. WO Patent 2002019779-A1, 2002.

- [32] A. Hagenbach. *Handbuch der Physik*, chapter Der elektrische Lichtbogen, pages 324–353. Springer, Berlin, 1927.
- [33] J. F. Waymouth. *Electric discharge lamps*. The M.I.T. Press, United States, 1971.
- [34] J. J. de Groot and J. A. J. M. van Vliet. *The high-pressure sodium lamp*. Kluwer, The Netherlands, 1986.
- [35] P. A. Seinen. High intensity discharge lamps with ceramic envelopes. In *Proc. 7th Int. Symp. Sci. Tech. Light Sources*, pages 101–109, 1995.
- [36] J. F. Waymouth. LTE and near-LTE lighting plasmas. *IEEE Trans. Ind. App.*, 19(6):1003–1012, 1991.
- [37] W. Elebaas. *The high pressure mercury vapour discharge*. North Holland Publishing Company, The Netherlands, 1951.
- [38] M. S. Rea, editor. *IES lighting handbook*. Illuminating Engineering Society of North America, United States, New York, 9 edition, 2000.
- [39] A. G. Jack and M. Koedam. Energy balances for some high pressure gas-discharge lamps. *J. Illum. Eng. Soc.*, 3:323–329, 1974.
- [40] K. Charrada, G. Zissis, and M. Stambouli. A study of the convective flow as a function of external parameters in high-pressure mercury lamps. *J. Phys. D: Appl.*, 29:753–760, 1996.
- [41] E. Fischer. Axial segregation of additives in mercury metal halide arcs. *J. Phys. D: Appl.*, 47:2954–2960, 1976.
- [42] R. J. Zollweg. Arc instability in mercury and metal halide arc lamps. *J. Illum. Eng. Soc.*, pages 90–94, 1979.
- [43] P. C. Drop and W. J. van den Hoek. Characterization of diffuse and constricted high pressure arcs by magnetic balancing. *J. Light. Res. Tech.*, 12:83–87, 1980.
- [44] A. J. Flikweert. *Spectroscopy on Metal-Halide Lamps under Varying Gravity Conditions*. PhD thesis, Eindhoven University of Technology, Den Dolech 2, Eindhoven, 2008.
- [45] G. Kroesen, M. Haverlag, E. Dekkers, J. Moere, R. de Kluijver, P. Brinkgreve, C. Groothuis, J. van der Mullen, W. Stoffels, R. Keijser, M. Bax, D. van den Akker, G. Schiffelers, P. Kemps, F. van den Hout, and A. Kuipers. ARGES: radial segregation and helical instabilities in metal halide lamps studied under microgravity conditions in the International Space Station. *J. Microgravity Sci. Tec.*, 16:191–195, 2008.

- [46] F. S. Scholtz. Characterisation of acoustic resonance in discharge lamps. *J. Illum. Eng. Soc.*, pages 713–717, 1970.
- [47] J. Hirsch, B. Baumann, M. Wolff, S. Bhosle, and R. V. Barrientos. Acoustic resonances in HID lamps: model and measurements. *J. Phys. D: Appl.*, 43(23):234002, 2010.
- [48] W. Yan and S. Y. R. Hui. Experimental study on acoustic resonance phenomena in ageing high-intensity discharge lamps. In *Proc. IEEE Sci. Meas. Tech. conf.*, volume 153, pages 181–187, 2006.
- [49] W. Yan, Y. K. E. Ho, and S. Y. R. Hui. Stability study and control methods for small-wattage high-intensity-discharge (HID) lamps. *IEEE Trans. Ind. Appl.*, 37(5):1522–1530, 2001.
- [50] S. Hollow, J. Szanto, and B. Nyiri. *Ignition phenomena in the electrode region of HID lamps studied by high speed camera*, volume 4, pages 272–280. Pennington, 1988.
- [51] M. W. Fellows. A study of the high intensity discharge lamp-electronic ballast interface. In *Proc. 38th IEEE IAS conf.*, volume 2, pages 1043–1048, 2003.
- [52] G. A. Trestman. Minimizing cost of HID lamp electronic ballast. In *Proc. 28th IEEE IECON conf.*, volume 2, pages 1214–1218, 2002.
- [53] E. E. Hammer and T. K. McGowan. Characterization of F40 fluorescent systems at 60Hz and high frequency. *IEEE Trans. Ind. Appl.*, IA-21(1):11–16, 1985.
- [54] J. M. Davenport and R. J. Petti. Acoustic resonance phenomena in low wattage metal halide lamps. *J. Illum. Eng. Soc.*, pages 633–642, 1985.
- [55] J. M. Denneman. Acoustic resonances in high frequency operated low wattage metal halide lamp. *Philips J. Res.*, 38:263–272, 1983.
- [56] L. Laskai, P. Enjeti, and I. J. Pitel. A unity power factor electronic ballast for metal halide lamps. In *Proc. 9th IEEE APEC conf.*, volume 1, pages 31–37, 1994.
- [57] H. Purch, H. Schoepp, M. Kettlitz, and H. Hess. Arc attachments and fall voltage on the cathode of an ac high-pressure mercury discharge. *J. Phys. D: Appl. Phys.*, 35:1757–1760, 2002.
- [58] P. Tielemans and F. Oostvogels. Electrode temperature in high pressure gas-discharge lamps. *Philips J. Res.*, 38:214–223, 1983.
- [59] G. M. J. F. Luijks, S. Nijdam, and H. van Esveld. Electrode diagnostics and modeling for ceramic metal halide lamps. *J. Phys. D: Appl.*, 38:3163–3169, 2005.

- [60] A. Lamouri, A. Naruka, J. Sulcs, C. V. Varanasi, and T. R. Brumleve. Influence of electrode, buffer gas and control gear on metal halide lamp performance. *J. Phys. D: Appl.*, 38:3028–3032, 2005.
- [61] L. Cifuentes. High pressure discharge lamps: approaches to modeling. *J. Light. Res. Techn.*, 23(4):161–165, 1991.
- [62] P. H. Herrick. Mathematical models for high-intensity discharge lamps. *IEEE Tran. Ind. Appl.*, IA-16(5):648–654, 1980.
- [63] W. D. Partlow and R. J. Spreadbury. Metal halide lamp load modeling for computer ballast simulations. *J. Illum. Eng. Soc.*, pages 70–77, 1983.
- [64] J. J. Lowke and R. J. Zollweg. Theoretical prediction of ac characteristics of mercury arc lamps. *J. Illum. Eng. Soc.*, pages 253–259, 1975.
- [65] J. F. Waymouth. An elementary arc model of the high pressure sodium lamp. *J. Illum. Eng. Soc.*, 4:131–139, 1977.
- [66] E. L. Laskowski and J. F. Donoghue. A model of a mercury arc lamp’s terminal V-I behavior. *IEEE Trans. Ind. Appl.*, 1A-17(4):419–426, 1981.
- [67] G. Eardley, B. F. Jones, D. A. J. Mottram, and D. O. Wharmby. A simple model of metal-halide arcs. *J. Phys. D: Appl.*, 12:1101–1115, 1979.
- [68] P. Flesch and M. Neiger. Ac modelling of D2 automotive HID lamps including plasma and electrodes. *J. Phys. D: Appl.*, 37(20):2848–2862, 2004.
- [69] E. Fischer. Modeling of low-power high-pressure discharge lamps. *Philips J. Res.*, 42:58–85, 1997.
- [70] R. H. Springer and W. H. Lake. Thermal balances of HID electrodes. *J. Illum. Eng. Soc.*, 13:304–307, 1984.
- [71] R. Böttcher and W. Böttcher. Numerical modeling of a dynamic mode change of arc attachment to cathodes of high-intensity discharge lamps. *J. Phys. D: Appl.*, 34:1110–1115, 2001.
- [72] R. Böttcher, W. Graser, and A. Kloss. Cathodic arc attachment in a HID model lamp during a current step. *J. Phys. D: Appl.*, 37:55–63, 2004.
- [73] W. Yan, S. Y. R. Hui, and H. Chung. Non-linear high-intensity discharge lamp model including a dynamic electrode drop. In *Proc. IEE Sci. Meas. Technol. conf.*, volume 150, pages 161–167, 2003.
- [74] R. O. Schaffner. Theoretical properties of several metal halide arcs assuming LTE. *Proc. IEEE*, 59(4):622–628, 1971.

- [75] N. Bashlov and G. Zissis. Simulation of the high-pressure mercury discharge lamp during the middle phase of the start-up. *J. Phys. D: Appl.*, 27:494–503, 1994.
- [76] M. Stambouli and A. Asselman. Experimental study of a mercury high-pressure discharge in the course of its start-up phase. *J. Phys. D: Appl.*, 79:99–103, 1996.
- [77] K. M. Hantos and I. T. Cameron. *Process modelling and model analysis*, volume 4. Academic Press, 2001.
- [78] J. Luhmann, S. Lichtenberg, O. Langenscheidt, M. S. Benilov, and J. Mentel. Determination of HID electrode falls in a model lamp II: Lanmuir-probe measurements. *J. Phys. D: Appl.*, 35:1631–1638, 2002.
- [79] A. Kloss, H. Scheidenbach, H. Schöpp, and H. Hess. Electrode-sheath voltage in high pressure mercury arcs. *J. Phys. D: Appl.*, 88(3):1271–1275, 2000.
- [80] R. Keijser. Electronic operation of HID lamps. In *Proc. 9th Int. Symp. Sci. Tech. Light Sources*, number I27, pages 103–111, 2001.
- [81] H. J. Faehnrich and E. Rasch. Electronic ballast for metal halide lamps. *J. Illum. Eng. Soc.*, 17:131–140, 1988.
- [82] T. W. Beeston and L. S. Attrill. Power supply for arc lamps. US Patent 4485434, 1982.
- [83] M. A. Co, C. Z. Rezende, D. S. L. Simonetti, and J. L. F. Vieira. Micro-controlled electronic gear for HID lamps comparisons with electromagnetic ballast. In *Proc. 28th IEEE IECON conf.*, volume 1, pages 468–472, 2002.
- [84] C. M. Huang, T. J. Liang, R. L. Lin, and J. F. Chen. Novel constant power control circuit for HID electronic ballast. *IEEE Trans. Power Electron.*, 22(3):854–862, 2007.
- [85] M. Rico-Secades, E.L. Corominas, J.M. Alonso, J. Ribas, J. Cardesin, A. J. Calleja, and J. Garcia-Garcia. Complete low cost two-stage electronic ballast for 70 W high pressure sodium vapor lamp based on current-mode-controlled buck-boost inverter. In *Proc. 37th IEEE IAS conf.*, volume 3, pages 1841–1846, 2002.
- [86] T. J. Liang, C. A. Cheng, and W. S. Lai. A novel two-stage high-power-factor low-frequency HID electronic ballast. In *Proc. 28th IEEE IECON conf.*, volume 3, pages 2607–2612, 2003.
- [87] M. Marx, D. Schröder, B. Ertl, and F. Bernitz. Single-stage high power-factor electronic ballast. In *Proc. 7th EPE PEMC conf.*, pages 296–300, 1996.

- [88] M. A. Dalla-Costa, D. A. Alvarez, J. M. Alonso, J. Garcia, and J. Cardesin. Design and implementation of a microcontroller based high power factor electronic ballast to supply metal halide lamps. In *Proc. 32th IEEE IECON conf.*, pages 1944–1949, 2006.
- [89] J. Zhao, M. Shen, M. Chen, and Z. Qian. A novel low-frequency square wave electronic ballast for low-wattage HID lamps. In *Proc. 38th IEEE IAS conf.*, volume 1, pages 321–324, 2003.
- [90] F. J. Diaz, J. Azcondo, R. Casanueva, and R. Zane C. Branas. Digital control of a low-frequency square-wave electronic ballast with resonant ignition. *IEEE Trans. Ind. Electron.*, 55(9):3180–3191, 2008.
- [91] J. Zhou, F. Tao, F. C. Lee, N. Onishi, and M. Okawa. High power density electronic ballast for HID lamps. In *Proc. 37th IEEE IAS conf.*, volume 3, pages 1875–1880, 2002.
- [92] M. Shen, Z. Qian, and F. Z. Peng. Design of a two-stage low-frequency square-wave electronic ballast for HID lamps. *IEEE Trans. Ind. Appl.*, 39(2):424–430, 2003.
- [93] J. Qian. *Advanced single-stage power factor correction techniques*. PhD thesis, Virginia Polytechnic Institute and State University, Blacksburg, 1997.
- [94] M. A. Co, M. Brumatti, D. S. L. Simonetti, and J. L. F. Vieira. Single stage electronic ballast for HID lamps. In *Proc. 38th IEEE IAS conf.*, volume 1, pages 339–344, 2003.
- [95] E. B. Shen. *Alternative topological approaches to the electronic lamp-driver*. PhD thesis, Massachusetts institute of technology, 77 Massachusetts Avenue, Cambridge, 1993.
- [96] F. C. Lee, J. D. van Wyk, D. Boroyevich, G. Lu, and Z. Liang. Technology trends toward a system-in-a-module in power electronics. Technical report, IEEE Circuits and Systems Magazine, 2002.
- [97] Y. Jiang, W. Liu, Y. Liang, J. D. van Wyk, and F. C. Lee. An integrated electronic ballast for high intensity discharge (HID) lamps. In *Proc. 22th IEEE APEC conf.*, volume 1, pages 274–280, 2007.
- [98] Y. Jiang. *Three dimensional passive integrated electronic ballast for low wattage HID lamps*. PhD thesis, Virginia polytechnic institute, 1444 Diamond Springs Rd, Virginia Beach, 2009.
- [99] Electromagnetic compatibility (EMC)-Part 3-2: limits for harmonic current emissions. Technical Report IEC 61000-3-2, International Standard, 2009.
- [100] L. Wuidart. Inherent high power factor topologies. In *Proc. IEEE PEDS conf.*, volume 1, pages 24–28, 1997.

- [101] A. Calleja, J. M. Alonso, J. Ribas, and E. Lopez. Electronic ballast based on single-stage high-power-factor topologies: a comparative study. In *Proc. 28th IEEE IECON conf.*, volume 2, pages 1196–1201, 2002.
- [102] V. Grigore. *Topological issues in single-phase power factor correction*. PhD thesis, Helsinki University of Technology, FIN-02015 HUT, 2001.
- [103] C. Branas, F. J. Azcondo, and S. Bracho. Evaluation of an electronic ballast circuit for HID lamps with passive power factor correction. In *Proc. 28th IEEE IECON conf.*, pages 371–376, 2002.
- [104] O. Garcia, J. A. Cobos, R. Prieto, P. Alou, and J. Uceda. Single phase power factor correction: a survey. *IEEE Trans. Ind. App.*, 18(3):749–755, 2003.
- [105] M.M. Jovanović and Y.J. Jang. State-of-the-art, single-phase, active power-factor-correction techniques for high-power applications- an overview. *IEEE Trans. Ind. App.*, 52(3):701–708, 2005.
- [106] B. Singh, B. N. Singh, A. Chandra, K. Al-Haddadand, A. Pandey, and D. P. Kothari. A review of single-phase improved power quality ac-dc converters. *IEEE Trans. Ind. App.*, 50(5):962–981, 2003.
- [107] L. Huber, B. T. Irving, and M. M. Jovanović. Effect of valley switching and switching-frequency limitation on line-current distortions of DCM/CCM boundary boost PFC converters. *IEEE Trans. Ind. App.*, 24(2):339–347, 2009.
- [108] M. Pieniz, J. R. Pinheiro, and H. L. Hey. An investigation of the boost inductor volume applied to PFC converters. In *Proc. 37th IEEE PESC conf.*, volume 1, pages 1–7, 2006.
- [109] J. Zhang, J. Shao, P. Xu, F. C. Lee, and M. M. Jovanović. Evaluation of input current in the critical mode boost PFC converter for distributed power systems. In *Proc. 16th IEEE APEC conf.*, volume 1, pages 130–136, 2001.
- [110] C. Adragna. Control loop modeling of L6561 based TM PFC. Application note AN1089, STMicroelectronics, 2000.
- [111] L. Huber, B. T. Irving, and M. M. Jovanović. Line current distortions of DCM/CCM boundary boost PFC converter. In *Proc. 23th IEEE APEC conf.*, number 1, pages 702–708, 2008.
- [112] I. Lindroth, P. Melchert, and T. Sahlstrom. Methods of improving efficiency in wide input range boost converters at low input voltages. In *Proc. 22th IEEE IECON conf.*, pages 424–431, 2000.

- [113] D. Maksimovic and R. Erickson. Universal-input, high-power-factor, boost doubler rectifiers. In *Proc. 10th IEEE APEC conf.*, volume 1, pages 459–465, 1995.
- [114] J. C. Salmon. Circuit topologies for single-phase voltage-doubler boost rectifiers. *IEEE Trans. Ind. App.*, 8(4):521–529, 1993.
- [115] A. Ikriannikov and S. Čuk. Direct ac/dc conversion without input rectification. In *Proc. 30th IEEE PESC conf.*, volume 1, pages 181–186, 1999.
- [116] K. S. Oh. MOSFET basics. Application note AN9010, Fairchild Semiconductor, 2000.
- [117] T. Ytterdal, Y. Cheng, and T. A. Fjeldly. *Device Modeling for Analog and RF CMOS Circuit Design*. Number ISBN 0-471-49869-6. John Wiley Sons Ltd., United States, 2003.
- [118] Single-ended metal halide lamps. Technical Report ANSI C78.43-2007, American National Standard, 2007.
- [119] J. H. Park and B. H. Cho. The zero voltage switching (ZVS) critical conduction mode (CRM) buck converter with tapped-inductor. In *Proc. 18th IEEE APEC conf.*, volume 2, pages 1077–1081, 2003.
- [120] S. Hiti and C. Boroyevich. Control of boost converter with adjustable output voltage and unknown resistive load. In *Proc. 25th IEEE PESC conf.*, volume 1, pages 294–300, 1994.
- [121] M. Orabi and T. Ninomiya. A unified design of single-stage and two-stage pfc converter. In *Proc. 34th IEEE PESC conf.*, volume 4, pages 1720–1725, 2003.
- [122] H. K. Unger. *DALI Manual*. DALI Activity Group, www.dali-ag.org, 2001.
- [123] A. F. J. Almering and H. A. I. Melai. Dc-ac converter for supplying a gas and/or vapour discharge lamp. EP Patent 0 279 489, 1988.
- [124] V. Vorpérian. Quasi-square-wave converters: topologies and analysis. *IEEE Trans. Power Electron.*, 3:183–191, 1988.
- [125] L. Saro, K. Dierberger, and R. Redl. High-voltage MOSFET behavior in soft-switching converters: analysis and reliability improvements. In *Proc. 20th IEEE INTELEC. conf.*, pages 30–40, 1998.
- [126] A. Fiel and T. Wu. MOSFET failure modes in the zero-voltage-switched full-bridge switching mode power supply applications. In *Proc. 16th IEEE APEC conf.*, volume 2, pages 1247–1252, 2001.

- [127] Y. Jiang, J. Zhou, and Z. Qian. A novel single stage single switch PFC converter with constant power control for ballast for medium HID lamps. In *Proc. 35th IEEE IAS conf.*, volume 5, pages 3415–3418, 2000.
- [128] Low-frequency square wave electronic ballasts for metal halide lamps. Technical Report ANSI C82.14-2006, American National Standard, 2006.
- [129] W. P. Moskowitz and J. Olsen. Measuring ripple generated by an HID ballast. In *Proc. 10th Int. Symp. Sci. Tech. Light Sources*, number P127, pages 439–440, 2004.
- [130] J. Olsen and W. P. Moskowitz. Detrimental effect of a small amount of ripple in a metal halide system. In *Proc. 40th IEEE IAS conf.*, volume 3, pages 1581–1587, 2005.
- [131] E. Santi, Z. Zhang, and S. Čuk. High frequency electronic ballast provides line frequency lamp current. *IEEE Trans. Power Electron.*, 16(5):667–675, 2001.
- [132] E. Deng and S. Čuk. Negative incremental impedance and stability of fluorescent lamp. In *Proc. 12th IEEE APEC conf.*, volume 2, pages 1050–1056, 1997.
- [133] J. Garcia-Garcia, M. Rico-Secades, E. L. Corominas, J. M. Alonso, J. Ribas, and et al. Using solid-state over-voltage protection devices for high intensity discharge lamps ignition. In *Proc. 37th IEEE IAS conf.*, volume 1, pages 363–368, 2002.
- [134] A.D. Jackson. Parasitic capacitance in pulse-start HID lighting systems. *J. Ill. Eng. Soc.*, 28(1):174–181, 1999.
- [135] C. Liu, C. Hu, and Z. Zhang. Analysis and design of igniter for HID ballast. In *Proc. 40th IEEE IAS conf.*, volume 3, pages 1949–1953, 2005.
- [136] W. S. Kim, B. H. Cho, and K. C. Lee. Design and analysis of high-voltage transformer for HID lamp igniter. In *Proc. 20th IEEE APEC conf.*, volume 2, pages 1043–1047, 2005.
- [137] R. H. Randall, A. Laprade, and B. Wood. Characterizing igbt switching losses for switched mode circuits. In *Proc. PCIM Europe conf.*, pages 269–275, 2000.
- [138] J. Ribas, J. M. Alonso, A. J. Calleja, E. Lopez, J. Cardesin, J. Garcia, and et al. Small-signal dynamic characterization of HID lamps. In *Proc. 37th IEEE IAS conf.*, volume 2, pages 1489–1493, 2002.
- [139] R. Osorio, M. A. Oliver, M. Ponce, S. E. Pinto, M. Juarez, and R. Katebi. Analysis and design of discrete-sliding-mode control for a square-waveform-ballast. In *Proc. 44th IEEE Dec. and Contr. conf.*, pages 584–589, 2005.

- [140] R. Osorio, M. Ponce, and M. A. Oliver. Analysis and design of a dimming control using sliding mode control strategy for electronic ballast free of acoustic resonances. In *Proc. 19th IEEE APEC conf.*, pages 159–163, 2004.
- [141] J. Ribas, J. M. Alonso, A. J. Calleja, E. Lopez, J. Cardesin, and J. Garcia. Arc stabilisation in low-frequency square-wave electronic ballast for metal halide lamps. In *Proc. 18th IEEE APEC conf.*, pages 1179–1184, 2003.
- [142] R. Guo, Y. Yang, and Z. Qian. Investigation on the start-up of low wattage metal halide lamp controlled by low-frequency square-wave ballast. In *Proc. 32th IEEE IECON conf.*, pages 815–819, 2005.
- [143] G. Sobierajski and W. Peterson. A wide bandwidth low noise xenon lamp-ballast. In *Proc. 38th IEEE IAS conf.*, volume 1, pages 316–320, 2003.
- [144] F. J. Azcondo, F. J. Diaz, R. Casanueva, C. Branas, and R. Zane. Low frequency square wave electronic ballast with resonant ignition using digital mode and power control. In *Proc. 21th IEEE APEC conf.*, pages 1044–1050, 2006.
- [145] S. Glozman and S. Ben Yaakov. Dynamic interaction of high frequency electronic ballasts and fluorescent lamps. In *Proc. 31th IEEE PESC conf.*, volume 3, pages 1363–1368, 2000.
- [146] K. Günther. Electronic optimization of HID lamps. In *Proc. 7th Int. Symp. Sci. Tech. Light Sources*, pages 93–100, 1995.
- [147] I. K. Lee, S. J. Choi, K. C. Lee, and B. H. Cho. Modeling and control of automotive HID lamp-ballast. In *Proc. IEEE PEDS conf.*, volume 1, pages 506–510, 1999.
- [148] J. Chen, R. Erickson, and D. Maksimovic. Average switch modeling of boundary conduction mode dc-to-dc converters. In *Proc. 27th IEEE IECON conf.*, pages 844–849, 2001.
- [149] S. Ben Yaakov and D. Adar. Average models as tools for studying the dynamics of switch mode dc-dc converters. In *Proc. 25th IEEE PESC conf.*, volume 2, pages 1369–1376, 1994.
- [150] P. D. Gregor, Y. M. Li, A. B. Budinger, and W. W. Byszewski. Arc tube transparency loss due to starting of HID lamps. *J. Illum. Eng. Soc.*, 25(2):150–159, 1996.
- [151] A. Lenef, B. Budinger, and C. Peters. Arc spot formation on cold cathodes in high-intensity discharge lamps. *IEEE Tran. Plasma Sci.*, 30(1):208–218, 2002.

- [152] D. C. Fromm and A. Hohlfeld. Reduced flickering of metal halide lamps optimized electrode design. In *Proc. 6th Int. Symp. Sci. Tech. Light Sources*, volume 22, pages 69–76, 1993.
- [153] G. H. Derra, E. H. Fischer, H. G. Ganser, T. Krücken, H. Moench, and R. Snijkers. Long life discharge lamp operation circuit with reduced lamp flicker. WO Patent 2000036883, 2000.
- [154] L. A. Zadeh. Fuzzy sets. *J. Inform. Contr.*, 8:338–352, 1965.
- [155] P. Mattavelli, L. Rossetto, G. Spiazzi, and P. Tenti. General-purpose fuzzy controller for dc/dc converters. In *Proc. 10th IEEE APEC conf.*, volume 2, pages 723–730, 1995.
- [156] E. Schnedler and H. van Wijngaarde. Ultra high-intensity short-arc long-life lamp system. In *Proc. 26th SID Int. Symp.*, pages 131–134, 1995.
- [157] K. Strobl, T. Bartlett, M. Davis, and L. Yoder. Technology to enable micro-portable DLP projectors. In *SID Int. Symp. 32th*, pages 1278–1281, 2001.
- [158] E. Fischer and H. Hoerster. High pressure mercury vapour discharge lamp. US Patent 5109181, 1992.
- [159] D. Derra, H. Moench, E. Fischer, H. Giese, U. Hecktfischer, and G. Heusler. UHP lamp systems for projection applications. *J. Phys. D: Appl.*, 38:2995–3010, 2005.
- [160] H. Nieuwenhuizen, D. Vanderhaeghen, G. Derra, H. Regt, and A. Bock. High pressure discharge lamp. WO Patent 0077826, 2000.
- [161] H. Moench, G. Derra, E. Fischer, and X. Rieder. Arc stabilization for short arc projection lamps. In *Proc. 31th SID Int. Symp.*, pages 84–87, 2000.
- [162] H. Moench, G. Derra, E. Fischer, and X. Rieder. UHP lamps for projection systems. In *SID Int. Display Workshop 7th*, 2000.
- [163] M. Carpaij. *Tungsten transport process in Ultra-High Pressure mercury lamps*. PhD thesis, Universität Fridericiana Karlsruhe, Kaiserstraße 12, Karlsruhe, 2005.
- [164] A. Kunzman and G. Pettitt. White enhancement for color sequential DLP. In *Proc. 29th SID Int. Symp.*, page 121, 1998.
- [165] L. J. Hornbeck. Digital light processing for high-brightness high-resolution applications. In *Proc. SPIE*, volume 3013, pages 27–40, 1997.
- [166] DLP projection system. <http://www.dlp.com/technology/how-dlp-works>.

- [167] S. Arimoto. *Mathematical theory of learning with applications to robot control*, pages 379–388. Yale University, New Haven, Connecticut, USA, 1985.
- [168] P. Bondi, G. Casalino, and L. Gambardella. On the iterative learning control theory for robotic manipulators. *IEEE J. Rob. Aut.*, 4(1):14–22, 1988.
- [169] M. Q. Phan and R. W. Longman. A mathematical theory of learning control, of linear discrete multivariable systems. In *Proc. AIAA/AA Astro. Spec. conf.*, pages 740–746, 1988.
- [170] R. L. Tousain, E. van der Meche, and O. Bosgra. Design strategies for iterative learning control based on optimal control. In *Proc. 40th IEEE CDC conf.*, volume 5, pages 4463–4468, 2001.
- [171] K. L. Moore. A matrix fraction approach to higher-order iterative learning control : 2d dynamics through repetition-domain filtering. In *Proc. 2th Int. Work. Mult. Sys. conf.*, pages 99–104, 2000.
- [172] D. de Roover. *Motion control of a wafer stage: A design approach for speeding up IC production*. PhD thesis, Delft Univ. Tech, Mekelweg 2, Delft, 1997.
- [173] I. Rotariu, R. Ellenbroek, and M. Steinbuch. Time frequency analysis of a motion system with learning control. In *Proc. American Control conf.*, volume 4, pages 3650–3654, 2003.
- [174] B. G. Dijkstra. *Iterative learning control with application to a wafer stage*. PhD thesis, Delft Univ. Tech, Mekelweg 2, Delft, 2009.
- [175] S. Weiland and C. Scherer. Lecture notes DISC course on linear matrix inequalities in control. TU/e Department of Electrical Engineering P.O. Box 513; 5600 MB The Netherlands, 1999.
- [176] E. C. Guest, M. H. Girach, S. A. Mucklejohn, and U. Rast. Effects of dimming 150 W ceramic metal halide lamps on efficacy, reliability and lifetime. *J. Light. Res. Tech.*, 40(4):333–346, 2008.
- [177] G. H. Ellis. *Observers in control systems: a practical guide*. Academic Press, United States, 2 edition, 2002.
- [178] K. Rajashekara, A. Kawamura, and K. Matsuse, editors. *Sensorless control of ac motor drivers*. IEEE Press, United States, 1996.
- [179] T. G. M. M. Kappen. Status quo of ceramic material for metal halide discharge lamps. *J. Phys. D: Appl.*, 38(17):3033–3039, 2005.

-
- [180] W. van Erk. Transport processes in metal halide gas discharge lamps. In *Proc. 10th Pure Appl. Chem. conf.*, volume 72, page 21592166, 2000.
 - [181] R. Keijser. Dimming of metal halide lamps. In *Proc. 8th Int. Symp. Sci. Tech. Light Sources*, number C18, pages 226–227, 2001.
 - [182] D. C. Fromm, G. H. Lieder, and K. H. Gleixner. Investigation of the connection between plasma temperature and electrode temperature in metal-halide lamps. *J. Phys. D: Appl.*, 35(14):1668–1680, 2002.
 - [183] J. Mentel, J. Luhmann, and D. Nadelstädt. Experimental investigation of electrodes for high pressure discharge lamps. In *Proc. 35th IEEE IAS conf.*, volume 5, pages 3293 – 3300, 2000.
 - [184] G. C. Wei. Transparant ceramic lamp envelope materials. *J. Phys. D: Appl.*, 38(17):3057–3065, 2005.

Samenvatting

De steeds verder toenemende energie consumptie en de daarmee gepaard-gaande toepassing van fossiele brandstoffen vormen een bedreiging voor de natuurlijke voorraden en het klimaat op aarde. Wereldwijd verbruikt de net gekoppelde elektrisch verlichting 19 % van de totale globale elektriciteitsproductie. In dit perspectief speelt de transitie naar energiezuinige verlichting een belangrijke rol. Een van de belangrijke technologieën in deze transitie is hoge-druk gas-ontladings (HID) verlichting. De technische revolutie in gas-ontladings lampen heeft geresulteerd in de hoog-efficiënte lampen welke vandaag de dag beschikbaar zijn.

Vergelijkbaar met de meeste energie efficiënte lampen is voor het bedrijven van HID lampen een ballast noodzakelijk. Traditioneel waren elektromagnetische (EM) ballasten de enige mogelijkheid voor HID verlichtings-systemen. Vandaag de dag maken elektronische lamp-drivers additionele energiebesparing, flicker-vrij licht, en miniaturisatie mogelijk. Elektronisch lamp bedrijf biedt een aantal additionele vrijheidsgraden in lampstroom controle ten opzichte van conventionele EM ballasten. De lamp-driver systeemprestatie hangt af van zowel de dynamica van de lamp als van de driver.

Deze dissertatie focust op de optimalisatie van elektronisch bedreven HID verlichtingssystemen, hoog-efficiënte lamp-driver topologieën, en lamp-driver interactie regelingen. Ten eerste zijn hoog-efficiënte vermogens topologieën onderzocht om compacte HID lampen te bedrijven op een laag-frequente blokstroom. De voorgestelde tweetraps elektronische lamp-driver bestaat uit een ac-dc inverter (PFC) om aan de netstroom eisen te voldoen, en is sequentieel gekoppeld aan een gecascadeerde buck converter om de lampstroom te regelen. Beide secties worden bedreven in transition mode (TM) mode om de schakelverliezen te beperken. De resulterende tweetraps lamp-driver excelleert wat betreft goede bestuurbaarheid, hoge-efficiëntie, en grote vermogensdichtheid, en is geschikt voor “power sandwich packaging”.

Ten tweede, lamp-driver interactie (LDI) is bestudeerd in het simulatiedomein, en regelalgoritmes zijn onderzocht ten behoeve van het verbeteren van de stabiliteit en mogelijk maken van systeem optimalisatie. Twee HID lampmodellen zijn ontwikkeld. Het eerste model beschrijft het elektrische klein-signaal gedrag van een HID lamp ten behoeve van het bestuderen van de interactie stabiliteit. Het tweede HID lampmodel is gebaseerd op fysische vergelijkingen van de

boogontlading en het elektrode gedrag, en is geschikt voor lamp-driver simulaties en regelsysteem applicaties. Verificatie metingen laten zien dat de elektrische karakteristieken aan de lampklemmen voorspeld kunnen worden over een breed vermogens en frequentiegebied.

Gebruikmakend van de voorgestelde lampmodellen zijn drie LDI regelsysteem algoritmes onderzocht. Het eerste regelsysteem principe optimaliseert de LDI voor een breed scala van HID lampen bedreven op vol en gereduceerd vermogen. Deze aanpak bestaat uit twee regellussen geïntegreerd in een fuzzy-logic lamp-driver regelsysteem om de lampstroom te stabiliseren en de commutatie te optimaliseren. Het tweede regelprobleem betreft de toepassing van ultra high performance (UHP) HID lampen in projectie toepassingen. Deze stellen strenge eisen aan de kwaliteit van de lampstroom en de daaraan gecorreleerde lichtstroom opgewekt door de lamp. In deze systemen treden periodieke verstoringen op synchroon met de laag-frequent blokstroom commutatie periode. Iterative learning control (ILC) is onderzocht, en het is experimenteel geverifieerd dat deze repeterende verstoringen kan compenseren. Ten derde, elektronisch HID lamp bedrijf opent de deur voor het continue dimmen van HID lampen. Dit kan een additionele energiebesparing opleveren. Om stabiel dimmen mogelijk te maken is een regel principe ontwikkeld dat gebaseerd is op een HID lamp observer. Dit algoritme maakt een stabiel minimum dim niveau en het observeren van de gas-ontlading gedurende de gehele levensduur mogelijk. De HID lamp observer voorspeld fysische lamp grootheden die nauw verbonden zijn met de licht technische eigenschappen. Tenslotte, praktische metingen hebben het principe van het voorgestelde HID lamp observer regelsysteem bewezen.

Acknowledgements

Many people have contributed directly or indirectly to the concepts presented in this thesis. First and foremost, I would like to express my sincere gratitude to my supervisors dr. Jorge Duarte and ir. Marcel Hendrix for their continuous support of my PhD study, numerous fruitful discussions and reviewing comments. Their guidance helped me throughout my research to move forward with the investigations and to finalise this thesis step by step. Special acknowledgement and appreciation goes to prof. Elena Lomonova and prof. André Vandenput (who passed away on 11 January 2008) for their encouragement and insightful scientific advice.

I want to thank the Philips LightLabs department supervisors for giving me permission to commence this thesis, do the necessary research work and use departmental data. My sincere thanks goes to my former colleagues from Philips Lighting who supported me in my research work. Particular acknowledgement goes to dr. Rob Tousain both for sharing his knowledge and for his cooperative work on the ILC experiments that resulted in joint publications. Outside the lab, I would like to thank Ivan Josifović MSc for his valuable contributions to this research regarding power density packaging of HID lamp-drivers.

Finally, I would like to thank my family and friends and everybody who was important to the successful realisation of this thesis.

Curriculum Vitae

Dolf van Casteren was born on September 2th 1972 in Oss, the Netherlands. After finishing his secondary education he started the Electrical Engineering program at the Fontys University of Applied Sciences, Eindhoven and received his BSc degree in 1996. Thereafter, he went to the Eindhoven University of Technology (TU/e) and received his MSc degree in 1999. During his first traineeship at AKZO-Nobel he worked on improving the reliability of an industrial power plant with heat-power coupling. Subsequently, at KEMA Transport & Distribution he investigated the protection of solar systems. The topic of his MSc graduation project was “Dimming of metal halide lamps” carried out by Philips Lighting Electronics. In September 1999 he started as a development engineer at Philips Lighting. Since then he has worked in several project teams and contributed to product innovations. These activities have resulted in several publications and patents. In 2004, he started as a part-time PhD student in the group of electromechanics and power electronics (EPE) at the electrical engineering faculty at the TU/e. He has worked on the topic of “Electronic operation and control of high-intensity gas-discharge lamps”, of which this thesis is the result.